NONLOCAL NONLINEAR OPTICS IN GRAPHENE AND THE OPTICS OF WEYL SEMIMETALS

A Dissertation

by

ARJUNEN RYAN KUTAYIAH

Submitted to the Office of Graduate and Professional Studies of
Texas A&M University
in partial fulfillment of the requirements for the degree of

DOCTOR OF PHILOSOPHY

Chair of Committee,	Alexey Belyanin
Committee Members,	Ohannes Eknoyan
	Joseph Ross
	Aleksei Zheltikov
Head of Department,	Grigory Rogachev

May 2019

Major Subject: Physics

ABSTRACT

Theoretical models are constructed for various nonlocal nonlinear optical processes in graphene. Specifically, difference frequency generation of surface plasmon-polaritons in Landau quantized graphene; the generation of entangled surface plasmon-polariton-photon states and laser-driven paramatric instability via stimulated parametric down-converstion are explored. Difference generation and parametric down-conversion are three-wave mixing processes that are mediated by the nonlocal nonlinear (second-order) in-plane susceptibility.

Systematic theoretical studies of both the bulk and surface electromagnetic eigenmodes, or polaritons, in Weyl semimetals are developed. The tensors of the bulk and surface conductivity are presented. Information about the electronic structure of Weyl semimetals, such as position and separation of Weyl nodes, Fermi energy, and Fermi arc surface states, can be extracted from measurements of the dispersion, transmission, reflection, and polarization of electromagnetic waves.

DEDICATION

To my maternal relatives.

ACKNOWLEDGMENTS

Above all else, I would like to thank God.

I would like to thank my advisor and mentor Dr. Alexey Belyanin. His enthusiasm for physics is infectious, his knowledge inspiring, and his patience admirable. I count myself fortunate to be among his students. I am deeply appreciative of his willingness to solve problems with me and have extended discussions. I especially enjoyed those discussions where Alexey would stare out the window, seemingly searching for an answer to a problem I presented him with. Lo and behold, on most occasions he would produce the solution. If only my office had windows!

I am grateful to my committee members for allowing me to have a portion of their valuable time. I am appreciative of your insights and suggestions. Thank you.

I would like to thank former and present members of the Belyanin group, Sultan Almutairi, Qianfan Chen, Zhongqu Long, Xianghan Yao, and Yongrui Wang, for the numerous discussions we have had throughout the years. I especially owe a debt of gratitude to Yongrui Wang who has guided me through uncharted territories when I first began my research journey.

I am grateful to the faculty and staff of Texas A&M University's physics department for facilitating a smooth and enjoyable transit through the doctorate program. I was particularly fond of the Physics Festival, thank you Tatiana Erukhimova.

I would like to thank my friends for their companionship and support. Amin Barzegar and Sunny Guha, aside from being badminton and squash buddies, have been instrumental in helping me work through some of my coding issues.

I am beholden to my maternal side of the family: mom, nanny and nana, aunty Bedo, aunty Jean, aunty Sati, uncle Rick and their respective spouses. They are the embodiment of love, generosity and compassion. Were it not for them, my brother Brian and I would not be where we are today. I would especially like to thank my mother Sarah, my aunt Jean and my grandmother Chan as they have made many sacrifices so that Brian, and I would have the best in life (relative to what they could provide). To Brian, I could not ask for a better brother. You have been my best friend

and have always been there for me. To Anthony Ramdass, thank you for being my unfailing best friend for 17 years. We have been through much together. (Long live the Tripod!)

Alas, I come now to acknowledging my wonderful wife, Erica. Thank you for listening to my endless “nerd-talk." Thank you for your love, support, patience and understanding. I know this journey has been a difficult one for you especially since many tasks fell to you while I was trying to wrap-up my studies. I appreciate the sacrifices you have made. Thank you for proofreading my dissertation even though it is no where near as exciting that the fantasy books you read. I would say it is even more exciting! To my son Archer, you have made this journey simultaneously more enjoyable and challenging. But I would not have it any other way! Archer and Erica, thank you for the many distractions you have provided, welcomed or not!

CONTRIBUTORS AND FUNDING SOURCES

Contributors

This work was supported by a dissertation committee consisting of Professors Alexey Belyanin [advisor/chair], Joseph Ross, and Aleksei Zheltikov of the Department of Physics & Astronomy and Professor Ohannes Eknoyan of the Department of Electrical & Computer Engineering.

The initial idea for all projects presented in this dissertation were proposed by Dr. Alexey Belyanin and collaborator Dr. Mikhail Tokman of the Institute of Applied Physics, Russian Academy of Sciences.

Dr. Tokman lead the project presented in Chapter 3. Many of the calculations and theoretical developments are attributed to him. Dr. Yongrui Wang of the Department of Physics & Astronomy at Texas A&M University made two figures and developed part of the theory. In the same chapter, Dr. Ivan Oladyshkin of the Institute of Applied Physics, Russian Academy of Sciences also contributed to the theoretical development.

A fellow member of the Belyanin group, Qianfan "Paul" Chen, lead the project presented in Chapter 4. He made fifteen figures, although it should be noted that there was some overlap since we made some of the same figures independently. He developed part of the theory as well and calculated the matrix elements necessary to obtain the conductivity tensors. In the same chapter, Dr. Ivan Oladyshkin of the Institute of Applied Physics, Russian Academy of Sciences also contributed to the theoretical development.

All other work conducted for the dissertation was completed by the student independently.

Funding Sources

Graduate study was supported by the following fellowships from Texas A&M University: the Louis Stokes Alliance for Minority Participation Bridge to the Doctorate Program and the Graduate Merit Fellowship.

TABLE OF CONTENTS

Page

ABSTRACT ii

DEDICATION iii

ACKNOWLEDGMENTS iv

CONTRIBUTORS AND FUNDING SOURCES vi

TABLE OF CONTENTS vii

LIST OF FIGURES x

1. INTRODUCTION 1

    1.1 Tools of the Trade 1
        1.1.1 Density Matrix Equation 2
        1.1.2 Kubo-Greenwood Conductivity 5
        1.1.3 Three-Wave Mixing: DFG 9
    1.2 Graphene 15
        1.2.1 Tight-Binding Model 17
        1.2.2 Magnetic Field 27

2. DIFFERENCE FREQUENCY GENERATION OF SURFACE PLASMON-POLARITONS IN LANDAU QUANTIZED GRAPHENE 33

    2.1 Opening Remarks 33
    2.2 Introduction 33
    2.3 Optical Fields in a Waveguide 34
    2.4 Optical Selection Rules 40
    2.5 Linear Optical Conductivity 44
    2.6 Surface Charge Density 45
    2.7 Surface Plasmon-Polaritons 48
    2.8 Difference Frequency Generation of Surface Plasmon-Polaritons 55
    2.9 Poynting Flux in a SPP Mode 58
    2.10 Absorption by Graphene 63
    2.11 Summary 66

3. LASER-DRIVEN PARAMETRIC INSTABILITY AND GENERATION OF ENTANGLED PHOTON-PLASMON STATES IN GRAPHENE 67

3.1 Opening Remarks 67
3.2 Introduction 67
3.2.1 Heisenberg-Langevin Equation 69
3.3 Quantized SPP Field in Graphene 75
3.4 Parametric Instability in Graphene 80
3.5 A Coupled Oscillators Model for Parametric Gain 84
3.6 The Spectrum and Magnitude of Parametric Gain 85
3.7 Generated Idler Field Flux 88
3.8 Plasmon-Photon Entanglement 89
3.9 Summary 91

4. OPTICAL PROPERTIES AND ELECTROMAGNETIC MODES OF WEYL SEMIMETALS 92

4.1 Opening Remarks 92
4.2 Introduction 92
4.2.1 Weyl Fermions 94
4.2.2 Berry Phase 100
4.3 Effective Hamiltonian 107
4.3.1 Hamiltonians 1 and 2 109
4.3.1.1 Bulk States 109
4.3.1.2 Reflection from the Boundary: Surface States and Fermi Arcs 111
4.3.2 Hamiltonian 3 113
4.3.2.1 Bulk States Near the Boundary 114
4.3.2.2 Surface States 114
4.3.3 The Boundary Orthogonal to the Gyrotropy Axis 116
4.3.4 Comparison of Hamiltonians 1, 2, and 3 116
4.4 Optical Transitions and the Tensors of Bulk and Surface Conductivity 118
4.4.1 Evaluation of Tensors of the Bulk and Surface Conductivity 120
4.4.1.1 The Matrix Elements of the Current Density Operator 121
4.4.1.2 The Bulk Optical Conductivity Tensor 123
4.4.1.3 The Surface Conductivity Tensor 128
4.4.1.4 Drude-like Low-Frequency Limit 130
4.4.1.5 Small b Expansion 131
4.4.2 Discussion of the Conductivities 132
4.5 Bulk Polaritons in Weyl Semimetals 138
4.5.1 Propagation Perpendicular to the Anisotropy Axis 138
4.5.2 Propagation Perpendicular to the y Axis 142
4.5.3 Oblique Propagation of Bulk Polaritons 145
4.6 Boundary Conditions 146
4.7 Reflection from the Surface of a Weyl Semimetal 153
4.7.1 Reflection with Excitation of an O-mode 153
4.7.2 Reflection with Excitation of an X-mode 154
4.7.2.1 Reflection in The Vicinity of Plasmon Resonance 156
4.8 Surface Plasmon-Polaritons 161

4.8.1 Quasielectrostatic Approximation 161
4.8.1.1 Neglecting Surface States 163
4.8.1.2 Including Surface States 164
4.8.2 Surface Waves Beyond the Quasielectrostatic Approximation 165
4.9 Summary 170

5. CONCLUSION 171

REFERENCES 173

LIST OF FIGURES

FIGURE Page

1.1 Sketch of carbon-carbon bonding in graphene. Adapted from [5]. 16
1.2 Honeycomb lattice in graphene. 17

1.3 FBZ given by green hexagon. Reciprocal lattice vectors $\boldsymbol{b}_1$ and $\boldsymbol{b}_1$. Corners of the FBZ given by $\boldsymbol{K}$ and $\boldsymbol{K}'$. 24

2.1 Two counter-propagating pump fields incident on a waveguide with graphene at the interface of dielectrics ϵ_2 and ϵ_3. 35
2.2 Waveguide configurations. Adapted with permission from [13]. 36

2.3 Sketch of LLs and resonant coupling of particular components and frequencies of the pump fields to LLs. Adapted with permission from [13]. 44

2.4 Sketch of DFG scheme and resonant coupling of all EM modes to LLs. $\mathcal{E}_F$ is the Fermi level. Reprinted with permission from [13]. 49

2.5 The DFG frequency resonant to the transition between Landau-level numbers 2 and 4 as a function of the magnetic field strength. Reprinted with permission from [13]. 60

2.6 DFG power per 1 W of a pump power as a function of the waveguide core thickness for the magnetic field strength 1T. In the legend of the plot “middle” means that graphene is in the middle of the core dielectric ϵ_2; “interface” means that graphene is located at the interface of dielectrics ϵ_2 and ϵ_3. “1T" and “3T" stands for 1 and 3 Tesla magnetic field. Reprinted with permission from [13]. 60

2.7 DFG power per 1 W of a pump power as a function of core thickness for the magnetic field strength 3 T. A higher magnetic field is chosen to avoid THz absorption in Si. Reprinted with permission from [13]. 61

2.8 The DFG power per 1 W of a pump power as a function of the magnetic field for several waveguide structures and geometries. In the legend of the plot “middle” means that graphene is in the middle of the core dielectric ϵ_2; “interface” means that graphene is located at the interface of dielectrics ϵ_2 and ϵ_3. Reprinted with permission from [13]. 61

2.9 Absorption length for pump field intensity and DFG plasmon-polaritons as a function of core thickness for a symmetric GaAs waveguide with graphene at the interface. The magnetic field is 1T. Reprinted with permission from [13]. 64

2.10 Absorption length for pump field intensity and DFG plasmon-polaritons as a function of the magnetic field for a symmetric GaAs waveguide with graphene at the interface. The core thickness is $0.06\lambda_1$. Reprinted with permission from [13]. 65

3.1 Schematic of the parametric decay process. Reprinted with permission from [27]. ... 69

3.2 Gain Re$[G]$ (solid blue line) and the plasmon frequency corresponding to phase matching conditions (green dashed line) as a function of the angle θ_{1i} between the direction of the idler wavevector in medium 1 and the normal. Reprinted with permission from [27]. 86

3.3 Pumping intensity I_p needed to reach the parametric instability threshold, Re$[G] = \gamma_s$ in Eq. (3.66), as a function of the plasmon decay rate γ_s. Reprinted with permission from [27]..... 87

4.1 Bulk energy dispersion for Hamiltonian 2 on the surface $k_z = 0$. Here the energy is normalized by $\hbar v_F b$ and $k_{x,y}$ are normalized by b. Reprinted with permission from [59]..... 110

4.2 (a) Contours of constant energy surfaces for Hamiltonian 2 on the surface $k_z = 0$. The dotted circle is the boundary of a region $k_x^2 + k_y^2 \leq b^2$ where surface states exist. (b) Contours of constant energy surfaces for Hamiltonian 1 on the surface $k_z = 0$. Here $x, y = k_{x,y}/b$. The dotted lines indicate the boundary of a region $k_x^2 \leq b^2$ where surface states exist. Reprinted with permission from [59]..... 117

4.3 Real and imaginary parts of the ε_{xx} component of the dielectric tensor as a function of frequency for $\hbar v_F b = 100$ meV, dephasing rate $\gamma = 10$ meV, and $\varepsilon_{xx}^{(0)} = 10$. Reprinted with permission from [59]..... 134

4.4 Real and imaginary parts of the ε_{yy} component of the dielectric tensor as a function of frequency for $\hbar v_F b = 100$ meV, dephasing rate $\gamma = 10$ meV, and $\varepsilon_{yy}^{(0)} = 10$. Reprinted with permission from [59]..... 135

4.5 Real and imaginary parts of the ε_{zz} component of the dielectric tensor as a function of frequency for $\hbar v_F b = 100$ meV, dephasing rate $\gamma = 10$ meV, and $\varepsilon_{zz}^{(0)} = 10$. Reprinted with permission from [59]..... 136

4.6 Real and imaginary parts of $g = \frac{4\pi\sigma_{yz}^B}{\omega}$ as a function of frequency for $\hbar v_F b = 100$ meV and dephasing rate $\gamma = 10$ meV. 137

4.7 Real and imaginary parts of the refractive index n_O of an O-wave as a function of frequency for $E_F = 80$ meV, $\hbar v_F b = 100$ meV, and dephasing rate $\gamma = 10$ meV. Reprinted with permission from [59]. 139

4.8 Real and imaginary parts of the refractive index n_X of an X-wave as a function of frequency for different values of the propagation angle θ. Other parameters are $E_F = 80$ meV, $\hbar v_F b = 100$ meV, and dephasing rate $\gamma = 10$ meV. Reprinted with permission from [59]. 141

4.9 Real part of the bulk plasmon resonance frequency at normal incidence $\theta = 0$ as a function of the Fermi energy. Reprinted with permission from [59]. 142

4.10 Spectra of real and imaginary parts of the polarization coefficient $K_X = E_z/E_y$ for an incident wave linearly polarized in y-direction after traversing a 1-μm film in x-direction. Reprinted with permission from [59]. 144

4.11 Spectra of the real and imaginary parts of the xx component of the surface conductivity at several values of the Fermi momentum for $\hbar v_F b = 100$ meV and dephasing rate $\gamma = 10$ meV. Reprinted with permission from [59]. 149

4.12 Spectra of the real and imaginary parts of the yy component of the surface conductivity at several values of the Fermi momentum for $\hbar v_F b = 100$ meV and dephasing rate $\gamma = 10$ meV. Reprinted with permission from [59]. 150

4.13 Spectra of the real and imaginary parts of the zz component of the surface conductivity at several values of the Fermi momentum for $\hbar v_F b = 100$ meV and dephasing rate $\gamma = 10$ meV. Reprinted with permission from [59]. 151

4.14 Spectra of the real and imaginary parts of the yz component of the surface conductivity at several values of the Fermi momentum for $\hbar v_F b = 100$ meV and dephasing rate $\gamma = 10$ meV. Reprinted with permission from [59]. 152

4.15 Real part reflection obtained from equation Eq. (4.180) for $n_{up} = 1$, $\hbar v_F b = 100$ meV and two values of the electron Fermi momentum $k_F = 0.2b$ and $0.5b$. 159

4.16 Real part reflection obtained from equation Eq. (4.180) for $n_{up} = 1$, $\hbar v_F b = 100$ meV and two values of the electron Fermi momentum $k_F = 0.8b$ and $1.0b$. 160

4.17 Real part of the surface plasmon frequency as a function of real plasmon wavenumber obtained as a solution to the dispersion equation Eq. (4.190) for $\phi = \pi/2$, $\hbar v_F b = 100$ meV and two values of the electron Fermi momentum $k_F = 0.5b$ and $0.8b$. The surface plasmon frequency neglecting surface conductivity contribution is shown as a dashed line. Reprinted with permission from [59]. 168

4.18 Normalized confinement constants (a) $\mathrm{Re}[\kappa_{up}]/k_0 \simeq \mathrm{Re}[\sqrt{2\delta k/k_0}]$ and (b) $\mathrm{Re}[\kappa_W]/k_0$ as functions of frequency, for the Fermi momentum $k_F = 0.5b$. Other parameters are $\hbar v_F b = 100$ meV and $\gamma = 10$ meV. Reprinted with permission from [59]. 169

1. INTRODUCTION

Theoretical models for various nonlocal nonlinear optical processes in graphene with a focus on plasmonics are constructed. The study of difference frequency generation (DFG) of surface plasmon-polariton (SPP) in Landau quantized graphene is presented. The graphene monolayer serves as a nonlinear optical component of a monolithic photonic chip. It interacts with two input pump fields; through the process of nonlinear frequency mixing, DFG is achieved. It will be shown that surface plasmon-polaritons are generated at the difference frequency of the input pump beams. Laser-driven parametric instability and generation of photon-plasmon entangled state in graphene are explored. The in-plane second-order nonlinear response of graphene to an obliquely incident strong pump field gives rise to parametric instability. The pump field, by way of parametric down-conversion, decays into two lower frequency fields: a photon and surface plasmon-polariton. The generated modes are entangled. A theoretical model is developed to explore the optics of Weyl semimetals (with broken time-reversal symmetry). Tensors of the bulk and surface conductivities are derived. Bulk and surface electromagnetic eigenmodes are investigated. Measurements of the dispersion, transmission, reflection, and polarization of electromagnetic waves serve as a diagnostic tool for the electronic structure of Weyl semimetals (such as position and separation of Weyl nodes, Fermi energy, and Fermi arc surface states).

1.1 Tools of the Trade

The topics addressed in this section serve as a prerequisite for a good portion of this dissertation. Of particular utility, is the von Neumann equation which is used to find the elements of the density matrix, and the Kubo-Greenwood formula for conductivity. In addition, a short introduction to three-wave mixing processes with a focus on difference frequency generation (DFG) is presented. My derivations for the density matrix equation and the three-wave mixing process will

follow Boyd's [1].

1.1.1 Density Matrix Equation

The density matrix formulation is used when the exact state of a quantum mechanical system is not known. A system may start out in a known state but events, such as collisions, may modify the initial state. The lack of knowledge regarding the exact state of the system is taken into account by the density matrix formulation. Specifically, a classical probability $p(s)$ is introduced to find the probability of the system being in a state s. For a system in a state s with corresponding wave function $\psi_s(\boldsymbol{r}, t)$ the wave function can be expanded in terms of the energy eigenfunctions $u_n(\boldsymbol{r})$

$$\psi_s(\boldsymbol{r}, t) = \sum_n c_n^s(t) u_n(\boldsymbol{r}). \tag{1.1}$$

The Hamiltonian considered in this section will be of the form

$$H = H^0 + H^{int}(t) \tag{1.2}$$

where

$$H^0 u_n(\boldsymbol{r}) = \mathcal{E}_n u_n(\boldsymbol{r}), \tag{1.3}$$

and $\mathcal{E}_n$ is the energy value of the n-th eigenstate u_n. The expectation value of an operator O is

$$\langle O \rangle = \int \psi_s^*(\boldsymbol{r}, t) O \psi_s(\boldsymbol{r}, t)\, d^3r = \sum_{m,n} c_m^{s*}(t) c_n^s(t) \int u_m^*(\boldsymbol{r}) O u_n(\boldsymbol{r})\, d^3r \tag{1.4}$$

$$\langle O \rangle = \sum_{m,n} \rho_{nm} O_{mn} = \mathrm{tr}(\rho O). \tag{1.5}$$

Here $\rho_{nm} = c_m^{s*}(t)c_n^s(t)$ is the density matrix; clearly, one knows that the system is in state s. If the state of the system is modified such that it is not known exactly then the expectation value $\langle O \rangle$ is

$$\langle O \rangle = \sum_s \sum_{m,n} p(s) c_m^{s*}(t) c_n^s(t) \int u_m^*(\boldsymbol{r}) O u_n(\boldsymbol{r})\, d^3r \tag{1.6}$$

$$\langle O \rangle = \sum_{m,n} \rho_{nm} O_{mn} = \mathrm{tr}(\rho O). \tag{1.7}$$

Here the density matrix is given by

$$\rho_{nm} = \sum_s p(s) c_m^{s*}(t) c_n^s(t). \tag{1.8}$$

The time-evolution of the density matrix is

$$\dot{\rho}_{nm} = \sum_s \left[(\partial_t p(s)) c_m^{s*} c_n^s + p(s)(\partial_t c_m^{s*}) c_n^s + p(s) c_m^{s*} (\partial_t c_n^s) \right] \tag{1.9}$$

where $\partial_t c_m^{s*}$ and $\partial_t c_n^s$ can be found using Schrödinger's equation

$$i\hbar \partial_t \psi_s = H \psi_s \implies i\hbar \partial_t \sum_n c_n^s(t) u_n(\boldsymbol{r}) = H \sum_n c_n^s(t) u_n(\boldsymbol{r}) \tag{1.10}$$

$$\implies i\hbar \partial_t c_m^s(t) = \sum_n H_{mn} c_n^s(t). \tag{1.11}$$

The orthonormality of the energy eigenstates was used, i.e.

$$\int u_m^*(\boldsymbol{r}) u_n(\boldsymbol{r})\, d^3r = \delta_{mn}.$$

Using Eq. (1.11), and the fact that the Hamiltonian is Hermitian (a requirement for real observables) Eq. (1.9) becomes

$$\dot{\rho}_{nm} = -\frac{i}{\hbar}[H, \rho]_{nm} - \gamma_{nm}(\rho_{nm} - \rho_{nm}^{(eq)}) \tag{1.12}$$

where the term $\sum_s \partial_t p(s) c_m^{s*} c_n$ is accounted for (in the simplest way) through the phenomenological damping term $-\gamma_{nm}(\rho_{nm} - \rho_{nm}^{(eq)})$. γ_{nm} is the phenomenological decay rate at which ρ_{nm} relaxes to its equilibrium value $\rho_{nm}^{(eq)}$. Note that $\gamma_{nm} = \gamma_{mn}$. The calculation of γ_{nm} is far from trivial since γ_{nm} includes impurity and disorder scattering, electron-phonon scattering, electron-electron scattering, etc. Further complications arise when the pump fields create a high number of nonequilibrium carriers. In this case, one would need to incorporate scattering rates for nonequilibrium carriers directly into the density matrix equations coupled with Maxwell's equations for all interacting fields. However, I will assume that the Rabi frequencies of the pump fields are smaller than the carrier relaxation rate, so that the optical population transfer is not important. I will also assume that scattering from impurity is the dominant mechanism for relaxation (especially for pristine graphene or graphene encapsulated by hexagonal boron nitride). Note $\rho_{nm}^{(eq)} = 0$ for $n \neq m$, since the incoherent process of thermal excitation cannot produce any coherent superpositions of atomic states.

The density matrix equation can be solved perturbatively, wherein

$$\rho_{nm} \to \sum_{N=0} \lambda^N \rho_{nm}^{(N)} \tag{1.13}$$

$$H^{int} \to \lambda H^{int}. \tag{1.14}$$

λ is a parameter that varies between zero and one. When Eqs. (1.13) and (1.14) are substituted into in Eq. (1.12) each power of λ holds separately, resulting in the set of equations

$$\dot{\rho}_{nm}^{(N)} = -i(\omega_{nm} - i\gamma_{nm})\rho_{nm}^{(N)} - \frac{i}{\hbar}\left[H^{int}, \rho^{(N-1)}\right]_{nm} \tag{1.15}$$

where $\hbar\omega_{nm} = \mathcal{E}_n - \mathcal{E}_m$. Eqs. (1.15) can be integrated directly. Before doing so, note that the zeroth-order term describes the free evolution of the system, where no perturbation is present ($H^{int} = 0$). For example, if $H^{int}(t)$ corresponds to perturbation by an optical field, then the zeroth-order term corresponds to the density matrix element in the absence of the external field.

The steady state solution of the zeroth-order density matrix equation results in $\rho_{nm}^{(0)} = \rho_{nm}^{(eq)}$. Keep in mind that $\rho_{nm}^{(eq)}$ has no off-diagonal terms. Equipped with the zeroth-order term enables one to proceed in finding the N-th order term. Suppose

$$\rho_{nm}^{(N)}(t) = S_{nm}^{(N)}(t) e^{-i(\omega_{nm} - i\gamma_{nm})t} \tag{1.16}$$

then substituting Eq. (1.16) into Eq. (1.15) gives

$$\dot{S}_{nm}^{(N)}(t) = -\frac{i}{\hbar} \left[H^{int}, \rho^{(N-1)}\right]_{nm} e^{i(\omega_{nm} - i\gamma_{nm})t} \tag{1.17}$$

$$\implies S_{nm}^{(N)}(t) = -\frac{i}{\hbar} \int_{-\infty}^{t} \left[H^{int}, \rho^{(N-1)}\right]_{nm} e^{i(\omega_{nm} - i\gamma_{nm})t'} \, dt'. \tag{1.18}$$

Upon inserting Eq. (1.18) into Eq. (1.16) one obtains an iterative solution for the density matrix

$$\rho_{nm}^{(N)} = -\frac{i}{\hbar} \int_{-\infty}^{t} \left[H^{int}, \rho^{(N-1)}\right]_{nm} e^{i(\omega_{nm} - i\gamma_{nm})(t'-t)} \, dt'. \tag{1.19}$$

By an iterative solution, I mean that first one would solve for $\rho_{nm}^{(1)}$ in terms of $\rho_{nm}^{(0)}$, then solve for $\rho_{nm}^{(2)}$ in terms of $\rho_{nm}^{(1)}$, and so on until the N-term is obtained.

1.1.2 Kubo-Greenwood Conductivity

Below I will derive the Kubo-Greenwood formula for conductivity in the semi-classical approach. Semi-classical, meaning the dielectric medium is quantized while the incident optical field is assumed to be classical. An alternative derivation can be found in Marder's *Condensed Matter Physics* [2] or in Kubo's paper [3].

I will begin by introducing the expectation value of the current density operator

$$\langle \boldsymbol{j} \rangle = \mathrm{tr}(\rho \boldsymbol{j}) = \sum_{nm} \rho_{nm} \left(-\frac{e}{V} \boldsymbol{v}\right)_{mn} = -\frac{e}{V} \sum_{nm} \rho_{nm} \boldsymbol{v}_{mn} \tag{1.20}$$

where V is the volume $\boldsymbol{v}_{mn}$ is the matrix element of the velocity operator and ρ_{nm} is the element of the density matrix.

The linear optical conductivity will be obtained using $\rho_{nm} \rightarrow \rho^{(1)}_{nm}$. $\rho^{(1)}_{nm}$ will be found by making use of Eq. (1.19). For interaction of a dielectric with an optical field the Hamiltonian is given by $H = H^0 + H^{int}(t)$ where

$$H^{int}(t) = -\boldsymbol{d} \cdot \tilde{\boldsymbol{E}}(t). \tag{1.21}$$

$\boldsymbol{d}$ is the electric dipole moment operator (induced in the atom by interaction with an external field) given by

$$\boldsymbol{d} = -e\boldsymbol{r}. \tag{1.22}$$

$\boldsymbol{r}$ is the position operator. $\tilde{\boldsymbol{E}}(t)$ is the electric field of the incident electromagnetic (EM) wave

$$\tilde{\boldsymbol{E}}(t) = \mathrm{Re}[\boldsymbol{E}_R e^{-i\omega t}] = \mathrm{Re}[\boldsymbol{E} e^{i\boldsymbol{k}\cdot\boldsymbol{r} - i\omega t}]. \tag{1.23}$$

Note that $\tilde{\boldsymbol{E}}(t)$ is a classical field and not an operator. In the electric-dipole approximation, which is used when the wavelength of the incident optical field is much longer than the lattice spacing of the medium, $e^{i\boldsymbol{k}\cdot\boldsymbol{r}} \rightarrow 1$. This means that the spatial dispersion of the field is neglected. The field is now $\tilde{\boldsymbol{E}}(t) \rightarrow \mathrm{Re}[\boldsymbol{E}e^{-i\omega t}]$. Note that $\mathrm{Re}[\boldsymbol{E}e^{-i\omega t}] = \boldsymbol{E}e^{-i\omega t} + c.c.$ and $\boldsymbol{E} = (1/2)\boldsymbol{E}_0$.

I will now proceed to solve for the density matrix element $\rho^{(1)}_{nm}$ using Eq. (1.19) and the interaction Hamiltonian given by Eq. (1.21) in the electric-dipole approximation

$$\rho^{(1)}_{nm} = -\frac{i}{\hbar}\int_{-\infty}^{t} \left[-\boldsymbol{d}\cdot(\boldsymbol{E}e^{-i\omega t'} + c.c.), \rho^{(0)}\right]_{nm} e^{i(\omega_{nm} - i\gamma_{nm})(t'-t)}\, dt'. \tag{1.24}$$

Since $\boldsymbol{E}e^{-i\omega t'} + c.c.$ is not an operator it can be taken out of the commutator leaving

$$[\boldsymbol{d}, \rho^{(0)}]_{nm} = \sum_l \left(\boldsymbol{d}_{nl}\rho^{(0)}_{lm} - \rho^{(0)}_{nl}\boldsymbol{d}_{lm}\right). \tag{1.25}$$

As explained in Sec. 1.1.1, $\rho^{(0)} = \rho^{(eq)}$ and $\rho^{(eq)}$ only has diagonal elements. Also, the matrix element of the dipole moment is off-diagonal for states with definite parity; that is $\langle n|\boldsymbol{r}|n\rangle = 0$

and $\langle m|\boldsymbol{r}|m\rangle = 0$. The operation of parity takes $\boldsymbol{r} \to -\boldsymbol{r}$, which is spatial inversion. So the parity of a function tells if it is odd or even where an even function is defined as $f(-\boldsymbol{r}) = f(\boldsymbol{r})$ and an odd function as $f(-\boldsymbol{r}) = -f(\boldsymbol{r})$. I will give a not-so-rigorous argument as to why the diagonal matrix elements of the dipole moment is zero. Consider the matrix element $\langle n|\boldsymbol{r}|n\rangle = 0$, while examining whether each term involved is odd or even under spatial inversion. This procedure gives parity$(n)\times$parity$(\boldsymbol{r})\times$parity$(n) =$ odd. Here, parity(n) means parity of the state $|n\rangle$ (or its wavefunction $\langle \boldsymbol{r}|n\rangle$). Since parity$(n)\times$parity$(n) =$ even (for parity(n) odd or even and assuming definite parity) and parity$(\boldsymbol{r}) =$ odd, parity$(n)\times$parity$(\boldsymbol{r})\times$parity$(n) =$ even$\times$odd $=$ odd. In evaluating $\langle n|\boldsymbol{r}|n\rangle$ or $\langle m|\boldsymbol{r}|m\rangle$, one integrates an odd function over symmetric limits. Such an integral is equal to zero. Using the arguments presented in this paragraph, the commutator becomes

$$[\boldsymbol{d}, \rho^{(0)}]_{nm} = \left(\rho^{(0)}_{mm} - \rho^{(0)}_{nn}\right) \boldsymbol{d}_{nm}. \tag{1.26}$$

The density matrix element is then

$$\begin{aligned}
\rho^{(1)}_{nm} &= \frac{i}{\hbar}\left(\rho^{(0)}_{mm} - \rho^{(0)}_{nn}\right) \boldsymbol{d}_{nm} \cdot \boldsymbol{E} e^{i(\omega_{nm} - i\gamma_{nm})t} \int_{-\infty}^{t} (e^{-i\omega t'} + c.c.) e^{i(\omega_{nm} - i\gamma_{nm})t'}\, dt' \\
\rho^{(1)}_{nm} &= \frac{i}{\hbar}\left(\rho^{(0)}_{mm} - \rho^{(0)}_{nn}\right) \boldsymbol{d}_{nm} \cdot \boldsymbol{E} \left(\frac{e^{-i\omega t}}{i\left(\omega_{nm} - \omega - i\gamma_{nm}\right)} + \frac{e^{i\omega t}}{i\left(\omega_{nm} + \omega - i\gamma_{nm}\right)}\right).
\end{aligned} \tag{1.27}$$

In the rotating wave approximation the term $\propto \omega_{nm} + \omega$ is dropped, leaving

$$\rho^{(1)}_{nm}(t) = \frac{\left(\rho^{(0)}_{mm} - \rho^{(0)}_{nn}\right) \boldsymbol{d}_{nm} \cdot \boldsymbol{E} e^{-i\omega t}}{\hbar\left(\omega_{nm} - \omega - i\gamma_{nm}\right)}. \tag{1.28}$$

The rotating wave approximation will be upheld throughout the dissertation unless the contrary is explicitly stated.

One can express $\boldsymbol{r}_{nm}$ in terms of $\boldsymbol{v}_{nm}$ using the Heisenberg equation

$$i\hbar\dot{\boldsymbol{r}}_{nm} = [\boldsymbol{r}, H]_{nm} = \left[\boldsymbol{r}, H^0 + H^{int}\right]_{nm} = \left[\boldsymbol{r}, H^0\right]_{nm} + \underbrace{\left[\boldsymbol{r}, -\boldsymbol{d}\cdot\tilde{\boldsymbol{E}}\right]_{nm}}_{=0} \tag{1.29}$$

$$i\hbar\dot{\boldsymbol{r}}_{nm} = i\hbar\boldsymbol{v}_{nm} = \langle n|\left(\boldsymbol{r}H^0 - H^0\boldsymbol{r}\right)|m\rangle = (\mathcal{E}_m - \mathcal{E}_n)\boldsymbol{r}_{nm} \tag{1.30}$$

$$\implies \boldsymbol{r}_{nm} = \frac{i\hbar}{\mathcal{E}_m - \mathcal{E}_n}\boldsymbol{v}_{nm}. \tag{1.31}$$

Observe that $\boldsymbol{d} = -e\boldsymbol{r} \implies \boldsymbol{d}_{nm} = (-i\hbar e\boldsymbol{v}_{nm})/(\mathcal{E}_m - \mathcal{E}_n)$ which can be used to replace $\boldsymbol{d}_{nm}$ in Eq. (1.28)

$$\rho^{(1)}_{nm}(t) = i\hbar e\frac{\rho^{(0)}_{nn} - \rho^{(0)}_{mm}}{\mathcal{E}_m - \mathcal{E}_n}\frac{\boldsymbol{v}_{nm}\cdot\boldsymbol{E}e^{-i\omega t}}{\hbar\left(\omega_{nm} - \omega - i\gamma_{nm}\right)}. \tag{1.32}$$

The expectation value of the current density given by Eq. (1.20) for $\rho^{(1)}_{nm}$ given by Eq. (1.32) is

$$\langle\boldsymbol{j}\rangle = -\frac{i\hbar e^2}{V}\sum_{m,n}\frac{\rho^{(0)}_{nn} - \rho^{(0)}_{mm}}{\mathcal{E}_m - \mathcal{E}_n}\frac{\boldsymbol{v}_{mn}\boldsymbol{v}_{nm}\cdot\boldsymbol{E}e^{-i\omega t}}{\hbar\left(\omega_{nm} - \omega - i\gamma_{nm}\right)}. \tag{1.33}$$

The conductivity tensor can be extracted from Eq. (1.33) using $\boldsymbol{j}(\omega) = \boldsymbol{\sigma}(\omega)\boldsymbol{E}(\omega)$

$$\sigma_{rl}(\omega) = -\frac{i\hbar e^2}{V}\sum_{m,n}\frac{\rho^{(0)}_{nn} - \rho^{(0)}_{mm}}{\mathcal{E}_m - \mathcal{E}_n}\frac{v^r_{mn}v^l_{nm}}{\hbar\left(\omega_{nm} - \omega - i\gamma_{nm}\right)}. \tag{1.34}$$

One can extract the linear susceptibility from the linear conductivity by using the the continuity equation. Assuming harmonic dependence $\propto e^{i\boldsymbol{k}\cdot\boldsymbol{r} - i\omega t}$ for relevant quantities, the conservation of charge

$$-\partial_t\rho = \nabla\cdot\boldsymbol{j} \implies i\omega\rho = i\boldsymbol{k}\cdot\boldsymbol{j} \tag{1.35}$$

along with $\rho = -\nabla\cdot\boldsymbol{P} = -i\boldsymbol{k}\cdot\boldsymbol{P}$, $\boldsymbol{P} = \boldsymbol{\chi}\boldsymbol{E}$ and $\boldsymbol{j} = \boldsymbol{\sigma}\boldsymbol{E}$ gives the relationship between the linear conductivity and susceptibility

$$\chi_{rl}(\omega) = i\omega^{-1}\sigma_{rl}(\omega). \tag{1.36}$$

1.1.3 Three-Wave Mixing: DFG

Strong pump fields incident upon a material with nonlinear response results in new frequency components in the polarization of the medium [1]. The new frequency components in the polarization act as a driving, or source, term in the wave equation. They drive (or act as sources of) new frequency components of EM fields. [1].

From Maxwell's equations:

$$\nabla(\nabla \cdot \tilde{\boldsymbol{E}}) - \nabla^2 \tilde{\boldsymbol{E}} - \frac{1}{c^2}\partial_t^2 \tilde{\boldsymbol{D}} = 0, \tag{1.37}$$

where

$$\tilde{\boldsymbol{D}} = \tilde{\boldsymbol{E}} + 4\pi \tilde{\boldsymbol{P}}. \tag{1.38}$$

Nonlinear terms are included in $\tilde{\boldsymbol{P}}$ by expanding in powers of the electric field

$$\tilde{P}_i = \sum_j \chi_{ij}^{(1)} \tilde{E}_j + \sum_{j,k} \chi_{ijk}^{(2)} \tilde{E}_j \tilde{E}_k + \dots \tag{1.39}$$

$$\tilde{\boldsymbol{P}} = \tilde{\boldsymbol{P}}^{(1)} + \tilde{\boldsymbol{P}}^{(2)} + \dots, \tag{1.40}$$

for the series to converge $\boldsymbol{\chi}^{(1)} > \boldsymbol{\chi}^{(2)} > \dots$. The wave equation, Eq. (1.37), can be written in a form where it is obvious that the nonlinear polarization is a source term

$$\nabla^2 \tilde{\boldsymbol{E}} - \frac{1}{c^2}\partial_t^2 \tilde{\boldsymbol{D}}^{(1)} = \frac{4\pi}{c^2}\partial_t^2 \tilde{\boldsymbol{P}}^{(NL)} \tag{1.41}$$

where $\tilde{\boldsymbol{D}} = \tilde{\boldsymbol{D}}^{(1)} + 4\pi\tilde{\boldsymbol{P}}^{(NL)}$, $\tilde{\boldsymbol{D}}^{(1)} = (1 + 4\pi\boldsymbol{\chi}^{(1)})\tilde{\boldsymbol{E}} \equiv \boldsymbol{\epsilon}^{(1)}\tilde{\boldsymbol{E}}$, $\tilde{P}_i^{(NL)} = \sum_{j,k} \chi_{ijk}^{(2)} \tilde{E}_j \tilde{E}_k + \dots$, and $\nabla(\nabla \cdot \tilde{\boldsymbol{E}}) = 0$ was used. Note that one can expand $\tilde{\boldsymbol{E}}$, $\tilde{\boldsymbol{D}}$ $\tilde{\boldsymbol{P}}$ in terms of their frequency

components. Let $\tilde{\boldsymbol{F}}$ represent $\tilde{\boldsymbol{E}},\ \tilde{\boldsymbol{D}},\ \tilde{\boldsymbol{P}}$ then

$$\tilde{\boldsymbol{F}}(\boldsymbol{r},t) = \sum_n \tilde{\boldsymbol{F}}_n(\boldsymbol{r},t), \tag{1.42}$$

$$\tilde{\boldsymbol{F}}_n(\boldsymbol{r},t) = \mathrm{Re}[\boldsymbol{F}_n(\boldsymbol{r})e^{-i\omega_n t}] = \frac{1}{2}\boldsymbol{F}_n(\boldsymbol{r})e^{-i\omega_n t} + \mathrm{c.c.}, \tag{1.43}$$

$$\text{and} \quad \boldsymbol{F}_n(\boldsymbol{r}) = (F_{ox}, F_{oy}, F_{oz})e^{i\boldsymbol{q}_n\cdot\boldsymbol{r}}. \tag{1.44}$$

n runs over positive frequency terms only. When the relations Eqs. (1.42), (1.43) and (1.44) are taken into consideration, Eq. (1.41) will hold for each frequency component, i.e.

$$\nabla^2\tilde{\boldsymbol{E}}_n - \frac{\boldsymbol{\epsilon}^{(1)}(\omega_n)}{c^2}\partial_t^2\tilde{\boldsymbol{E}}_n = \frac{4\pi}{c^2}\partial_t^2\tilde{\boldsymbol{P}}_n^{(NL)}. \tag{1.45}$$

In this dissertation I only consider three-wave mixing processes, in particular, DFG and parametric down-conversion (the latter will not be addressed in this section.) Therefore, I only need to expand $\tilde{\boldsymbol{P}}$ to second-order in $\tilde{\boldsymbol{E}}$, and the nonlinear polarization will be of second-order only. Suppose a two-color optical field

$$\tilde{\boldsymbol{E}} = \frac{1}{2}\left[\boldsymbol{E}_1 e^{-i\omega_1 t} + \boldsymbol{E}_2 e^{i\omega_2 t} + \mathrm{c.c.}\right] \tag{1.46}$$

is incident upon medium that possesses a non-zero second-order response. The nonlinear polarization is given by

$$\tilde{\boldsymbol{P}}^{(NL)} = \boldsymbol{\chi}^{(2)}\tilde{\boldsymbol{E}}\tilde{\boldsymbol{E}} \implies \tilde{P}_i^{(NL)} = \sum_{j,k}\chi_{ijk}^{(2)}\tilde{E}_j\tilde{E}_k. \tag{1.47}$$

There are 16 terms in the product $\tilde{E}_j\tilde{E}_k$ in Eq. (1.47) for $\tilde{\boldsymbol{E}}$ given by Eq. (1.46). However, the number of terms can be reduced by invoking intrinsic permutation symmetry (see pg. 35 of [1]), that is, the second-order susceptibility $\chi_{ijk}^{(2)}$ remains invariant under interchange of the indices j,k. This argument is made on the grounds that, physically, it does not matter which field (E_j or E_k) comes first so $\chi_{ijk}^{(2)}E_jE_k = \chi_{ikj}^{(2)}E_kE_j$. If the second-order susceptibility is invariant under interchange of

j and k then so is $\tilde{P}_i^{(NL)}$. Thus,

$$\tilde{P}_i^{(NL)} = \frac{1}{4}\sum_{j,k}(\chi_{ijk}^{(2)}(\omega_3;\omega_1,\omega_1)E_{1j}E_{1k}e^{-2i\omega_1 t} + \chi_{ijk}^{(2)}(\omega_3;-\omega_1,-\omega_1)E_{1j}^*E_{1k}^*e^{2i\omega_1 t}$$
$$+ \chi_{ijk}^{(2)}(\omega_3;\omega_2,\omega_2)E_{2j}E_{2k}e^{-2i\omega_2 t} + \chi_{ijk}^{(2)}(\omega_3;-\omega_2,-\omega_2)E_{2j}^*E_{2k}^*e^{2i\omega_2 t}$$
$$+ 2\chi_{ijk}^{(2)}(\omega_3;\omega_1,\omega_2)E_{1j}E_{2k}e^{-i(\omega_1+\omega_2)t} + 2\chi_{ijk}^{(2)}(\omega_3;-\omega_1,-\omega_2)E_{1j}^*E_{2k}^*e^{+i(\omega_1+\omega_2)t}$$
$$+ 2\chi_{ijk}^{(2)}(\omega_3;\omega_1,-\omega_2)E_{1j}E_{2k}^*e^{-i(\omega_1-\omega_2)t} + 2\chi_{ijk}^{(2)}(\omega_3;-\omega_1,\omega_2)E_{1j}^*E_{2k}e^{i(\omega_1-\omega_2)t}$$
$$+ 2\chi_{ijk}^{(2)}(\omega_3;\omega_1,-\omega_1)E_{1j}E_{1j}^* + 2\chi_{ijk}^{(2)}(\omega_3;\omega_2,-\omega_2)E_{2j}E_{2j}^*). \tag{1.48}$$

The frequency ω_3 depends on the frequencies ω_1 and ω_2, for example, ω_c in $\chi_{ijk}^{(2)}(\omega_c;\omega_a,\omega_b)$ is defined as $\omega_c = \mathrm{sgn}(a)\omega_a + \mathrm{sgn}(b)\omega_b$. $\mathrm{sgn}(a)$ and $\mathrm{sgn}(b)$ takes values ± 1 depending on the sign of frequency $\omega_{a,b}$. Furthermore, since the polarization is an observable, it must be purely real (see Eq. (1.43)), so terms such as $\chi_{ijk}^{(2)}(\omega_c = -\omega_a - \omega_b; -\omega_a - \omega_b) = \chi_{ijk}^{(2)*}(\omega_c = \omega_a + \omega_b; \omega_a + \omega_b)$. By Eqs. (1.42) and (1.43) $\tilde{P}_i^{(NL)}$ can be expressed as

$$\tilde{P}_i^{(NL)} = \frac{1}{2}\sum_n P_i(\omega_n)e^{-i\omega_n t}. \tag{1.49}$$

where I used a more compact notation for Eqs. (1.42) and (1.43). This is achieved by $\tilde{P}_{in} \rightarrow \tilde{P}_i(\omega_n)$, and include both positive and negative frequency values for n. Note $\omega_{-n} = -\omega_n$ and $P_{in}(\omega_{-n}) = P_{in}(-\omega_n) = P_{in}^*(\omega_n)$. Comparing Eqs. (1.48) and (1.49) one obtains the different

frequency components of a three-wave mixing processes:

$$\text{SHG:} \quad P_i(\omega_3 = 2\omega_{1,2}) = \frac{1}{2}\sum_{j,k} \chi^{(2)}_{ijk}(\omega_3; \omega_{1,2}, \omega_{1,2}) E_{(1,2)j} E_{(1,2)k} \tag{1.50}$$

$$\text{SFG:} \quad P_i(\omega_3 = \omega_1 + \omega_2) = \sum_{j,k} \chi^{(2)}_{ijk}(\omega_3; \omega_1, \omega_2) E_{1j} E_{2k} \tag{1.51}$$

$$\text{DFG:} \quad P_i(\omega_3 = \omega_1 - \omega_2) = \sum_{j,k} \chi^{(2)}_{ijk}(\omega_3; \omega_1, -\omega_2) E_{1j} E^*_{2k} \tag{1.52}$$

$$\text{OR:} \quad P_i(\omega_3 = 0) = \sum_{j,k} \left[\chi^{(2)}_{ijk}(\omega_3; \omega_1, -\omega_1) E_{1j} E^*_{1k} + \chi^{(2)}_{ijk}(\omega_3; \omega_2, -\omega_2) E_{2j} E^*_{2k} \right]. \tag{1.53}$$

SHG is second-harmonic generation. SFG is sum frequency generation. DFG is difference frequency generation. OR is optical rectification. There are also complex conjugate terms corresponding to $-\omega_3$ to the equations above (except for the last one).

Even though the three-wave mixing processes of SHG, SFG, DFG and OR are possible, they do not occur simultaneously in an efficient way. Typically, one needs to satisfy the phase matching condition to achieve efficient three-wave mixing at a particular frequency. I will examine the phase matching condition for DFG. For simplicity I will assume that two monochromatic, collimated, continuous pumps interact with a lossless nonlinear medium. The frequencies of the input pump beams are ω_1 and ω_2. The pump beams are assumed to be normally incident upon the medium. In addition, both pump beams are assumed to be travelling in the positive x-direction and the length of the medium in this direction is L. I will also assume that the amplitudes A_1 and A_2 of the pump fields are undepelted as the pumps travel the length L; therefore, they can be taken as constants.

Since Eq. (1.45) holds for each frequency component of the field then it must hold at a particular frequency, say ω_3. The homogeneous (source term is absent) solution of Eq. (1.45) is

$$\tilde{E}_3(x,t) = \frac{1}{2} A_3 e^{ik_3 x - i\omega_3 t} + \text{c.c.} \tag{1.54}$$

where

$$k_3 = \frac{n_3 \omega_3}{c}, \quad n_3^2 = \epsilon^{(1)}(\omega_3), \tag{1.55}$$

and A_3 is constant. Eq. (1.45) is inhomogeneous (has a source or driving term). Here source term is taken as

$$\tilde{P}_3(x,t) = P_3 e^{-i\omega_3 t} + \text{c.c.} \tag{1.56}$$

where $P_3 \to P(\omega_3)$ and $P(\omega_3)$ is given in Eqs. (1.50)-(1.53). For DFG $P(\omega_3) = P(\omega_1 - \omega_2) = \chi^{(2)'}(\omega_1 - \omega_2)E_1 E_2^* = \chi^{(2)'}(\omega_1 - \omega_2)A_1 A_2^* e^{i(k_1 - k_2)x}$, and $\chi^{(2)'}$ is defined for some polarization where one may write it as a scalar. One can take Eq. (1.54) as a trial solution for Eq. (1.45) if A_3 is no longer constant but $A_3 \to A_3(x)$. A_1 and A_2 should also be functions of x but I assume that only a small percent of the incident fields are converted to the DFG field. Then I can treat $A_{1,2}$ as constants. With these considerations Eq. (1.45) becomes

$$\left[\frac{d^2A_3}{dx^2} + 2ik_3\frac{dA_3}{dx} - k_3^2 A_3 + \frac{\epsilon^{(1)}(\omega_3)\omega_3^2}{c^2}A_3\right]e^{ik_3 x - i\omega_3 t} + \text{c.c.}$$
$$= -\frac{4\pi\omega_3^2\chi^{(2)'}}{c^2}A_1 A_2^* e^{i(k_1-k_2)x - i\omega_3 t} + \text{c.c.} \tag{1.57}$$

The complex conjugate terms can be dropped and the equality will still hold. Assuming

$$\left|\frac{d^2A_3}{dx^2}\right| \ll \left|k_3\frac{dA_3}{dx}\right|, \tag{1.58}$$

leads to

$$\frac{dA_3}{dx} = \frac{i2\pi\omega_3^2\chi^{(2)'}}{k_3 c^2}A_1 A_2^* e^{i\Delta k x} \tag{1.59}$$

where the the relation given in Eq. (1.58) is called the slowly-varying amplitude approximation and

$$\Delta k \equiv k_1 - k_2 - k_3 \tag{1.60}$$

is called the phase mismatch. The phase matching condition is defined as $\Delta k = 0$. Note that different wave-mixing processes will have a different Δk, for example, for SHG $\Delta k = k_1 + k_2 - k_3$.

I will now show that DFG is most efficient when the phase matching condition, $\Delta k = 0$, is

satisfied. Assuming $A_{1,2}$ are constants, the solution to Eq. (1.59) when $\Delta k = 0$ is

$$A_3(x) = \frac{i2\pi\omega_3^2\chi^{(2)'}}{k_3c^2}A_1A_2^*x \tag{1.61}$$

with boundary condition $A_3(0) = 0$. One sees that inside the medium, the amplitude of the DFG field varies linearly with x. Because the intensity is proportional to the modulus of the amplitude squared ($I \propto |A_3|^2$), it varies quadratically with x. Simply put, when the conversion of the input pump fields to DFG is low, the intensity of the DFG field grows quadratically inside the medium.

When the phase matching condition is not satisfied, i.e. when $\Delta k \neq 0$ the DFG field intensity is less than when $\Delta k = 0$. To see this one solves Eq. (1.59) while keeping in mind that the sample is in the range $0 \leq x \leq L$

$$\begin{aligned} A_3(x) &= \frac{i2\pi\omega_3^2\chi^{(2)'}}{k_3c^2}A_1A_2^*\int_0^L e^{i\Delta kx}\,dx \\ \implies A_3(x) &= \frac{i2\pi\omega_3^2\chi^{(2)'}}{k_3c^2}A_1A_2^*\left[\frac{e^{i\Delta kL}-1}{i\Delta k}\right] \qquad (1.62) \\ \implies I &\propto L^2\left[\frac{\sin(\Delta kL/2)}{\Delta kL/2}\right]^2. \qquad (1.63) \end{aligned}$$

The function $\dfrac{\sin(\Delta kL/2)}{\Delta kL/2}$ is 1 when $\Delta k = 0$ and < 1 otherwise. Clearly, the conversion of the input pump fields to the DFG field is optimized when the $\Delta k = 0$, i.e. $k_3 = k_1 - k_2$.

If I now suppose the pump field of amplitude A_1 is strong and the pump field of amplitude A_2 is significantly weaker, then A_1 can be treated as undepleted and A_2 can be treated in the slowly-varying amplitude approximation. With these conditions, the DFG process now has two coupled equations: Eq. (1.59) and

$$\frac{dA_2}{dx} = \frac{i2\pi\omega_2^2\chi^{(2)'}}{k_2c^2}A_1A_3^*e^{i\Delta kx}. \tag{1.64}$$

If perfect phase matching is assumed, taking the derivative of Eq. (1.59) with respect to x leads to

an expression that depends on the complex conjugate of Eq. (1.64), giving

$$\frac{d^2A_3}{dx^2} = \frac{4\pi^2\omega_2^2\omega_3^2|\chi^{(2)\prime}|^2}{k_2k_3c^4}|A_1|^2A_3. \tag{1.65}$$

Eq. (1.65) has a solution

$$A_3(x) = a\cosh(gx) + b\sinh(gx), \tag{1.66}$$

where

$$g^2 \equiv \frac{4\pi^2\omega_2^2\omega_3^2|\chi^{(2)\prime}|^2}{k_2k_3c^4}|A_1|^2 \tag{1.67}$$

a, b depends on the boundary conditions. In particular, $A_3(x=0) = 0 \implies a = 0$ so $A_3 = b\sinh(gx)$. b can be found by solving Eq. (1.59), assuming $\Delta k = 0$, and using $A_1(x=0) = A_1(0)$, where $A_1(0)$ is arbitrary. One finds that $b = iA_2^*(0)\sqrt{k_2\omega_3^2/k_3\omega_2^2}(A_1/|A_1|)$ thus,

$$\begin{aligned} A_2(x) &= A_2(0)\cosh(gx), \text{ and} \\ A_3(x) &= i\sqrt{\frac{k_2\omega_3^2}{k_3\omega_2^2}}\frac{A_1}{|A_1|}A_2^*(0)\sinh(gx). \end{aligned} \tag{1.68}$$

For $gx \gg 1$, field amplitudes $|A_{2,3}|$ experience exponential growth.

1.2 Graphene

Graphite, the dark grey substance commonly found in pencils, is an allotrope of carbon. Graphite is composed of weakly bonded layers that are as thick as a carbon atom. The bonds between layers are so weak that just a bit of pressure, for example by pressing pencil to paper, is enough to break the interlayer bond and exfoliate graphite onto the paper. In contrast, the bonds between carbon atoms within each sheet are relatively strong. Since the thickness of a sheet is on the atomic scale (roughly the size of a carbon atom) it is considered two-dimensional (2D). The 2D sheets are called graphene.

An isolated carbon atom has 6 electrons which are configurated as $1s^22s^22p^2$. When carbon atoms form bonds with each other, their electronic wavefunctions overlap. In the case of graphene,

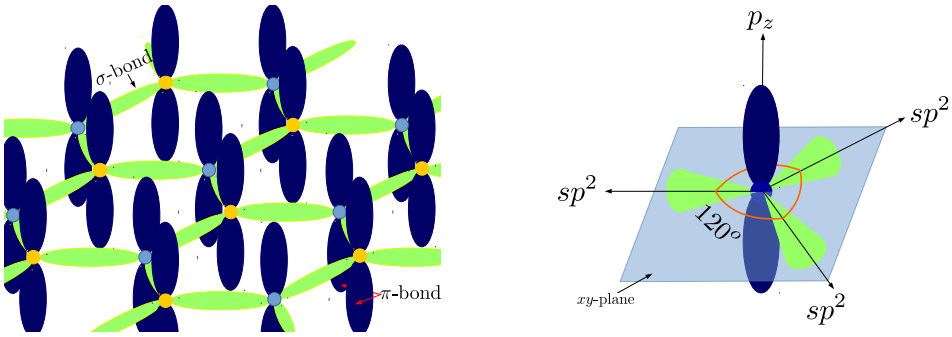

(a) σ bonds among sp^2 orbitals represented by bright green ellipses. p_z orbitals are represented by dark blue ellipses; π bonds among these orbitals are not shown.

(b) The three sp^2-hybridized orbitals are coplanar and 120° apart. The $2p_z$ orbitals are orthogonal to the sp^2 orbitals.

Figure 1.1: Sketch of carbon-carbon bonding in graphene. Adapted from [5].

enough energy is gained in the bonding process to promote an electron from the $2s$ orbital to the $2p$ orbital - consult [4] for further details. This leads to a hybridization of the $2s$ and $2p$ states, dubbed sp^2-hybridization. Specifically, three of the four electrons in the $2s^2$ and $2p^2$ states participate in sp^2-hybridization. The remaining electron is in an unhybridized $2p_z$ state.

The unhybridized $2p_z$ electrons form π bonds whereas, the hybridized electrons form σ bonds, see Fig. 1.1a. The σ bonded electrons lie in the same plane and are 120° apart, leading to graphene's trigonal planar structure [5], see Fig. 1.1b and its honeycomb lattice. However, the honeycomb lattice is not a Bravais lattice. In fact, graphene has two ineqivalent traingular Bravais sublattices denoted by A and B, see Fig. 1.2a.

Graphene was first considered theoretically by Wallace [6] in 1947. But it did not gain prominence until it was isolated by Novoselov and Geim [7] in 2004. Wallace studied nearest-neighbor (nn) hopping among p_z electrons in the tight-binding approximation and showed that the energy dispersion is linear. Below I will use the same considerations as Wallace since the properties of interest stem from the low-energy excitations of the p_z electrons. In addition, I will follow the

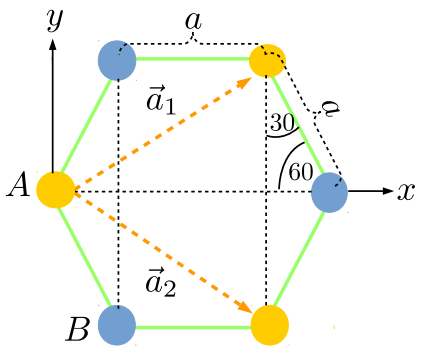

(a) Both yellow and blue dots are carbon atoms. They are colored differently to indicate sublattices. Nearest-neighbor distance $a = 0.142$ nm, $\boldsymbol{a}_{1,2}$ are basis vectors for sublattice A.

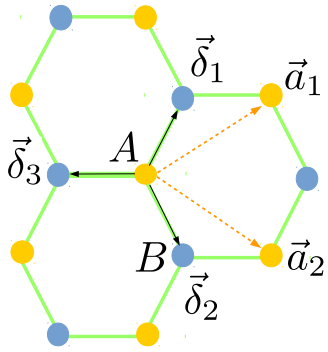

(b) Nearest-neighbor distances given by $\boldsymbol{\delta}$. Sublattice A has nearest-neighbor on sublattice B and vice-versa. Adapted from [5].

Figure 1.2: Honeycomb lattice in graphene.

derivations given in [8, 9].

1.2.1 Tight-Binding Model

In Sec. 1.2 it was mentioned that the honeycomb lattice is not a Bravais. However, graphene's honeycomb lattice can be viewed as a triangular lattice with a two atom basis. In this case, the unit cell has two atoms. A trial wavefunction can be written as [8]

$$\Psi_k(\boldsymbol{r}) = a_{\boldsymbol{k}}\psi^{(A)}_{\boldsymbol{k}}(\boldsymbol{r}) + b_{\boldsymbol{k}}\psi^{(B)}_{\boldsymbol{k}}(\boldsymbol{r}), \tag{1.69}$$

where $a_{\boldsymbol{k}}$ and $b_{\boldsymbol{k}}$ are complex functions of the Bloch wavevector $\boldsymbol{k}$. The Bloch wavevector gives the quasimomentum $\boldsymbol{p} = \hbar\boldsymbol{k}$. $\psi^{(j)}_{\boldsymbol{k}}(\boldsymbol{r})$ are Bloch functions given by

$$\psi^{(j)}_{\boldsymbol{k}}(\boldsymbol{r}) = \frac{1}{\sqrt{N}}\sum_{\boldsymbol{R}_l} e^{i\boldsymbol{k}\cdot\boldsymbol{R}_l}\phi^{(j)}(\boldsymbol{r} + \boldsymbol{d}_j - \boldsymbol{R}_l). \tag{1.70}$$

N is the number of unit cells. The index j take values A or B (which labels the sublattices). $\phi^{(j)}(\boldsymbol{r} + \boldsymbol{d}_j - \boldsymbol{R}_l)$ are the $2p_z$ orbitals and are eigenstates of a bound state atomic Hamiltonian

$$H^a\phi^{(j)}(\boldsymbol{r} + \boldsymbol{d}_j - \boldsymbol{R}_l) = \mathcal{E}^{(j)}\phi^{(j)}(\boldsymbol{r} + \boldsymbol{d}_j - \boldsymbol{R}_l), \tag{1.71}$$

where $\mathcal{E}^{(j)}$ are the (energy) eigenvalues, sometimes called eigenenergy, of the j orbital. H^a is given by

$$H^a = -\frac{\hbar^2}{2m}\nabla^2 + V(\boldsymbol{r} + \boldsymbol{d}_j - \boldsymbol{R}_l). \tag{1.72}$$

$\boldsymbol{R}_l = m_j\boldsymbol{a}_1 + n_j\boldsymbol{a}_2$ is a Bravais lattice vector and n_j, m_j are integers; $\boldsymbol{a}_{1,2}$ are primitive vectors. They can be found by examining Fig. 1.2a which reveals that the y component of $\boldsymbol{a}_1$ is $a_{1y} = a\sin 60 = (\sqrt{3}/2)a$ and the x component is $a_{1x} = a + a\cos 60 = (3/2)a$. Thus,

$$\boldsymbol{a}_1 = \frac{a}{2}(3, \sqrt{3}), \tag{1.73}$$

$$\boldsymbol{a}_2 = \frac{a}{2}(3, -\sqrt{3}). \tag{1.74}$$

In Eq. (1.70) $\boldsymbol{d}_j$ is the vector which connects the sites of the underlying Bravais lattice with the site of the j atom within the unit cell. Following [8], I will choose sublattice A to coincide with the Bravais lattice, thus $\boldsymbol{d}_A = (0, 0)$ and $\boldsymbol{d}_B = \boldsymbol{d}_{AB} = \boldsymbol{\delta}_3 = (-a, 0)$, see Fig. 1.2b. For definiteness, I have chosen the origin to coincide with the point labeled A in Fig. 1.2b.

The trial wavefunction given in Eq. (1.69) satisfies the eigenvalue equation

$$H\Psi_{\boldsymbol{k}}(\boldsymbol{r}) = E_{\boldsymbol{k}}\Psi_{\boldsymbol{k}}(\boldsymbol{r}), \tag{1.75}$$

where the Hamiltonian is

$$H = -\frac{\hbar^2}{2m}\nabla^2 + \sum_{\boldsymbol{R}_l}^{N} V(\boldsymbol{r} + \boldsymbol{d}_j - \boldsymbol{R}_l). \tag{1.76}$$

Using Eq. (1.72) one can write Eq. (1.76) as

$$H = H^a + \Delta V, \tag{1.77}$$

$$\Delta V = \sum_{\boldsymbol{R}_m \neq \boldsymbol{R}_l}^{N} V(\boldsymbol{r} + \boldsymbol{d}_j - \boldsymbol{R}_m), \tag{1.78}$$

where ΔV given in Eq. (1.78) is the contribution to the potential energy from all other ions at sites $\boldsymbol{R}_{m\neq l}$. The potential energy at $\boldsymbol{R}_{m=l}$ is accounted for in H^a. The expectation value of the Hamiltonian H is:

$$\langle \Psi_{\boldsymbol{k}}(\boldsymbol{r})|H|\Psi_{\boldsymbol{k}}(\boldsymbol{r})\rangle = E_{\boldsymbol{k}} \langle \Psi_{\boldsymbol{k}}(\boldsymbol{r})|\Psi_{\boldsymbol{k}}(\boldsymbol{r})\rangle , \tag{1.79}$$

which can be rewritten as

$$\begin{pmatrix} a_{\boldsymbol{k}}^* & b_{\boldsymbol{k}}^* \end{pmatrix} \begin{pmatrix} \mathcal{H}_{\boldsymbol{k}}^{(AA)} & \mathcal{H}_{\boldsymbol{k}}^{(AB)} \\ \mathcal{H}_{\boldsymbol{k}}^{(BA)} & \mathcal{H}_{\boldsymbol{k}}^{(BB)} \end{pmatrix} \begin{pmatrix} a_{\boldsymbol{k}} \\ b_{\boldsymbol{k}} \end{pmatrix} = E_{\boldsymbol{k}} \begin{pmatrix} a_{\boldsymbol{k}}^* & b_{\boldsymbol{k}}^* \end{pmatrix} \begin{pmatrix} \mathcal{S}_{\boldsymbol{k}}^{(AA)} & \mathcal{S}_{\boldsymbol{k}}^{(AB)} \\ \mathcal{S}_{\boldsymbol{k}}^{(BA)} & \mathcal{S}_{\boldsymbol{k}}^{(BB)} \end{pmatrix} \begin{pmatrix} a_{\boldsymbol{k}} \\ b_{\boldsymbol{k}} \end{pmatrix}; \tag{1.80}$$

where $\mathcal{H}_{\boldsymbol{k}}^{(ij)}$ and $\mathcal{S}_{\boldsymbol{k}}^{(ij)}$ are the elements of Hermitian matrices $\mathcal{H}_{\boldsymbol{k}}$ and $\mathcal{S}_{\boldsymbol{k}}$. The matrix elements are:

$$\mathcal{H}_{\boldsymbol{k}}^{(ij)} = \left\langle \psi_{\boldsymbol{k}}^{(i)*}(\boldsymbol{r}) \middle| H \middle| \psi_{\boldsymbol{k}}^{(j)}(\boldsymbol{r}) \right\rangle , \tag{1.81}$$

$$\mathcal{S}_{\boldsymbol{k}}^{(ij)} = \left\langle \psi_{\boldsymbol{k}}^{(i)*}(\boldsymbol{r}) \middle| \psi_{\boldsymbol{k}}^{(j)}(\boldsymbol{r}) \right\rangle . \tag{1.82}$$

Substituting Eq. (1.70) into Eq. (1.81), one finds

$$\mathcal{H}_{\boldsymbol{k}}^{(ij)} = \frac{1}{N} \sum_{\boldsymbol{R}_m, \boldsymbol{R}_n} e^{i\boldsymbol{k}\cdot(\boldsymbol{R}_n - \boldsymbol{R}_m)} \int d\boldsymbol{r}\, \phi^{(i)*}(\boldsymbol{r} + \boldsymbol{d}_i - \boldsymbol{R}_m) H \phi^{(j)}(\boldsymbol{r} + \boldsymbol{d}_j - \boldsymbol{R}_n), \tag{1.83}$$

let $\boldsymbol{x} = \boldsymbol{r} + \boldsymbol{d}_i - \boldsymbol{R}_m$ so $\boldsymbol{r} = \boldsymbol{x} - \boldsymbol{d}_i + \boldsymbol{R}_m$ and $\boldsymbol{r} + \boldsymbol{d}_j - \boldsymbol{R}_n = \boldsymbol{x} - \boldsymbol{d}_i + \boldsymbol{R}_m + \boldsymbol{d}_j - \boldsymbol{R}_n = \boldsymbol{x} + \boldsymbol{d}_{ij} - \boldsymbol{R}_l$; $\boldsymbol{d}_{ij} = \boldsymbol{d}_j - \boldsymbol{d}_i$ and $\boldsymbol{R}_l = \boldsymbol{R}_n - \boldsymbol{R}_m$ then

$$\mathcal{H}_{\boldsymbol{k}}^{(ij)} = \sum_{\boldsymbol{R}_l} e^{i\boldsymbol{k}\cdot\boldsymbol{R}_l} \int d\boldsymbol{x}\, \phi^{(i)*}(\boldsymbol{x}) H \phi^{(j)}(\boldsymbol{x} + \boldsymbol{d}_{ij} - \boldsymbol{R}_l). \tag{1.84}$$

$\sum_{\boldsymbol{R}_n, \boldsymbol{R}_m} \to N \sum_{\boldsymbol{R}_l}$ was used. Making use of Eq. (1.77) yields

$$\mathcal{H}_{\boldsymbol{k}}^{(ij)} = \sum_{\boldsymbol{R}_l} e^{i\boldsymbol{k}\cdot\boldsymbol{R}_l} \int d\boldsymbol{x}\, \phi^{(i)*}(\boldsymbol{x})(H^a + \Delta V)\phi^{(j)}(\boldsymbol{x} + \boldsymbol{d}_{ij} - \boldsymbol{R}_l), \tag{1.85}$$

$$\mathcal{H}_{\boldsymbol{k}}^{(ij)} = \mathcal{E}^{(j)} S_{\boldsymbol{k}}^{(ij)} + t_{\boldsymbol{k}}^{(ij)}, \tag{1.86}$$

where

$$S_{\boldsymbol{k}}^{(ij)} = \sum_{\boldsymbol{R}_l} e^{i\boldsymbol{k}\cdot\boldsymbol{R}_l} \int d\boldsymbol{x}\, \phi^{(i)*}(\boldsymbol{x})\phi^{(j)}(\boldsymbol{x} + \boldsymbol{d}_{ij} - \boldsymbol{R}_l), \tag{1.87}$$

$$t_{\boldsymbol{k}}^{(ij)} = \sum_{\boldsymbol{R}_l} e^{i\boldsymbol{k}\cdot\boldsymbol{R}_l} \int d\boldsymbol{x}\, \phi^{(i)*}\Delta V\phi^{(j)}(\boldsymbol{x} + \boldsymbol{d}_{ij} - \boldsymbol{R}_l). \tag{1.88}$$

One can write Eq. (1.80) in component form

$$\sum_{i,j} c_i^* c_j \mathcal{H}_{\boldsymbol{k}}^{(ij)} = E_{\boldsymbol{k}} \sum_{i,j} c_i^* c_j \mathcal{S}_{\boldsymbol{k}}^{(ij)}, \tag{1.89}$$

$$\implies E_{\boldsymbol{k}} = \frac{\sum_{i,j} c_i^* \mathcal{H}_{\boldsymbol{k}}^{(ij)} c_j}{\sum_{i,j} c_i^* \mathcal{S}_{\boldsymbol{k}}^{(ij)} c_j}, \tag{1.90}$$

where i, j runs from A to B, $c_A = a_{\boldsymbol{k}}$, and $c_B = b_{\boldsymbol{k}}$.

Using the variational principle, one can minimize the energy with respect to the parameter c_n^* i.e.

$$\frac{\partial E_{\boldsymbol{k}}}{\partial c_n^*} = 0 = \frac{\partial}{\partial c_n^*}\left(\frac{\sum_{i,j} c_i^* \mathcal{H}_{\boldsymbol{k}}^{(ij)} c_j}{\sum_{i,j} c_i^* \mathcal{S}_{\boldsymbol{k}}^{(ij)} c_j}\right) \tag{1.91}$$

$$
\begin{aligned}
\implies 0 &= \frac{1}{\sum_{i,j} c_i^* \mathcal{S}_{\boldsymbol{k}}^{(ij)} c_j} \frac{\partial}{\partial c_n^*} \sum_{i,j} c_i^* \mathcal{H}_{\boldsymbol{k}}^{(ij)} c_j - \frac{\sum_{i,j} c_i^* \mathcal{H}_{\boldsymbol{k}}^{(ij)} c_j}{(\sum_{i,j} c_i^* \mathcal{S}_{\boldsymbol{k}}^{(ij)} c_j)^2} \frac{\partial}{\partial c_n^*} \sum_{i,j} c_i^* \mathcal{S}_{\boldsymbol{k}}^{(ij)} c_j \\
\implies 0 &= \frac{\partial}{\partial c_n^*} \sum_{i,j} c_i^* \mathcal{H}_{\boldsymbol{k}}^{(ij)} c_j - \frac{E_{\boldsymbol{k}} \sum_{i,j} c_i^* \mathcal{S}_{\boldsymbol{k}}^{(ij)} c_j}{\sum_{i,j} c_i^* \mathcal{S}_{\boldsymbol{k}}^{(ij)} c_j} \frac{\partial}{\partial c_n^*} \sum_{i,j} c_i^* \mathcal{S}_{\boldsymbol{k}}^{(ij)} c_j \\
\implies & \sum_{i,j} \delta_{in} (\mathcal{H}_{\boldsymbol{k}}^{(ij)} c_j - E_{\boldsymbol{k}} \mathcal{S}_{\boldsymbol{k}}^{(ij)} c_j) = 0 \\
\implies & \sum_{j} (\mathcal{H}_{\boldsymbol{k}}^{(ij)} - E_{\boldsymbol{k}} \mathcal{S}_{\boldsymbol{k}}^{(ij)}) c_j = 0. \qquad (1.92)
\end{aligned}
$$

Eq. (1.92) has non-trivial solutions when

$$\det[\mathcal{H}_{\boldsymbol{k}}^{(ij)} - E_{\boldsymbol{k}} \mathcal{S}_{\boldsymbol{k}}^{(ij)}] = 0. \qquad (1.93)$$

With the help of Eq. (1.86), Eq. (1.93) may be rewritten as

$$\det[t_{\boldsymbol{k}}^{(ij)} - (E_{\boldsymbol{k}} - \mathcal{E}^{(0)}) \mathcal{S}_{\boldsymbol{k}}^{(ij)}] = 0. \qquad (1.94)$$

In the last equation $\mathcal{E}^{(j)} \to \mathcal{E}^{(0)}$ since the onsite energy is the same for both sublattices. This term can be dropped since it corresponds to a constant shift in energy bands [9]. If one neglects the overlap corrections then $S_{\boldsymbol{k}}^{(ij)} = \delta_{ij}$. With these considerations Eq. (1.94) becomes

$$\det[t_{\boldsymbol{k}}^{(ij)} - E_{\boldsymbol{k}} \delta_{ij}] = 0. \qquad (1.95)$$

If only hopping between nearest-neighbors is considered, which is called the nearest-neighbor (nn) approximation, then the hopping matrix $t_{\boldsymbol{k}}^{(ij)}$ becomes

$$t_{\boldsymbol{k}}^{(ij)} = t f(\boldsymbol{k}). \qquad (1.96)$$

With the help of Eq. (1.96) the Hamiltonian $\mathcal{H}_{\boldsymbol{k}}$ can be written as

$$\mathcal{H}_{\boldsymbol{k}} = \begin{pmatrix} 0 & tf(\boldsymbol{k}) \\ tf^*(\boldsymbol{k}) & 0 \end{pmatrix} \tag{1.97}$$

where

$$t = \int \phi^{(A)*}(\boldsymbol{x}) \Delta V \phi^{(B)}(\boldsymbol{x} + \boldsymbol{\delta}_3)\, d^2x \approx -3\mathrm{eV}, \tag{1.98}$$

t is the nn hopping amplitude and $f(\boldsymbol{k})$ is

$$f(\boldsymbol{k}) = \sum_{\boldsymbol{R}_l \in nn} e^{i\boldsymbol{k}\cdot\boldsymbol{R}_l}. \tag{1.99}$$

The nns are depicted in Fig. 1.2b where one sees that the nn of an electron in sublattice A is on sublattice B and vice-versa. Therefore, $t_{\boldsymbol{k}}^{(ij)}$ is off-diagonal in the nn approximation (diagonal terms correspond to next-nearest-neighbor hopping). For a site on sublattice A one can obtain the equivalent site on sublattice B by the displacement $\boldsymbol{d}_{AB} = \boldsymbol{\delta}_3$. The nn vectors can be obtained by examining Fig. 1.2b:

$$\boldsymbol{\delta}_1 = \frac{a}{2}(1, \sqrt{3}), \tag{1.100}$$

$$\boldsymbol{\delta}_2 = \frac{a}{2}(1, -\sqrt{3}), \tag{1.101}$$

$$\boldsymbol{\delta}_3 = (-a, 0). \tag{1.102}$$

One uses the equation $\boldsymbol{\delta}_l = \boldsymbol{d}_{AB} + \boldsymbol{R}_l = \boldsymbol{\delta}_3 + \boldsymbol{R}_l$ for $l = 1,\, 2,\, 3$ to find the $\boldsymbol{R}_l$ which satisfy the nn vectors given in Eqs. (1.100), (1.101), (1.102). One finds that $\boldsymbol{\delta}_3$ corresponds to $\boldsymbol{R}_l = \boldsymbol{R}_3 = \boldsymbol{0}$, $\boldsymbol{\delta}_2$ corresponds to $\boldsymbol{R}_l = \boldsymbol{R}_2 = \boldsymbol{a}_2$, and $\boldsymbol{\delta}_1$ corresponds to $\boldsymbol{R}_l = \boldsymbol{R}_1 = \boldsymbol{a}_1$. Using these values for $\boldsymbol{R}_l$ in Eq. (1.99) results in

$$f(\boldsymbol{k}) = 1 + e^{i\boldsymbol{k}\cdot\boldsymbol{a}_1} + e^{i\boldsymbol{k}\cdot\boldsymbol{a}_2}. \tag{1.103}$$

Eqs. (1.103), and (1.96) are used in solving the secular equation, i.e. Eq. (1.95), for the energy:

$$\begin{vmatrix} -E_{\boldsymbol{k}} & tf(\boldsymbol{k}) \\ tf^*(\boldsymbol{k}) & -E_{\boldsymbol{k}} \end{vmatrix} = 0 \tag{1.104}$$

$$\implies E^{\lambda}(\boldsymbol{k}) = \lambda t|f(\boldsymbol{k})|. \tag{1.105}$$

$\lambda = \pm 1$; $+1$ corresponds to the conduction band while -1 corresponds to the valence band. The energy is zero when $|f(\boldsymbol{k})|$ is zero. There may be some wavevector $\tilde{\boldsymbol{k}}$ such that $|f(\tilde{\boldsymbol{k}})| = 0$. $\tilde{\boldsymbol{k}}$ can be found by solving:

$$\mathrm{Re}[f(\tilde{\boldsymbol{k}})] = 0 = 1 + \cos\left(\frac{\tilde{k}_x 3a}{2} + \frac{\tilde{k}_y\sqrt{3}a}{2}\right) + \cos\left(\frac{\tilde{k}_x 3a}{2} - \frac{\tilde{k}_y\sqrt{3}a}{2}\right), \tag{1.106}$$

$$\mathrm{Im}[f(\tilde{\boldsymbol{k}})] = 0 = \sin\left(\frac{\tilde{k}_x 3a}{2} + \frac{\tilde{k}_y\sqrt{3}a}{2}\right) + \sin\left(\frac{\tilde{k}_x 3a}{2} - \frac{\tilde{k}_y\sqrt{3}a}{2}\right). \tag{1.107}$$

Let $\alpha = \tilde{k}_x 3a/2$ and $\beta = \tilde{k}_y\sqrt{3}a/2$, using $\cos(\alpha \pm \beta) = \cos(\alpha)\cos(\beta) \mp \sin\alpha\sin(\beta)$ and $\sin(\alpha \pm \beta) = \sin(\alpha)\cos(\beta) \pm \sin(\beta)\cos(\alpha)$, Eqs. (1.106) and (1.107) becomes

$$1 + 2\cos(\alpha)\cos(\beta) = 0, \tag{1.108}$$

$$2\sin(\alpha)\cos(\beta) = 0. \tag{1.109}$$

Of course, these equations must be satisfied simultaneously. The equations above are satisfied when

$$\alpha = 2\pi n \implies \frac{\tilde{k}_x 3a}{2} = 2\pi n, \quad \cos(\beta) = -\frac{1}{2} \implies \cos\left(\frac{\tilde{k}_y\sqrt{3}a}{2}\right) = -\frac{1}{2} \tag{1.110}$$

$$\text{or} \quad \alpha = (2n+1)\pi \implies \frac{\tilde{k}_x 3a}{2} = (2n+1)\pi, \quad \cos(\beta) = +\frac{1}{2} \implies \cos\left(\frac{\tilde{k}_y\sqrt{3}a}{2}\right) = +\frac{1}{2}, \tag{1.111}$$

where n is an integer. $n = 0$ gives two solutions $\tilde{\boldsymbol{k}} = (0, +4\pi/(3\sqrt{3}a)$ and $\tilde{\boldsymbol{k}}' = (0, -4\pi/(3\sqrt{3}a)$.

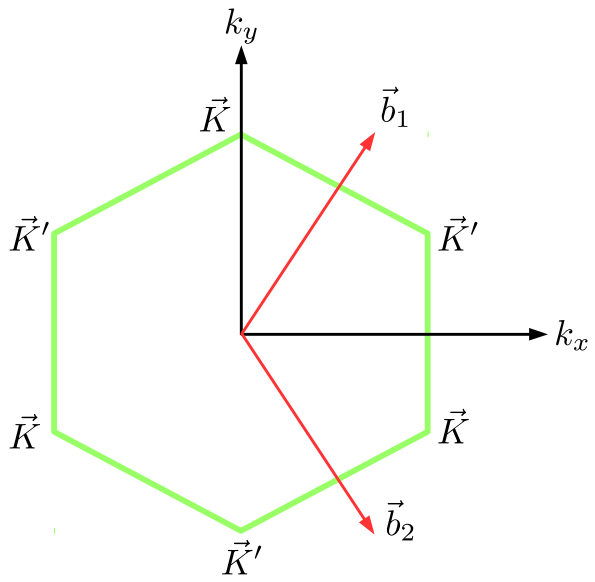

Figure 1.3: FBZ given by green hexagon. Reciprocal lattice vectors $\boldsymbol{b}_1$ and $\boldsymbol{b}_1$. Corners of the FBZ given by $\boldsymbol{K}$ and $\boldsymbol{K}'$.

(These are not the only solutions.) $\tilde{\boldsymbol{k}}$ and $\tilde{\boldsymbol{k}}'$ correspond to the crystallographic points $\boldsymbol{K}$ and $\boldsymbol{K}'$ which are two corners of the first Brillouin zone (FBZ) in graphene, see Fig. 1.3. There are 6 corners in graphene's FBZ. But only two ($\boldsymbol{K}$ and $\boldsymbol{K}'$) are inequivalent since the rest can be reached by a reciprocal lattice vector. Using $\boldsymbol{a}_i \cdot \boldsymbol{b}_j = 2\pi\delta_{ij}$ one finds reciprocal lattice vectors $\boldsymbol{b}_1$, $\boldsymbol{b}_2$:

$$\boldsymbol{b}_1 = \frac{2\pi}{3a}(1, \sqrt{3}), \tag{1.112}$$

$$\boldsymbol{b}_2 = \frac{2\pi}{3a}(1, -\sqrt{3}). \tag{1.113}$$

Suppose $f'(\boldsymbol{k}) = e^{i\vartheta_{\boldsymbol{k}}} f(\boldsymbol{k})$ then $|f'(\boldsymbol{k})| = |f(\boldsymbol{k})|$. Since the eigenvalue $E^\lambda \propto |f(\boldsymbol{k})|$ it remains unchanged if $f(\boldsymbol{k})$ is multiplied by a phase factor $e^{i\vartheta_{\boldsymbol{k}}}$ provided that the function $\vartheta_{\boldsymbol{k}}$ is real and non-singular. Let $\vartheta_{\boldsymbol{k}} = \boldsymbol{k} \cdot \boldsymbol{\delta}_3 + \pi/2$ then

$$f(\boldsymbol{k}) \to e^{i(\boldsymbol{k}\cdot\boldsymbol{\delta}_3 + \pi/2)} f(\boldsymbol{k}) = e^{i\pi/2} \sum_{i=1}^{3} e^{i\boldsymbol{k}\cdot\boldsymbol{\delta}_i}. \tag{1.114}$$

Having worked through the problem before hand, I found that the phase factor of $e^{i\pi/2}$ gives the desired result (shortly, one will see what I mean by "desired result"). The phase factor $e^{i\boldsymbol{k}\cdot\boldsymbol{\delta}_3}$ allows one to write $f(\boldsymbol{k})$ in a more symmetric fashion, leading to an expression which is convenient for series expansion [8].

The low-energy excitations are found by series expansion of $f(\boldsymbol{k})$ in the equation above near $\boldsymbol{K}$ or $\boldsymbol{K}'$. I will expand around $\boldsymbol{K}$ so $\boldsymbol{k} = \boldsymbol{K} + \boldsymbol{q}$. Here $|\boldsymbol{q}|$ is small compared to $|\boldsymbol{K}| \sim 1/a$, i.e. $|\boldsymbol{q}|a \ll 1$. Using $\boldsymbol{k} = \boldsymbol{K} + \boldsymbol{q}$ in Eq. (1.114) results in

$$
\begin{aligned}
f(\boldsymbol{q}) &= e^{i\pi/2} \sum_{j=1}^{3} e^{i\boldsymbol{K}\cdot\boldsymbol{\delta}_j} e^{i\boldsymbol{q}\cdot\boldsymbol{\delta}_j} \\
&= e^{i\pi/2} \left[e^{i2\pi/3} e^{i\boldsymbol{q}\cdot\boldsymbol{\delta}_1} + e^{-i2\pi/3} e^{i\boldsymbol{q}\cdot\boldsymbol{\delta}_2} + e^{i\boldsymbol{q}\cdot\boldsymbol{\delta}_3} \right] \\
&= e^{i\pi/2} \left[e^{i2\pi/3}(1 + i\boldsymbol{q}\cdot\boldsymbol{\delta}_1) + e^{-i2\pi/3}(1 + i\boldsymbol{q}\cdot\boldsymbol{\delta}_2) + (1 + i\boldsymbol{q}\cdot\boldsymbol{\delta}_3) + \mathcal{O}((|\boldsymbol{q}|a)^2) \right] \\
&\approx e^{i\pi/2} \left[e^{i2\pi/3}(1 + i\frac{a}{2}q_x + i\frac{\sqrt{3}a}{2}q_y) + e^{-i2\pi/3}(1 + i\frac{a}{2}q_x - i\frac{\sqrt{3}a}{2}q_y) + (1 - iaq_x) \right] \\
&= e^{i\pi/2} \left[1 + 2\cos\left(\frac{2\pi}{3}\right) + iaq_x \left(\cos\left(\frac{2\pi}{3}\right) - 1 \right) - \sqrt{3}aq_y \sin\left(\frac{2\pi}{3}\right) \right] \\
&= e^{i\pi/2} \left[-i\frac{3a}{2}(q_x - iq_y) \right] \\
&= \frac{3a}{2}(q_x - iq_y).
\end{aligned}
\tag{1.115}
$$

where terms of order 2 and greater contained in $\mathcal{O}((|\boldsymbol{q}|a)^2)$ were dropped and the phase $e^{i\pi/2}$ was used to get rid of $-i$.

In the low-energy limit $f(\boldsymbol{k})$ is given by Eq. (1.115) and Hamiltonian in Eq. (1.97) is

$$
\mathcal{H}_{\boldsymbol{q}}^{\boldsymbol{K}} = \frac{3|t|a}{2} \begin{pmatrix} 0 & q_x - iq_y \\ q_x + iq_y & 0 \end{pmatrix} = \hbar v_F \boldsymbol{q}\cdot\boldsymbol{\sigma}, \tag{1.116}
$$

where $v_F = 3|t|a/(2\hbar) \approx c/300$ is the Fermi velocity, c is the speed of light in vacuum, and

$$\boldsymbol{\sigma} = \boldsymbol{e}_x \sigma_x + \boldsymbol{e}_y \sigma_y \tag{1.117}$$

$$\sigma_x = \begin{pmatrix} 0 & 1 \\ 1 & 0 \end{pmatrix}, \quad \sigma_y = \begin{pmatrix} 0 & -i \\ i & 0 \end{pmatrix}. \tag{1.118}$$

$\sigma_{x,\,y}$ are Pauli matrices, $\boldsymbol{e}_{x,\,y}$ are unit vectors along the x and y directions, respectively. Eq. (1.116) resembles the Dirac equation for massless fermions, therefore the low-energy p_z electrons in graphene behave like massless Dirac fermions. However, they move with a velocity v_F instead of c.

One could carry out the expansion around $\boldsymbol{K}'$ and obtain a similar expression. According to [8] the two expansions can be combined into one Hamiltonian

$$\mathcal{H}^{\varsigma}_{\boldsymbol{q}} = \varsigma \hbar v_F (q_x \sigma_x + q_y \sigma_y) = \hbar v_F \tau_z \otimes \boldsymbol{q} \cdot \boldsymbol{\sigma}, \tag{1.119}$$

$\varsigma = \pm 1$ is the valley pseudospin which is $+1$ for $\boldsymbol{K}$ and -1 for $\boldsymbol{K}'$,

$$\tau_z = \begin{pmatrix} 1 & 0 \\ 0 & -1 \end{pmatrix}, \quad \tau_z \otimes \boldsymbol{\sigma} = \begin{pmatrix} \boldsymbol{\sigma} & 0 \\ 0 & -\boldsymbol{\sigma} \end{pmatrix}. \tag{1.120}$$

Basically, there are two copies of the Dirac equation, one corresponding to the $\boldsymbol{K}$ point and the other corresponding to $\boldsymbol{K}'$. Since the electrons near the $\boldsymbol{K}$ and $\boldsymbol{K}'$ points are massless Dirac fermions, these points are sometimes given the moniker Dirac points.

The energy eigenvalue corresponding to the Hamiltonian in Eq. (1.119) is

$$E^{\lambda}_{\boldsymbol{q},\,\varsigma=\pm} = \lambda \hbar v_F |\boldsymbol{q}|. \tag{1.121}$$

It is independent of valley pseudospin ς therefore, it has a two-fold valley degeneracy. The eigen-

states are four-spinors

$$\Psi^{\varsigma=+}_{\boldsymbol{q},\lambda} = \frac{1}{\sqrt{2}}\begin{pmatrix} 1 \\ \lambda e^{i\phi_{\boldsymbol{q}}} \\ 0 \\ 0 \end{pmatrix}, \quad \Psi^{\varsigma=-}_{\boldsymbol{q},\lambda} = \frac{1}{\sqrt{2}}\begin{pmatrix} 0 \\ 0 \\ 1 \\ -\lambda e^{i\phi_{\boldsymbol{q}}} \end{pmatrix}, \tag{1.122}$$

where $\phi_{\boldsymbol{q}} = \arctan(q_y/q_x)$.

The eigenstates may equivalently be written as

$$\Psi^{\varsigma=+}_{\boldsymbol{q},\lambda} = \frac{1}{\sqrt{2A}} e^{i\boldsymbol{q}\cdot\boldsymbol{r}} \begin{pmatrix} \lambda \\ e^{i\phi_{\boldsymbol{q}}} \\ 0 \\ 0 \end{pmatrix}, \quad \Psi^{\varsigma=-}_{\boldsymbol{q},\lambda} = \frac{1}{\sqrt{2A}} e^{i\boldsymbol{q}\cdot\boldsymbol{r}} \begin{pmatrix} 0 \\ 0 \\ -\lambda \\ e^{i\phi_{\boldsymbol{q}}} \end{pmatrix}, \tag{1.123}$$

where $\boldsymbol{q} = (q_x, q_y)$, $\boldsymbol{r} = (x, y)$, and A is the area of the graphene monolayer.

1.2.2 Magnetic Field

In this section I will derive the Hamiltonian, eigenenergy and eigenstates for graphene in a constant magnetic field. Here and in all the sections (concerning graphene) that follows I will only deal with the case where the valley pseudospin $\varsigma = +1$ or equivalently, consider the low-energy expansion near $\boldsymbol{K}$. This is justified because the energy is independent of valley pseudospin. My derivation will follow [8, 10, 11].

Electrons in a lattice subjected to a magnetic field $\boldsymbol{B} = \nabla \times \boldsymbol{A}(\boldsymbol{r})$ can be described by making the Peierls substitution, that is, replacing the canonical momentum $\boldsymbol{p}$ by the gauge-invariant kinetic momentum $\boldsymbol{\pi}$

$$\boldsymbol{p} \to \boldsymbol{\pi} = \boldsymbol{p} + \frac{e}{c}\boldsymbol{A}(\boldsymbol{r}). \tag{1.124}$$

$\boldsymbol{A}(\boldsymbol{r})$ is the vector potential, e is the elementary charge, $\boldsymbol{p} = \hbar\boldsymbol{q}$ is the quasimomentum. The Peierls substitution is valid as long as the lattice spacing is much smaller than $\sqrt{\hbar c/(eB)}$. Under

$\boldsymbol{p} \to \boldsymbol{\pi}$ the Hamiltonian in Eq. (1.116) becomes

$$H^B = v_{\boldsymbol{F}} \begin{pmatrix} 0 & \pi_x - i\pi_y \\ \pi_x + i\pi_y & 0 \end{pmatrix} = v_F \boldsymbol{\sigma} \cdot \boldsymbol{\pi}. \tag{1.125}$$

It is convenient to express the Hamiltonian in Eq. (1.125) in terms of ladder operators $\hat{a}$ and $\hat{a}^\dagger$. To this end, one first finds the commutator

$$\begin{aligned} [\pi_m, \pi_n] &= [p_m + (e/c)A_m, p_n + (e/c)A_n] \\ &= \underbrace{[p_m, p_n]}_{=0} + (e/c)\underbrace{[p_m, A_n]}_{\text{(a)}} + (e/c)\underbrace{[A_m, p_n]}_{\text{(b)}} + (e/c)^2 \underbrace{[A_m, A_n]}_{=0}. \end{aligned} \tag{1.126}$$

Note that

$$\text{(a).} \quad [p_m, A_n] = -i\hbar[\partial_m, A_n] = -i\hbar\partial_m A_n, \tag{1.127}$$

$$\text{(b).} \quad [A_m, p_n] = +i\hbar[\partial_n, A_m] = +i\hbar\partial_n A_m, \tag{1.128}$$

so Eq. (1.126) is then

$$\begin{aligned} [\pi_m, \pi_n] &= -i\hbar\frac{e}{c}(\partial_m A_n - \partial_n A_m) \\ &= -i\hbar^2 \frac{e}{\hbar c} \sum_{m,n} \varepsilon_{kmn} \partial_m A_n = -i\hbar^2 \frac{e}{\hbar c}(\nabla \times \boldsymbol{A})_k = -i\hbar^2 \frac{eB_k}{\hbar c}. \end{aligned} \tag{1.129}$$

ε_{kmn} is the Levi-Civita symbol, $\partial_n = \partial/\partial x^n$; $n = 1, 2, 3$ and $x^1 = x$, $x^2 = y$, $x^3 = z$. For a magnetic field along the z-direction $\boldsymbol{B} = \boldsymbol{e}_z B$

$$[\pi_x, \pi_y] = -i\frac{\hbar^2}{l_B^2}, \tag{1.130}$$

$$l_B = \sqrt{\frac{\hbar c}{eB}} \tag{1.131}$$

l_B is called the magnetic length. Here the graphene sheet is in the xy-plane.

With the commutator of the conjugate pair π_x and π_y, one is able to introduce ladder operators

$$\hat{a} = \frac{l_B}{\sqrt{2}\hbar}(\pi_x - i\pi_y), \quad \hat{a}^\dagger = \frac{l_B}{\sqrt{2}\hbar}(\pi_x + i\pi_y). \tag{1.132}$$

This definition of the ladder operators ensures

$$\left[\hat{a}, \hat{a}^\dagger\right] = 1. \tag{1.133}$$

One can immediately write the Hamiltonian given in Eq. (1.125) in terms of the ladder operators given in Eq. (1.132)

$$H^B = \hbar\omega_c \begin{pmatrix} 0 & \hat{a} \\ \hat{a}^\dagger & 0 \end{pmatrix}, \tag{1.134}$$

where $\omega_c = \sqrt{2}v_F/l_B$. The eigenvalues and eigenstates are found by solving

$$H^B\psi_n = \mathcal{E}_n\psi_n, \quad \psi_n = \begin{pmatrix} u_n \\ v_n \end{pmatrix}, \tag{1.135}$$

which gives

$$\hbar\omega_c\hat{a}v_n = \mathcal{E}_n u_n, \quad \text{and} \quad \hbar\omega_c\hat{a}^\dagger u_n = \mathcal{E}_n v_n \tag{1.136}$$

$$\implies \hat{a}^\dagger\hat{a}v_n = \left(\frac{\mathcal{E}_n}{\hbar\omega_c}\right)^2 v_n. \tag{1.137}$$

Note that $\hat{a}^\dagger\hat{a}$ is the number operator which satisfies:

$$\hat{a}^\dagger\hat{a}h_n(\boldsymbol{r}) = nh_n(\boldsymbol{r}) \tag{1.138}$$

where [10]

$$h_n(\boldsymbol{r}) = \frac{(\hat{a}^\dagger)^n}{\sqrt{n}} h_0(\boldsymbol{r}). \tag{1.139}$$

In addition, the following holds true

$$\hat{a} h_0(\boldsymbol{r}) = 0, \tag{1.140}$$

$$\hat{a} h_n(\boldsymbol{r}) = \sqrt{n} h_{n-1}(\boldsymbol{r}), \tag{1.141}$$

$$\hat{a}^\dagger h_n(\boldsymbol{r}) = \sqrt{n+1} h_{n+1}(\boldsymbol{r}). \tag{1.142}$$

If one identifies the spinor component v_n as the number state $h_n(\boldsymbol{r})$ and then compare Eqs. (1.137) and (1.138) one sees that

$$\mathcal{E}_n = \mathrm{sgn}(n)\hbar\omega_c\sqrt{|n|}, \tag{1.143}$$

where

$$\mathrm{sgn}(n) = \begin{cases} +1 & n > 0, \\ 0 & n = 0, \\ -1 & n < 0. \end{cases}$$

$\mathrm{sgn}(n) = 0$ corresponds to the zeroth Landau level, $\mathrm{sgn}(n) = +1$ corresponds to the conduction band, whereas, $\mathrm{sgn}(n) = -1$ corresponds to the valence band. $n = 0, \pm 1, \pm 2, \ldots$ indexes the Landau levels (LLs) with energy $\mathcal{E}_n$.

For a constant magnetic field along the z direction $\boldsymbol{B} = \boldsymbol{e}_z B$, there is some freedom in selecting the vector potential $\boldsymbol{A}$ since, in general, it is not unique. In fact, for $A_x = c_x y B$, $A_y = c_y x B$, and $A_z = 0$, any real constants c_x, c_y satisfying $c_y - c_x = 1$ will give $\boldsymbol{B} = \boldsymbol{e}_z B$. I will select $c_y = 0 \implies c_x = -1 \implies \boldsymbol{A} = -\boldsymbol{e}_x y B$. For this choice of the vector potential, the ladder operators in Eq. (1.132) becomes

$$\hat{a} = \frac{l_B}{\sqrt{2}}\left[-i\partial_x - \left(\partial_y + \frac{y}{l_B^2}\right)\right], \quad \hat{a}^\dagger = \frac{l_B}{\sqrt{2}}\left[-i\partial_x + \left(\partial_y - \frac{y}{l_B^2}\right)\right]. \tag{1.144}$$

To find the state $h_0(\boldsymbol{r})$ one solves Eq. (1.140) using $\hat{a}$ given in Eq. (1.144) and separation of variables $h_0(\boldsymbol{r}) = X(x)\phi(y)$. Once $h_0(\boldsymbol{r})$ is found one normalizes it and then finds $h_n(\boldsymbol{r})$ using Eq. (1.139) and $\hat{a}^\dagger$ given in Eq. (1.144). Performing these steps and keeping in mind that $u_n \propto \hat{a}v_n = \hat{a}h_n = \sqrt{n}h_{n-1}$ yields the wavefunction [11]

$$\psi_{nk}(\boldsymbol{r}) = \frac{C_n}{\sqrt{L}} e^{ikx} \begin{pmatrix} \mathrm{sgn}(n) i^{|n|-1} \phi_{|n|-1,k}(y) \\ i^{|n|} \phi_{|n|,k}(y) \end{pmatrix}, \tag{1.145}$$

where

$$\phi_{|n|,k}(y) = \frac{H_{|n|}((y - kl_B^2)/l_B)}{\sqrt{2^{|n|}|n|!}\sqrt{\pi} l_B} \exp\left[-\frac{1}{2} \left(\frac{y - kl_B^2}{l_B} \right)^2 \right], \tag{1.146}$$

and

$$C_n = \begin{cases} 1 & n = 0 \\ \frac{1}{\sqrt{2}} & n \neq 0. \end{cases} \tag{1.147}$$

$H_n(y)$ is the Hermite polynomial. The energy eigenstates given in Eq. (1.145) are orthonormal and forms a complete set in area S (of the graphene monolayer)

$$\langle \alpha' | \alpha \rangle = \delta_{\alpha'\alpha}, \quad \sum_{\alpha \in n,k} |\alpha\rangle \langle \alpha| = \mathbb{1}. \tag{1.148}$$

Here $|\alpha\rangle \equiv |n, k\rangle$ (n is the LL index and k is the Bloch wavevector) and $\psi_{nk}(\boldsymbol{r}) = \langle \boldsymbol{r} | \alpha \rangle$. Since the energy eigenstates are complete and orthonormal, one is able to expand a function as a linear combination of the energy eigenstates

$$\Psi(\boldsymbol{r}) = \sum_\alpha c_\alpha \psi_\alpha(\boldsymbol{r}). \tag{1.149}$$

I will calculate the Landau level degeneracy, that is, the number of quantized cyclotron orbits in the area $S = L_x L_y$ of the graphene monolayer. If one assumes periodic boundary conditions in

the x-direction then e^{ikx} in Eq. (1.145) at the boundaries $x = 0$ and $x = L_x$ gives

$$e^{ik0} = e^{ikL_x} \implies k = \frac{2\pi}{L_x} m, \tag{1.150}$$

where $m = 0, 1, 2, \ldots$ In Eq. (1.146) one may write the numerator of the argument of the Hermite polynomial and the exponential as $y - y_0$ where $y_0 = kl_B^2$. Note that $0 < y_0 < L_y$ since, in the y-direction, the graphene monolayer is assumed to span the length between $y = 0$ and $y = L_y$. Thus,

$$0 < kl_B^2 < L_y \implies 0 < k < \frac{L_y}{l_B^2}. \tag{1.151}$$

Using Eqs. (1.150) and (1.151) one finds

$$0 < m < \frac{L_x L_y}{2\pi l_B^2}. \tag{1.152}$$

The total LL degeneracy is

$$\varkappa = g_s g_\nu \frac{L_x L_y}{2\pi l_B^2} = 2\frac{L_x L_y}{\pi l_B^2}, \tag{1.153}$$

where $g_s = 2$, $g_\nu = 2$ is the spin and valley degeneracy, respectively. It is convenient (for my purposes) to write the steps above in another way, i.e. as the sum over k states [12]:

$$\sum_k \to g_s g_\nu \int_0^{k_{max}} \frac{\mathrm{dk}}{\frac{2\pi}{L_x}} = g_s g_\nu \frac{L_x k_{max}}{2\pi} = 2\frac{L_x L_y}{\pi l_B^2} = \varkappa. \tag{1.154}$$

The limits of integration follow from Eq. (1.151) so k_{max} is the upper bound of k given in this equation.

2. DIFFERENCE FREQUENCY GENERATION OF SURFACE PLASMON-POLARITONS IN LANDAU QUANTIZED GRAPHENE*

2.1 Opening Remarks

This chapter is based on a publication of the same title that I coauthored [13]. Parts of the publication may appear verbatim in the sections that follow. I was the lead author of this publication.

As for my contributions: I contributed to aspects of the theory, carried out all simulations, created all illustrative figures and plots and was involved in the writing process (as lead author). This project was done in collaboration with A. Belyanin, M.D. Tokman, Y. Wang.

2.2 Introduction

In Sec. 1.2.1 I showed that the low-energy excitations of graphene are massless Dirac fermions. These massless Dirac fermions are responsible for many of the unique transport, thermal, and optical properties of graphene [5]. Graphene was shown to support highly-confined surface plasmon modes [14, 15]; it has relatively long-lived plasmon-polariton modes due to large intrinsic carrier mobilities and doping tunability [16, 17, 18], excellent electro-optic tunability [19], and large third-order and second-order optical nonlinearity [20, 21, 22, 23, 24]. The latter is surprising since graphene is a centrosymmetric medium for low-energy in-plane excitations. For centrosymmetric materials the second order-response should be zero [1] in the electric-dipole approximation. However, one may circumvent this apparent problem if one is able to induce in-plane anisotropy. In-plane anisotropy can be induced by obliquely incident, or in-plane EM waves with non-zero wavevector in the graphene plane [25, 21, 22, 23, 24]. In particular, the effects of spatial dispersion, or in real space, nonlocal effects beyond the electric dipole approximation is responsible for induced in-plane anisotropy.

While any surface has anisotropy between its in-plane and out-of-plane excitations, it was

*Reprinted with permission from "Difference Frequency Generaration of Surface Plasmon-Polaritons in Landau Quantized Graphene" by A. Ryan Kutayiah, Mikhail Tokman, Yongrui Wang, and Alexey Belyanin, 2018. Phys. Rev. B, 98, 115410, Copyright 2018 by The American Physical Society.

shown [26] that the second-order response due to out-of-plane anisotropy is small. As such, it will be neglected. In contrast, second-order in-plane nonlinearity is actually quite large [25, 23, 24, 27, 28]. A particularly large value of $\chi^{(2)} \sim 10^{-3}$ m/V [24] is reached at low frequencies, for the processes of frequency down-conversion such as difference frequency generation (DFG) [23, 24, 29, 30, 31] or parametric down-conversion [27]. Further enhancement of the nonlinear generation efficiency is possible when the DFG signal is frequency- and phase-matched to surface plasmon-polaritons in graphene [23].

Here, I consider a graphene monolayer that acts as a nonlinear medium and is integrated in a monolithic photonic chip. The photonic chip provides confinement of the electromagnetic (EM) modes and thus allow for maximizing the overlap of the in-plane amplitude of the pump fields with the graphene monolayer. Furthermore, graphene is placed in a uniform magnetic field along the z-direction and the monolayer is assumed to reside in the xy-plane. The magnetic field results in Laudau levels (see Sec. 1.2.2), which in turn allows for resonant transitions by electromagnetic fields, leading to an enhancement in the second-order response $\chi^{(2)}$. In addition, Landau level degeneracy enhances the density of states which also enhances $\chi^{(2)}$. I will show that for a magnetic field in the range of $1 - 10$ T, the power conversion efficiency is on the order of tens μW/W^2 for waveguide structures of 10-100 μm.

2.3 Optical Fields in a Waveguide

In order to elicit a second-order response from graphene, two transverse electric (TE) polarized counter-propagating optical fields of frequency ω_1 and ω_2 are fed into a photonic chip at opposite ends, see Fig. 2.1. TE polarization is chosen as opposed to transverse magnetic (TM) polarization because there are two components $\sigma^{(2)}_{xyy}$ and $\sigma^{(2)}_{yyx}$ of the second-order conductivity tensor for TE and only one component $\sigma^{(2)}_{xxx}$ for TM [24]. Furthermore, $|\sigma^{(2)}_{xyy}| > |\sigma^{(2)}_{xxx}|$ [24]. Regarding the latter two statements, Ref. [24] considered DFG in graphene where the input pump fields were in the mid-infrared range and scattering losses for pristine graphene.

The pump field of frequency ω_1 is assumed to be propagating in the $+x$-directions, while the field of frequency ω_2 is assumed to be traveling in the opposite direction, see Fig. 2.1. In addition,

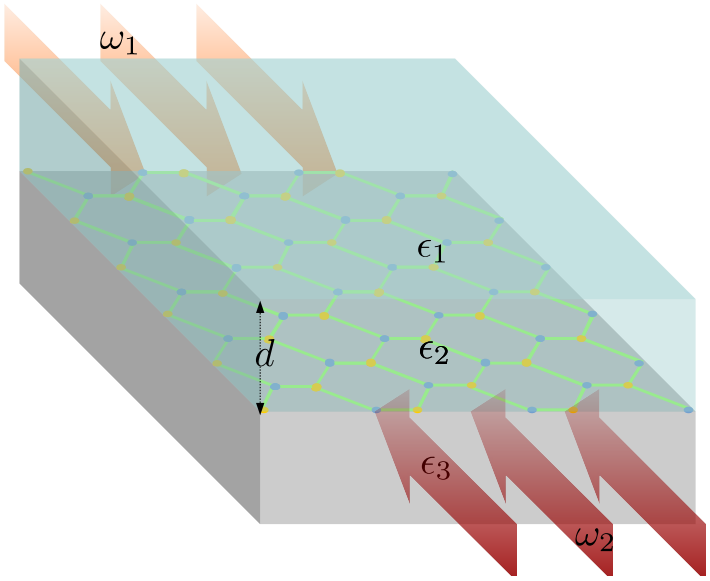

Figure 2.1: Two counter-propagating pump fields incident on a waveguide with graphene at the interface of dielectrics ϵ_2 and ϵ_3.

the fields are assumed to have no variation in the y-direction.

The waveguide structure is such that interfaces are located in the plane $z = d/2$ and $z = -d/2$, where d is the thickness of the core layer, see Figs. 2.2a and 2.2b. The dielectric constants of the waveguide along z is then:

$$\epsilon_j = \begin{cases} \epsilon_1 & z > d/2, \\ \epsilon_2 & -d/2 < z < d/2, \\ \epsilon_3 & z < -d/2. \end{cases} \tag{2.1}$$

I will consider two locations for graphene, one where graphene is located at the interface of the core layer (with dielectric constant ϵ_2) and the bottom cladding (with dielectric constant ϵ_3); this case is depicted in Fig. 2.2a. The other instance is where graphene is located in the middle of the core layer as depicted in Fig. 2.2b. In both cases the graphene monolayer is assumed to be encapsulated in hexagonal boron nitride (hBN). This is done to prevent disorder arising from lattice mismatch between graphene and the adjacent dielectric layers of the waveguide. Such disorder would be detrimental for carrier mobility and optical linewidth transition in graphene.

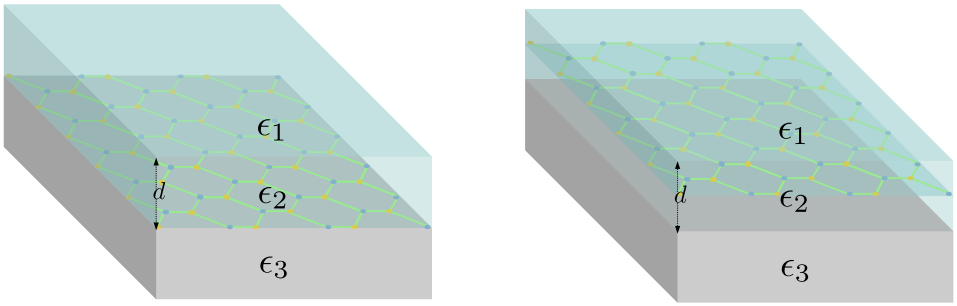

(a) Graphene is located at the interface of dielectrics ϵ_2 and ϵ_3 which is the plane $z = -d/2$.

(b) Graphene is located in the middle of the waveguide core ϵ_2 which is the plane $z = 0$.

Figure 2.2: Waveguide configurations. Adapted with permission from [13].

The contribution of graphene and hBN to the pump distribution in the waveguide will be neglected since they are both thin; graphene is on the Angstrum scale while the hBN layers are assumed to be of nanometer thickness. There may be a concern that using a hBN substrate could possibly open up a gap in graphene, as indicated by an early theoretical work [32]; however, subsequent experiments have not found any gap [33, 34].

There are two waveguide configurations that I considered: the asymmetric waveguide given by $\epsilon_1 \neq \epsilon_2 \neq \epsilon_3$ and the symmetric waveguide given by $\epsilon_1 = \epsilon_3 \neq \epsilon_2$. For numerical examples (concerning this project) the dielectrics ϵ_1, ϵ_2, ϵ_3 are chosen as air, GaAs, Alas or air, Si, SiO_2 for the asymmetric waveguide. For the symmetric waveguide the top and bottom cladding are both chosen to be air. Furthermore, I will assume that the dimensions of the waveguide in the x- and y-directions coincide with that of the graphene monolayer.

Finding the distribution of an optical field in a slab waveguide is a standard textbook problem, see [35] for example . But for the sake of completeness, I will derive the conditions required to confine an optical field to the core of the waveguide and find its z-distribution.

I will assume plane waves for both TE polarized pump fields:

$$\boldsymbol{E}^{(l)}(x,z,t) = \mathrm{Re}[(0, E_y^{(l)}(z), 0)e^{i(\mathrm{sgn}(l)q_l x - \omega_l t)}], \tag{2.2}$$

where $l = 1, 2$ indexes the pump fields, $\mathrm{sgn}(l) = +1$ for $l = 1$, and -1 for $l = 2$. One solves the wave equation to find the modes that are confined to the core region of the waveguide

$$(\nabla^2 - \frac{\epsilon_j}{c^2}\partial_t^2)\boldsymbol{E}^{(l)}(x, z, t) = 0, \tag{2.3}$$

$$\implies \frac{d^2 E_y^{(l)}(z)}{dz^2} = \lambda_{jl} E_y^{(l)}(z), \tag{2.4}$$

$$\lambda_{jl} = \begin{cases} \kappa_{1l}^2 & z > d/2, \\ \kappa_{2l}^2 & -d/2 < z < d/2, \\ \kappa_{3l}^2 & z < -d/2. \end{cases} \tag{2.5}$$

ϵ_j is given by Eq. (2.1). The waveguide is assumed to be asymmetric since it is more general than the symmetric case. One can consider the symmetric waveguide as a special case of the asymmetric waveguide. I have neglected any effects that the graphene monolayer may have on the distribution of the pump fields in the waveguide. In other words, I will solve for the EM modes in a waveguide as if the graphene monolayer is absent.

For confinement of an EM mode to the core of the waveguide one expects the wave to oscillate in the region $-d/2 < z < d/2$ and exponentially decay otherwise. These conditions are satisfied when $\kappa_{(1,3)l}$ are real and κ_{2l} is complex, where κ_{jl} are defined as

$$\kappa_{(1,3)l} = \sqrt{q_l^2 - \epsilon_{1,3}\frac{\omega_l^2}{c^2}}, \tag{2.6}$$

$$\kappa_{2l} = i\alpha_l, \quad \alpha_l \equiv \sqrt{\epsilon_2 \frac{\omega_l^2}{c^2} - q_l^2}. \tag{2.7}$$

Sometimes the confinement condition is written as $(\omega/c)^2\epsilon_{1,3} < q_l^2 < (\omega_l/c)^2\epsilon_2$; for low losses (neglecting the imaginary part of the index of refraction) $\epsilon_j \approx n_j^2$ so the confinement condition

becomes $n_{1,3} < n_{\text{eff},l} < n_2$ where $n_{\text{eff},l} = (c/\omega_l)q_l$. Solving Eq. (2.4) results in

$$\boldsymbol{E}^{(l)}(x,z,t) = \boldsymbol{e}_y \operatorname{Re}[e^{i(\operatorname{sgn}(l)q_l x - \omega_l t)}] \begin{cases} a_l e^{-\kappa_{1l}(z-d/2)} & z > d/2 \\ b_l \cos(\alpha_l z - \phi_l) & -d/2 < z < d/2 \\ c_l e^{\kappa_{3l}(z+d/2)} & z < -d/2. \end{cases} \tag{2.8}$$

Integrating $\nabla \times \boldsymbol{E}^{(l)} = -c^{-1}\partial_t \boldsymbol{B}^{(l)}$ over the differential area $d\boldsymbol{A}$ and using Stokes' theorem one finds that the tangential component of the electric field is continuous at the boundaries. Using the continuity of the tangential component of $\boldsymbol{E}$ at the boundaries $z = \pm d/2$, one finds that $a_l = b_l \cos(\alpha_l d/2 - \phi_l)$ and $c_l = b_l \cos(\alpha_l d/2 + \phi_l)$. Only one undetermined coefficient remains, b_l, which I will relabel as $\mathcal{A}_l$. Thus, Eq. (2.8) can be written as

$$\boldsymbol{E}^{(l)}(x,z,t) = \boldsymbol{e}_y \operatorname{Re}[e^{i(\operatorname{sgn}(l)q_l x - \omega_l t)}] \mathcal{A}_l f_{jl}(z), \tag{2.9}$$

where

$$f_{jl}(z) = \begin{cases} \cos(\alpha_l d/2 - \phi_l) e^{-\kappa_{1l}(z-d/2)} & z > d/2 \\ \cos(\alpha_l z - \phi_l) & -d/2 < z < d/2 \\ \cos(\alpha_l d/2 + \phi_l) e^{\kappa_{3l}(z+d/2)} & z < -d/2. \end{cases} \tag{2.10}$$

The coefficient $\mathcal{A}_l$ can be found by normalizing the Poynting flux. The Poynting vector is given by

$$\boldsymbol{S}^{(l)} = \frac{c}{4\pi}(\boldsymbol{E}^{(l)} \times \boldsymbol{B}^{(l)}) \tag{2.11}$$

$$\boldsymbol{S}^{(l)} = \frac{c}{4\pi}\left(\frac{1}{2}\operatorname{Re}[\boldsymbol{E}_R^{(l)} \times \boldsymbol{B}_R^{(l)*}] + \frac{1}{2}\operatorname{Re}[(\boldsymbol{E}_R^{(l)} \times \boldsymbol{B}_R^{(l)}) e^{-2i\omega t}]\right) \tag{2.12}$$

where I have used $\boldsymbol{F} = \operatorname{Re}[\boldsymbol{F}_R e^{-i\omega t}] = (1/2)\boldsymbol{F}_R e^{-i\omega t} + (1/2)\boldsymbol{F}_R^* e^{i\omega t}$ and $\boldsymbol{F}$ represent the real fields $\boldsymbol{E}, \boldsymbol{B}$; $\boldsymbol{F}_R = (F_x, F_y, F_z)e^{i\boldsymbol{k}\cdot\boldsymbol{r}}$. The time average of the Poynting vector is $\langle \boldsymbol{S} \rangle = T^{-1}\int_0^T \boldsymbol{S}\,\mathrm{dt}$ or

$$\left\langle \boldsymbol{S}^{(l)} \right\rangle = \frac{c}{8\pi}\operatorname{Re}[\boldsymbol{E}_R^{(l)} \times \boldsymbol{B}_R^{(l)*}]; \tag{2.13}$$

I used the fact that the second term in Eq. (2.12) averages to zero over the period $T = 2\pi/\omega$. The average Poynting flux is then

$$\left\langle \Phi_S^{(l)} \right\rangle = \int \left\langle \boldsymbol{S}^{(l)} \right\rangle \cdot d\boldsymbol{A}^{(l)}. \tag{2.14}$$

Since the pump fields are propagating in the $\pm x$-directions the Poynting vector for TE polarized fields are given by $\boldsymbol{S}^{(l)} = \boldsymbol{e}_x S_x^{(l)} = \boldsymbol{e}_x (c/8\pi) E_{yR}^{(l)}(x,z) B_{zR}^{(l)*}(x,z)$, $d\boldsymbol{A}^{(l)} = \boldsymbol{e}_x \mathrm{sgn}(l) dydz$, but I assumed there is no variation in the y-direction, therefore any integration over dy simply results in multiplying by L_y. Equivalently, dy can directly be replaced by L_y. Thus, $d\boldsymbol{A}^{(l)} = \boldsymbol{e}_x \mathrm{sgn}(l) L_y dz$.

For a TE polarized pump fields one finds from $\nabla \times \boldsymbol{E}^{(l)} = -c^{-1}\partial_t \boldsymbol{B}^{(l)}$ that $\boldsymbol{B}_{zR}^{(l)*}(x,z) = \mathrm{sgn}(l)(q_l c/\omega_l) E_{yR}^{(l)*}(x,z)$. The average Poynting flux is then

$$\left\langle \Phi_S^{(l)} \right\rangle = (\mathrm{sgn}(l))^2 \frac{c^2 q_l L_y}{8\pi\omega_l} |\mathcal{A}_l|^2 \int_{-\infty}^{+\infty} |f_{jl}(z)|^2 \, dz. \tag{2.15}$$

Note that the integral is to be evaluated in a piecewise manner since f_{jl} is a piecewise function. Obviously, $(\mathrm{sgn}(l))^2 = 1$ since $\mathrm{sgn}(l) = \pm 1$. If the average Poynting flux is normalized to the input pump power P_o (where I have assumed for simplicity that both pumps have initial power P_o but one can assume different powers P_{ol}) then $\mathcal{A}_l$ is

$$\mathcal{A}_l = \sqrt{\frac{8\pi\omega_l P_o}{L_y c^2 q_l F_l}}, \tag{2.16}$$

where $F_l = \int_{-\infty}^{+\infty} |f_{jl}(z)|^2 \, dz$.

To calculate F_l one needs to know the phase ϕ_l given in Eq. (2.10). From $\nabla \times \boldsymbol{E}^{(l)} = c^{-1}\partial_t$ one finds $B_x^{(l)} = ic\omega_l^{-1}\partial_z E_y^{(l)}$. Integrating $\nabla \times \boldsymbol{B}^{(l)} = \epsilon_j c^{-1}\partial_t \boldsymbol{E}^{(l)}$ over $d\boldsymbol{A} = \boldsymbol{e}_y dxdz$ one finds that $B_x^{(l)}$ is continuous; therefore, $\partial_z E_y^{(l)}$ is continuous. Using the continuity of $\partial_z E_y^{(l)}$ at the boundaries $z = \pm d/2$ gives

$$2\phi_l = m\pi - \tan^{-1}(\kappa_{1l}/\alpha_l) + \tan^{-1}(\kappa_{3l}/\alpha_l) \tag{2.17}$$

$$\alpha_l d = m\pi + \tan^{-1}(\kappa_{1l}/\alpha_l) + \tan^{-1}(\kappa_{3l}/\alpha_l), \tag{2.18}$$

where m is the mode number. I will select the zeroth mode for all calculations. The transcendental equation, Eq. (2.18) gives the dependence of the parameters α_l, $\kappa_{(1,3)l}$ (which should really be written as $\alpha_{m,l}$, $\kappa_{m,(1,3)l}$) on the core thickness d.

2.4 Optical Selection Rules

In this section I will derive the selection rules for an optical field interacting with Landau quantized graphene. From the selection rules one will see that resonant coupling occurs between EM fields and LLs in magnetized graphene. To begin I will find the interaction Hamiltonian.

If one extends the vector potential $\boldsymbol{A}$ in Eq. (1.124) to include an optical field, i.e. $\boldsymbol{A} \rightarrow \boldsymbol{A}_B + \boldsymbol{A}_{opt}(t)$ then the Hamiltonian given in Eq. (1.125) can be written as

$$H = v_F \boldsymbol{\sigma} \cdot \boldsymbol{\pi} = v_F \boldsymbol{\sigma} \cdot (\hbar \boldsymbol{k} + \frac{e}{c}[\boldsymbol{A}_B + \boldsymbol{A}_{opt}(t)]) = H^B + H^{int}(t) \tag{2.19}$$

where I have added a subscript B to the vector potential $\boldsymbol{A}$ (of the external magnetic field) to distinguish it from the vector potential of the optical field, A_{opt}. In Eq. (2.19) the term H^B corresponds to graphene in a magnetic field as given by Eq. (1.125), with one exception, I relabeled $\boldsymbol{q}$ as $\boldsymbol{k}$ since I am using $\boldsymbol{q}_l$ as the wavevector for the pump fields. H^{int}, the interaction Hamiltonian, gives the interaction between graphene and an optical field; in particular

$$H^{int}(t) = \frac{v_F e}{c} \boldsymbol{\sigma} \cdot \boldsymbol{A}_{opt}(t). \tag{2.20}$$

If the optical field oscillates with a term $\propto e^{-i\omega_l t}$, using $\boldsymbol{E}^{(l)} = -c^{-1}\partial_t \boldsymbol{A}^{(l)}_{opt}$ one finds

$$\boldsymbol{A}^{(l)}_{opt}(t) = \frac{c}{i\omega_l} \boldsymbol{E}^{(l)}(t) \tag{2.21}$$

and the interaction Hamiltonian becomes

$$H^{int}(t) = \frac{v_F e}{i\omega_l} \boldsymbol{\sigma} \cdot \boldsymbol{E}^{(l)}(t). \tag{2.22}$$

Consider a linearly polarized optical field $\boldsymbol{E}^{(l)} = \mathrm{Re}[\boldsymbol{E}_R^{(l)} e^{-i\omega_l t}]$, $\boldsymbol{E}_R^{(l)} = (\boldsymbol{e}_x E_x + \boldsymbol{e}_y E_y) e^{\boldsymbol{q}_l \cdot \boldsymbol{r}}$. A change of basis

$$\boldsymbol{e}_\pm = \frac{\boldsymbol{e}_x \pm i\boldsymbol{e}_y}{\sqrt{2}}, \tag{2.23}$$

$$\text{or} \quad \boldsymbol{e}_x = \frac{\sqrt{2}}{2}(\boldsymbol{e}_+ + \boldsymbol{e}_-), \tag{2.24}$$

$$\text{and} \quad \boldsymbol{e}_y = \frac{\sqrt{2}}{2i}(\boldsymbol{e}_+ - \boldsymbol{e}_-), \tag{2.25}$$

results in transforming the polarization from linear to circular, thus $\boldsymbol{E}_R^{(l)} \rightarrow \tilde{\boldsymbol{E}}_R^{(l)} = (\boldsymbol{e}_+ \tilde{E}_+^{(l)} + \boldsymbol{e}_- \tilde{E}_-^{(l)}) e^{\boldsymbol{q}_l \cdot \boldsymbol{r}}$ and

$$\tilde{E}_\pm^{(l)} = \frac{\sqrt{2}}{2}(E_x^{(l)} \mp i E_y^{(l)}). \tag{2.26}$$

Note that for a TE polarized field $E_x^{(l)} = 0$ so $\tilde{E}_\pm^{(l)} = \pm i\sqrt{2} E_y^{(l)}/2$. To connect with Sec. 2.3 the $\boldsymbol{E}$ field field given in Eq. (2.9) can be written as $\boldsymbol{E}^{(l)} = \mathrm{Re}[\tilde{\boldsymbol{E}}_R^{(l)} e^{i\omega_l t}] = \mathrm{Re}[(\boldsymbol{e}_+ \tilde{E}_+^{(l)} + \boldsymbol{e}_- \tilde{E}_-^{(l)}) e^{i(\mathrm{sgn}(l) q_l x - \omega_l t)}]$ where

$$\tilde{E}_\pm^{(l)} = \mp \frac{i\sqrt{2}}{2} \mathcal{A}_l f_{jl}(z). \tag{2.27}$$

Since the interaction Hamiltonian contains the dot product of the vector of Pauli matrices $\boldsymbol{\sigma}$ and the optical field $\boldsymbol{E}$ it is convenient to express $\boldsymbol{\sigma}$ in the circular basis $\boldsymbol{\sigma} = \boldsymbol{e}_+ \sigma^+ + \boldsymbol{e}_- \sigma^-$ where

$$\sigma^+ = \begin{pmatrix} 0 & 0 \\ \sqrt{2} & 0 \end{pmatrix}, \quad \text{and} \quad \sigma^- = \begin{pmatrix} 0 & \sqrt{2} \\ 0 & 0 \end{pmatrix}. \tag{2.28}$$

The following dot products will be useful

$$\boldsymbol{e}_\pm \cdot \boldsymbol{e}_\mp = 1, \quad \text{and} \quad \boldsymbol{e}_\pm \cdot \boldsymbol{e}_\pm = 0. \tag{2.29}$$

Using Eqs. (2.28), (2.29) and $\boldsymbol{E}^{(l)}(t)$ in the circular basis, the interaction Hamiltonian becomes

$$\begin{aligned} H^{int}(t) &= v_F(\boldsymbol{e}_+\sigma^- + \boldsymbol{e}_-\sigma^+)\cdot\left[\left(\frac{e}{2i\omega_l}\boldsymbol{e}_+\tilde{E}_+^{(l)} + \boldsymbol{e}_-\tilde{E}_-^{(l)}\right)e^{i\boldsymbol{q}_l\cdot\boldsymbol{r}-i\omega_l t} + \text{c.c}\right] \\ &= \frac{ev_F}{i\omega_l}(\sigma^- E_+^{(l)} + \sigma^+ E_-^{(l)})e^{i\boldsymbol{q}_l\cdot\boldsymbol{r}-i\omega_l t} + \ldots, \end{aligned} \tag{2.30}$$

where $E_\pm^{(l)} = (1/2)\tilde{E}_\pm^{(l)}$. Henceforth, in Eq. (2.30) I will drop the terms contained in $+\ldots$.

The selection rules are obtained by taking the matrix element of the interaction Hamiltonian. Let $|\beta\rangle = |m, k'\rangle$ where m is the Landau level index and k' is the Bloch wavevector of p_z electrons in magnetized graphene then the wavefunction is given by $\langle \boldsymbol{r}|m, k'\rangle = \psi_{m,k'}(\boldsymbol{r})$ (see Eq. (1.145)). The matrix elements of the interaction Hamiltonian, in the electric-dipole approximation ($\boldsymbol{q}_l \to 0$), is

$$\langle n, k|H^{int}|m, k'\rangle = \frac{ev_F}{i\omega_l}(\underbrace{\langle n, k|\sigma^-|m, k'\rangle}_{\text{(a)}}E_+^{(l)} + \underbrace{\langle n, k|\sigma^+|m, k'\rangle}_{\text{(b)}}E_-^{(l)})e^{-i\omega_l t}. \tag{2.31}$$

The matrix elements of $\sigma^\pm$, given by (a) and (b) in Eq. (2.31), are evaluated below:

$$\begin{aligned} \text{(a).}\quad \langle n, k|\sigma^-|m, k'\rangle \equiv \sigma^-_{\alpha\beta} &= \frac{C_n^* C_m}{L}\int e^{i(k'-k)x}\,dx \\ &\times \int \begin{pmatrix} \text{sgn}(n)i^{1-|n|}\phi^*_{|n|-1,k}(y) & i^{-|n|}\phi^*_{|n|,k}(y)\end{pmatrix}\begin{pmatrix} 0 & \sqrt{2} \\ 0 & 0\end{pmatrix} \\ &\times \begin{pmatrix} \text{sgn}(m)i^{|m|-1}\phi_{|m|-1,k'}(y) \\ i^{|m|}\phi_{|m|,k'}(y)\end{pmatrix}dy \\ \implies \sigma^-_{\alpha\beta} &= \sqrt{2}C_nC_m\text{sgn}(n)\delta_{kk'}\delta_{|n|-1,|m|}; \end{aligned} \tag{2.32}$$

similarly, (2.33)

$$\text{(b).}\quad \sigma^+_{\alpha\beta} = \sqrt{2}C_nC_m\text{sgn}(m)\delta_{kk'}\delta_{|n|+1,|m|}. \tag{2.34}$$

In the derivations above I used the fact that C_n is real, $\phi_{|m|,k'}(y)$ is orthonormal and

$$\int e^{i(k'-k)x}\,dx = L\delta_{kk'}. \tag{2.35}$$

Using Eqs. (2.32) and (2.34), Eq. (2.31), the matrix element of the interaction Hamiltonian, becomes

$$H^{int}_{\alpha\beta}(t) = \frac{\sqrt{2}C_nC_nev_F}{i\omega_l}\delta_{kk'}(\mathrm{sgn}(n)\delta_{|n|-1,|m|}E^{(l)}_{+} + \mathrm{sgn}(m)\delta_{|n|+1,|m|}E^{(l)}_{-})e^{-i\omega_l t}. \tag{2.36}$$

It is instructive to look at the matrix elements of dipole moment $\boldsymbol{d}_{\alpha\beta} = -e\boldsymbol{r}_{\alpha\beta}$. Following [22], I will use the Heisenberg equation of motion to find $\boldsymbol{r}_{\alpha\beta}$

$$\begin{aligned} &i\hbar\dot{\boldsymbol{r}} = [\boldsymbol{r}, H] + \partial_t\boldsymbol{r} = [\boldsymbol{r}, H^B] + [\boldsymbol{r}, H^{int}] + \underbrace{\partial_t\boldsymbol{r}}_{=0} \\ &\implies i\hbar\dot{\boldsymbol{r}} = [\boldsymbol{r}, H^B] + \frac{e}{c}\underbrace{[\boldsymbol{r}, \boldsymbol{A}_{opt}(\boldsymbol{r})]}_{=0}e^{-i\omega_l t} \\ &\implies i\hbar\boldsymbol{v}_{\alpha\beta} = (\mathcal{E}_\beta - \mathcal{E}_\alpha)\boldsymbol{r}_{\alpha\beta} \implies \boldsymbol{r}_{\alpha\beta} = -\frac{i\hbar}{\mathcal{E}_\alpha - \mathcal{E}_\beta}\boldsymbol{v}_{\alpha\beta}. \end{aligned} \tag{2.37}$$

Now it remains to find $\boldsymbol{v}_{\alpha\beta}$. Note that the velocity operator for graphene near the Dirac point is $\boldsymbol{v} = v_F\boldsymbol{\sigma}$ [22]. Therefore, the matrix elements of the velocity operator depends on the matrix elements of $\boldsymbol{\sigma}$ which was already found in Eqs. (2.32) and (2.34); thus

$$\boldsymbol{d}_{\alpha\beta}\cdot\boldsymbol{E}^{(l)} = \frac{i\hbar ev_F}{\mathcal{E}_\alpha - \mathcal{E}_\beta}\sqrt{2}C_nC_m\delta_{kk'}(\mathrm{sgn}(n)\delta_{|n|-1,|m|}E^{(l)}_{+} + \mathrm{sgn}(m)\delta_{|n|+1,|m|}E^{(l)}_{-})e^{-i\omega_l t} + \ldots \tag{2.38}$$

where the electric-dipole approximation was used.

Comparing Eqs. (2.36) and (2.38), one sees that $H^{int}_{\alpha\beta} = \boldsymbol{d}_{\alpha\beta}\cdot\boldsymbol{E}^{(l)}$ when the $+\ldots$ terms are dropped in Eq. (2.38) and when $\mathcal{E}_\alpha - \mathcal{E}_\beta \equiv \hbar\omega_{\alpha\beta} = \hbar\omega_l$ (recall $\mathcal{E}_m = \hbar(\mathrm{sgn}(m)\omega_c\sqrt{|m|}) \implies \omega_m = \mathrm{sgn}(m)\omega_c\sqrt{|m|}$). To be clear, $\boldsymbol{d}_{\alpha\beta}$ is defined as the dipole moment at exact resonance with the optical field of frequency ω_l. Thus, for an optical field of frequency ω_l, the $E^{(l)}_{+}$ component couples to a transition $|m| \to |n| = |m| + 1$ provided that the energy of this transition is resonant with the energy of the photon, i.e. $\mathcal{E}_{|m|+1} - \mathcal{E}_m = \hbar(\omega_{|m|+1} - \omega_m) \approx \hbar\omega_l$. A similar argument holds for the $E^{(l)}_{-}$ component which couples to the transition $|m| \to |n| = |m| - 1$. Note that $|m|$ is the initial state and $|n|$ is the final state. The selection rules for allowed optical transitions in the

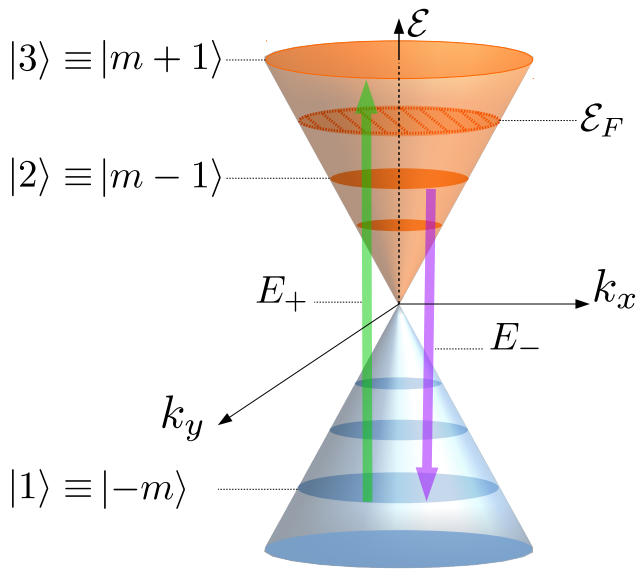

Figure 2.3: Sketch of LLs and resonant coupling of particular components and frequencies of the pump fields to LLs. Adapted with permission from [13].

electric-dipole approximation are

$$|n| - |m| \equiv \Delta|m| = \pm 1. \tag{2.39}$$

Recall that the index $l = 1, 2$ denotes the pump fields. For definiteness I will select the pump fields such that the field with frequency ω_1 is resonant with the transition $|m| \to |m| + 1$ and the field with frequency ω_2 is resonant with $|m| \to |m| - 1$, where I have chosen $m < 0$. For convenience I will label the states as follows $m \to |1\rangle$, $|m| - 1 \to |2\rangle$ and $|m| + 1 \to |3\rangle$. As such, $E_+^{(1)}$ couples to the transition $|1\rangle \to |3\rangle$ and $E_-^{(2)}$ couples to $|1\rangle \to |2\rangle$, see Fig. 2.3. The assumptions in this paragraph will be upheld throughout this chapter.

2.5 Linear Optical Conductivity

The linear optical conductivity can be obtained by the Kubo-Greenwood formula as given by Eq. (1.34). Keep in mind that the dipole moment is defined at exact resonance as stated in Sec. 2.4.

The linear optical conductivity is

$$\boldsymbol{j}^{(l)}(t) = \frac{ie^2}{S\hbar\omega_l} \sum_{\alpha,\beta} \frac{\boldsymbol{v}_{\beta\alpha}(\boldsymbol{v}_{\alpha\beta} \cdot \boldsymbol{E}_R^{(l)})(f_\alpha - f_\beta)}{\omega_{\alpha\beta} - \omega_l - i\gamma_{\alpha\beta}} e^{-i\omega_l t} \tag{2.40}$$

using $\boldsymbol{j}^{(l)}(t) = \boldsymbol{j}(\omega_l)e^{-i\omega_l t}$, $\boldsymbol{j}(\omega_l) = \boldsymbol{\sigma}_{con}(\omega_l)\boldsymbol{E}_R^{(l)}$, and Eq. (2.40) one finds components of the conductivity tensor $\boldsymbol{\sigma}_{con}(\omega_l)$

$$\sigma_{con}^{pr}(\omega_l) = \frac{ie^2 v_F^2}{S\hbar\omega_l} \sum_{\alpha,\beta,r\neq p} \frac{(f_\alpha - f_\beta)\sigma_{\beta\alpha}^p \sigma_{\alpha\beta}^r}{\omega_{\alpha\beta} - \omega_l - i\gamma_{\alpha\beta}}. \tag{2.41}$$

where p, r takes values $+$ or $-$ since they index the circular basis. The sum $\sum_{r\neq p}$ comes from using the circular basis vectors. Note that Eq. (2.41) is the Kubo-Greenwood formula for the optical conductivity of graphene in the electric-dipole approximation.

There are only two non-zero components of the conductivity tensor: σ_{con}^{-+} and σ_{con}^{+-}. The other components, σ_{con}^{++} and σ_{con}^{--}, are both zero since $p = r$ in this case. A more rigorous way to see that they are zero is to take the sum over α and β of $\sigma_{\beta\alpha}^{+}\sigma_{\alpha\beta}^{+}$. When this is done one should see that the delta functions contained in the matrix elements of σ_{con}^{++} cannot be simultaneously satisfied since $\sigma_{con}^{++} \propto \sum_{\alpha\beta} \sigma_{\beta\alpha}^{+}\sigma_{\alpha\beta}^{+} \propto \sum_{m,n} \delta_{|n|-1,|m|}\delta_{|n|+1,|m|} = 0$. Where $\sigma_{\alpha\beta}^{+}$ is obtained from Eq. (2.34) and $\sigma_{\beta\alpha}^{+}$ is found by interchanging m and n. Similarly, one finds that $\sigma_{con}^{--} \propto \sum_{\alpha\beta} \sigma_{\beta\alpha}^{-}\sigma_{\alpha\beta}^{-} = 0$.

2.6 Surface Charge Density

The EM pump fields incident upon the Landau quantized graphene monolayer displaces its electrons from equilibrium. The cumulative displacement of the electrons leads to a polarization

$$\boldsymbol{P} = \boldsymbol{P}^{(L)} + \boldsymbol{P}^{(NL)} \tag{2.42}$$

where $\boldsymbol{P}^{(L)}$ is the linear polarization (same as $\tilde{\boldsymbol{P}}^{(1)}$ in Sec. 1.1.3) and $\boldsymbol{P}^{(NL)}$ is the nonlinear polarization (same as $\tilde{\boldsymbol{P}}^{(NL)}$ in Sec. 1.1.3). The polarization is related to the charge density by

$$\rho(\boldsymbol{r}) = -\nabla \cdot \boldsymbol{P}(\boldsymbol{r}). \tag{2.43}$$

The surface charge density of Landau quantized graphene is given by

$$\rho(\boldsymbol{r}) = -e\Psi^*(\boldsymbol{r})\Psi(\boldsymbol{r}) = -e\sum_{\alpha,\beta} c^*_\beta c_\alpha \psi^*_\beta(\boldsymbol{r})\psi_\alpha(\boldsymbol{r}) \tag{2.44}$$

$$\implies \rho(\boldsymbol{r}) = -e\sum_{\alpha,\beta} \rho_{\alpha\beta}\psi^*_\beta(\boldsymbol{r})\psi_\alpha(\boldsymbol{r}) \tag{2.45}$$

where $\rho_{\alpha\beta}$ is the density matrix (see Sec. 2.5) and ψ_α is the energy eigenstate of graphene in a magnetic field (see Eq. (1.145)).

Next, I will consider the spatial Fourier transform of the charge density $\rho(\boldsymbol{r})$

$$\rho(\boldsymbol{r}) = \sum_{\boldsymbol{q}} \rho_{\boldsymbol{q}} e^{i\boldsymbol{q}\cdot\boldsymbol{r}}, \quad \text{and} \quad \rho_{\boldsymbol{q}} = \frac{1}{S}\int \rho(\boldsymbol{r}) e^{-i\boldsymbol{q}\cdot\boldsymbol{r}}\, d^2r \tag{2.46}$$

$\boldsymbol{q}$ and $\boldsymbol{r}$ are both in the plane of the graphene monolayer. Inserting Eq. (2.45) into the second of Eqs. (2.46) results in

$$\rho_q = -\frac{e}{S}\sum_{\alpha,\beta}\rho_{\alpha\beta}\int \psi^*_\beta(\boldsymbol{r}) e^{-i\boldsymbol{q}\cdot\boldsymbol{r}}\psi_\alpha(\boldsymbol{r})\, d^2r. \tag{2.47}$$

The expression above can be written in a more compact way

$$\rho_q = -\frac{e}{S}\sum_{\alpha,\beta} F_{\beta\alpha}(-\boldsymbol{q})\rho_{\alpha\beta} \tag{2.48}$$

where $F_{\beta\alpha}(-\boldsymbol{q}) = \int \psi^*_\beta(\boldsymbol{r}) e^{-i\boldsymbol{q}\cdot\boldsymbol{r}}\psi_\alpha(\boldsymbol{r})\, d^2r = \langle m, k'|e^{-i\boldsymbol{q}\cdot\boldsymbol{r}}|n,k\rangle$. Note that $F^*_{\beta\alpha}(-\boldsymbol{q}) = F_{\alpha\beta}(\boldsymbol{q})$.

Assuming $\boldsymbol{q} = \boldsymbol{e}_x q$ one obtains

$$
\begin{aligned}
F_{\alpha\beta}(q) = F_{nkmk'}(q) = \langle n,k|e^{iqx}|m,k'\rangle &= \frac{C_n C_m}{L}\int dx\, e^{i(k'-(k-q))x} \\
&\times \int dy\ \left(\mathrm{sgn}(n) i^{-|n|+1}\phi_{|n|-1,k}(y), i^{-|n|}\phi_{|n|,k}(y)\right)\begin{pmatrix}\mathrm{sgn}(m) i^{|m|-1}\phi_{|m|-1,k'}(y)\\ i^{|m|}\phi_{|m|,k'}(y)\end{pmatrix} \\
= \frac{C_n C_m}{L} L\delta_{k',k-q} i^{|m|-|n|}&\int dy\,[\mathrm{sgn}(n)\mathrm{sgn}(m)\phi_{|n|-1,k}(y)\phi_{|m|-1,k-q}(y) + \phi_{|n|,k}(y)\phi_{|m|,k-q}(y)] \\
F_{nkmk'}(q) = C_n C_m i^{|m|-|n|}&\delta_{k',k-q}[\mathrm{sgn}(n)\mathrm{sgn}(m)\left\langle\phi_{|n|-1,k}\middle|\phi_{|m|-1,k-q}\right\rangle + \left\langle\phi_{|n|,k}\middle|\phi_{|m|,k-q}\right\rangle].
\end{aligned}
\tag{2.49}
$$

Introducing the notation

$$
F_{nkmk'} = \tilde{F}_{nkm}\delta_{k',k-q} \tag{2.50}
$$

and comparing equations (2.49) and (2.50) one sees that

$$
\tilde{F}_{nkm} = C_n C_m i^{|m|-|n|}[\mathrm{sgn}(n)\mathrm{sgn}(m)\left\langle\phi_{|n|-1,k}\middle|\phi_{|m|-1,k-q}\right\rangle + \left\langle\phi_{|n|,k}\middle|\phi_{|m|,k-q}\right\rangle]; \tag{2.51}
$$

where

$$
\mathrm{sgn}(n)\mathrm{sgn}(m) = \begin{cases} +1 & \text{intraband transitions} \\ -1 & \text{interband transitions}\end{cases}. \tag{2.52}
$$

Eqs. (2.49) and (2.52) holds for $m,\ n \neq 0$. If $n \to |m|+1$ and $m \to |m|-1$ (i.e. an intraband dipole-forbidden transition) then

$$
F_{nkmk'}(q) = \delta_{k',k-q}\tilde{F}_{nkm}(q) \to \delta_{k'k-q}\tilde{F}_{|m|+1,k,|m|-1}(q). \tag{2.53}
$$

Using Eq. (2.51) to find $\tilde{F}_{|m|+1,k,|m|-1}$ gives

$$
\begin{aligned}
\tilde{F}_{|m|+1,k,|m|-1}(q) &= C_{|m|+1}C_{|m|-1}i^{|m|-1-(|m|+1)}[\left\langle\phi_{|m|,k}\middle|\phi_{|m|-2,k-q}\right\rangle + \left\langle\phi_{|m|+1,k}\middle|\phi_{|m|-1,k-q}\right\rangle] \\
\tilde{F}_{|m|+1,k,|m|-1}(q) &= -\frac{1}{2}[\left\langle\phi_{|m|,k}\middle|\phi_{|m|-2,k-q}\right\rangle + \left\langle\phi_{|m|+1,k}\middle|\phi_{|m|-1,k-q}\right\rangle].
\end{aligned}
\tag{2.54}
$$

It is straightforward to write down the matrix element $F_{|m|+1,k,|m|-1,k'}(q)$

$$F_{|m|+1,k,|m|-1,k'}(q) = -\frac{1}{2}[\langle \phi_{|m|,k} | \phi_{|m|-2,k-q} \rangle + \langle \phi_{|m|+1,k} | \phi_{|m|-1,k-q} \rangle]\delta_{k',k-q}. \tag{2.55}$$

To give a concrete example I will assume that the initial state has a LL index $m = -3$ then

$$\begin{aligned}
\tilde{F}_{4k2}(q) &= -\left[\frac{24(2+\sqrt{2}) - 4(4+\sqrt{2})l_B^2q^2 + l_B^4q^4}{128\sqrt{3}}\right] \times l_B^2q^2e^{-(l_B^2q^2/4)} \\
\tilde{F}_{4k2}(q) &\approx -\left[\frac{24(2+\sqrt{2})}{128\sqrt{3}}\right] l_B^2q^2
\end{aligned} \tag{2.56}$$

where the approximation $l_Bq \ll 1$ was used. This is always a good approximation since q scales as $(v_F/c)(1/l_B)$ times a number of the order of 10, if the LL numbers involved in the DFG process are not too high: around 2–4.

For $F_{\alpha\beta}(q)$ given by Eq. (2.50), the Fourier component of the charge density ρ_q given in Eq. (2.48) becomes

$$\begin{aligned}
\rho_q &= -\frac{e}{S}\sum_{nkmk'} F_{mk'nk}(-q)\rho_{nkmk'} = -\frac{e}{S}\sum_{nkmk'} \tilde{F}_{mk'n}(-q)\delta_{k,k'+q}\rho_{nkmk'} \\
\rho_q &= -\frac{e}{S}\sum_{nkm} \tilde{F}_{mk'n}(-q)\rho_{nkmk'}\Big|_{k'=k-q}
\end{aligned} \tag{2.57}$$

where $F_{mk'nk}(-q) = F^*_{nkmk'}(q) = \tilde{F}_{mk'n}(-q)\delta_{k,k'+q}$ and $\tilde{F}_{mk'n}(-q) = \tilde{F}^*_{nkm}(q)$ was used. $\tilde{F}_{nkm}(q)$ is given in Eq. (2.51).

2.7 Surface Plasmon-Polaritions

The nonlinear polarization in Eq. (2.42) is responsible for three-wave mixing processes. As shown in Sec. 1.1.3, DFG is one of these three-wave mixing processes which occurs at the frequency $\omega_3 = \omega_1 - \omega_2$. Furthermore, the nonlinear polarization with frequency component ω_3 is the source for an EM field of the same frequency. In other words, the nonlinear polarization generates an EM field at ω_3. I will relabel ω_3 as ω_d where $\omega_d = \omega_1 - \omega_2$ is the difference frequency. The

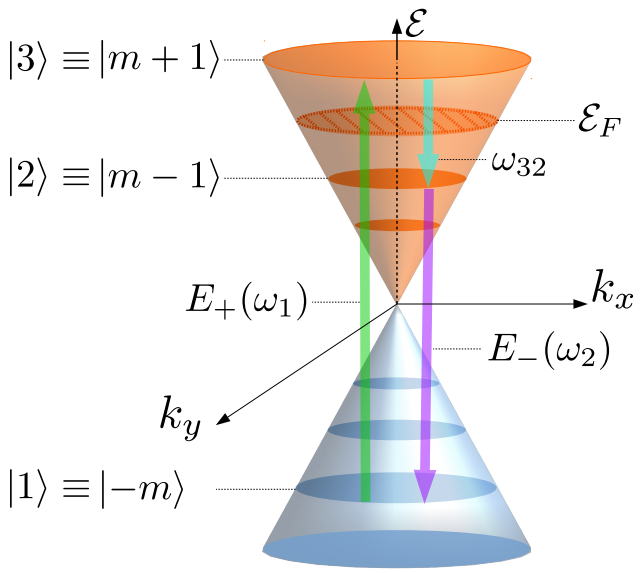

Figure 2.4: Sketch of DFG scheme and resonant coupling of all EM modes to LLs. $\mathcal{E}_F$ is the Fermi level. Reprinted with permission from [13].

pump fields are chosen such that the field of frequency ω_1 is resonant with the LL transition of frequency ω_{31} and the field of frequency ω_2 is resonant with LL transition ω_{21} (see Sec. 2.4). Note that $\omega_{31} - \omega_{21} = \omega_{32}$ and the left-hand side is $\approx \omega_d$ thus the difference frequency ω_d is resonant with the LL transition $|m+1\rangle \rightarrow |m-1\rangle$. The resonant DFG scheme is shown in Fig. 2.4. This transition is dipole-forbidden because it does not obey the selection rules obtained in the electric-dipole approximation, see Eq. (2.39). Therefore a mode excited by the difference frequency process must be treated beyond the electric-dipole approximation.

Note that the type of EM field generated by the nonlinear polarization could be a radiative mode (photon) or a bound mode (surface plasmon-polariton). Polaritons are quasi-particles composed of an EM wave coupled to an excitation of a medium. Surface plasmons are longitudinal oscillations of the surface charge density of a medium (an excitation). Thus, surface plasmon-polaritons are longitudinal oscillations in the charge density coupled to an EM wave. Another example of a polariton is the phonon-polariton which are lattice vibrations coupled to an EM wave. Conversion efficiency is higher for a surface plasmon because it has greater overlap with graphene due to tight confinement and its amplitude is enhanced at plasmon resonance [23]. Therefore, I will select the

generated EM field to be a mode localized at the surface of the graphene layer (the plane $z = -d/2$) and propagating in the x-direction. By definition, the localized mode decays exponentially away from the plane to which it is confined; it is evanescent. As such, one seeks the homogeneous solution to Eq. (1.45) for an evanescent wave.

Before doing so one should note the following. Recall that the graphene monolayer is integrated into a waveguide, as described in Sec. 2.3, where the monolayer is assumed to be either at the interface of the waveguide core with dielectric constant ϵ_2 and the bottom cladding with dielectric constant ϵ_3 or in the middle of the core layer. I will assume graphene is located at the interface of dielectrics ϵ_2 and ϵ_3. I will also assume that the generated EM wave is transverse magnetic (TM) polarized.

For a TM polarized wave propagating in the $x-$direction (assuming no variation in the y direction)

$$\boldsymbol{E} = (E_x(z), 0, E_z(z))e^{iqx-i\omega_q t} \tag{2.58}$$

$$\boldsymbol{B} = (0, B_y(z), 0)e^{iqx-i\omega_q t}. \tag{2.59}$$

I have chosen the frequency of the SPP field to be ω_q. It will be shown that $\omega_q \approx \omega_d$.

One solves the homogeneous wave equation for the longitudinal component which, in this case, is E_x. Assuming graphene is located at $z = -d/2$, solutions are sought in the regions $z > -d/2$ and $z < -d/2$ which give

$$\left(\frac{d^2}{dz^2} - q^2 + \epsilon_j \frac{\omega_q^2}{c^2}\right) E_{jx}(z)e^{iqx-i\omega_q t}, \tag{2.60}$$

where $j = 2$ for $z > -d/2$ and $j = 3$ for $z < -d/2$. Let

$$p_j = \sqrt{q^2 - \epsilon_j \frac{\omega_q^2}{c^2}} \tag{2.61}$$

then the solution to Eq. (2.60) for an evanescent wave is

$$E_{jx}(z) = \begin{cases} E_{2x}(z) = A_{2x}e^{-p_2(z+d/2)} & z > -d/2 \\ E_{3x}(z) = A_{3x}e^{+p_3(z+d/2)} & z < -d/2 \end{cases} \tag{2.62}$$

E_{jx} is continuous at the boundary $z = -d/2$ since it is the tangential component of the TM polarized field; therefore, $A_{2x} = A_{3x} \equiv E_{ox}(-d/2)$. $E_{ox}(-d/2)$ is the amplitude of the SPP field taken at the location of the graphene monolayer. The equation above can be written in a shortened way

$$E_{jx}(z) = E_{ox}e^{\mathrm{sgn}(j)p_j(z+d/2)} \tag{2.63}$$

where

$$\mathrm{sgn}(j) \equiv \begin{cases} -1 & z > -d/2 \\ +1 & z < -d/2. \end{cases} \tag{2.64}$$

If the monolayer was located at $z = 0$ then the solution for an evanescent wave localized on this plane can be obtained by simply setting $-d/2 \to 0$ in the equations above. Also the SPP amplitude on the monolayer would be given by $E_{ox}(0)$ and $d_3 \to d_2$.

The dispersion relation for SPP in graphene is obtained from integrating $\nabla \cdot \boldsymbol{D} = 4\pi\rho_{3D}$, where $\rho_{3D} = \rho(\boldsymbol{r})\delta(z + d/2)$ and $\rho(\boldsymbol{r})$ is given by Eqs. (2.45) and (2.47)

$$D_{2z}(-d/2) - D_{3z}(-d/2) = 4\pi\rho \tag{2.65}$$

$$\epsilon_2 E_{2z}(-d/2) - \epsilon_3 E_{3z}(-d/2) = 4\pi\rho. \tag{2.66}$$

E_{jz} can be expressed in terms of E_{jx} using $\nabla \cdot \boldsymbol{E} = 0 \implies \partial_z E_z(x, z, t) = -\partial_x E_x(x, z, t)$ (which

holds in each region $z > -d/2$ and $z < -d/2$)

$$E_{jz}(z) = -iqE_{ox}(-d/2) \int e^{\mathrm{sgn}(j)p_j(z+d/2)}\, dz \tag{2.67}$$

$$\implies E_{jz}(z) = -\frac{iq}{\mathrm{sgn}(j)p_j} E_{ox} e^{\mathrm{sgn}(j)p_j(z+d/2)} = -\frac{iq}{\mathrm{sgn}(j)p_j} E_{jx}(z). \tag{2.68}$$

Using Eqs. (2.58), (2.63) and (2.68) the SPP field can be expressed as

$$\boldsymbol{E}(x,z,t) = \left(\boldsymbol{e}_x - \mathrm{sgn}(j)\frac{iq}{p_j}\boldsymbol{e}_z\right) E_{ox} e^{\mathrm{sgn}(j)p_j(z-d/2)} e^{iqx - i\omega_q t}. \tag{2.69}$$

Inserting Eq. (2.68) into Eq. (2.66) and using $\rho = -\nabla\cdot\boldsymbol{P}^{(L)} = -\nabla\cdot(\chi_\parallel \boldsymbol{E}) = -iq\chi_\parallel E_x(-d/2)$ yields

$$\left(\frac{\epsilon_2}{p_2} + \frac{\epsilon_3}{p_3}\right) iqE_{ox}(-d/2) = -iq4\pi\chi_\parallel E_{ox}(-d/2) \tag{2.70}$$

or

$$\frac{\epsilon_2}{p_2} + \frac{\epsilon_3}{p_3} + 4\pi\chi_\parallel = 0. \tag{2.71}$$

where $\chi_\parallel(q,\omega_q)$ is the surface linear susceptibility.

In the quasielectrostatic approximation, that is, when the dispersion relation is far from the light line one has $\omega_q \ll cq$. In this regime, the time derivative of the magnetic field is negligible. This can be seen from the following $\nabla\times\boldsymbol{E} = -c^{-1}\partial_t\boldsymbol{B} \implies i\boldsymbol{q}\times\boldsymbol{E} = \frac{i\omega_q}{c}\boldsymbol{B} \implies \boldsymbol{e}_q\times\boldsymbol{E} = \frac{\omega_q}{cq}\boldsymbol{B}$. Using $\omega_q \ll cq$ gives $\boldsymbol{e}_q\times\boldsymbol{E} \approx 0$ or equivalently $\nabla\times\boldsymbol{E} \approx 0$. Thus, one may express the electric field in terms of the gradient of a scalar

$$\boldsymbol{E} = -\nabla\Phi. \tag{2.72}$$

Recall that the amplitude of the SPP field in the plane of the monolayer is given by the tangential component of the electric field $E_{ox}(-d/2)$, in light of Eq. (2.72), one may write

$$E_{ox}(-d/2) = -iq\phi_q \tag{2.73}$$

where $\Phi = \phi_q e^{iqx-i\omega t}$.

In the quasielectrostatic approximation, not only does $E_{ox} \to -iq\phi_q$ but $p_j \to q$ as well, which allows one to write Eq. (2.70) as

$$(\epsilon_2 + \epsilon_3)q\phi_q = 4\pi\rho_q. \tag{2.74}$$

Note that

$$\rho_q = -\chi_{\parallel} q^2 \phi_q. \tag{2.75}$$

With the help of Eq. (2.75) Eq. (2.74) can be rearranged as

$$1 + \frac{4\pi q}{\epsilon_2 + \epsilon_3}\chi_{\parallel}(q, \omega_q) = 0 \tag{2.76}$$

$$D(q, \omega_q) \equiv 1 + \frac{4\pi q}{\epsilon_2 + \epsilon_3}\chi_{\parallel}(q, \omega_q). \tag{2.77}$$

To find the surface linear susceptibility one uses Eqs. (2.48) and (2.75)

$$-\frac{e}{S}\sum_{\alpha,\beta} F_{\beta\alpha}(-\boldsymbol{q})\rho_{\alpha\beta} = -\chi_{\parallel}(q, \omega_q)q^2\phi_q$$

$$\implies \chi_{\parallel}(q, \omega_q) = \frac{e}{q^2\phi_q S}\sum_{\alpha,\beta} F_{\beta\alpha}(-\boldsymbol{q})\rho_{\alpha\beta}(\omega_q). \tag{2.78}$$

Evidently, one needs to find the density matrix element $\rho_{\alpha\beta}$. The procedure for finding the density matrix element is given in Sec. 1.1.1; see Eq. (1.19). However, in the present section the electric dipole approximation will not be used because spatial dispersion (dependence on the wavevector) or nonlocal effects needs to be taken into account. The von Neumann equation for the matrix element $\rho_{\alpha\beta}$ for an interaction Hamiltonian for a dipole-forbidden transition is given by

$$H^{int}_{\alpha\beta}(t) = \left[-e\phi_q e^{iqx-i\omega_q t}\right]_{\alpha\beta} = -e\phi_q \left[e^{iqx}\right]_{\alpha\beta} e^{-i\omega_q t} = -e\phi_q F_{\alpha\beta}(\boldsymbol{q})e^{-i\omega_q t}. \tag{2.79}$$

Using Eq. (1.19) one finds

$$\rho_{\alpha\beta}(\omega_q) = \frac{-eF_{\alpha\beta}(\boldsymbol{q})(f_\alpha - f_\beta)\phi_q}{\hbar(\omega_{\alpha\beta} - \omega_q - i\gamma_{\alpha\beta})} \tag{2.80}$$

where $\gamma_{\alpha\beta}$ is the phenomenological decay rate between LL $|\alpha\rangle$ and $|\beta\rangle$. The scattering rates for Landau-quantized graphene were calculated, e.g., in [36, 37, 38]. I assume that the Rabi frequencies of the pump fields are smaller than the carrier relaxation rate, so the optical population transfer is not important. As such, one can neglect the scattering effects (like Auger scattering) that arises from high concentrations of nonequilibrium carriers.

Inserting Eq. (2.80) into Eq. (2.78) gives the surface linear susceptibility

$$\chi_{\parallel}(q,\omega_q) = -\frac{e^2}{\hbar q^2 S}\sum_{\alpha,\beta}\frac{|F_{\alpha\beta}(\boldsymbol{q})|^2(f_\alpha - f_\beta)}{\omega_{\alpha\beta}-\omega_q - i\gamma_{\alpha\beta}}. \tag{2.81}$$

The dispersion relation given by Eq. (2.77) for $\chi_{\parallel}$ given in Eq. (2.81) becomes

$$D(\boldsymbol{q},\omega_q) = 1 - \frac{4\pi e^2}{(\epsilon_2+\epsilon_3)Sq}\sum_{\alpha,\beta}\frac{(f_\alpha - f_\beta)|F_{\alpha\beta}(\boldsymbol{q})|^2}{\mathcal{E}_\alpha - \mathcal{E}_\beta - \hbar\omega_q - i\hbar\gamma_{\alpha\beta}}. \tag{2.82}$$

In proceeding, I will assume that the initial state ($|1\rangle$) involved in the resonant DFG process has the LL with index $m=-3$. Furthermore, I will assume that the Fermi level is between states $|2\rangle$ and $|3\rangle$ with LL numbers $|m|-1=2$ and $|m|+1=4$ (respectively) but separated by more than k_BT. Since states $|1\rangle$ and $|2\rangle$ are below the Fermi level they are both occupied while state $|3\rangle$ is above the Fermi level so it is unoccupied. With these considerations the dispersion relation given by Eq. (2.82) may be written as

$$D(\omega_q,\boldsymbol{q}) = 1 + \frac{\omega_o(q)}{\omega_{32}-\omega_q - i\gamma_{32}} = 0 \tag{2.83}$$

where

$$\omega_o(q) = \frac{4\pi e^2(N_F/S)\xi(q)}{(\epsilon_2+\epsilon_2)\hbar q}, \quad \xi(q) = \frac{\sum_k |\tilde{F}_{3k2}(q)|^2}{\varkappa} \tag{2.84}$$

where $\varkappa = 2S/\pi l_B^2$ is the Landau level degeneracy, $N_F = f_F\varkappa$ is the number of particles in a completely filled Landau level, $f_{3k}=0$ since it is above the Fermi level and $f_F = f_{2k'}$. It follows

from Eq. (2.83) that

$$\mathrm{Re}[\omega_q] = \omega_{32} + \omega_o(q), \quad \mathrm{Im}[\omega_q] = -\gamma_{32}. \tag{2.85}$$

Examining the term $\xi(q)$ one finds

$$\xi(q) = \frac{\sum_k |\tilde{F}_{3k2}(q)|^2}{\varkappa} \propto q^4 l_B^4 \tag{2.86}$$

recall that here $\tilde{F}_{3k2}(q)$ corresponds to $\tilde{F}_{|m|+1,k,|m|-1}$ since state $|3\rangle = ||m|+1\rangle$ and $|2\rangle = ||m|-1\rangle$. For initial state $|1\rangle = |m=-3\rangle$ $\tilde{F}_{3k2}(q) \to \tilde{F}_{4k2}(q) \approx l_B^2 q^2$, see Eq. (2.56). In approximating $\xi(q)$ I used the fact that $\tilde{F}_{4k2}(q)$ is independent of k so it can be taken out of the sum and $\sum_k = \varkappa$ (see Eq. (1.154)). I also used $l_B = \sqrt{\hbar c/(eB)}$ as given in Eq. (1.131).

2.8 Difference Frequency Generation of Surface Plasmon-Polaritions

As mentioned in the previous section, the nonlinear polarization due to the pump fields generated a new frequency component, namely the difference frequency. This frequency gives rise to the SPP. In order to connect the SPP with its nonlinear roots I will expand the charge density in Eq. (2.74) to include the nonlinear part, i.e.

$$\rho_q = \rho_q^{(L)} + \rho_q^{(NL)} \tag{2.87}$$

where the linear part of the charge density is $\rho_q^{(L)} = -\chi_\parallel q^2 \phi_q$.

Next, I will substitute Eq. (2.87) into Eq. (2.74) and solve for the SPP amplitude in terms of the nonlinear charge density

$$\begin{aligned} (\epsilon_2 + \epsilon_3) q \phi_q &= 4\pi(-q^2 \chi_\parallel \phi_q + \rho_q^{(NL)}) \\ \implies \phi_q &= \frac{4\pi \rho_q^{(NL)}}{(\epsilon_2 + \epsilon_3) q D(q, \omega_q)}. \end{aligned} \tag{2.88}$$

At the plasmon resonance frequency, $\mathrm{Re}[\omega_q] = \omega_{32} + \omega_o(q)$ (see Eq.2.85), $\mathrm{Re}[D(q,\omega_q)] = 0$ which leads to an enhancement in the SPP amplitude ϕ_q. One needs to find the Fourier component

$\rho_q^{(NL)}$ of the nonlinear charge density by expressing it in terms of its matrix elements as done in Eq. (2.57) and then solve for the corresponding density matrix element. The density matrix equation corresponding to the nonlinear charge density (generated by the dipole-allowed pump fields) is given by

$$\begin{aligned}
\dot{\rho}_{3k2k'} + \gamma_{32}\rho_{3k2k'} &= -\frac{i}{\hbar}[H^0 + H^{int}, \rho]_{3k2k'} \\
\dot{\rho}_{3k2k'} + \gamma_{32}\rho_{3k2k'} &= -\frac{i}{\hbar}\sum_{l,k''}\left[(H^0 + H^{int})_{3klk''}\rho_{lk''2k'} - \rho_{3klk''}(H^0 + H^{int})_{lk''2k'}\right]
\end{aligned} \tag{2.89}$$

k' in the density matrix elements is evaluated according to Eq. (2.57) as prescribed by [39]. In order to solve the density matrix equation one should keep in mind that states f_{1k} and f_{2k} are fully occupied (below the Fermi level) so there are no transitions between states $|1\rangle$ and $|2\rangle$. Note also that $\rho_{3k1k'}$ is zero unless $k' = k - q_1$ since transitions between states $|1\rangle$ and $|3\rangle$ are driven by the pump field with in-plane wavevector q_1 and frequency ω_1; similarly, $\rho_{2k1k'}$ is zero unless $k' = k - q_2$. $\rho_{3k2k'}$ is zero unless $k' = k - q$ where $q = q_1 + q_2$. As mentioned previously, $f_3 \approx 0$ since it is above the Fermi level. With these considerations Eq. (2.89) becomes

$$\dot{\rho}_{3k2(k-q)} + i\omega_{32}\rho_{3k2(k-q)} + \gamma_{32}\rho_{3k2(k-q)} = -i\frac{d_{21}^* E_-^{(2)*}(-d/2)e^{i\omega_2 t}}{\hbar}\rho_{3k1(k-q_1)}. \tag{2.90}$$

Here and in all equations below the pump fields $E_+^{(1)}, E_-^{(2)*}$ are taken on the graphene monolayer located at $z = -d/2$. Therefore, below I will omit the argument $-d/2$ in the pump fields.

Observe that the density matrix equation for $|3\rangle \to |2\rangle$ transition depends on the linear perturbation of the density matrix element for the $|3\rangle \to |1\rangle$ transition. That being the case, one needs to solve for the density matrix element $\rho_{3k1(k-q_1)}$. A solution within the electric dipole approximation is readily obtained by following the procedure given in Sec. 1.1.2 and using the dipole moment

(defined at exact resonance) described in Sec. 2.4

$$\dot{\rho}_{3k1(k-q_1)} + i\omega_{31}\rho_{3k1(k-q_1)} + \gamma_{31}\rho_{3k1(k-q_1)} = i\frac{d_{31}E_+^{(1)}e^{-i\omega_1 t}}{\hbar}f_F, \tag{2.91}$$

$$\implies \rho_{3k1(k-q_1)}(t) = \frac{e^{-i\omega_1 t}f_F}{\omega_{31}-\omega_1-i\gamma_{31}}\frac{d_{31}E_+^{(1)}}{\hbar}. \tag{2.92}$$

Substituting Eq. (2.92) into Eq. (2.90) and solving for $\rho_{3k2(k-q)}$ yields

$$\rho_{3k2(k-q)}(t) = -\frac{e^{-i(\omega_1-\omega_2)t}f_F}{(\omega_{32}-(\omega_1-\omega_2)-i\gamma_{32})(\omega_{31}-\omega_1-i\gamma_{31})}\frac{d_{31}d_{21}^*E_+^{(1)}E_-^{(2)*}}{\hbar^2}. \tag{2.93}$$

Recall that $\omega_d \equiv \omega_1 - \omega_2$ is the difference frequency. The Fourier harmonic of nonlinear charge density obtained by using Eqs. (2.57) and (2.93) is

$$\rho_q^{(NL)}(\omega_d) = \frac{(N_F/S)\zeta(q)e^{-i\omega_d t}}{(\omega_{32}-\omega_d-i\gamma_{32})(\omega_{31}-\omega_1-i\gamma_{31})}\frac{ed_{31}d_{21}^*E_+^{(1)}E_-^{(2)*}}{\hbar^2}. \tag{2.94}$$

Where

$$\zeta(q) = \frac{1}{\varkappa}\sum_k \tilde{F}_{2k'3} \propto l_B^2 q^2, \quad \text{and} \quad \frac{N_F}{S}\zeta(q) = 2.235q^2. \tag{2.95}$$

$\zeta(q)$ is obtained in a similar fashion as $\xi(q)$ (see Sec. 2.7).

The second-order nonlinear susceptibility $\chi^{(2)}(q,\omega_d)$ can be extracted from nonlinear charge density Eq. (2.94) using $\rho_q^{(NL)} = -iq\chi^{(2)}E_+^{(1)}E_-^{(2)*}$

$$\chi^{(2)}(q,\omega_d) = \frac{i}{q}\frac{(N_F/S)\zeta(q)}{(\omega_{32}-\omega_d-i\gamma_{32})(\omega_{31}-\omega_1-i\gamma_{31})}\frac{ed_{31}d_{21}^*}{\hbar^2}. \tag{2.96}$$

The magnitude of $\chi^{(2)}$ scales linearly with q. For a range of q corresponding to DFG of THz plasmons by mid-infrared pumps, and for $B = 1$ T, $|\chi^{(2)}| \sim 2\times10^{-7}$ in CGS units. Just for the sake of comparison with nonlinear crystals, one can divide by graphene monolayer thickness ($\sim$ 0.1-0.3 nm, see [40]) to get the "bulk" magnitude of $|\chi_{3D}^{(2)}| \sim 3\times10^{-3}$ m/V, which is a very large number. Of course, the resulting DFG power efficiency depends on the magnitude of the surface (2D) $\chi^{(2)}$, as well as the overlap of modes with graphene and the sample size.

The Fourier harmonic of the SPP amplitude given by Eq.(2.88) can be expressed as

$$\phi_q = \frac{4\pi}{(\epsilon_2+\epsilon_3)qD(\omega_q,\boldsymbol{q})}\frac{ed_{31}d_{21}^*E_+^{(1)}E_-^{(2)*}(N_F/S)\zeta(q)}{\hbar^2(\omega_{32}-\omega_d-i\gamma_{32})(\omega_{31}-\omega_1-i\gamma_{31})}. \tag{2.97}$$

where Eq (2.94) was used. On substituting $D(\omega_q,\boldsymbol{q})$ from Eq. (2.83) into Eq. (2.97) one finds (after a bit of rearranging)

$$\phi_q = \frac{4\pi e(N_F/S)\zeta(q)}{(\epsilon_2+\epsilon_3)q}\frac{(d_{31}d_{21}^*E_+^{(1)}E_-^{(2)*})/\hbar^2}{(\underbrace{\omega_{32}+\omega_0(q)}_{\mathrm{Re}[\omega_q]}-\underbrace{(\omega_1-\omega_2)}_{\omega_d}-i\gamma_{32})(\omega_{31}-\omega_1-\gamma_{31})}. \tag{2.98}$$

As is obvious from Eq. (2.98), the excitation of the SPP mode at frequency ω_q given by Eq. (2.83) is most efficient when the difference frequency $\omega_d = \omega_1 - \omega_2$ of the two-color pump field is in resonance with ω_q, i.e., $\omega_d = \omega_q$.

2.9 Poynting Flux in a SPP Mode

In the quasielectrostatic approximation the time derivative of the magnetic field of the electromagnetic wave is negligible. In order to calculate the Poynting flux of the transverse magnetic (TM) SPP mode, one needs to go beyond the quasielectrostatic approximation. In Sec. 2.7 I gave the amplitude of the SPP on the graphene plane (see Eq. (2.73))

$$E_x(z=-d/2) \equiv E_{ox} = -iq\phi_q.$$

In the same section, I also found the electric field components of the TM polarized SPP field, $E_x(x,z,t)$ and $E_z(x,z,t)$, given by Eqs. (2.58), (2.63), and (2.68). They are restated below for convenience

$$E_x(x,z,t) = E_{ox}e^{\mathrm{sgn(j)}p_j(z-d/2)+iqx-i\omega_q t} \tag{2.99}$$

$$E_z(x,z,t) = -\mathrm{sgn(j)}\frac{iq}{p_j}E_x(x,z,t). \tag{2.100}$$

However, in that section I did not find the associated magnetic field $B_y(x,z,t)$. In order to calculate the Poynting flux, one needs the magnetic field. The y-component of $\boldsymbol{B}$ can be derived from the z component of $\nabla \times \boldsymbol{B} = c^{-1}\partial_t \boldsymbol{D}$:

$$B_y(x,z,t) = -\frac{\omega_q \epsilon_j}{qc} E_z(x,z,t), \tag{2.101}$$

The Poynting vector and flux was introduced in Sec. (2.3). The (average) Poynting vector for a TM mode is

$$\begin{aligned}\langle \boldsymbol{S} \rangle &= \frac{c}{8\pi}\,\mathrm{Re}[\boldsymbol{E} \times \boldsymbol{B}^*] = -\boldsymbol{e}_x \frac{c}{8\pi}\,\mathrm{Re}[E_z B_y^*] = -\boldsymbol{e}_x \frac{c}{8\pi} Re\left[E_z \left(-\frac{\omega_q \epsilon_j}{qc} E_z\right)^*\right] \\ &= \boldsymbol{e}_x \frac{q\omega_q}{8\pi}\frac{\epsilon_j}{p_j^2}|E_{ox}E_{ox}^*| e^{\mathrm{sgn}(j) 2p_j(z-d/2)} = \boldsymbol{e}_x \frac{q^3\omega_q}{8\pi}|\phi_q|^2 \frac{\epsilon_j}{p_j^2} e^{\mathrm{sgn}(j) 2p_j(z-d/2)}\end{aligned} \tag{2.102}$$

Upon integrating the average Poynting vector over the area element $d\boldsymbol{A} = \boldsymbol{e}_x dydz \to \boldsymbol{e}_x L_y dz$ (assuming no variation in the y-direction) one obtains the average Poynting flux (the power of the DFG mode)

$$P_{DFG} = \frac{L_y \omega_q q^3 |\phi_q|^2}{16\pi}\left(\frac{\epsilon_2}{p_2^3} + \frac{\epsilon_3}{p_3^3}\right). \tag{2.103}$$

In the approximation $q \gg \omega_q/c$ one can write $p_{2,3} \approx q$, $q^3(\epsilon_2/p_2^3 + \epsilon_3/p_3^3) \approx \epsilon_2 + \epsilon_3$. Using this approximation along with Eq. (2.98) gives the final expression for the SPP power:

$$P_{DFG} = \frac{\pi L_y \omega_q}{\epsilon_2 + \epsilon_3}\left[\frac{e(N_F/S)}{q}\right]^2 \left|\frac{(d_{31}d_{21}^* E_+^{(1)} E_-^{(2)*}/\hbar^2)\zeta(q)}{(\mathrm{Re}[\omega_q] - \omega_d - i\gamma_{32})(\omega_{31} - \omega_1 - i\gamma_{31})}\right|^2. \tag{2.104}$$

This expression was derived for the graphene monolayer at the interface of the dielectric waveguide core and cladding. Similar formulas can be obtained for any other location of graphene.

Figures 2.6-2.8 illustrate the dependence of the DFG power in Eq. (2.104) on various parameters for different waveguide compositions and locations of the graphene monolayer. The structure width L_y is chosen to be 100 μm. The power scales linearly with L_y. For the plots I chose the initial state $|1\rangle$ in Fig. 2.4 to have the Landau level index $n = -3$. Then the states $|2\rangle$ and $|3\rangle$ coupled

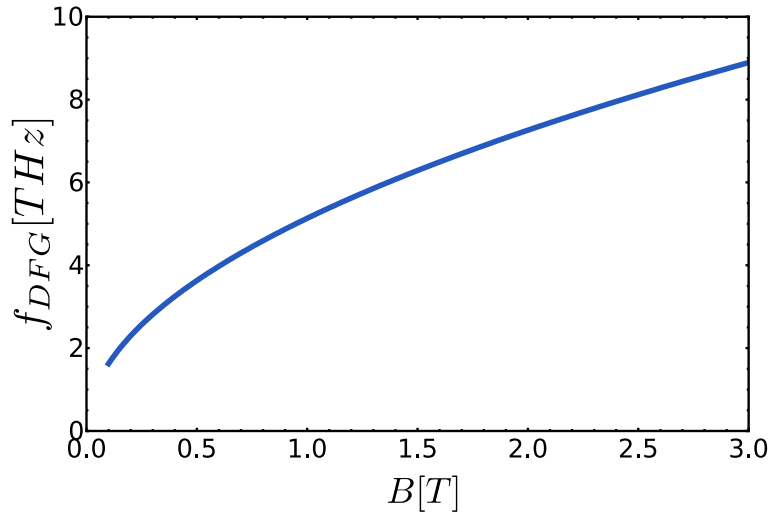

Figure 2.5: The DFG frequency resonant to the transition between Landau-level numbers 2 and 4 as a function of the magnetic field strength. Reprinted with permission from [13].

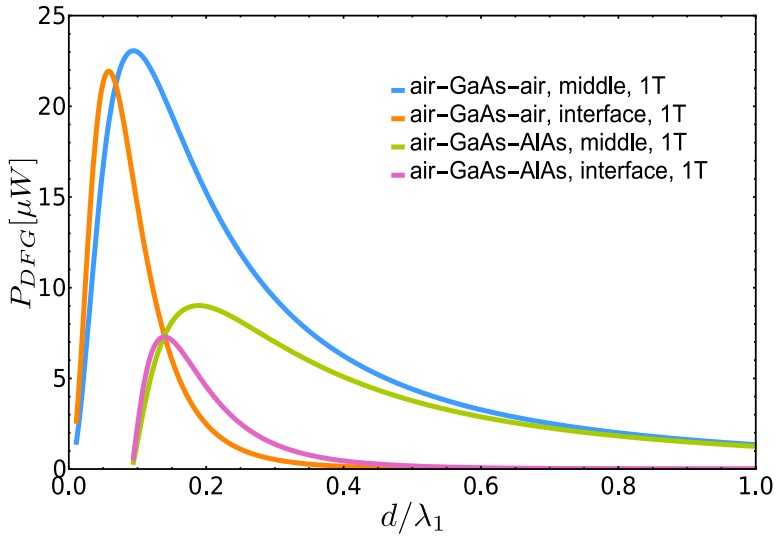

Figure 2.6: DFG power per 1 W of a pump power as a function of the waveguide core thickness for the magnetic field strength 1T. In the legend of the plot “middle” means that graphene is in the middle of the core dielectric ϵ_2; “interface” means that graphene is located at the interface of dielectrics ϵ_2 and ϵ_3. “1T" and “3T" stands for 1 and 3 Tesla magnetic field. Reprinted with permission from [13].

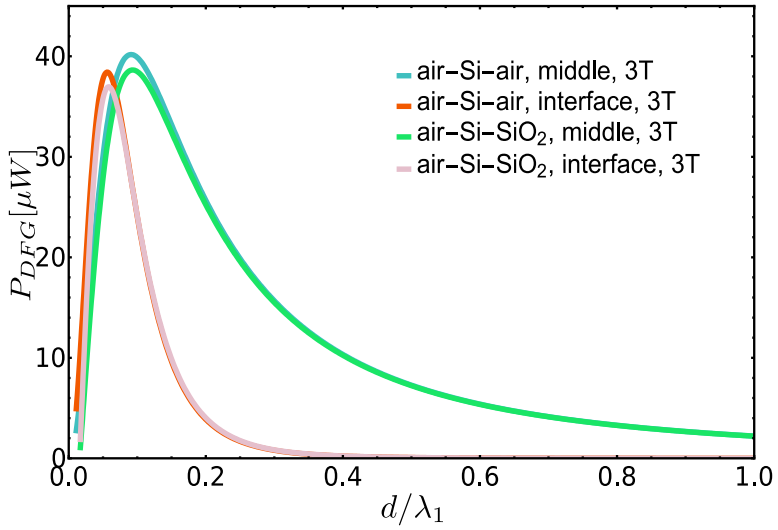

Figure 2.7: DFG power per 1 W of a pump power as a function of core thickness for the magnetic field strength 3 T. A higher magnetic field is chosen to avoid THz absorption in Si. Reprinted with permission from [13].

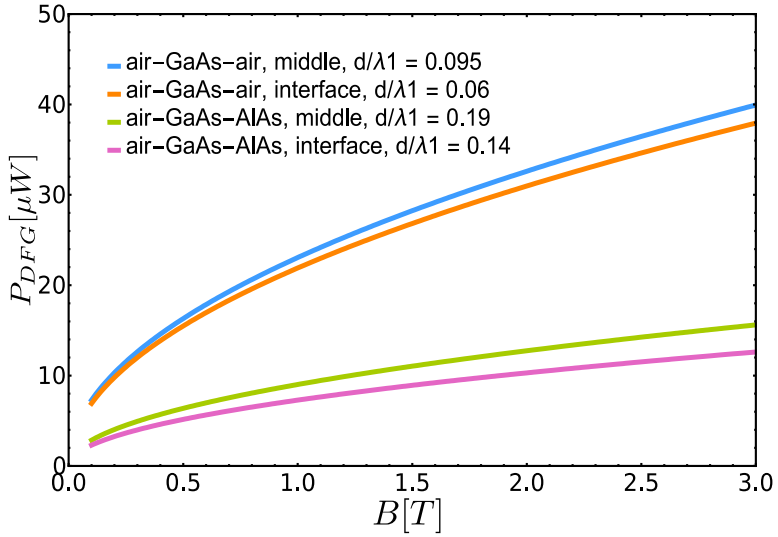

Figure 2.8: The DFG power per 1 W of a pump power as a function of the magnetic field for several waveguide structures and geometries. In the legend of the plot "middle" means that graphene is in the middle of the core dielectric ϵ_2; "interface" means that graphene is located at the interface of dielectrics ϵ_2 and ϵ_3. Reprinted with permission from [13].

to state $|1\rangle$ by electric dipole-allowed pump transitions have Landau level numbers $|n|-1=2$ and $|n|+1=4$, respectively (as discussed in Sec. 2.7).

The DFG frequency corresponding to the transition between these states is in the THz range; see Fig. 2.5. The pump wavelengths are in the mid-infrared; for example, at $B=1$ T they are 9.1 μm and 10.9 μm. All frequencies scale as $\sqrt{B}$. The pump powers are assumed to be 1 W in the figures, so that the plots actually show DFG power conversion efficiency in μW/W^2.

Figures 2.6 and 2.7 show the dependence of the DFG power on the thickness of the waveguide core for different positions of the graphene sheet and different waveguide materials at a fixed magnetic field. The DFG power depends on the magnitude of the in-plane components of the pump fields on graphene and the localization of the optical pump power. There is an optimal waveguide thickness which maximizes the DFG power for a given total power in the pump fields. For wider waveguide cores the in-plane component of the pump field amplitude on graphene gets smaller, whereas for narrower waveguides the pump field mode gets delocalized. Figs. 2.6 and 2.7 also indicate that it is beneficial to place graphene in the middle of the waveguide core.

With increasing magnetic field the peak DFG power in Eq. (2.104) scales as $\sqrt{B}$, provided the pump wavelengths are tuned in resonance with corresponding transitions. This dependence is illustrated in Fig. 2.8 for a particular choice of waveguide structures and geometries. Note that the choice of particular pump and DFG transitions for a given magnetic field is strongly influenced by absorption in the waveguide materials. For example, one should obviously avoid reststrahlen bands in all waveguide layers.

The DFG power can be further enhanced by stacking several monolayers together. However, there is a trade-off between the nonlinear conversion efficiency and absorption in graphene. I will calculate the absorption of both pump and difference frequency modes in the next section.

2.10 Absorption by Graphene

Absorption of the EM modes by graphene is unavoidable. I will calculate the absorption length. The absorption coefficient (for weak absorption) is given by [41]

$$a(\omega_r) \approx (4\pi/c)\mathrm{Re}[\sigma_{3D}(\omega_r)]\Gamma, \tag{2.105}$$

where $\sigma_{3D}(\omega_r) = \sigma_{2D}(\omega_r)/\Delta z$, Δz is the mononayer thickness 0.1-0.3 nm [40], $\sigma_{2D}(\omega_r)$ is the conductivity of graphene which is determined by Eq. (2.41) for the pump fields and $\sigma_{2D}(\omega_q) = -i\omega_q\chi_{\|}(q,\omega_q)$ for the DFG field. $\chi_{\|}(q,\omega_q)$ is given in Eq. (2.81). Γ is the overlap factor defined as

$$\Gamma = \frac{\langle \Phi_S^r(z_g)\rangle}{\langle \Phi_S^r(z)\rangle} = \frac{\Delta z L_y \langle S_x^r(z_g)\rangle}{L_y \int_{-\infty}^{\infty} \langle S_x^r(z)\rangle \, dz} \tag{2.106}$$

where z_g is the location of the graphene monolayer, $\langle \Phi_S^r\rangle$ is the average Poynting flux (one would use TE polarized fields for the Poynting flux of the pump fields and a TM polarized field for the Poynting flux of the SPP mode). Utilizing Eqs. (2.105) and (2.106) one arrives at

$$a(\omega_r) = \frac{4\pi \, \mathrm{Re}[\sigma_{2D}(\omega_r)] \, \langle S_x^r(z_g)\rangle}{c \int_{-\infty}^{\infty} \langle S_x^r(z)\rangle \, dz}. \tag{2.107}$$

The Poynting vector and flux (power) for the TE pump fields were calculated in Sec. 2.3 whereas the Poynting vector and flux for the TM SPP mode was calculated in Sec. 2.9. The absorption length is defined as the reciprocal of the absorption coefficient

$$l_a(\omega_r) = a(\omega_r)^{-1} = \left[\frac{4\pi \, \mathrm{Re}[\sigma_{2D}(\omega_r)] \, \langle S_x^r(z_g)\rangle}{c \int_{-\infty}^{\infty} \langle S_x^r(z)\rangle \, dz} \right]^{-1}. \tag{2.108}$$

For pump fields I will calculate the conductivity only keeping the resonant terms in the conductivity tensor given by Eq. (2.41). The pump field oscillating at frequency ω_1 is resonant with the $|1\rangle \rightarrow |3\rangle$ transition which corresponds to a transition from a state with LL $-|m|$ to a state $|m|+1$. Furthermore, this transition only couples to the E_+ component of the field, see Fig. 2.4.

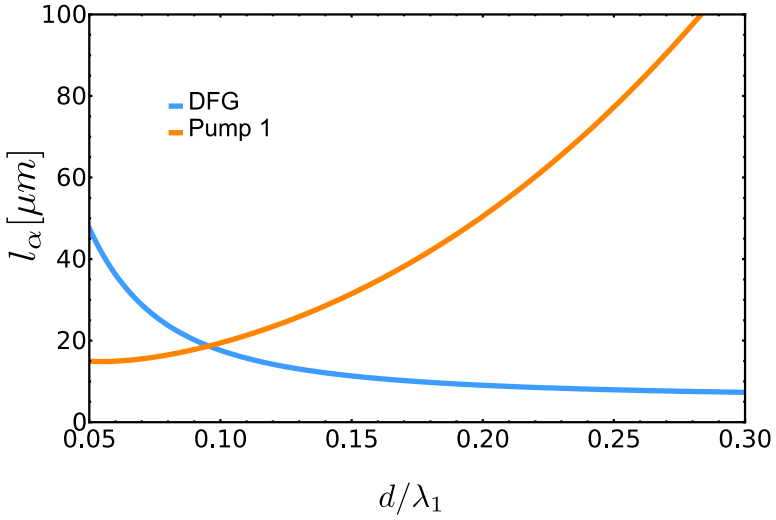

Figure 2.9: Absorption length for pump field intensity and DFG plasmon-polaritons as a function of core thickness for a symmetric GaAs waveguide with graphene at the interface. The magnetic field is 1T. Reprinted with permission from [13].

Using these states in Eq. (2.41) gives

$$\begin{aligned}\sigma^{+-}_{con}(\omega_l) &= -i\frac{e^2v_F^2}{S\hbar\omega_l}\sum_\alpha\sum_\beta\frac{(f_\alpha - f_\beta)\sigma^+_{\beta\alpha}\sigma^-_{\alpha\beta}}{(\omega_l - \omega_{\alpha\beta} + i\gamma_{\alpha\beta})} \\ &= -\frac{ie^2v_F^2}{\hbar\omega_l}\frac{1}{\pi l_B^2}\sum_m\frac{f_{|m|+1} - f_m}{\omega_l - \omega_{|m|+1,m} + i\gamma_{|m|+1,m}} \qquad (2.109)\end{aligned}$$

$$\sigma^{+-}_{con}(\omega_1) = -\frac{ie^2v_F^2}{\hbar\omega_1}\frac{1}{\pi l_B^2}\frac{f_4 - f_{-3}}{\omega_1 - \omega_{4,-3} + i\gamma_{4,-3}}. \qquad (2.110)$$

In going from the second-to-last line to the last line, I kept only the resonant terms so that the the sum over m can be dropped.

Similarly, the field at frequency ω_2 couples only to the $|2\rangle \rightarrow |1\rangle$ transition. Furthermore, only the E_- component couples to this transition and this transition is between LL with indices $-|m|$

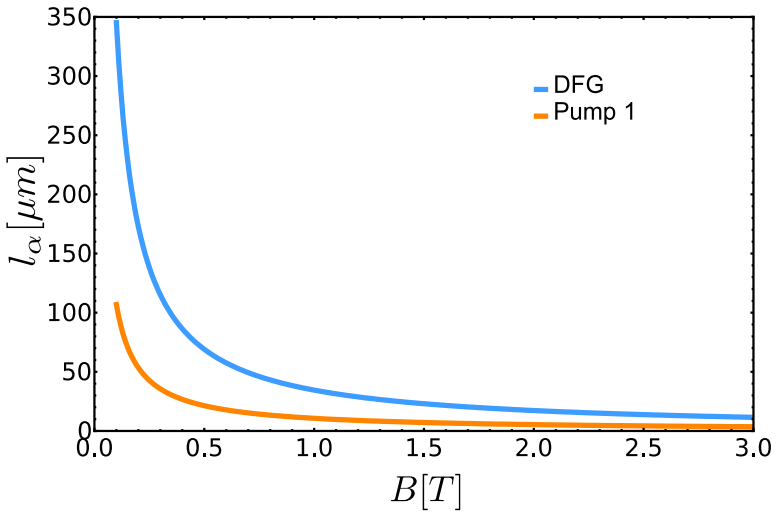

Figure 2.10: Absorption length for pump field intensity and DFG plasmon-polaritons as a function of the magnetic field for a symmetric GaAs waveguide with graphene at the interface. The core thickness is $0.06\lambda_1$. Reprinted with permission from [13].

and $|m|-1$.

$$\sigma^{-+}_{con}(\omega_l) = -i\frac{e^2v_F^2}{S\hbar\omega_l}\sum_\alpha\sum_\beta\frac{(f_\alpha - f_\beta)\sigma^-_{\beta\alpha}\sigma^+_{\alpha\beta}}{(\omega_l - \omega_{\alpha\beta} + i\gamma_{\alpha\beta})}$$
$$= -\frac{ie^2v_F^2}{\hbar\omega_l}\frac{1}{\pi l_B^2}\sum_m\frac{f_{|m|-1} - f_m}{\omega_l - \omega_{|m|-1,m} + i\gamma_{|m|-1,m}} \tag{2.111}$$
$$\sigma^{-+}_{con}(\omega_2) = -\frac{ie^2v_F^2}{\hbar\omega_2}\frac{1}{\pi l_B^2}\frac{f_2 - f_{-3}}{\omega_2 - \omega_{2,-3} + i\gamma_{2,-3}}. \tag{2.112}$$

Note that $f_2 - f_{-3} \approx 0$ since both states are assumed to be below the Fermi level and thus occupied. Among the two pump fields, the strongest absorption is experienced by the one at frequency ω_1 resonant with transition $|1\rangle \rightarrow |3\rangle$, because state $|1\rangle$ is below the Fermi level whereas state $|3\rangle$ is above the Fermi level.

The dependence of the absorption length on the magnetic field and the waveguide core thickness is shown in Figs. 2.9 and 2.10, assuming exact resonance with corresponding LL transitions and the linewidth of 10^{12} s^{-1}. This is a rather small linewidth corresponding to a high-quality

graphene encapsulated in hBN. Therefore the absorption rate for most samples is probably overestimated and the actual absorption length is longer. In any case, for structures longer than the absorption length the pump field mode should be excited by a beam coupled from the top rather than from the facet, in order to reduce the propagation length.

2.11 Summary

In summary, I investigated an electric-dipole-forbidden process of THz difference frequency generation in Landau-quantized graphene. The second-order susceptibility turned out to be surprisingly high, equivalent to the bulk magnitude of about 3×10^{-3} m/V. In particular the difference frequency generation of THz surface plasmon-polaritons in graphene integrated into a dielectric waveguide or cavity with strong vertical confinement of the optical pump modes was studied. The DFG power conversion efficiency of the order of tens μW/W^2 was predicted for structures of size around 100 μm. Analytic expressions for the DFG power were obtained and the results were presented for different structure geometries, composition, and magnetic field strengths.

3. LASER-DRIVEN PARAMETRIC INSTABILITY AND GENERATION OF ENTANGLED PHOTON-PLASMON STATES IN GRAPHENE*

3.1 Opening Remarks

This chapter is based on a publication of the same title that I coauthored [27]. A significant portion of the publication will appear verbatim in the sections that follow. However, I will supplement some sections with derivations that were not present in the published work.

As for my contributions; I was not the lead for this project. I contributed to derivations arising in the theory proposed by A. Belyanin and M. Tokman, carried out simulations, created illustrative figures and plots and was involved in the writing process. This project was done in collaboration with A. Belyanin, I. Oladyshkin, M. D. Tokman (lead author), and Y. Wang.

3.2 Introduction

In the previous section I dealt with magnetized graphene, in this section I will consider graphene without the presence of a magnetic field. The energy eigenstates and energy eigenfunctions for graphene were introduced in Ch. 1.2.1. Here I will investigate the process of parametric down-conversion in graphene. Parametric down-conversion is a second-order nonlinear process, as such the in-plane second-order susceptibility should be zero (since graphene is centrosymmetric). However, it was shown in Ch. 2 and by others [23, 25, 42] that in-plane second-order susceptibility is non-zero when its dependence on the in-plane wavevectors of the photons are taken into account, i.e. through spatial dispersion or nonlocal effects in real space. The effects of spatial dispersion on the the nonlinear susceptibility $\chi^{(2)}$ can be quite large because the Fermi velocity v_F in graphene is large. An additional enhancement of $\chi^{(2)}$ occurs at resonance between the pump frequency and twice the Fermi energy: $\omega_p = 2\epsilon_F/\hbar$.

The nonlinear process of parametric down-conversion entails the decay of a pump laser pho-

*Reprinted with permission from "Laser-Driven Parametric Instability and Generation of Entangled Photon-Plasmon States in Graphene" by Mikhail Tokman, Yongrui Wang, Ivan Oladyshkin, A. Ryan Kutayiah, and Alexey Belyanin, 2016. Phys. Rev. B, 93, 235422, Copyright 2016 by The American Physical Society.

ton into two lower-frequency photons (usually called “signal" and “idler"). It is perhaps the most popular method of generating entangled photon states [43]. At higher pump intensities, the parametric process can experience gain which leads to the instability and exponential amplification of coupled signal and idler fields. Stimulated parametric decay enables optical parametric amplifiers and oscillators as popular tunable sources of long-wavelength radiation from near- to far-infrared [44]. The phase-matching conditions for frequencies and wavevectors of the fields participating in a three-wave mixing interaction is:

$$\omega_s = \omega_p - \omega_i;\ \boldsymbol{k}_s = \boldsymbol{k}_p - \boldsymbol{k}_i, . \tag{3.1}$$

The efficiency of parametric down-conversion is enhanced when one of the generated fields is not a photon but a surface plasmon mode supported by a massless 2D electron layer. A non-zero value of the nonlocal in-plane $\chi^{(2)}$ and plasmon enhancement of the nonlinear signal were pointed out before for second-harmonic generation [25, 42] (which only included intraband transitions in a free-carrier model) and for difference-frequency generation [23].

Here the theory of the parametric decay in graphene is developed. It includes a fully quantum description of the nonlinear response and quantization of all fields. The same formalism can be applied to other systems of massless Dirac fermions, for example surface states in 3D topological insulators such as Bi_2Se_3. The theory is cast in the Heisenberg-Langevin approach. It is therefore sensible to present the basic ideas. This is done in the next section.

The schematic of the nonlinear process is shown in Fig. 3.1a and 3.1b. An obliquely incident pump photon decays into an “idler" photon and a “signal" plasmon of a much lower frequency $\omega_s = \omega_p - \omega_i \ll \omega_{p,i}$ but a comparable wavevector $q_s \sim q_p$. The second of phase matching conditions in Eqs. (3.1) is replaced by its in-plane projection $\boldsymbol{q}_s = \boldsymbol{q}_p - \boldsymbol{q}_i$. In addition, the signal frequency should match the real part of surface plasmon dispersion $\omega(q)$ shown in Fig. 3.1b: $\omega_s = \omega(q_s)$. Note that both positive and negative projections of the idler wavevector q_i are possible, where the positive direction is assumed to the right. In particular, negative values of q_i give access

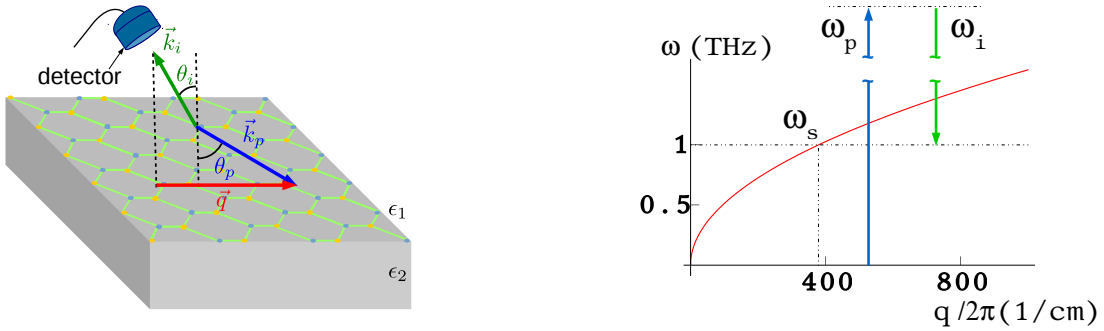

(a) Schematic of the parametric decay of the pump photon into an idler photon and a surface plasmon, which satisfies in-plane component of momentum.

(b) Shows matching of the signal frequency to the real part of surface plasmon frequency obtained by solving Eq. (3.1). Energy conservation is satisfied.

Figure 3.1: Schematic of the parametric decay process. Reprinted with permission from [27].

to larger plasmon wavevectors $q_s = q_p - q_i = |q_p| + |q_i|$ and frequencies.

3.2.1 Heisenberg-Langevin Equation

I will consider a simple model of a single harmonic oscillator mode interacting with a reservoir composed of many harmonic oscillator modes. The basic notions of fluctuation and dissipation can be understood through this model. My derivation will follow Scully's and Zubairy's *Quantum Optics* [45]. Consider the Hamiltonian of a system given by

$$\hat{H} = \hat{H}_0 + \hat{H}_{int} \tag{3.2}$$

$$\hat{H}_0 = \hbar\omega\hat{a}^\dagger\hat{a} + \sum_k \hbar\omega_k\hat{b}_k^\dagger\hat{b}_k \tag{3.3}$$

$$\hat{H}_{int} = \hbar\sum_k g_k(\hat{b}_k^\dagger a + \hat{a}^\dagger\hat{b}_k). \tag{3.4}$$

The Hamiltonian $\hat{H}$ describes a single mode field of frequency ω and number operator $\hat{a}^\dagger(t)\hat{a}(t)$ that interacts with a reservoir of closely spaced frequencies ω_k and number operators $\hat{b}_k^\dagger(t)\hat{b}_k(t)$. $\hat{H}_0$ gives the energy of the free field and the reservoir while $\hat{H}_{int}$ gives the interaction between the harmonic oscillator mode of frequency ω and the reservoir composed of many harmonic oscillator modes with frequencies ω_k. Assume for a given time t the operator of the single mode commutes

with the operators of the reservoir and that different modes of the reservoir also commute, i.e.

$$[\hat{a}, \hat{a}^\dagger] = 1, \quad [\hat{a}, \hat{a}] = [\hat{a}^\dagger, \hat{a}^\dagger] = 0, \tag{3.5}$$

$$[\hat{b}_k, \hat{b}_{k'}^\dagger] = \delta_{kk'}, \quad [\hat{b}_k, \hat{b}_{k'}] = [\hat{b}_k^\dagger, \hat{b}_{k'}^\dagger] = 0, \tag{3.6}$$

$$[\hat{a}, \hat{b}_k^\dagger] = 0, \quad [\hat{a}, \hat{b}_k] = 0, \quad [\hat{a}^\dagger, \hat{b}_k] = 0, \quad [\hat{a}^\dagger, \hat{b}_k^\dagger] = 0. \tag{3.7}$$

The equation of motion for the operators are given by the Heisenberg equation

$$\begin{aligned} \dot{\hat{a}} &= \frac{i}{\hbar}[\hat{H}, \hat{a}] = \frac{i}{\hbar}\left[\hbar\omega\hat{a}^\dagger\hat{a} + \sum_k \hbar\omega_k \hat{b}_k^\dagger \hat{b}_k + \hbar\sum_k g_k(\hat{b}_k^\dagger a + \hat{a}^\dagger \hat{b}_k), \hat{a}\right] \\ &= -i\omega\hat{a} - i\sum_k g_k \hat{b}_k. \end{aligned} \tag{3.8}$$

Similarly, one finds for $\dot{\hat{b}}$

$$\dot{\hat{b}}_k = -i\omega_k \hat{b}_k - i g_k \hat{a}. \tag{3.9}$$

A solution can be obtained by assuming $\hat{b}_k(t) = \hat{B}_k(t)e^{-i\omega_k t}$ and $\hat{B}_k(0) = \hat{b}_k(0)$.

$$\hat{b}_k(t) = \hat{b}_k(0)e^{-i\omega_k t} - i g_k \int_0^t \hat{a}(t')e^{-i\omega_k(t-t')}\, dt'. \tag{3.10}$$

Substituting Eq. (3.10) into Eq. (3.8) yields

$$\dot{\hat{a}} = -i\omega\hat{a} - \sum_k g_k^2 \int_0^t \hat{a}(t')e^{-i\omega_k(t-t')}\, dt' + \hat{f}_a(t) \tag{3.11}$$

$$\hat{f}_a(t) = -i\sum_k g_k \hat{b}_k(0)e^{-i\omega_k t} \tag{3.12}$$

$\hat{f}_a(t)$ is the noise operator since it depends on the reservoir operators $\hat{b}_k(0)$. Note that the expectation value of the mode of interest $\hat{a}$ will depend on the fluctuations in the reservoir since its equation of motion contains the reservoir-dependent noise operator. The presence of all reservoir frequencies causes the noise operator to vary rapidly. One can remove the rapid oscillations in the

mode of interest by transforming to the slowly varying annihilation operator

$$\hat{a}_s(t) = \hat{a}(t)e^{i\omega t}. \tag{3.13}$$

This transformation preserves the commutation relation

$$[\hat{a}_s, \hat{a}_s^\dagger] = e^{i\omega t}e^{-i\omega t}[\hat{a}, \hat{a}^\dagger] = 1. \tag{3.14}$$

Written in terms of the transformed operator $\hat{a}_s$, Eq. (3.11) becomes

$$\dot{\hat{a}}_s = -\sum_k g_k^2 \int_0^t \hat{a}_s(t')e^{-i(\omega_k-\omega)(t-t')}\,dt' + \hat{F}_{a_s}(t), \tag{3.15}$$

$$\hat{F}_{a_s}(t) = e^{i\omega t}\hat{f}_a(t) = -i\sum_k g_k\hat{b}_k(0)e^{-i(\omega_k-\omega)t}. \tag{3.16}$$

In order to proceed, one needs to evaluate the integral (also addressed in [45] and [46])

$$\sum_k g_k^2 \int_0^t \hat{a}_s(t')e^{-i(\omega_k-\omega)(t-t')}\,dt'. \tag{3.17}$$

Under the assumption that the frequencies ω_k are closely spaced one can expand the summation over k in by an integral:

$$\sum_k \to 2\int_0^{2\pi} d\phi \int_0^{\pi} \sin\theta\, d\theta \int_0^{\infty} \frac{k^2\,dk}{\left(\frac{2\pi}{L}\right)^3}. \tag{3.18}$$

The factor of 2 accounts for polarization of the photons, $L^3 = V$ the quantization volume, the integrals over the angles can be readily evaluated to give 4π. For a photon, one has $\omega_k = ck \implies k^2dk \to (1/c)^3\omega_k^2 d\omega_k$. So the sum becomes

$$\sum_k \to \frac{V}{\pi^2c^3}\int_0^{\infty} \omega_k^2\,d\omega_k. \tag{3.19}$$

Utilizing the results of Eq. (3.19) in Eq. (3.17) leads to

$$\sum_k g_k^2 \int_0^t \hat{a}_s(t') e^{-i(\omega_k-\omega)(t-t')}\, dt' \to \frac{V}{\pi^2 c^3} g_{k=\omega/c}^2 \int_0^\infty \omega_k^2\, d\omega_k \int_0^t \hat{a}_s(t') e^{-i(\omega_k-\omega)(t-t')}\, dt'. \quad (3.20)$$

Assuming ω_k varies only a little around the frequency ω then ω_k can be replaced by ω and taken out of the integral. In addition, the lower limit of integration can be taken as $-\infty$. Also let $g_{k=\omega/c} \equiv g(\omega)$ then:

$$\begin{aligned} &\frac{V}{\pi^2 c^3} g^2(\omega) \int_0^\infty \omega_k^2\, d\omega_k \int_0^t \hat{a}_s(t') e^{-i(\omega_k-\omega)(t-t')}\, dt' \\ &\quad \to \frac{V\omega^2}{\pi^2 c^3} g^2(\omega) \int_{-\infty}^\infty d\omega_k \int_0^t \hat{a}_s(t') e^{-i(\omega_k-\omega)(t-t')}\, dt' \end{aligned} \quad (3.21)$$

If one carries out the integration over ω_k first while keeping in mind that integral

$$\int_{-\infty}^\infty d\omega_k e^{-i(\omega_k-\omega)(t-t')} = 2\pi\delta(t-t') \quad (3.22)$$

then one obtains

$$\sum_k g_k^2 \int_0^t \hat{a}_s(t') e^{-i(\omega_k-\omega)(t-t')}\, dt' \approx \frac{1}{2}\gamma_s \hat{a}_s(t) \quad (3.23)$$

where

$$\gamma_s = 2\pi [g(\omega)]^2 D(\omega) \quad (3.24)$$

and $D(\omega) = \omega^2 V/(c^3\pi^2)$ is the density of states. Finally, by using results of Eq. (3.23) one obtains for Eq. (3.15)

$$\dot{\hat{a}}_s(t) = -\frac{1}{2}\gamma_s \hat{a}_s(t) + \hat{F}_{a_s}(t), . \quad (3.25)$$

Eq. (3.25) resembles the Langevin equation as such the operator $\hat{F}_{a_s}$ called is the Langevin noise operator and the equation above is the called the Heisenberg-Langevin equation. The presence of the noise term along with the dissipation term is a manifestation of the Fluctuation-Dissipation. Dissipation is accompanied by fluctuations. If one were to set the fluctuation to zero, i.e. $\hat{F}_{a_s} \to 0$

in Eq. (3.25) and solve for $\hat{a}_s$, one finds

$$\hat{a}_s(t) = \hat{a}_s(0)e^{-\gamma_s t/2}. \tag{3.26}$$

Upon evaluating the commutator of $\hat{a}_s$ and $\hat{a}_s^\dagger$ one finds

$$[\hat{a}_s(t), \hat{a}_s^\dagger(t)] = [\hat{a}_s(0), \hat{a}_s^\dagger(0)]e^{-\gamma_s t} = e^{-\gamma_s t}. \tag{3.27}$$

One sees the equal-time commutation relation $[\hat{a}_s(t), \hat{a}_s^\dagger(t)] = 1$ is not preserved. Now I will show that the equal-time commutation relation is preserved when the noise term is present. The solution to Eq. (3.25), in the presence of noise, is

$$\hat{a}_s(t) = \hat{a}_s(0)e^{-\gamma_s t/2} + \int_0^t \hat{F}_{a_s}(t')e^{-\gamma_s(t-t')/2}\, dt'. \tag{3.28}$$

I will evaluate the equal-time commutator by making use of the commutation relations given in the last line of Eqs. (3.7) which implies that the annihilation operator $\hat{a}_s(0)$ and the creation operator $\hat{a}_s(0)$ commutes with the operators of Langevin noise $\hat{F}_{a_s}$ and $\hat{F}_{a_s}^\dagger$ in any combination. This is obvious when one takes into account that the noise operators are composed of the reservoir operators at $t = 0$, i.e. $\hat{b}_k(0)$ and $\hat{b}_k^\dagger(0)$ according to Eq. (3.16)

$$\begin{aligned}
[\hat{a}_s(t), \hat{a}_s^\dagger(t)] &= \Big[\hat{a}_s(0)e^{-\gamma_s t/2} + \int_0^t \hat{F}_{a_s}(t')e^{-\gamma_s(t-t')/2}\, dt', \hat{a}_s^\dagger(0)e^{-\gamma_s t/2} \\
&\quad + \int_0^t \hat{F}_{a_s}^\dagger(t'')e^{-\gamma_s(t-t'')/2}\, dt''\Big] \qquad (3.29) \\
&= e^{-\gamma_s t} + \int_0^t dt' \int_0^t dt'' e^{-\gamma_s(t-t')/2}e^{-\gamma_s(t-t'')/2}\left[\hat{F}_{a_s}(t'), \hat{F}_{a_s}^\dagger(t'')\right] \qquad (3.30)
\end{aligned}$$

By way of Eq. (3.16)

$$\left[\hat{F}_{a_s}(t'), \hat{F}^{\dagger}_{a_s}(t'')\right] = \sum_{k,k'} g_k g^{\dagger}_{k'} e^{-i(\omega_k-\omega)t'} e^{+i(\omega_{k'}-\omega)t''} \underbrace{[\hat{b}_k(0), \hat{b}^{\dagger}_{k'}(0)]}_{\delta_{kk'}} \tag{3.31}$$

$$= \sum_k |g_k|^2 e^{-i(\omega_k-\omega)(t'-t'')} \tag{3.32}$$

$$= \gamma_s \delta(t'-t'') \tag{3.33}$$

The steps to go from the summation over k to an integral in $d\omega_k$, as outlined in Eqs. (3.18)-(3.24), were used in going from Eq. (3.32) to Eq. (3.33). Inserting Eq. (3.32) into Eq. (3.30) gives

$$[\hat{a}_s(t), \hat{a}^{\dagger}_s(t)] = e^{-\gamma_s t} + \int_0^t dt' \int_0^t dt'' e^{-\gamma_s(t-t')/2} e^{-\gamma_s(t-t'')/2} \gamma_s \delta(t'-t'') \tag{3.34}$$

$$= e^{-\gamma_s t} + \gamma_s \int_0^t dt' e^{-\gamma_s(t-t')} = e^{-\gamma_s t} + \gamma_s \left[\frac{e^{-\gamma_s(t-t')}}{\gamma_s}\right]\Bigg|_0^t = 1. \tag{3.35}$$

Thus, the equal-time commutation relation is preserved when dissipation is accompanied by fluctuations. I showed earlier that if fluctuations are neglected while dissipation is present, the equal-time commutation relation is violated.

Before moving on the the main items in this project I will give the thermal averages of the reservoir operators which will be used to derive some useful correlation functions of the noise operator. Suppose the reservoir of harmonic oscillators is in thermal equilibrium then

$$\left\langle \hat{b}_k(0) \right\rangle_R = \left\langle \hat{b}^{\dagger}_{k'}(0) \right\rangle_R = 0, \tag{3.36}$$

$$\left\langle \hat{b}^{\dagger}_k(0) \hat{b}_{k'}(0) \right\rangle_R = \delta_{kk'} n_k, \tag{3.37}$$

$$\left\langle \hat{b}_k(0) \hat{b}^{\dagger}_{k'}(0) \right\rangle_R = \left\langle \hat{b}^{\dagger}_k(0) \hat{b}_{k'}(0) + 1 \right\rangle_R = \delta_{kk'}(n_k+1), \tag{3.38}$$

$$\left\langle \hat{b}_k(0) \hat{b}_{k'}(0) \right\rangle_R = \left\langle \hat{b}^{\dagger}_k(0) \hat{b}^{\dagger}_{k'}(0) \right\rangle_R = 0 \tag{3.39}$$

Recall that the Langevin noise operators $\hat{F}_{a_s}(t)$ are given in terms of the reservoir operators $\hat{b}_k(0)$, see Eq. (3.16). The correlation functions for the noise operator is considered below for a reservoir

in thermal equilibrium.

$$\left\langle \hat{F}_{a_s}(t) \right\rangle_R = \left\langle \hat{F}^\dagger_{a_s}(t) \right\rangle_R = 0 \tag{3.40}$$

where Eqs. (3.36) were used.

$$\left\langle \hat{F}^\dagger_{a_s}(t)\hat{F}_{a_s}(t') \right\rangle_R = \sum_{k,k'} g_k g_{k'} \left\langle \hat{b}^\dagger_k(0)\hat{b}_{k'}(0) \right\rangle_R e^{i(\omega_k-\omega)t} e^{-i(\omega_{k'}-\omega)t'} \tag{3.41}$$

$$= \sum_k g_k^2 n_k e^{i(\omega_k-\omega)(t-t')} \tag{3.42}$$

$$= \gamma_s N_T \delta(t-t'). \tag{3.43}$$

In going from the second-to-last line to the last line in the equation above I used changed the sum to an integral as done earlier in this section. $N_T = n(\omega_k)$ is the Bose-Einstein distribution given by

$$N_T(\omega_k) = \left[e^{\hbar\omega_k/(k_B T)} - 1\right]^{-1}. \tag{3.44}$$

Similarly, one finds for $\left\langle \hat{F}_{a_s}(t)\hat{F}^\dagger_{a_s}(t') \right\rangle_R$

$$\left\langle \hat{F}_{a_s}(t)\hat{F}^\dagger_{a_s}(t') \right\rangle_R = \gamma_s (N_T+1)\delta(t-t'). \tag{3.45}$$

3.3 Quantized SPP Field in Graphene

Consider the geometry of Fig. 3.1a, i.e. a 2D layer of massless Dirac electrons in $z = 0$ plane between two media with dielectric constants ϵ_1 and ϵ_2. The plasmon frequency ω_s and in-plane wavevector $\boldsymbol{q}_s$ are related through the dispersion relation for a TM-polarized surface mode, see Eq. (2.71) and also [23]:

$$4\pi\chi_s + \frac{\epsilon_1}{p_1} + \frac{\epsilon_2}{p_2} = 0, \tag{3.46}$$

where $p_{1,2} = \sqrt{q_s^2 - \epsilon_{1,2}\frac{\omega_s^2}{c^2}}$. At THz frequencies smaller than twice the Fermi energy $2\epsilon_F/\hbar$ one needs only to take into account the intraband contributions to the linear 2D susceptibility $\chi_s(\omega_s, q_s)$,

which in the limit of strong degeneracy is given by [23]

$$\chi_s(\omega_s, q_s) = \frac{2e^2\epsilon_F}{\pi\hbar^2\omega_s}\frac{(\omega_s + i\gamma_s)}{(v_F q_s)^2}\left[1 - \frac{\omega_s + i\gamma_s}{\omega_s + i\gamma_s + v_F q_s}\sqrt{1 + \frac{2v_F q_s}{\omega_s + i\gamma_s - v_F q_s}}\right]. \tag{3.47}$$

Where ϵ_F is the Fermi energy and γ_s is the decay rate of the fermion momentum at the surface plasmon frequency.

The z-distribution of the field $\boldsymbol{E}_s(z)$ can be obtained from Eq. (2.69) while keeping in mind that graphene is on the $z = 0$ plane (at the interface of two dielectrics ϵ_1 and ϵ_2):

$$\boldsymbol{E}_s(z) = \left(\boldsymbol{e}_x \pm \boldsymbol{e}_z \frac{iq_s}{p_{1,2}}\right) E_{s0} e^{\mp p_{1,2} z}, \tag{3.48}$$

where the upper and lower signs correspond to $z > 0$, and $z < 0$, respectively.

The quantization for the plasmon field in the limit of weak dissipation $\omega_s \gg \gamma_s$ consists of two steps. First, a standard quantization procedure is applied neglecting any dissipation [39, 45, 47, 48]. Second, Heisenberg equations of motion for the field operators are formulated which include interaction with a dissipative reservoir and the effects of external and nonlinear currents. The first step leads to

$$\hat{\boldsymbol{E}} = \sum_{\boldsymbol{q}_s} \boldsymbol{E}_s(z)\hat{a}_s e^{i\boldsymbol{q}_s \boldsymbol{r}_\parallel - i\omega_s t} + \text{H.c.}, \tag{3.49}$$

where $\boldsymbol{r}_\parallel = (x, y)$ and $\hat{a}_s, \hat{a}_s^\dagger$ are annihilation and creation operators of surface plasmon modes. Similar to the case of propagating fields [45, 49], the energy of the plasmon field inside a volume V can be written as

$$\hat{H} = \frac{1}{8\pi}\sum_s (\hat{a}_s^\dagger \hat{a}_s + \hat{a}_s \hat{a}_s^\dagger) \int_V \left(\boldsymbol{E}_s^* \frac{\partial(\omega\tilde{\epsilon})}{\partial\omega}\boldsymbol{E}_s + \boldsymbol{B}_s \boldsymbol{B}_s^*\right) d^3 r, \tag{3.50}$$

where $\tilde{\epsilon}$ is the dielectric permittivity tensor.

The normalization constant E_{s0} can be chosen so that the Hamiltonian for the plasmon field

takes the standard form: $\hat{H}_s = \sum_{\boldsymbol{q}_s} \hbar\omega_s(\boldsymbol{q}_s)\left(\hat{a}_s^\dagger \hat{a}_s + 1/2\right)$. This is achieved if the following normalization condition is assumed, (which is similar to the case of a photon field [49, 50]):

$$\hat{H}_s = \int_V \left(\boldsymbol{E}_s^* \frac{\partial(\omega\tilde{\epsilon})}{\partial\omega} \boldsymbol{E}_s + \boldsymbol{B}_s \boldsymbol{B}_s^* \right) d^3r = 4\pi\hbar\omega_s. \tag{3.51}$$

Here $\tilde{\epsilon}$ is the dielectric permittivity tensor; the volume V is formed by a closed cylindrical surface that crosses the (x, y) plane along the boundary of the area $A = 1$.

One can show that when the flux of the complex vector $\boldsymbol{E}_s \times \boldsymbol{B}_s^*$ through the surface of the quantized volume is equal to zero (which is the case, for example, for periodic boundary conditions or in a resonator), then $\int_V d^3r \boldsymbol{B}_s \boldsymbol{B}_s^* = \int_V d^3r \boldsymbol{E}_s \tilde{\epsilon} \boldsymbol{E}_s^*$. This condition allows one to transform the volume integral in Eq. (3.51) in the following way:

$$\begin{aligned} &\int_V \left(\boldsymbol{E}_s^* \frac{\partial(\omega\tilde{\epsilon})}{\partial\omega} \boldsymbol{E}_s + \boldsymbol{B}_s \boldsymbol{B}_s^* \right) d^3r \\ &= \int_V \boldsymbol{E}_s^* \frac{\partial(\omega^2\tilde{\epsilon})}{\omega\partial\omega} \boldsymbol{E}_s d^3r = \int_{-\infty}^{+\infty} \boldsymbol{E}_s^* \frac{\partial(\omega^2\tilde{\epsilon})}{\omega\partial\omega} \boldsymbol{E}_s dz. \end{aligned} \tag{3.52}$$

Next, one substitutes into Eq. (3.52) the z-dependence of the dielectric permittivity which follows from the geometry of the system:

$$\epsilon_{xy} = \epsilon_{yx} = \epsilon_{xz} = \epsilon_{zx} = \epsilon_{yz} = \epsilon_{zy} = 0,$$

$$\epsilon_{xx} = \epsilon_{yy} = \begin{cases} \epsilon_1 & \text{for } z > 0 \\ 1 + 4\pi\chi_s\delta(z) & \text{for } z = 0 \\ \epsilon_2 & \text{for } z < 0, \end{cases}$$

$$\epsilon_{zz} = \begin{cases} \epsilon_1 & \text{for } z > 0 \\ 1 & \text{for } z = 0 \\ \epsilon_2 & \text{for } z < 0, \end{cases}$$

and use Eqs. (3.51) and (3.52) with Eq. (3.48) to arrive at

$$|E_{s0}|^2\left[\left(\frac{q_s^2}{p_1^2}-1\right)\frac{\epsilon_1}{p_1}+\left(\frac{q_s^2}{p_2^2}-1\right)\frac{\epsilon_2}{p_2}\right.$$
$$\left.+4\pi\omega_s Re\left(\frac{\partial\chi_s}{\partial\omega}\right)\right]=4\pi\hbar\omega_s. \tag{3.53}$$

In the quasielectrostatic approximation $p_{1,2}^2 \to q_s^2$ and Eq. (3.53) reduces to

$$|E_{s0}|^2=\hbar\left(\mathrm{Re}(\partial\chi_s/\partial\omega)\right)^{-1}. \tag{3.54}$$

The effect of dissipation of a plasmon field (within $\omega_s \gg \gamma_s$) and its nonlinear interaction with other fields can be taken into account within the Heisenberg-Langevin approach [45]. For quasi-monochromatic wave fields, it is convenient to consider a wave packet of surface plasmon modes with frequencies and wavevectors concentrated in a narrow spectral range $\Delta\omega \ll \omega_s$, $\Delta q \ll q_s$ near a central component $\propto e^{i\boldsymbol{q}_s\boldsymbol{r}_\parallel - i\omega_s t}$ [39, 51, 47, 48]. Within this approach one can introduce the annihilation and creation operators $\hat{a}_s(\boldsymbol{r}_\parallel, t)$ and $\hat{a}_s^\dagger(\boldsymbol{r}_\parallel, t)$ that are slowly varying in time and space relative to ω_s and q_s. Their commutator is equal to the number of quantized modes per unit area $S = L_x \times L_y = 1$ within the spectral interval $\Delta\omega$, i.e.

$$[\hat{a}_s, \hat{a}_s^\dagger] = \frac{\Delta Z}{S}$$

where $\Delta Z = (L_x/2\pi)\Delta k$ is the number of propagating modes (in the x-direction). Note that $\Delta k \sim (\partial k/\partial\omega)\Delta\omega = (1/v_s)\Delta\omega$. Thus,

$$[\hat{a}_s, \hat{a}_s^\dagger] = \frac{\Delta\omega}{2\pi L_y v_s} \tag{3.55}$$

where v_s is the group velocity of a surface plasmon which determines its spectral density of states and L_y is the aperture size of the beam. The commutation relations for the Fourier components of the creation and annihilation operators of the plasmon field envelope $\hat{a}_s = \int d\omega\, \hat{a}_{s\omega} e^{-i(\omega-\omega_s)t}$ and

$\hat{a}_s^\dagger = \int d\omega\, \hat{a}_{s\omega}^\dagger e^{i(\omega-\omega_s)t}$ have the form

$$\left[\hat{a}_{s\omega}, \hat{a}_{s\omega'}^\dagger\right] = \frac{\delta(\omega-\omega')}{2\pi L_y v_s}. \tag{3.56}$$

Eq. (3.49) for the field operator remains valid for a wave packet after one replaces constant operators $\hat{a}_s$ and $\hat{a}_s^\dagger$ with slowly varying operator amplitudes and remove the summation over wavevectors.

Equations for a slowly varying field amplitude of a surface plasmon wave packet can be obtained in the same way as for the propagating optical fields; see e.g. [39, 47, 48]:

$$\frac{\partial \hat{a}_s}{\partial t} + v_s \frac{\partial \hat{a}_s}{\partial x} + \gamma_s \hat{a}_s = \frac{i}{\hbar}\hat{P}_s^{(2)} E_{s0}^* + \hat{F}_s, \tag{3.57}$$

where $\gamma_s = \hbar^{-1}(\mathrm{Im}[\chi_s])|E_{s0}^2|$, $\hat{F}_s(t)$ is the operator of the Langevin noise, and $\hat{\boldsymbol{P}}_s^{(2)} = \boldsymbol{x}_0 \hat{P}_s^{(2)} e^{iq_s x - i\omega_s t} +$ H.c. is the second-order nonlinear component of the polarization operator.

The Langevin noise source ensures a correct expression for the commutator of the plasmon field in the presence of its interaction with a dissipative reservoir as was seen in Sec. 3.2.1. It is convenient to define the properties of the noise source in terms of its spectral components $\hat{F}_s = \int \hat{F}_{s\omega} e^{-i\omega t}\, d\omega$ and $\hat{F}_{s\omega}^\dagger = \hat{F}_{s;-\omega}$. Assuming a dissipative reservoir in thermal equilibrium and adjusting Eqs. (3.43) and (3.45) for the 2D geometry and taking position into account, one can write [39, 45]

$$\begin{aligned}
\left\langle \hat{F}_{\omega'}^\dagger(x')\hat{F}_\omega(x)\right\rangle &= \frac{\gamma_s N_T(\omega_s)}{\pi L_y}\delta(\omega-\omega')\delta(x-x'), \\
\left\langle \hat{F}_\omega(x)\hat{F}_{\omega'}^\dagger(x')\right\rangle &= \frac{\gamma_s (N_T(\omega_s)+1)}{\pi L_y}\delta(\omega-\omega')\delta(x-x'),
\end{aligned} \tag{3.58}$$

where $\langle ... \rangle$ means averaging over both an initial quantum state in the Heisenberg picture and the statistics of the dissipative reservoir, $N_T(\omega_s) = \left(\mathrm{e}^{\hbar\omega_s/(k_B T)} - 1\right)^{-1}$, see Eq. (3.44).

In the absence of the nonlinear polarization, the solution of Eqs. (3.57), (3.58) in the limit $\gamma_s x/v_s \to \infty$ corresponds to thermal equilibrium:

$$\left\langle \hat{a}_s^\dagger \hat{a}_s \right\rangle \to \left\langle \hat{a}_s^\dagger \hat{a}_s \right\rangle_T = \frac{N_T(\omega_s)\Delta\omega}{2\pi L_y v_s}. \tag{3.59}$$

Eq. (3.59) satisfies a general property of the thermal emission: its power $\approx L_y v_s \hbar\omega_s \left\langle \hat{a}_s^\dagger \hat{a}_s \right\rangle_T$ received by a matched antenna does not depend on the size and shape of the aperture [52].

3.4 Parametric Instability in Graphene

Generation of surface plasmons in graphene is possible with both transverse magnetic or P-polarized (see [23]) and transverse electric or S-polarized optical pumping. The theory is developed in the same way for both polarizations. The difference is that in the case of P-polarized photons only the $\chi^{(2)}_{xxx}$ component of the second-order susceptibility is involved, whereas for S-polarized pumping both xyy and yyx components contribute to the parametric process. S-polarized radiation maximizes the in-plane projection of the electric field. In addition, theory predicts a larger magnitude of the xyy component compared to the xxx component. Therefore, I will consider only the case of S-polarization, assuming an S-polarized bichromatic pump+idler field incident from the $z > 0$ half-space:

$$\hat{\boldsymbol{E}} = \sum_{j=p,i} \hat{\boldsymbol{E}}_j;\ \hat{\boldsymbol{E}}_j = \boldsymbol{e}_y E_{j0} \hat{c}_j \mathrm{e}^{-ik_j z + iq_j x - i\omega_j t} + \mathrm{H.c.},$$

where the normalization fields $|E_{j0}|^2 = 2\pi\hbar\omega_j/n_1^2$ are defined for a unit quantization volume, $\hat{c}_j$ are Heisenberg operators of slowly varying amplitudes corresponding to a finite spectral width $\Delta\omega$ [39, 47, 48, 50]. The nonlinear 2D polarization at frequencies $\omega_{p,i,s}$ generated in the graphene

plane $z = 0$ is given by

$$\begin{aligned}
\hat{\boldsymbol{P}}_s^{(2)} &= \boldsymbol{e}_x \chi_{xyy}^{(s,2)} \hat{\mathcal{E}}_i^{\dagger} \hat{\mathcal{E}}_p + \text{H.c.}, \\
\hat{\boldsymbol{P}}_i^{(2)} &= \boldsymbol{e}_y \chi_{yyx}^{(i,2)} E_{s0}^{*} \hat{a}_s^{\dagger} \hat{\mathcal{E}}_p \mathrm{e}^{-iq_s x + i\omega_s t} + \text{H.c.}, \\
\hat{\boldsymbol{P}}_p^{(2)} &= \boldsymbol{e}_y \chi_{yyx}^{(p,2)} E_{s0} \hat{a}_s \hat{\mathcal{E}}_i \mathrm{e}^{iq_s x - i\omega_s t} + \text{H.c.},
\end{aligned} \tag{3.60}$$

where $\hat{\mathcal{E}}_{p,i}$ are the $\propto \exp(-i\omega t)$ parts of the electric field operators at the pump and idler frequencies $\omega_{p,i}$ in the graphene plane. The second-order susceptibilities at corresponding frequencies are $\chi_{xyy}^{(s,2)} = \chi_{xyy}^{(2)}(\omega_s = \omega_p - \omega_i)$, $\chi_{yyx}^{(i,2)} = \chi_{yyx}^{(2)}(\omega_i = \omega_p - \omega_s)$, $\chi_{yyx}^{(p,2)} = \chi_{yyx}^{(2)}(\omega_p = \omega_i + \omega_s)$. Index α in $\chi_{\alpha\beta\gamma}^{(2)}(\omega = \omega' \mp \omega'')$ corresponds to the polarization of the field at the mixing frequency ω, and the index β corresponds to the polarization of the field at a larger of the two frequencies ω', ω''.

Now I will consider the boundary conditions connecting the fields on both sides of the graphene layer. Besides the continuity of the electric field, I will use the relationships for magnetic field components:

$$\begin{aligned}
&\hat{\mathcal{B}}_z^{(i,p)}(z = +0) = \hat{\mathcal{B}}_z^{(i,p)}(z = -0), \\
&\hat{\mathcal{B}}_x^{(i,p)}(z = +0) - \hat{\mathcal{B}}_x^{(i,p)}(z = -0) = -4\pi \frac{i\omega_{i,p} \hat{P}_{i,p}^{(2)}}{c},
\end{aligned}$$

where $\hat{\mathcal{B}}_{z,x}^{(i,p)}$ are operators of the magnetic field components that are related to the electric field operators by standard Maxwell's equations.

Using the nonlinear polarizations and boundary conditions for the fields, Eq. (3.57) becomes

$$\frac{\partial \hat{a}_s}{\partial t} + v_s \frac{\partial \hat{a}_s}{\partial x} + (\gamma_s - \hat{G}) \cdot \hat{a}_s = \hat{J} + \hat{F}_s, \tag{3.61}$$

where

$$\hat{J} = \Gamma \chi_{xyy}^{(s,2)} \hat{c}_i^\dagger \hat{c}_p,\ \Gamma = i \frac{2\pi\sqrt{\omega_i \omega_p}}{n_1^2} T_i T_p E_{s0}^*,$$
$$\hat{G} = |\Gamma|^2 \frac{n_1}{c} \left(\frac{\chi_{xyy}^{(s,2)} \chi_{yyx}^{(i,2)*} \hat{c}_p^\dagger \hat{c}_p}{T_i \cos\theta_{1i}} - \frac{\chi_{xyy}^{(s,2)} \chi_{yyx}^{(p,2)} \hat{c}_i^\dagger \hat{c}_i}{T_p \cos\theta_{1p}} \right).$$

Here $T_{p,i} = 2n_1 \cos\theta_{1p,i} / (n_1 \cos\theta_{1p,i} + n_2 \cos\theta_{2p,i})$ are Fresnel transmission coefficients for S-polarized pump and idler fields with incidence angles $\theta_{1p,i}$ and refraction angles $\theta_{2p,i}$. Eq. (3.61) was derived neglecting the terms of the order $\alpha|\chi^{(2)}|^2$ and $|\chi^{(2)}|^3$ where $\alpha = e^2/\hbar c$.

The terms $\hat{J}$ and $\hat{G}$ in Eq. (3.61) include all possible three-wave mixing processes. The term $\hat{J}$ describes difference frequency generation of surface plasmons in graphene by a bichromatic quantum field. For classical fields this process has been predicted in [23] and observed in [53]. The operator $\hat{G}$ describes the creation of plasmons by a parametric decay of the pump photons.

When solving operator-valued equations, in addition to the fields incident from $z > 0$ one also needs to specify operators of noise fields incident from $z < 0$ [50]. This allows one to take into account the current fluctuations in a graphene layer caused by zero-point and thermal fluctuations of the field in the region $z < 0$. It is easy to show that in this case one should replace $\hat{c}_{p,i} \to \hat{c}_{p,i} + \hat{c}_{p,i}^{(-)}$, $\hat{c}_{p,i}^\dagger \to \hat{c}_{p,i}^\dagger + \hat{c}_{p,i}^{\dagger(-)}$ in Eq. (3.61), where creation and annihilation operators $\hat{c}_{p,i}^{(-)}$ and $\hat{c}_{p,i}^{\dagger(-)}$ correspond to the waves incident on a graphene layer from $z < 0$ at angles $\theta_{2(p,i)}$. The corresponding terms can be treated as a modification of the Langevin source term in Eq. (3.61). However, under the condition $\hbar\omega_s \ll k_B T \ll \hbar\omega_p$ the effect of this modification on the plasmon field correlator $\langle \hat{a}_s^\dagger \hat{a}_s \rangle$ is negligible compared to the standard Langevin fluctuations given by Eq. (3.58).

The operator-valued Eq. (3.61) has a stationary solution given by

$$\hat{a}_s = \exp\left(\frac{\hat{G}-\gamma_s}{v_s}x\right) \times \left\{\hat{a}_s(0) + \int_0^x \left[\exp\left(\frac{\hat{G}-\gamma_s}{v_s}x'\right)\right]^{-1}\left(\hat{J}+\hat{F}_s\right)\frac{dx'}{v_s}\right\}, \tag{3.62}$$

where $\hat{a}_s(0)$ is the corresponding boundary condition, $\left[\exp\left(\frac{\hat{G}-\gamma_s}{v_s}x\right)\right]^{-1}$ is the operator inverse to $\exp\left(\frac{\hat{G}-\gamma_s}{v_s}x\right)$.

Below I will assume that the pump field at frequency ω_p is a coherent classical field whereas the field at the idler frequency ω_i is present only as a quantum and/or thermal noise.

Whenever the contribution of electromagnetic noise incident from the half-space $z < 0$ can be neglected, one can also neglect the term $\hat{J}$ compared to the Langevin noise term. For a coherent pumping, the operator $\hat{G}$ can be replaced by a c-number:

$$G \approx |\Gamma|^2 \frac{n_1}{c}\frac{\chi^{(s,2)}_{xyy}\chi^{(i,2)*}_{yyx}\left\langle \hat{c}_p^\dagger \hat{c}_p\right\rangle}{T_i \cos\theta_{1i}}. \tag{3.63}$$

Taking the thermal noise as a boundary condition and taking into account Eqs. (3.58) and (3.62) one can get

$$\hat{a}_s^\dagger \hat{a}_s = \exp\left[2\frac{\mathrm{Re}[G]-\gamma_s}{v_s}x\right](\hat{a}_s^\dagger \hat{a}_s)_T \times \left[1+\frac{\gamma_s}{\mathrm{Re}[G]-\gamma_s}\left(1-\exp\left[-2\frac{\mathrm{Re}[G]-\gamma_s}{v_s}x\right]\right)\right], \tag{3.64}$$

where the operator $(\hat{a}_s^\dagger \hat{a}_s)_T$ corresponds to the thermal field and has an average value given by Eq. (3.59). Note that there is a $1/v_s$ dependence in the gain factor in Eq. (3.64) which describes the enhancement in the gain for slowly moving plasmons compared to photons.

From Eq. (3.64) one can obtain an important result, namely the criterion for parametric instability:

$$\mathrm{Re}(\chi_{xyy}^{(s,2)}\chi_{yyx}^{(i,2)*}) > 0, \tag{3.65}$$

$$\mathrm{Re}[G] \approx |\Gamma|^2 \frac{\mathrm{Re}\left[\chi_{xyy}^{(s,2)}\chi_{yyx}^{(i,2)*}\right] I_p}{c^2\hbar\omega_p} \frac{n_1^2}{T_i \cos\theta_{1i}} > \gamma_s, \tag{3.66}$$

where I_p is the incident pump intensity.

3.5 A Coupled Oscillators Model for Parametric Gain

The instability condition Eqs. (3.65), (3.66) can be easily interpreted and understood within the classical model of two parametrically coupled oscillators. Consider a classical pump beam of amplitude E_p and ω_p incident on a nonlinear 2D layer in vacuum. The pump field decays into a surface plasmon field within a unit area $A_s = 1$ and an idler photon field at frequency ω_i within a volume of a cylinder of length l oriented at an angle θ_i with respect to the normal to area A_s. In this mean-field zero-dimensional (0D) model, one can derive the following coupled differential equations for the complex amplitudes of the plasmon and idler fields:

$$\frac{\partial E_s}{\partial t} + \gamma_s E_s = i\zeta_s E_p E_i^*, \tag{3.67}$$

$$\frac{\partial E_i^*}{\partial t} + \gamma_i E_i^* = -i\zeta_i^* E_p^* E_s, \tag{3.68}$$

where

$$\zeta_s = \frac{1}{2}\chi_{xyy}^{(s,2)} \left[\mathrm{Re}\left(\frac{\partial \chi_s}{\partial \omega}\right)\right]^{-1}, \; \zeta_i = \frac{\pi}{l\cos\theta_i}\omega_i \chi_{yyx}^{(i,2)*},$$

$\gamma_i = c/l$ is the effective decay rate of the idler field in the 0D model. Equations (3.67) and (3.68) have an exponentially growing solution for both parametrically coupled waves [44] if $\mathrm{Re}(\zeta_s\zeta_i^*)|E_p|^2 > \gamma_s\gamma_i$, which coincides with Eqs. (3.65), (3.66) if one uses Eq. (3.54) and assume

$n_2 = n_1 = 1$.

3.6 The Spectrum and Magnitude of Parametric Gain

To calculate the magnitude of the parametric gain one needs to substitute the components of the second-order susceptibility tensor. Their derivation is straightforward but cumbersome, see [27] for details. Their salient feature is the presence of resonances when one of the three frequencies involved in three-wave mixing is close to $2\epsilon_F = 2\hbar v_F k_F$. This is a weaker resonance than the one that exists in coupled quantum wells [54] where $\chi^{(2)}$ would scale as a product of two Lorentzians. Still, it enhances the value of $\chi^{(2)}$ by a factor of ω/γ where γ is the decay rate of the optical polarization. A similar resonance exists in the third-order nonlinear response of graphene [55].

Far from resonance, when $|\omega_p - 2v_F k_F| \gg \gamma$, one can neglect dissipation. In this case, all components of the nonlinear susceptibility tensor satisfy symmetry properties

$$\chi^{(s,2)}_{xyy} = \chi^{(i,2)}_{yyx} = \chi^{(p,2)*}_{yyx} \tag{3.69}$$

which ensure Manley-Rowe relationships [56, 57].

Close to resonance one has to include the imaginary part of the frequency which describes the decay rate of the optical or plasmon polarization. If dissipation is included, Eqs. (3.69) can be violated. In this case one has to use a more general procedure outlined in [27]. From the derivation in [27] one can obtain that if the resonance condition is satisfied for the idler photon frequency, $|\omega_i - 2v_F k_F| < \gamma$, then $\chi^{(s,2)}_{xyy} = -\chi^{(i,2)*}_{yyx}$. In this case the inequality in Eq. (3.65) is violated, i.e. the parametric instability is impossible. At the same time, when the resonance exists for the pump frequency, $|\omega_p - 2v_F k_F| < \gamma$, one obtains

$$\chi^{(s,2)}_{xyy} = \chi^{(i,2)*}_{yyx} \approx \frac{3e^3 v_F^2}{8\pi\hbar^2} \frac{q_p}{\omega_i \omega_s^2 \gamma}, \tag{3.70}$$

which satisfies Eq. (3.65). Therefore, I will assume that the frequency of the pump field is close to $2v_F k_F$. The $\chi^{(2)}_{xxx}$ component of the nonlinear susceptibility tensor was evaluated (see [27]) and found that its value is 3 times lower at resonance compared to Eq. (3.70). This means that the parametric gain for a P-polarized pump is more than an order of magnitude lower as compared to a S-polarized pump (if one takes into account a smaller in-plane projection of the electric field and the $|\chi^{(2)}|^2$ scaling of the gain). If one assumes $\omega_{p,i} \gg \omega_s \gg \gamma_s$ and considers strongly degenerate graphene then one gets a resonant enhancement of the nonlinearity. In addition to a resonant enhancement of the nonlinearity, the former assumptions allow one to eliminate interband absorption losses for the plasmons and reduces electron scattering.

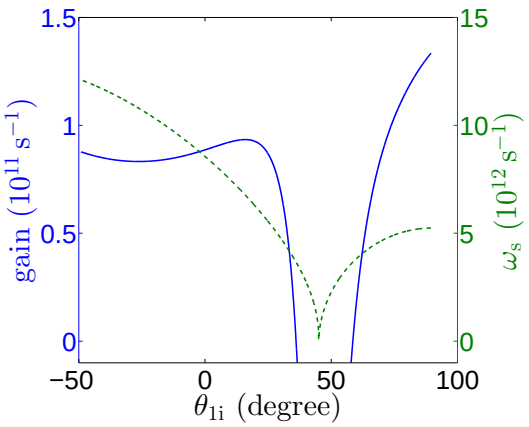

Figure 3.2: Gain Re$[G]$ (solid blue line) and the plasmon frequency corresponding to phase matching conditions (green dashed line) as a function of the angle θ_{1i} between the direction of the idler wavevector in medium 1 and the normal. Reprinted with permission from [27].

Figure 3.2 shows the gain (left-hand side of Eq. (3.66)) and the plasmon frequency corresponding to phase matching conditions as a function of the emission angle of the idler field θ_{1i}. Negative angles correspond to negative projections of q_i. For the plot I took $n_1 = 1$ and $n_2 = 2$, $\gamma_{p,i} = 10^{12}$ s^{-1}, the pump beam at a 10-μm wavelength and incidence angle of $\pi/4$. The pumping intensity

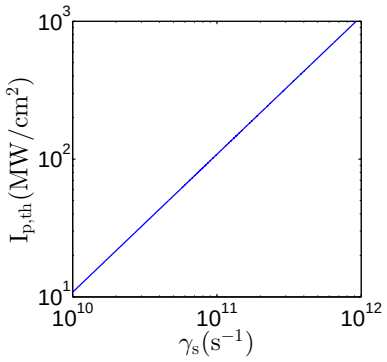

Figure 3.3: Pumping intensity I_p needed to reach the parametric instability threshold, $\mathrm{Re}[G] = \gamma_s$ in Eq. (3.66), as a function of the plasmon decay rate γ_s. Reprinted with permission from [27].

was assumed to be $I_p = 100$ MW/cm^2, which is 10 times lower than the intensities in the experiment [53]. The gain is only weakly dependent on the idler emission angle except for a narrow range around $\theta_{1i} = \pi/4$ where $q_p \simeq q_i$ and therefore $q_s, \omega_s \to 0$. In this range the gain becomes negative; however, the approximation $\omega_s \gg \gamma_s$ becomes invalid, so this case requires a separate investigation.

Fig. 3.3 shows the pumping intensity I_p needed to reach the parametric instability threshold, $\mathrm{Re}[G] = \gamma_s$, as a function of plasmon decay rate γ_s, for the same numerical parameters as in Fig. 3.2 and for the idler emitted at $\theta_{1i} = 20$ degrees. In this case the phase matching condition is satisfied when the plasmon frequency $\omega_s/2\pi$ is equal to 1 THz (see Fig. 3.2). The magnitude of the gain can be further increased by non-Bernal stacking of multiple graphene layers, which will reduce the threshold intensity.

Low-energy surface states of a 3D topological insulator Bi_2Se_3 are massless 2D Dirac fermions described by the effective Hamiltonian $H = v_F(\vec{\sigma} \times \vec{p})_z$ [58], where v_F is two times smaller than in graphene. The states have different chirality compared to those in graphene but the same matrix elements of the interaction Hamiltonian and the same structure of the optical response. Repeating the same derivation, one can show that the parametric gain for a Bi_2Se_3 film (i.e. two uncoupled surfaces) will have a magnitude lower by a factor of $\sim 2^6$ due to a two times lower v_F and two times lower degeneracy.

3.7 Generated Idler Field Flux

The outgoing flux of idler photons generated as a result of parametric decay of the pump carries information on the intensity of generated surface plasmon field, the surface nonlinearity, and even the quantum state of plasmons. Therefore, the detection of idler photons is a valuable diagnostic tool, especially in the experiments where the direct detection of surface plasmons is problematic. To calculate the operator of the idler field generated by the nonlinear current $\partial_t \hat{\boldsymbol{P}}_i^{(2)}$, one uses Eqs. (3.60) and standard boundary conditions from the previous section, arriving at

$$\delta\hat{\boldsymbol{E}}_i = \boldsymbol{y}_0 E_{i0}\hat{c}_i^{(2)} \mathrm{e}^{ik_i z + iq_i x - i\omega_i t} + \text{H.c.},\ \hat{c}_i^{(2)} = \frac{n_1 \Gamma \chi_{yyx}^{(i,2)}}{c\cos\theta_{1i}} \hat{a}_s^\dagger \hat{c}_p.$$

If one only needs to know the average flux of the idler photons on the detector of transverse area A_D, $\left\langle \hat{\Pi}_i^{(2)} \right\rangle = \left\langle \frac{cA_D}{n_1} \hat{c}_i^\dagger \hat{c}_i \right\rangle$, it is enough to calculate the average value of the plasmon quanta $\left\langle \hat{a}_s^\dagger \hat{a}_s \right\rangle$ generated from length L_x. Using Eq. (3.64) one obtains

$$\begin{aligned} \left\langle \hat{a}_s^\dagger \hat{a}_s \right\rangle &= \frac{1}{L_x}\int_0^x \left\langle \hat{a}_s^\dagger \hat{a}_s \right\rangle dx \approx \left\langle \hat{a}_s^\dagger \hat{a}_s \right\rangle_T \frac{e^\Xi - 1}{\Xi}, \\ \Xi &= 2\frac{\mathrm{Re}[G] - \gamma_s}{v_s} L_x. \end{aligned} \tag{3.71}$$

The resulting average flux of the idler photons on the detector is given by

$$\left\langle \hat{\Pi}_i^{(2)} \right\rangle = \frac{n_1^2 |\Gamma|^2 |\chi_{yyx}^{(i,2)}|^2 I_p L_x \Delta\omega}{2\pi c^2 v_s \hbar \omega_p \cos\theta_{1i}} \left(\frac{e^\Xi - 1}{\Xi} N_T(\omega_s) + 1 \right).$$

Close to the parametric instability threshold, when $\dfrac{e^\Xi - 1}{\Xi} \sim 1$, the idler photon flux is

$$\left\langle \hat{\Pi}_i^{(2)} \right\rangle \sim \frac{\Delta\omega \gamma_s L_x}{2\pi v_s} N_T(\omega_s), \tag{3.72}$$

i.e. it is of the order of the thermal flux at a much lower surface plasmon frequency, $N_T(\omega_s) \gg N_T(\omega_p)$, collected from the length equal to the plasmon decay length, $L_x \sim v_s/\gamma_s$. Far above

threshold, both idler and surface plasmon fluxes increase exponentially, $\propto e^{\Xi}$.

3.8 Plasmon-Photon Entanglement

The total idler field propagating away from the graphene layer to the detector consists of the reflected and transmitted noise field and the generated parametric field calculated above:

$$\hat{c}_r \approx R_i \hat{c}_i + \sqrt{1 - R_i^2}\hat{c}_i^{(-)} + \frac{n_1 \Gamma \chi_{yyx}^{(i,2)}}{c \cos\theta_{1i}} \hat{a}_s^\dagger \hat{c}_p, \tag{3.73}$$

where $R_i = \dfrac{n_1 \cos\theta_{1i} - n_2 \cos\theta_{2i}}{n_1 \cos\theta_{1i} + n_2 \cos\theta_{2i}}$ is the Fresnel reflection coefficient for the S-polarized field. Here I neglected absorption in monolayer graphene $\sim \pi\alpha$. It could be easily included by redefining R_i. Calculating quantum-mechanical averages of the quantities quadratic with respect to the reflected field, it is easy to see that Eq. (3.73) corresponds to an entangled plasmon-photon state (see also [39]).

In general, the calculations of quantum-mechanical averages of any physical quantities are much easier to perform in the Heisenberg picture using Eq. (3.73) for Heisenberg operators, without converting to the Schrödinger picture. In particular, it is obvious from Eq. (3.73) that for a given spectrum of the pump field any physical observable for a surface plasmon field can be related to a corresponding observable for the idler field at frequency ω_i. For example, if the pump field spectrum is much narrower than the spectrum of the plasmon fluctuations, then the spectrum of surface plasmons is related to the spectrum of idler photons. However, to demonstrate how the entangled state is formed, the Schrödinger picture be will discussed as well, with certain simplifications. Namely, consider the equation of motion Eq. (3.57) for the plasmon field in the particular case of single-mode fields, classical pumping, and neglecting dissipation. This means that one can take $\mathcal{E}_p$ to be a c-number, $\partial_x \to 0$, $\gamma, \hat{F}_s \to 0$, and $\chi_{xyy}^{(s,2)} = \chi_{yyx}^{(i,2)} = \chi^{(2)}$. I will also assume for simplicity that the media on both sides of the graphene sheet have dielectric constants equal to 1. In this case Eqs. (3.57) and (3.60) yield

$$\dot{\hat{a}}_s = \frac{i}{\hbar}\chi^{(2)} \mathcal{E}_p E_{s0}^* E_{i0}^* \hat{c}_i^\dagger, \tag{3.74}$$

and the Hermitian-conjugate equation

$$\dot{\hat{a}}_s^\dagger = \frac{i}{\hbar}\chi^{(2)}\mathcal{E}_p^* E_{s0} E_{i0}\hat{c}_i. \tag{3.75}$$

For single-mode fields, the normalizations I chose correspond to $[\hat{a}_s, \hat{a}_s^\dagger] = [\hat{c}_s, \hat{c}_s^\dagger] = 1$, Eqs. (3.74) and (3.75) can be interpreted as Heisenberg equations in the interaction representation:

$$\dot{\hat{a}}_s = \frac{i}{\hbar}\left[\hat{V}, \hat{a}_s\right],\ \dot{\hat{a}}_s^\dagger = \frac{i}{\hbar}\left[\hat{V}, \hat{a}_s^\dagger\right]. \tag{3.76}$$

Here the interaction Hamiltonian is

$$\hat{V} = -\xi\hat{a}_s^\dagger\hat{c}_i^\dagger - \xi^*\hat{a}_s\hat{c}_i, \tag{3.77}$$

where $\xi = \chi^{(2)}\mathcal{E}_p E_{s0}^* E_{i0}^*$.

Solving the Schrödinger equation in the interaction representation gives:

$$i\hbar\dot{\Psi} = \hat{V}\Psi. \tag{3.78}$$

Starting for simplicity with the initial condition in the form $\Psi(t=0) = |0\rangle_s|0\rangle_i$, the solution to Eq. (3.78) can be written as

$$\Psi = \sum_{n=0}^{\infty} C_n|n\rangle_s|n\rangle_i, \tag{3.79}$$

where the coefficients C_n can be found from equations

$$\begin{aligned}
&\dot{C}_0 + \frac{i}{\hbar}\xi^* C_1 = 0,\\
&\dot{C}_{n\neq 0} - \frac{i}{\hbar}\xi n C_{n-1} + \frac{i}{\hbar}\xi^*(n+1)C_{n+1} = 0,
\end{aligned} \tag{3.80}$$

with initial conditions $C_0(t=0)=1$, $C_{n\neq 0}=0$. It is clear that at $t>0$ the solution (3.79) is entangled, i.e. it cannot be factorized as $\Psi=(\sum_{n=0}^{\infty}A_n|n\rangle_s)\times(\sum_{n=0}^{\infty}B_n|n\rangle_i)$. In particular, within the perturbation theory, the solution can be expressed via Bell states $\Phi_{\pm}=(1/\sqrt{2})\,(|0\rangle_s|0\rangle_i\pm|1\rangle_s|1\rangle_i)$:

$$\begin{aligned}\Psi &\approx \frac{|0\rangle_s|0\rangle_i+\tilde{C}|1\rangle_s|1\rangle_i}{\sqrt{1+|\tilde{C}|^2}}\\ &= \frac{1+\tilde{C}}{\sqrt{1+|\tilde{C}|^2}}\frac{\Phi_+}{\sqrt{2}}+\frac{1-\tilde{C}}{\sqrt{1+|\tilde{C}|^2}}\frac{\Phi_-}{\sqrt{2}},\end{aligned} \tag{3.81}$$

where $\tilde{C}=\frac{i}{\hbar}\xi t\ll 1$.

3.9 Summary

In summary, the feasibility of observing both spontaneous and stimulated parametric decay of photons of a strong laser pump obliquely incident on graphene was shown. The flux of surface plasmons and idler photons generated by parametric decay of the pump was calculated, and the entanglement of these modes was demonstrated. A rigorous quantum theory of the process including quantization of all fields and fluctuations has been developed.

4. OPTICAL PROPERTIES AND ELECTROMAGNETIC MODES OF WEYL SEMIMETALS*

4.1 Opening Remarks

This chapter is based on a publication of the same title that I coauthored [59]. Most of the publication will appear verbatim in the sections that follow with some additions and rearrangements.

As for my contributions: I was not the lead but second author for this project. I contributed to derivations arising from the theory, carried out simulations, created figures and plots and was involved in the writing process. I will include a couple of figures below that were not in the published work. This project was done in collaboration with Q. Chen (lead author), A. Belyanin, I. Oladyshkin and M. D. Tokman.

4.2 Introduction

Weyl semimetals (WSMs) have attracted a lot of interest as a new class of gapless three-dimensional topological materials. Their Brillouin zone contains an even number of band-touching points, or Weyl nodes. The Weyl nodes can be described by topological invariants which are defined as integrals over the two-dimensional Fermi surface. For each pair of Weyl nodes, these invariants can be viewed as topological chiral charges of opposite signs [60] (the signs are determined by the chirality). The electron dispersion near each Weyl node corresponds to three-dimensional massless Weyl fermions. For crystals with broken time-reversal or inversion symmetry (or both), the Weyl nodes of opposite chirality are separated in momentum space. The separation makes them stable against small perturbations and also gives rise to surface states with Fermi arcs. For reviews of WSMs discovered so far and their properties, see [61, 62, 63, 64, 65, 66].

Hitherto, much of the research has been focused on measuring and modeling the electronic structure of WSMs and topological signatures in electron transport. However, it is becoming in-

*Reprinted with permission from "Optical Properties and Electromagnetic Modes of Weyl Semimetals" by Qianfan Chen, A. Ryan Kutayiah, Ivan Oladyshkin, Mikhail Tokman, and Alexey Belyanin, 2019. Phys. Rev. B, 99, 075137, Copyright 2019 by The American Physical Society.

creasingly clear that optical studies in the terahertz to mid-infrared spectral regions (e.g. [67]) can provide a sensitive and sometimes more selective probe into the unique properties of these materials as compared to other methods. For a WSM in a magnetic field several proposals explored the signatures of the chiral anomaly in the interband optical absorption and plasmon mode properties; see e.g. the calculations of the magnetooptical conductivity in the quasiclassical limit [68, 69, 70, 71, 72, 73, 74] and the quantum-mechanical theory in a strong magnetic field [75, 76]. Note that these studies did not include finite separation of Weyl nodes in a microscopic Hamiltonian.

Here, the study of the electromagnetic eigenmodes of WSMs in the presence of finite separation between Weyl nodes in momentum space and without an external magnetic field is considered. To calculate the optical response, one needs to determine a realistic low-energy Hamiltonian that captures the essential topological structure of WSMs. While many WSMs discovered in experiments have a complicated arrangement of several pairs of Weyl nodes, it is sufficient to consider a model with only two Weyl nodes separated in momentum space. Such a model adequately captures the essential physics and electronic properties of WSMs. These models serve as a usual starting point for theoretical studies of transport and optical phenomena. Perhaps the simplest approach (to construct one such model) is to add a Zeeman-like constant shift term to the Hamiltonian for a Dirac semimetal, which preserves the linear form of the Hamiltonian with respect to momentum operators [77]. The bulk optical conductivity for this model was calculated in [78]. In another approach, developed in [79] and used in many optical response studies to date, a phenomenological axion θ-term is introduced in the action for the electromagnetic field. This gives rise to the gyrotropic terms in the dielectric permittivity tensor and associated effects of Faraday and Kerr rotation, linear dichroism, modification of surface plasmon dispersion etc.; see e.g. [80, 81, 82, 66].

In yet another approach, Okugawa and Murakami [83] derived a minimal 2x2 Hamiltonian (one conduction and one valence band). Their Hamiltonian contains one parameter which describes the phase transition from a normal insulator to a WSM (with two Weyl nodes separated in momentum space) and eventually to a topological insulator in the bulk. In the WSM phase, this

Hamiltonian allows for surface state solutions with Fermi arcs. The beauty of this theory is that a single microscopic Hamiltonian can be used to describe optical transitions between the bulk states, the surface states, and the surface-to-bulk states. As a result, both bulk and surface tensors of the optical conductivity can be derived. The Hamiltonian of [83] has been recently used to develop a quantum-mechanical theory of surface plasmons (Fermi arc plasmons) and their dissipation [84].

Here, a slightly more general Hamiltonian is used. It is free of certain surface state pathologies to perform quantum-mechanical derivation of the tensors of both bulk and surface conductivity. All possible combinations of transitions between bulk and surface electron states are considered. Once this is done, one is able to then determine the properties of bulk and surface electromagnetic eigenmodes, or polaritons. It will be shown that information about the electronic structure of WSMs, such as position and separation of Weyl nodes, Fermi energy, surface states, Fermi arcs, etc. can be extracted from the transmission, dispersion, reflection, and polarization of electromagnetic modes. The most sensitive optical signatures of the electronic properties of WSMs are identified and the potential use of WSM thin films for optoelectronic applications is discussed.

4.2.1 Weyl Fermions

The low-energy excitations of Weyl semimetals are Weyl fermions much like the low-energy excitations of graphene are massless Dirac fermions. In the previous chapters, I dealt with graphene using the tight-binding model in the nearest-neighbor approximation to show that in the low-energy limit the Hamiltonian for graphene resembles the two-dimensional massless Dirac equation (where the speed of light is replaced by the Fermi velocity).

In this section, I will start by directly writing down the Dirac equation, then introduce Weyl's simplification to the Dirac equation; the Weyl equation. I will show that the Weyl equation admits chiral fermions as its solution. The contents of this section is primarily based on the following papers [85, 86, 64]. For an introduction to the Dirac equation (and quantum field theory) see [87] and/or [88]. The Dirac equation is given by

$$(i\hbar c\gamma^{\mu}\partial_{\mu} - mc^2)\psi = 0 \tag{4.1}$$

where $\partial_\mu = (\partial_0, \nabla)$, $\partial_0 = c^{-1}\partial_t$. γ^μ are 4×4 matrices called the gamma-matrices and obey the Clifford algebra

$$\{\gamma^\mu, \gamma^\nu\} = 2\eta^{\mu\nu}\mathbb{1}, \tag{4.2}$$

where $\eta^{\mu\nu}$ is the metric tensor; its off diagonal elements are zero whereas, $\eta^{00} = 1$ and $\eta^{jj} = -1$; $\mathbb{1}$ is the identity matrix. From the anticommutation relation one finds that $(\gamma^0)^2 = \mathbb{1}$ and $(\gamma^j)^2 = -\mathbb{1}$. In addition, the γ-matrices satisfy

$$(\gamma^\mu)^\dagger = \gamma^0\gamma^\mu\gamma^0. \tag{4.3}$$

The γ-matrices are not unique. It is to possible show that a similarity transformation preserves the anticommutation relation of the gamma-matrices. Let

$$\tilde{\gamma}^\mu = S\gamma^\mu S^{-1} \tag{4.4}$$

then

$$\{\tilde{\gamma}^\mu, \tilde{\gamma}^\nu\} = S\gamma^\mu S^{-1} S\gamma^\nu S^{-1} + S\gamma^\nu S^{-1} S\gamma^\mu S^{-1} = S\underbrace{\{\gamma^\mu, \gamma^\nu\}}_{2\eta^{\mu\nu}\mathbb{1}} S^{-1} = 2\eta^{\mu\nu}\mathbb{1}. \tag{4.5}$$

The similarity transformation does not change the metric tensor. According to [89] the matrix S involved in the similarity transformation should be unitary $S^{-1} \rightarrow S^\dagger$ in order to preserve the hermicity condition $(\gamma^\mu)^\dagger = \gamma^0\gamma^\mu\gamma^0$, see Eq. (4.3). Thus, to the transformation between representations is given by

$$\tilde{\gamma}^\mu = S\gamma^\mu S^\dagger. \tag{4.6}$$

This does not change the anticommutation relation and indeed it preserves hermicity

$$(\tilde{\gamma}^\mu)^\dagger = (S\gamma^\mu S^\dagger)^\dagger = S(\gamma^\mu)^\dagger S^\dagger = S\gamma^0\gamma^\mu\gamma^0 S^\dagger = S\gamma^0 S^\dagger S\gamma^\mu S^\dagger S\gamma^0 S^\dagger = \tilde{\gamma}^0\tilde{\gamma}^\mu\tilde{\gamma}^0. \tag{4.7}$$

Now comes Weyl's contribution: Weyl considered the case where $m = 0$ and noted that in odd

spatial dimensions $d = 2k + 1$ one can define a matrix

$$\gamma_5 = i^k \gamma^0 \gamma^1 \dots \gamma^d \tag{4.8}$$

where γ_5 is Hermitian and anticommutes with the gamma matrices γ^μ. I will restrict the spatial dimension to three since it is relevant for discussion on Weyl semimetals. In 3D it is easy to show that γ_5 is Hermitian and that it anticommutes with the γ_μ matrices.

$$\begin{aligned}\gamma_5^\dagger &= (i\gamma^0\gamma^1\gamma^2\gamma^3)^\dagger = -i(\gamma^3)^\dagger(\gamma^2)^\dagger(\gamma^1)^\dagger(\gamma^0)^\dagger = -i(\gamma^0\gamma^3\gamma^0)(\gamma^0\gamma^2\gamma^0)(\gamma^0\gamma^1\gamma^0)(\gamma^0\gamma^0\gamma^0) \\ &= -i\gamma^0\gamma^3\gamma^2\gamma^1 = i\gamma^0\gamma^1\gamma^2\gamma^3 = \gamma_5\end{aligned} \tag{4.9}$$

where I have made use of Eq. (4.3), $(\gamma^0)^2 = 1$ and Eq. (4.2), in that order. To prove that γ_5 anticommutes with γ_μ, I will show that γ_5 anticommutes with γ_0 and γ_j

$$\begin{aligned}\{\gamma_5, \gamma_0\} &= i\eta_{00}\{\gamma^0\gamma^1\gamma^2\gamma^3, \gamma^0\} = i(\gamma^0\gamma^1\gamma^2\gamma^3\gamma^0 + \gamma^0\gamma^0\gamma^1\gamma^2\gamma^3) \\ &= i[(-1)^3\gamma^0\gamma^0\gamma^1\gamma^2\gamma^3) + \gamma^0\gamma^0\gamma^1\gamma^2\gamma^3)] = 0,\end{aligned} \tag{4.10}$$

similarly (for $j = 1$),

$$\begin{aligned}\{\gamma_5, \gamma_1\} &= i\eta_{11}\{\gamma^0\gamma^1\gamma^2\gamma^3, \gamma^1\} = -i(\gamma^0\gamma^1\gamma^2\gamma^3\gamma^1 + \gamma^1\gamma^0\gamma^1\gamma^2\gamma^3) \\ &= -i[(-1)^2\gamma^0\gamma^1\gamma^1\gamma^2\gamma^3) + (-1)\gamma^0\gamma^1\gamma^1\gamma^2\gamma^3)] = 0.\end{aligned} \tag{4.11}$$

Using the same method above one finds that for $j = 2, 3$ γ_j anticommutes with γ_5. Below I will consider the Weyl or chiral representation of the γ-matrices but one can go to some other representation (Dirac, Majorana, etc...) by an appropriate transformation, see Eq. (4.6).

The γ-matrices in the Weyl or chiral representation is given by

$$\gamma^0 = \begin{pmatrix} 0 & \mathbb{1} \\ \mathbb{1} & 0 \end{pmatrix}, \quad \gamma^j = \begin{pmatrix} 0 & \sigma^j \\ -\sigma^j & 0 \end{pmatrix} \tag{4.12}$$

where σ^j are the usual Pauli matrices, $\sigma^{1,2,3} \rightarrow \sigma^{x,y,z}$. Note that the matrices in Eqs. (4.12) are 4×4 matrices, for example

$$\begin{pmatrix} 0 & \mathbb{1} \\ \mathbb{1} & 0 \end{pmatrix} \rightarrow \begin{pmatrix} 0 & 0 & 1 & 0 \\ 0 & 0 & 0 & 1 \\ 1 & 0 & 0 & 0 \\ 0 & 1 & 0 & 0 \end{pmatrix}. \tag{4.13}$$

The chirality operator γ_5 it is given by

$$\gamma_5 = i\gamma^0\gamma^1\gamma^2\gamma^3. \tag{4.14}$$

In the Weyl basis γ_5 is diagonal (as opposed to the Dirac basis where γ^0 is diagonal). Below γ_5 is given in the Weyl basis

$$\gamma_5 = \begin{pmatrix} -\mathbb{1} & 0 \\ 0 & \mathbb{1} \end{pmatrix}. \tag{4.15}$$

Below I will state some properties of γ_5 and then show how one decomposes a Dirac spinor into right- and left-chiral spinors:

$$\{\gamma_\mu, \gamma_5\} = 0, \quad (\gamma_5)^\dagger = \gamma_5, \quad (\gamma_5)^2 = \mathbb{1}. \tag{4.16}$$

I have shown the first two but not the last. The last property is easy to show especially if one utilizes the second-to-last property i.e.

$$(\gamma_5)^2 = \gamma_5\gamma_5 = \gamma_5\gamma_5^\dagger = (i\gamma^0\gamma^1\gamma^2\gamma^3)(-i)(\gamma^3)^\dagger(\gamma^2)^\dagger(\gamma^1)^\dagger(\gamma^0)^\dagger = \mathbb{1} \tag{4.17}$$

The last property allows one to write [86]

$$\mathbb{1} = \underbrace{\frac{1}{2}(\mathbb{1} - \gamma_5)}_{P_L} + \underbrace{\frac{1}{2}(\mathbb{1} + \gamma_5)}_{P_R}. \tag{4.18}$$

$P_{R,L}$ are the right-chiral and left-chiral projection operators, explicitly given by

$$P_L = \frac{1}{2}(\mathbb{1} - \gamma_5) = \begin{pmatrix} \mathbb{1} & 0 \\ 0 & 0 \end{pmatrix}, \quad P_R = \frac{1}{2}(\mathbb{1} + \gamma_5) = \begin{pmatrix} 0 & 0 \\ 0 & \mathbb{1} \end{pmatrix}. \tag{4.19}$$

One may write a spinor as

$$\psi = \underbrace{\frac{1}{2}(\mathbb{1} - \gamma_5)\psi}_{\psi_L} + \underbrace{\frac{1}{2}(\mathbb{1} + \gamma_5)\psi}_{\psi_R}. \tag{4.20}$$

Note that P_R and P_L are orthogonal, i.e. $P_R P_L = 0$, thus

$$P_R\psi = \psi_R, \quad \text{and} \quad P_L\psi = \psi_L \tag{4.21}$$

where $\psi_{R,L}$ are two-component spinors. The subscript $R\,, L$ denotes the right- and left-chiral components. The four-component Dirac spinor ψ is composed of two two-component spinors ψ_R and ψ_L. In the case of the massless Dirac equation $\psi_{R,L}$ are Weyl spinors. The eigenvalues of γ_5 acting on the right- and left-chiral spinors as given by Eq. (4.21) are

$$\gamma_5\psi_R = \gamma_5 P_R\psi = \gamma_5\left(\frac{\mathbb{1} + \gamma_5}{2}\right)\psi = \left(\frac{\gamma_5 + \mathbb{1}}{2}\right)\psi = P_R\psi = +\psi_R \tag{4.22}$$

$$\gamma_5\psi_L = \gamma_5 P_L\psi = \gamma_5\left(\frac{\mathbb{1} - \gamma_5}{2}\right)\psi = \left(\frac{\gamma_5 - \mathbb{1}}{2}\right)\psi = -P_L\psi = -\psi_L. \tag{4.23}$$

One can therefore distinguish between left- and right- chiral fermions by the eigenvalues of γ_5. In particular, a right-chiral fermion has eigenvalue $+1$ and a left-chiral fermion has eigenvalue -1 when the spinor is acted upon by γ_5. The eigenvalues of γ_5 are called the chirality.

For the massive Dirac equation the mass term mixes the left and right chiral fermion fields as

can be seen in the Lagrangian [88]

$$\mathcal{L} = \bar{\psi}(i\hbar c\gamma^\mu \partial_\mu - mc^2)\psi = \bar{\psi}_L i\hbar c\gamma^\mu \partial_\mu \psi_L + \bar{\psi}_R i\hbar c\gamma^\mu \partial_\mu \psi_R - mc^2(\bar{\psi}_L \psi_R + \bar{\psi}_R \psi_L). \quad (4.24)$$

However, for the massless case, which corresponds to the Weyl equation right- and left-chiral spinors are not mixed. A right-chiral fermion will maintain its chirality when acted upon by the kinetic energy term $i\hbar c\gamma^\mu \partial_\mu$, likewise a left-chiral fermion will maintain its chirality. I will show this below

$$\gamma_5 i\hbar c\gamma^\mu \partial_\mu \psi = 0, \quad (4.25)$$

using $\{\gamma^\mu, \gamma_5\} = 0$ one finds

$$\begin{aligned} &- i\hbar c\gamma^\mu \partial_\mu(\gamma_5\psi) = 0 \\ \text{or} \quad &i\hbar\gamma^0 \partial_t(\gamma_5\psi) = c\gamma^j \underbrace{(-i\hbar\partial_j)}_{p_j}(\gamma_5\psi). \end{aligned} \quad (4.26)$$

Using the Weyl representation of the gamma matrices gives

$$\begin{pmatrix} 0 & i\hbar\partial_t \\ i\hbar\partial_t & 0 \end{pmatrix} \begin{pmatrix} -\psi_L \\ +\psi_R \end{pmatrix} = \begin{pmatrix} 0 & +c\hat{\boldsymbol{\sigma}} \cdot \hat{\boldsymbol{p}} \\ -c\hat{\boldsymbol{\sigma}} \cdot \hat{\boldsymbol{p}} & 0 \end{pmatrix} \begin{pmatrix} -\psi_L \\ +\psi_R \end{pmatrix} \quad (4.27)$$

or

$$i\hbar\partial_t \psi_{R,L} = \hat{H}\psi_{R,L} \quad (4.28)$$

where

$$\hat{H} = \pm c\hat{\boldsymbol{\sigma}} \cdot \hat{\boldsymbol{p}}. \quad (4.29)$$

The top sign corresponds to ψ_R and the bottom sign corresponds to ψ_L. In the case of a Weyl semimetal, the speed of light c is replaced with the Fermi velocity v_F and the Hamiltonian is

written as

$$\hat{H} = \pm v_F \hat{\boldsymbol{\sigma}} \cdot \hat{\boldsymbol{p}}. \tag{4.30}$$

For materials with Hamiltonians similar to the one above, the low-energy excitations will be Weyl fermions which are massless and chiral.

4.2.2 Berry Phase

The Berry phase plays an important role in helping to identify the topological aspects of condensed matter physics. In the specific case of Weyl semimetals the band touching points, or Weyl nodes, are associated with a quantized Berry flux through a surface enclosing the nodes [90, 64]. It will be shown that the Weyl nodes acts as topological chiral charges (when one considers the Berry flux through a 2D surface in the Brillouin zone). To this end I will derive the Berry phase. My derivation will follow [64, 90, 91, 92].

Consider a time-dependent Hamiltonian $\hat{H}(t)$ satisfying the eigenvalue equation

$$\hat{H}(t)\psi_n(t) = E_n(t)\psi_n(t) \tag{4.31}$$

where the eigenfunctions $\psi_n(t)$ are complete and orthonormal at equal times, i.e.

$$\langle \psi_n(t) | \psi_m(t) \rangle = \delta_{nm}. \tag{4.32}$$

The general solution to the time-dependent Schrödinger equation,

$$i\hbar\partial_t \Psi(t) = \hat{H}(t)\Psi(t), \tag{4.33}$$

can be expressed as a linear combination of the eigenfunctions

$$\Psi(t) = \sum_n \bar{c}_n(t)\psi_n(t). \tag{4.34}$$

Upon inserting the wave function Eq. (4.34) into the Schrödinger equation Eq. (4.33) one obtains

$$i\hbar \sum_n (\dot{\bar{c}}_n \psi_n + \bar{c}_n \dot{\psi}_n) = \sum_n \bar{c}_n E_n \psi_n. \tag{4.35}$$

Exploiting the orthonormality of the eigenfunctions (by taking the inner product with ψ_m) results in

$$\dot{\bar{c}}_m + \sum_n \bar{c}_n \left\langle \psi_m \middle| \dot{\psi}_n \right\rangle = -\frac{i}{\hbar} \bar{c}_m E_m. \tag{4.36}$$

Let

$$\bar{c}_n(t) = c_n(t) e^{i\theta_n(t)} \tag{4.37}$$

then

$$\begin{aligned} \dot{c}_m e^{i\theta_m} + i\dot{\theta}_m c_m e^{i\theta_m} + \sum_n c_n e^{i\theta_n} \left\langle \psi_m \middle| \dot{\psi}_n \right\rangle &= -\frac{i}{\hbar} c_m e^{i\theta_m} E_m \\ \dot{c}_m + \sum_n c_n e^{i(\theta_n - \theta_m)} \left\langle \psi_m \middle| \dot{\psi}_n \right\rangle &= -\frac{i}{\hbar} (\hbar\dot{\theta}_m + E_m) c_m. \end{aligned} \tag{4.38}$$

Setting

$$\begin{aligned} \dot{\theta}_m(t) &= -\frac{1}{\hbar} E_m(t) \\ \implies \theta_m(t) &= -\frac{1}{\hbar} \int_0^t E_m(t')\, dt'. \end{aligned} \tag{4.39}$$

Thus,

$$\begin{aligned} \dot{c}_m &= -\sum_n c_n e^{i(\theta_n - \theta_m)} \left\langle \psi_m \middle| \dot{\psi}_n \right\rangle \\ \text{or} \quad \dot{c}_m &= -c_m \left\langle \psi_m \middle| \dot{\psi}_m \right\rangle - \sum_{n \neq m} c_n e^{i(\theta_n - \theta_m)} \left\langle \psi_m \middle| \dot{\psi}_n \right\rangle \end{aligned} \tag{4.40}$$

where I have explicitly separated the $n = m$ and $n \neq m$ terms in going from the first line to the second line in Eq. (4.40). In order to find an alternative expression for $\left\langle \psi_m \middle| \dot{\psi}_n \right\rangle$, one differentiates

Eq. (4.31) with respect to time

$$\dot{\hat{H}}\psi_n + \hat{H}\dot{\psi}_n = \dot{E}_n\psi_n + E_n\dot{\psi}_n. \tag{4.41}$$

Once again, making use of the orthonormality of the eigenfunctions gives

$$\langle\psi_m|\dot{\hat{H}}|\psi_n\rangle + \left\langle\psi_m\middle|\hat{H}\middle|\dot{\psi}_n\right\rangle = \dot{E}_n\delta_{nm} + E_n\left\langle\psi_m\middle|\dot{\psi}_n\right\rangle. \tag{4.42}$$

Utilizing the hermicity of $\hat{H}$ and selecting only the $n \neq m$ terms leads to

$$\left\langle\psi_m\middle|\dot{\psi}_n\right\rangle = \frac{\langle\psi_m|\dot{\hat{H}}|\psi_n\rangle}{E_n - E_m} \tag{4.43}$$

Substituting the right-hand side of Eq. (4.43) for $\left\langle\psi_m\middle|\dot{\psi}_n\right\rangle$ in Eq. (4.40) gives

$$\dot{c}_m = -c_m\left\langle\psi_m\middle|\dot{\psi}_m\right\rangle - \sum_{n\neq m} c_n\frac{\langle\psi_m|\dot{\hat{H}}|\psi_n\rangle}{E_n - E_m}e^{(-i/\hbar)\int_0^t[E_n(t')-E_m(t')]dt'}. \tag{4.44}$$

In the adiabatic approximation, one assumes that $\dot{\hat{H}}$ is sufficiently small such that one may drop the second term in Eq. (4.44). According to [91] a rigorous proof of the previous statement is not trivial, however a justification can be found in [93]. Eq. (4.44) is now

$$\dot{c}_m(t) = -c_m\left\langle\psi_m\middle|\dot{\psi}_m\right\rangle. \tag{4.45}$$

A solution can be readily obtained by direct integration

$$c_m(t) = c_m(0)\exp\left[i\left(i\int_0^t\langle\psi_m(t')|\partial_{t'}\psi_m(t')\rangle\ dt'\right)\right]. \tag{4.46}$$

Let

$$\gamma_m(t) \equiv i\int_0^t\langle\psi_m(t')|\partial_{t'}\psi_m(t')\rangle\ dt' \tag{4.47}$$

then

$$c_m(t) = c_m(0)e^{i\gamma_m(t)}. \tag{4.48}$$

Note that γ_m is real since

$$\begin{aligned} \frac{d}{dt}\underbrace{\langle\psi_m|\psi_m\rangle}_{1} &= \underbrace{\left\langle \dot{\psi_m}\middle|\psi_m\right\rangle + \left\langle \psi_m\middle|\dot{\psi_m}\right\rangle}_{2\,\mathrm{Re}[\left\langle \psi_m\middle|\dot{\psi_m}\right\rangle]} \\ \implies 0 &= 2\,\mathrm{Re}[\left\langle \psi_m\middle|\dot{\psi_m}\right\rangle], \end{aligned} \tag{4.49}$$

in other words $\left\langle \psi_m\middle|\dot{\psi_m}\right\rangle$ is imaginary (since its real part is zero) and γ_m is real since $\gamma_m \propto i\left\langle \psi_m\middle|\dot{\psi_m}\right\rangle \propto i\,\mathrm{Im}[\left\langle \psi_m\middle|\dot{\psi_m}\right\rangle]$.

Since $c_m(t)$ given in Eq. (4.48) changes by, at most, a phase under time evolution while remaining in the eigenstate m the wave function given by Eq. (4.34) becomes

$$\Psi_m(t) = e^{i\theta_m(t)}e^{i\gamma_m(t)}\psi_m(t). \tag{4.50}$$

In other words, if the particle is in an initial eigenstate m where $c_m(0) = 1$ and $c_n = 0$ for $m \neq n$, and it is then acted upon by a Hamiltonian, the particle remains in the mth eigenstate but changes by the phase factor $e^{i[\theta_m(t)+\gamma_m(t)}]$. Of course, this all happens under the assumption that adiabatic approximation holds.

Now suppose the system gains time dependence through a set of N parameters (which I will write as a vector) $\boldsymbol{R}(t) \equiv (R_1(t), R_2(t), \ldots, R_N(t))$. Assume the parameters change slowly over time so that the adiabatic approximation is valid then Eq (4.47) can be written as

$$\gamma_n(t) = i\int_0^t \langle\psi_n|\nabla_R\psi_n\rangle \cdot \frac{d\boldsymbol{R}}{dt'}dt' = i\int_{\boldsymbol{R}_i}^{\boldsymbol{R}_f} \langle\psi_n|\nabla_R\psi_n\rangle \cdot d\boldsymbol{R} \tag{4.51}$$

If the Hamiltonian returns to itself after time-evolution say from time $t = 0$ to $t = T$ then $\boldsymbol{R}(0) =$

$\boldsymbol{R}(T)$ (where I have identified $\boldsymbol{R}_i$ with $\boldsymbol{R}(0)$ and $\boldsymbol{R}_f$ with $\boldsymbol{R}(T)$) and

$$\gamma_n(T) = i \oint_{\mathcal{C}} \langle \psi_n | \nabla_R \psi_n \rangle \cdot d\boldsymbol{R}, \tag{4.52}$$

where $\mathcal{C}$ is a closed path in parameter-space. Eq (4.52) is called the Berry phase [94]. Defining a vector-valued function called the Berry connection

$$\boldsymbol{\mathcal{A}}_n(\boldsymbol{R}) = i \langle \psi_n | \nabla_R \psi_n \rangle \tag{4.53}$$

allows one to write

$$\gamma_n = \oint_{\mathcal{C}} \boldsymbol{\mathcal{A}}_n(\boldsymbol{R}) \cdot d\boldsymbol{R}. \tag{4.54}$$

$\boldsymbol{A}_n$ is a gauge-dependent quantity. To see this, make a gauge transformation of the form

$$\psi_n(\boldsymbol{R}) \to e^{i\zeta(\boldsymbol{R})} \boldsymbol{\psi}_n(\boldsymbol{R}) \tag{4.55}$$

where $\zeta(\boldsymbol{R})$ is smooth and single-valued. With this gauge transformation the Berry connection becomes

$$\boldsymbol{\mathcal{A}}_n(\boldsymbol{R}) \to \boldsymbol{\mathcal{A}}_n(\boldsymbol{R}) - \nabla_R \zeta(\boldsymbol{R}). \tag{4.56}$$

Taking the inner product of Eq. (4.55) with itself but at $\boldsymbol{R}(0)$ and $\boldsymbol{R}(T)$ gives

$$\langle \psi_n(\boldsymbol{R}(0)) | \psi_n(\boldsymbol{R}(T)) \rangle \to e^{i[\zeta(\boldsymbol{R}(T)) - \zeta(\boldsymbol{R}(0))]} \langle \psi_n(\boldsymbol{R}(0)) | \psi_n(\boldsymbol{R}(T)) \rangle . \tag{4.57}$$

For a closed path $\boldsymbol{R}(0) = \boldsymbol{R}(T)$ which leads to

$$\begin{aligned} 1 &= e^{i[\zeta(\boldsymbol{R}(T)) - \zeta(\boldsymbol{R}(0))]} \\ \implies \zeta(\boldsymbol{R}(T)) - \zeta(\boldsymbol{R}(0)) &= 2\pi N \end{aligned} \tag{4.58}$$

where N is an integer. Therefore, for a closed path, the Berry phase given by Eq. (4.54) is gauge

invariant.

Using Stokes' theorem one may recast the Berry phase equation as

$$\gamma_n = \oint_{\mathcal{C}} \boldsymbol{\mathcal{A}}_n(\boldsymbol{R}) \cdot d\boldsymbol{R} \underbrace{\longrightarrow}_{Stokes} \int_{\mathcal{S}} (\nabla_R \times \boldsymbol{\mathcal{A}}_n) \cdot d\boldsymbol{S}. \tag{4.59}$$

Eq. (4.54) looks rather familiar; it should bring to mind the flux of a magnetic field through a surface S bounded by the curve C. Continuing with the analogy, one may define

$$\boldsymbol{\mathcal{B}}_n = \nabla_R \times \boldsymbol{\mathcal{A}}_n = i\nabla_R \times \langle \psi_n | \nabla_R \psi_n \rangle \tag{4.60}$$

where $\boldsymbol{\mathcal{B}}$ is called the Berry curvature. It can be thought of as a "magnetic" field in parameter space; in the same spirit, the Berry phase can be thought of as a "magnetic flux." Note that $\mathcal{B}$ is allowed to have magnetic monopoles whereas, the actual magnetic field $\boldsymbol{B}$ does not.

I will now focus on applying the Berry phase in the context of a crystal lattice. The Berry connection is defined in momentum space and parametrized by the quasimomentum $\boldsymbol{k}$ of the lattice. The eigenfunctions are Bloch functions $u(\boldsymbol{k})$. The eigenvalue equation for such a system can be written as

$$\hat{H}(\boldsymbol{k})u(\boldsymbol{k}) = E(\boldsymbol{k})u(\boldsymbol{k}) \tag{4.61}$$

the Berry curvature Eq. (4.60) written in the context of a crystal lattice is

$$\boldsymbol{\mathcal{B}}(\boldsymbol{k}) = \nabla_{\boldsymbol{k}} \times \boldsymbol{\mathcal{A}}(\boldsymbol{k}). \tag{4.62}$$

The generic Hamiltonian for a Weyl semimetal near the Weyl node is given by Eq (4.30), I will rewrite it below in $\boldsymbol{k}$-space ($\boldsymbol{p} \to \hbar\boldsymbol{k}$) for convenience

$$\hat{H}(\boldsymbol{k}) = \pm\hbar v_F \hat{\boldsymbol{\sigma}} \cdot \boldsymbol{k}. \tag{4.63}$$

The eigenstates of the Hamiltonian for chirality $+1$ is given by the spinor [95]

$$|u_R(k,\theta,\phi)\rangle = \begin{pmatrix} \sin\frac{\theta}{2} \\ -e^{i\phi}\cos\frac{\theta}{2} \end{pmatrix} \tag{4.64}$$

where $\cos\theta \equiv k_z/k$ and $k = \sqrt{k_x^2 + k_y^2 + k_z^2}$. In order to find the Berry connection, one needs the gradient of the eigenstate given above. In spherical coordinates, one has

$$\begin{aligned} \nabla_{\boldsymbol{k}} |u_R(k,\theta,\phi)\rangle &= (\boldsymbol{e}_k\partial_k + \boldsymbol{e}_\theta k^{-1}\partial_\theta + \boldsymbol{e}_\phi(k\sin\theta)^{-1}\partial_\phi) \begin{pmatrix} \sin\frac{\theta}{2} \\ -e^{i\phi}\cos\frac{\theta}{2} \end{pmatrix} \\ &= \boldsymbol{e}_k \begin{pmatrix} 0 \\ 0 \end{pmatrix} + \boldsymbol{e}_\theta \frac{1}{k} \begin{pmatrix} \frac{1}{2}\cos\frac{\theta}{2} \\ \frac{1}{2}e^{i\phi}\sin\frac{\theta}{2} \end{pmatrix} + \boldsymbol{e}_\phi \frac{1}{k\sin\theta} \begin{pmatrix} 0 \\ -ie^{i\phi}\cos\frac{\theta}{2} \end{pmatrix} \end{aligned} \tag{4.65}$$

The Berry connection, given by $\boldsymbol{\mathcal{A}} = i\langle u_R|\nabla_k u_R\rangle$, is

$$\boldsymbol{\mathcal{A}} = (A_k, A_\theta, A_\phi) = \left(0, 0, -\frac{\cos^2\frac{\theta}{2}}{k\sin\theta}\right) \tag{4.66}$$

and the Berry curvature, $\boldsymbol{\mathcal{B}} = \nabla_k \times \boldsymbol{\mathcal{A}}$, is

$$\boldsymbol{\mathcal{B}} = \boldsymbol{e}_k(k\sin\theta)^{-1}[\partial_\theta(A_\phi\sin\theta)] - \boldsymbol{e}_\theta k^{-1}\partial_k(kA_\phi) = \frac{1}{2k^2}\boldsymbol{e}_k. \tag{4.67}$$

Choosing a spherical surface to enclose the Weyl node one finds that the Berry phase or flux is

$$\gamma = \int_0^{2\pi} d\phi \int_0^{\pi} k^2\sin\theta\frac{1}{2k^2} = 2\pi. \tag{4.68}$$

The Churn number is defined as

$$C_n = \frac{1}{2\pi}\int d^2k\boldsymbol{e}_{k_\perp}\cdot\boldsymbol{\mathcal{B}} = \frac{\gamma}{2\pi} \tag{4.69}$$

where d^2k is a Fermi surface, $\boldsymbol{e}_{k_\perp}$ is the unit vector normal to the Fermi surface and $\boldsymbol{\mathcal{B}}$ is the Berry curvature. For the case of the Weyl semimetal, the Churn number associated with the right-handed chiral spinor is

$$C_n = +1 \tag{4.70}$$

Since the flux through the Fermi surface enclosing the Weyl node is nonzero, by Gauss' law one may interpret the Weyl node as a monopole charge. Equivalently, the Churn number can be regarded as a topological charge of the Weyl node where the sign of the charge is determined by the chirality. Indeed for the case of the right-handed chiral spinor with chirality $+1$ the Churn number is $+1$ (when the Fermi surface encloses the Weyl node). Carrying out a similar analysis on the left-handed chiral state where the Hamiltonian is given by $-\hbar v_F \hat{\boldsymbol{\sigma}} \cdot \boldsymbol{k}$ with eigenspinor

$$|u_L(k,\theta,\phi)\rangle = \begin{pmatrix} \cos\frac{\theta}{2} \\ e^{i\phi}\sin\frac{\theta}{2} \end{pmatrix} \tag{4.71}$$

one finds the Berry curvature to be $\boldsymbol{\mathcal{B}} = -\boldsymbol{e}_k(1/2k)$ and the corresponding Churn number is $C_n = -1$.

In summary, when the flux of the Berry curvature through a 2D Fermi surface is nonzero then there is a point (monopole) source or sink of the Berry curvature [65]. The Churn number associated with Berry curvature defines a topological charge.

4.3 Effective Hamiltonian

This section deals with the family of Hamiltonians that serve as a microscopic basis in this study. From these Hamiltonians one can derive properties of bulk and surface electron states and use them to calculate the optical conductivity. Consider a family of Hamiltonians of the type

$$\hat{H} = v_F \left(\frac{\hat{Q}^2 - \hbar^2 m(z)}{2\hbar b}\hat{\sigma}_x + \hat{p}_y\hat{\sigma}_y + \hat{p}_z\hat{\sigma}_z \right), \tag{4.72}$$

where the function $m(z)$ takes into account that the system may be nonuniform along z and, in particular, has boundaries. Here $\hat{\sigma}_{x,y,z}$ are Pauli matrices and the operator $\hat{Q}^2$ is defined by one of the following three expressions:

$$\begin{aligned}
&(1) \quad \hat{Q}^2 = \hat{p}_x^2 \\
&(2) \quad \hat{Q}^2 = \hat{p}_x^2 + \hat{p}_y^2 \\
&(3) \quad \hat{Q}^2 = \hat{p}_x^2 + \hat{p}_y^2 + \hat{p}_z^2
\end{aligned}$$

The first option is the original Hamiltonian in [83].

The derivation of surface states can be made more convenient [83], if one applies the unitary transformation $\hat{H} \to \hat{S}^{-1}\hat{H}\hat{S}$ to Eq. (4.72), where $\hat{S} = \frac{1}{\sqrt{2}}\left(1 - i\hat{\sigma}_x\right)$. This gives

$$\hat{H} = v_F \left(\frac{\hat{Q}^2 - \hbar^2 m(z)}{2\hbar b} \hat{\sigma}_x + \hat{p}_z \hat{\sigma}_y - \hat{p}_y \hat{\sigma}_z \right). \tag{4.73}$$

One can check that this Hamiltonian violates time-reversal symmetry due to the term proportional to $\hat{\sigma}_x$. The gyrotropy axis is the x-axis. In $\boldsymbol{k}$-representation the Hamiltonian of Eq. (4.73) becomes

$$\hat{H}_{\boldsymbol{k}} = \hbar v_F \left(K_x(\boldsymbol{k}) \hat{\sigma}_x + k_z \hat{\sigma}_y - k_y \hat{\sigma}_z \right), \tag{4.74}$$

where $K_x(\boldsymbol{k})$ for the same three Hamiltonians is given by

$$\begin{aligned}
&(1) \quad K_x = \frac{k_x^2 - m}{2b} \\
&(2) \quad K_x = \frac{k_x^2 + k_y^2 - m}{2b} \\
&(3) \quad K_x = \frac{k_x^2 + k_y^2 + k_z^2 - m}{2b}.
\end{aligned}$$

In all three cases, the Weyl nodes are located at the points $(k_x, k_y, k_z) = (\pm\sqrt{m}, 0, 0)$ assuming that $m > 0$.

4.3.1 Hamiltonians 1 and 2

4.3.1.1 Bulk States

The stationary spinor eigenstate of the Hamiltonian in Eq. (4.74) is

$$|\Psi_{\boldsymbol{k}}\rangle = \begin{pmatrix} \Psi_1 \\ \Psi_2 \end{pmatrix} e^{i\boldsymbol{k}\boldsymbol{r} - i\frac{E}{\hbar}t}, \tag{4.75}$$

where the components are determined from

$$\begin{pmatrix} -k_y - \frac{E}{\hbar v_F} & K_x(\boldsymbol{k}) - ik_z \\ K_x(\boldsymbol{k}) + ik_z & k_y - \frac{E}{\hbar v_F} \end{pmatrix} \begin{pmatrix} \Psi_1 \\ \Psi_2 \end{pmatrix} = 0. \tag{4.76}$$

From Eq. (4.76) one obtains the eigenenergy of the bulk states $E(\boldsymbol{k})$

$$E = s\hbar v_F \sqrt{K_x^2 + k_y^2 + k_z^2}, \tag{4.77}$$

and corresponding components of the spinor eigenstate in Eq. (4.75):

$$\begin{pmatrix} \Psi_1 \\ \Psi_2 \end{pmatrix} = \frac{1}{\sqrt{2V}} \begin{pmatrix} \sqrt{1 - s\cos\theta_{\boldsymbol{k}}}\, e^{-i\phi_{\boldsymbol{k}}} \\ s\sqrt{1 + s\cos\theta_{\boldsymbol{k}}} \end{pmatrix}, \tag{4.78}$$

where $\cos\theta_{\boldsymbol{k}} = \frac{k_y}{\sqrt{K_x^2+k_y^2+k_z^2}}$, $e^{i\phi_{\boldsymbol{k}}} = \frac{K_x+ik_z}{\sqrt{K_x^2+k_z^2}}$; $s = \pm 1$ denotes the conduction and valence bands, and V is the quantization volume.

To visualize the dispersion of electron states, let $m = b^2$ for simplicity . The 3D plot for one projection of 3D dispersion of the Hamiltonian 2 is shown in Fig. 4.1. For small energies $|\frac{E}{\hbar v_F}| \ll b$, the constant energy surface consists of two disconnected spheres, each of them enclosing a corresponding Weyl point; see Fig. 4.2. At $|\frac{E}{\hbar v_F}| = \frac{b}{2}$ a separatrix isoenergy surface is a 3D "figure

of eight". For $|\frac{E}{\hbar v_F}| > \frac{b}{2}$ the constant energy surface is simply connected and encloses both Weyl points. Figures 4.2a and 4.2b show contours of constant energy surfaces on the plane $k_z = 0$ for the Hamiltonians 2 and 1, respectively. The electron dispersion is strongly anisotropic. This will result in different values for the diagonal elements of the bulk dielectric permittivity tensor, as in two-axial crystals. The dotted circle in Fig. 4.2a is the boundary of a region that contains surface states. For Hamiltonian 1 in Fig. 4.2b the surface states exist between the dotted lines.

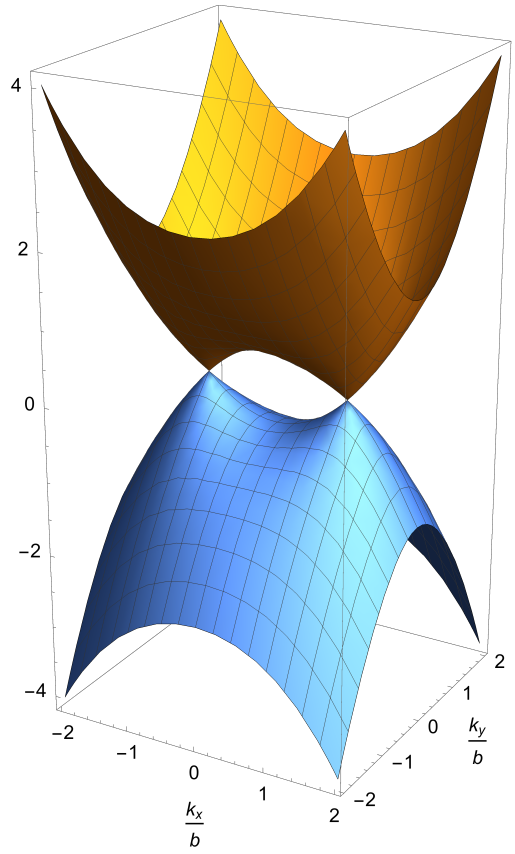

Figure 4.1: Bulk energy dispersion for Hamiltonian 2 on the surface $k_z = 0$. Here the energy is normalized by $\hbar v_F b$ and $k_{x,y}$ are normalized by b. Reprinted with permission from [59].

4.3.1.2 Reflection from the Boundary: Surface States and Fermi Arcs

Following [83], one can define the boundary as a jump in the parameter m, so that $m = b^2$ inside the WSM and $m = -m_\infty$ outside. Then Eqs. (4.74) and (4.76) will contain the parameter *m* as a function of the coordinate r_j orthogonal to the boundary, and the corresponding component of the quasimomentum k_j is replaced by $k_j \to -i\frac{\partial}{\partial r_j}$.

For the boundary parallel to the gyrotropy axis x, I will assume that it coincides with the surface $z = 0$ and the WSM fills the halfspace $z < 0$. In this case, $m = b^2$ for $z < 0$ whereas, for $z > 0$, $m = -m_\infty$ where $m_\infty \to \infty$.

For Hamiltonian 3, the Schrödinger equation given by Eq. (4.76) is a fourth-order differential equation, since its matrix elements contain ∂_z^2 . For Hamiltonians 1 and 2, one gets a second-order set of equations. The velocity operator $\hat{v}_z = (i/\hbar)\,[H, z]$ for Hamiltonian 3 is $\hat{v}_z = (-iv_F/b)\hat{\sigma}_x\partial_z + v_F\hat{\sigma}_y$, i.e. it depends on the coordinate derivative. In contrast, the velocity operator $\hat{v}_z = v_F\hat{\sigma}_y$ for Hamiltonians 1 and 2 does not depend on the coordinate derivative. Therefore for Hamiltonian 3 at $z = 0$, the continuity of both the eigenstate and its derivative are required, whereas one only needs the continuity of the eigenstates for Hamiltonians 1 and 2.

Using Eq. (4.76) one finds that the eigenstate of Hamiltonians 1 and 2 in the region $z > 0$ at $m_\infty \to \infty$ is $|\Psi_\infty\rangle \propto \begin{pmatrix} 1 \\ 0 \end{pmatrix} e^{ik_x x + ik_y y - \frac{m_\infty}{2b} z}$. In the region $z < 0$ one takes the eigenstate $|\Psi_B\rangle$ which is given by Eq. (4.78). Stitching together these two eigenstates $|\Psi_\infty\rangle$ and $|\Psi_B\rangle$ at the boundary, yields the following expression for the bulk state:

$$|\Psi_B\rangle = \frac{e^{ik_x x + ik_y y}}{2\sqrt{V}} \left[\begin{pmatrix} \sqrt{1 - s\cos\theta_{\boldsymbol{k}}}\, e^{-i\phi_{\boldsymbol{k}}} \\ s\sqrt{1 + s\cos\theta_{\boldsymbol{k}}} \end{pmatrix} e^{ik_z z} - \begin{pmatrix} \sqrt{1 - s\cos\theta_{\boldsymbol{k}}}\, e^{i\phi_{\boldsymbol{k}}} \\ s\sqrt{1 + s\cos\theta_{\boldsymbol{k}}} \end{pmatrix} e^{-ik_z z} \right], \qquad (4.79)$$

where the quantization volume is limited from one side by the $z = 0$ plane. The eigenenergy is still given by Eq. (4.77), and the angles $\theta_{\boldsymbol{k}}$ and $\phi_{\boldsymbol{k}}$ are defined below Eq. (4.78).

If $\frac{E^2}{\hbar^2 v_F^2} < k_y^2 + K_x^2$ the value of k_z in Eq. (4.77) is imaginary: $k_z = \pm i\kappa$. In order to connect the

eigenstate $|\Psi_\infty\rangle \propto \begin{pmatrix} 1 \\ 0 \end{pmatrix}$ in $z > 0$ with the eigenstate localized at $z < 0$ which is $e^{\kappa z}$, the localized eigenstate should be also a spinor $\begin{pmatrix} 1 \\ 0 \end{pmatrix}$. After replacing $k_z \to -i\kappa$ in Eq. (4.76), one obtains the following eigenenergies and eigenvectors for surface states in the limit $m_\infty \to \infty$:

$$\frac{E}{\hbar v_F} = -k_y,\ |\Psi_S\rangle = \sqrt{\frac{2\kappa}{S}} \begin{pmatrix} 1 \\ 0 \end{pmatrix} \Theta(-z) e^{\kappa z + ik_x x + ik_y y}, \tag{4.80}$$

where Θ is a step function, S is the quantization area, $\kappa = -K_x > 0$. For Hamiltonian 2 the surface states exist inside a dashed circle $b^2 > k_x^2 + k_y^2$ in Fig. 4.2a. For Hamiltonian 1 the surface states exist in the region $b^2 > k_x^2$ in Fig. 4.2b.

If a WSM occupies the region $z > 0$, instead of Eqs. (4.80) one obtains

$$\frac{E}{\hbar v_F} = +k_y,\ |\Psi_S\rangle = \sqrt{\frac{2\kappa}{S}} \begin{pmatrix} 0 \\ 1 \end{pmatrix} \Theta(z) e^{-|\kappa| z + ik_x x + ik_y y}, \tag{4.81}$$

where $\kappa = +K_x < 0$. Equations (4.80),(4.81) can be easily generalized to the case where a parameter $m(z)$ varies continuously between the values b^2 and $-m_\infty$ [83]. For example, instead of Eqs. (4.80) one gets

$$\frac{E}{\hbar v_F} = -k_y,\ |\Psi_S\rangle = N \begin{pmatrix} 1 \\ 0 \end{pmatrix} e^{ik_x x + ik_y y} \begin{cases} e^{\int_0^z \frac{m(z) - k_x^2}{2b}\, dz} & \text{for Hamiltonian 1} \\ e^{\int_0^z \frac{m(z) - k_x^2 - k_y^2}{2b}\, dz} & \text{for Hamiltonian 2} \end{cases} \tag{4.82}$$

where N is a normalization factor.

Note that the constant surface energy lines $k_y = \text{const}$ are tangent to the points where the bulk-state constant energy surface intersects the boundary of the surface states, shown as dotted lines in Fig. 4.2a and 4.2b. The union of these $k_y = \text{const}$ lines and the bulk-state constant energy surface is a set of bulk and surface energy states with the same energy. In particular, at the energy equal to

the Fermi energy E_F the $k_y = E_F/(\hbar v_F)$ line forms a Fermi arc.

4.3.2 Hamiltonian 3

For a fourth-order set of differential equations the construction of electron states including their interaction with a boundary is more complicated.

First, one uses Eq. (4.77) to find the value of k_z for given $k_{x,y}$ and E. Consider the parameter range $m \leq b^2$, including both positive and negative values of m. If $\frac{E^2}{\hbar^2 v_F^2} > k_y^2 + \frac{\left(k_x^2+k_y^2-m\right)^2}{4b^2}$, one always has two real solutions $k_{z1} = -k_{z2} > 0$ together with two imaginary solutions corresponding to evanescent states: $k_{z3,4} = i\kappa_{3,4}$, where $0 < \kappa_3 = -\kappa_4$. If $\frac{E^2}{\hbar^2 v_F^2} < k_y^2 + \frac{\left(k_x^2+k_y^2-m\right)^2}{4b^2}$, all four solutions are imaginary and correspond to evanescent states: $k_{z1,2,3,4} = i\kappa_{1,2,3,4}$, where $0 < \kappa_1 = -\kappa_3$, $0 < \kappa_2 = -\kappa_4$. In the region $z > 0$ (i.e. outside the sample, where $m = -m_\infty$) it is reasonable to take the solution as a superposition of two localized modes $e^{-|\kappa_{3,4}|z}$. In this case for $z < 0$, i.e. inside the sample where $m = b^2$, there could be two options:

(i) A superposition of two counterpropagating waves with quasimomenta $k_{z1} = -k_{z2}$ together with a localized wave $e^{\kappa_3 z}$. The localized solution cannot be discarded, since without it the number of constants becomes smaller than the number of the boundary conditions.

(ii) A superposition of two localized waves i.e. the surface state. In this option the number of constants is always smaller than the number of the boundary conditions, so such a state can exist only at certain values of energy.

The procedure of stitching the spinor components and their derivatives is simplified if $m_\infty \to \infty$ since in this limit the continuity of the derivative is equivalent to setting both components of a spinor $\Psi_{1,2}$ equal to zero in the cross section $z = 0$.

4.3.2.1 Bulk States Near the Boundary

In case (i) one obtains

$$|\Psi_B\rangle \approx \frac{e^{ik_x x+ik_y y}}{2\sqrt{V}} \times \left[\begin{pmatrix} \sqrt{1-s\cos\theta_{\boldsymbol{k}}}e^{-i\phi_{\boldsymbol{k}}} \\ s\sqrt{1+s\cos\theta_{\boldsymbol{k}}} \end{pmatrix} e^{ik_z z} + r\begin{pmatrix} \sqrt{1-s\cos\theta_{\boldsymbol{k}}}e^{i\phi_{\boldsymbol{k}}} \\ s\sqrt{1+s\cos\theta_{\boldsymbol{k}}} \end{pmatrix} e^{-ik_z z} + l\begin{pmatrix} \sqrt{1-s\cos\theta_{\boldsymbol{k}}}e^{\alpha_\kappa} \\ -s\sqrt{1+s\cos\theta_{\boldsymbol{k}}} \end{pmatrix} e^{\kappa z}\right] \tag{4.83}$$

where

$$k_z = \sqrt{2b\sqrt{\frac{E^2}{\hbar^2 v_F^2}+k_x^2} - \left(k_x^2+k_y^2+b^2\right)},\ \kappa = \sqrt{2b\sqrt{\frac{E^2}{\hbar^2 v_F^2}+k_x^2} + \left(k_x^2+k_y^2+b^2\right)},$$

$$r = -\frac{e^{\alpha_\kappa}+e^{-i\phi_{\boldsymbol{k}}}}{e^{\alpha_\kappa}+e^{i\phi_{\boldsymbol{k}}}},\ \sinh\alpha_\kappa = \frac{\kappa}{\sqrt{\frac{E^2}{\hbar^2 v_F^2}-k_y^2}},\ l = 2i\frac{\sin\phi_{\boldsymbol{k}}}{e^{\alpha_\kappa}+e^{i\phi_{\boldsymbol{k}}}}.$$

Clearly, $|r|^2 = 1$, which corresponds, as expected, to the total reflection from the boundary. The quantization volume in Eq. (4.83) is chosen in such a way that its length along the z axis is much larger than $k_z^{-1} > \kappa^{-1}$. Therefore, the last term in the brackets in Eq. (4.83) is unimportant in a sense that it does not affect the eigenstate normalization or the matrix elements.

4.3.2.2 Surface States

To construct the surface states (option (ii)) it is convenient to to go back to Eq. (4.76), use $m = b^2$, and make the substitution $k_z = -i\kappa$:

$$\begin{pmatrix} -k_y - \frac{E}{\hbar v_F} & \frac{k_x^2+k_y^2-\kappa^2-b^2}{2b} - \kappa \\ \frac{k_x^2+k_y^2-\kappa^2-b^2}{2b} + \kappa & k_y - \frac{E}{\hbar v_F} \end{pmatrix} \begin{pmatrix} \Psi_1 \\ \Psi_2 \end{pmatrix} = 0 \tag{4.84}$$

Consider the solution of Eq. (4.84), corresponding to different positive values of $\kappa_{1,2}$ but the

same spinor constant $\begin{pmatrix} a \\ b \end{pmatrix}$. One can build a nontrivial localized solution $|\Psi_S\rangle \propto \begin{pmatrix} a \\ b \end{pmatrix} \Theta(-z)\left(e^{\kappa_1 z} - e^{\kappa_2 z}\right)$, which corresponds to the null boundary conditions at the surface $z = 0$. Such a solution of Eq. (4.84) is possible under the following conditions: $-k_y - \frac{E}{\hbar v_F} = \frac{k_x^2+k_y^2-\kappa^2-b^2}{2b} + \kappa = 0$, or $k_y - \frac{E}{\hbar v_F} = \frac{k_x^2+k_y^2-\kappa^2-b^2}{2b} - \kappa = 0$, or $k_y - \frac{E}{\hbar v_F} = \frac{k_x^2+k_y^2-\kappa^2-b^2}{2b} - \kappa = 0$, where $\begin{pmatrix} a \\ b \end{pmatrix} = \begin{pmatrix} 1 \\ 0 \end{pmatrix}$ or $\begin{pmatrix} a \\ b \end{pmatrix} = \begin{pmatrix} 0 \\ 1 \end{pmatrix}$ respectively. It is easy to see that the first option corresponds to the surface state when the WSM occupies the halfspace $z < 0$, whereas the second option corresponds to the WSM in the region $z > 0$, since in this case the values of $\kappa_{1,2}$ are negative. The resulting states are as follows.

(i) WSM in $z < 0$:

$$\frac{E}{\hbar v_F} = -k_y,\ |\Psi_S\rangle = \sqrt{\frac{2}{S\left(\frac{1}{\kappa_1} + \frac{1}{\kappa_2} - \frac{4}{\kappa_1+\kappa_2}\right)}} \begin{pmatrix} 1 \\ 0 \end{pmatrix} \Theta(-z)\left(e^{\kappa_1 z} - e^{\kappa_2 z}\right) \cdot e^{ik_x x + ik_y y}; \quad (4.85)$$

(ii) WSM in $z > 0$:

$$\frac{E}{\hbar v_F} = k_y,\ |\Psi_S\rangle = \sqrt{\frac{2}{S\left(\frac{1}{\kappa_1} + \frac{1}{\kappa_2} - \frac{4}{\kappa_1+\kappa_2}\right)}} \begin{pmatrix} 1 \\ 0 \end{pmatrix} \Theta(z)\left(e^{-\kappa_1 z} - e^{-\kappa_2 z}\right) \cdot e^{ik_x x + ik_y y}. \quad (4.86)$$

Here $\kappa_{1,2} = b \mp \sqrt{k_x^2 + k_y^2}$.

In the region $b^2 < k_x^2 + k_y^2$ there is only one localized evanescent solution for any fixed value of energy, which is not enough to satisfy the boundary conditions. Therefore, the region $b^2 > k_x^2 + k_y^2$, where the surface states exist, is the same in the models described by the Hamiltonian 2 and Hamiltonian 3 (see the dotted circle in Fig. 2a).

Taking into account a finite value of m_∞ modifies the above expression, but their general struc-

ture remains the same. For example, when a WSM fills the halfspace $z < 0$, then the eigenstate in Eq. (4.85) is replaced by

$$|\Psi_{S;z<0}\rangle \propto \begin{pmatrix} 1 \\ 0 \end{pmatrix} \left(e^{\kappa_1 z} - \zeta e^{\kappa_2 z}\right) e^{ik_x x + ik_y y},$$

$$|Psi_{S;z>0}\rangle \propto \begin{pmatrix} 1 \\ 0 \end{pmatrix} \frac{\kappa_2 - \kappa_1}{\kappa_2 + \sqrt{m_\infty}} e^{-\sqrt{m_\infty} z} e^{ik_x x + ik_y y}, \tag{4.87}$$

where $\zeta = \dfrac{\kappa_1 + \sqrt{m_\infty}}{\kappa_2 + \sqrt{m_\infty}}$.

4.3.3 The Boundary Orthogonal to the Gyrotropy Axis

Any Hamiltonian, 1, 2, or 3, contains the second derivative ∂_x^2. Therefore, the analysis of the bulk and surface states near the boundary orthogonal to the gyrotropy axis is similar to the one for the boundary parallel to the gyrotropy axis when the Hamiltonian contains the second derivative ∂_z^2. Repeating the same arguments as in the previous section, one obtains that the orthogonal boundary is trivial and does not contain surface states.

4.3.4 Comparison of Hamiltonians 1, 2, and 3

The only principal difference between the eigenstates of the effective Hamiltonians considered above is the region where the surface states exist. Such a region is determined by the inequality $b > \sqrt{k_x^2 + k_y^2}$ for Hamiltonians 2 and 3, and the inequality $b > |k_x|$ for Hamiltonian 1. The latter condition leads to an infinite density of surface states, which is unphysical and would have to be restricted artificially. Therefore, it is better to work with Hamiltonian 2 or 3. Hamiltonian 2 leads to a simpler z-component of the velocity operator: $\hat{v}_z = v_F \hat{\sigma}_y$ instead of $\hat{v}_z = (-iv_F/b)\hat{\sigma}_x \partial_z + v_F \hat{\sigma}_y$, which corresponds to Hamiltonian 3. The velocity operator of Hamiltonian 2 makes calculations of the surface current easier without losing any essential physics. Therefore, Hamiltonian 2 will be used for subsequent calculations of the optical properties.

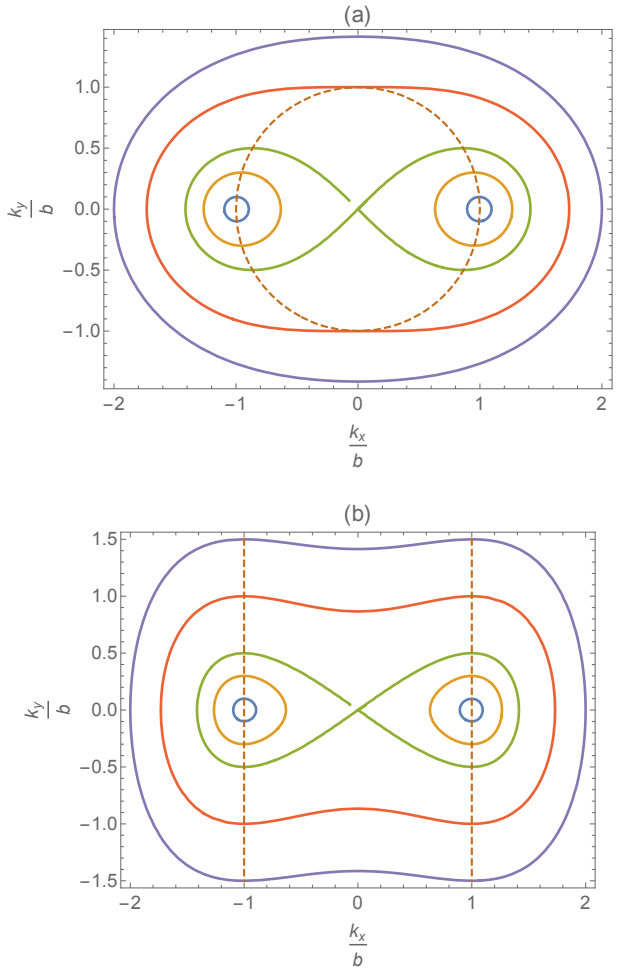

Figure 4.2: (a) Contours of constant energy surfaces for Hamiltonian 2 on the surface $k_z = 0$. The dotted circle is the boundary of a region $k_x^2 + k_y^2 \leq b^2$ where surface states exist. (b) Contours of constant energy surfaces for Hamiltonian 1 on the surface $k_z = 0$. Here $x, y = k_{x,y}/b$. The dotted lines indicate the boundary of a region $k_x^2 \leq b^2$ where surface states exist. Reprinted with permission from [59].

4.4 Optical Transitions and the Tensors of Bulk and Surface Conductivity

In the presence of external fields one should replace $\hat{\boldsymbol{p}} \to \hat{\boldsymbol{p}} - \frac{e}{c}\boldsymbol{A}$, and also add the electrostatic potential $\hat{H} \to \hat{H} + e\varphi\mathbb{1}$ in Eq. (4.73). Particles are assumed to have charge e where $-e$ is the magnitude of the electron charge. If the potential has a coordinate dependence $\boldsymbol{A}(\boldsymbol{r})$ one assumes symmetrized operators

$$\left(\hat{p}_{x,y,z} - \frac{e}{c}A_{x,y,z}\right)^2 \to \hat{p}^2_{x,y,z} + \frac{e^2}{c^2}A^2_{x,y,z} - \frac{e}{c}\left(\hat{p}_{x,y,z}A_{x,y,z} + A_{x,y,z}\hat{p}_{x,y,z}\right),$$

and in the expressions for the velocity operator one needs to replace

$$-i\partial_{x,y,z} \to -i\partial_{x,y,z} - \frac{e}{c\hbar}A_{x,y,z}.$$

Throughout this work, I will consider the potentials corresponding to a monochromatic electromagnetic field propagating in the arbitrary direction $\boldsymbol{r}$ with angular frequency ω and wavevector $\boldsymbol{q}$, i.e.

$$\phi = \frac{1}{2}\phi(\omega)e^{-i\omega t + i\boldsymbol{q}\cdot\boldsymbol{r}} + c.c., \tag{4.88}$$

$$\boldsymbol{A} = \frac{1}{2}[\boldsymbol{e}_x A_x(\omega) + \boldsymbol{e}_y A_y(\omega) + \boldsymbol{e}_z A_z(\omega)]e^{-i\omega t + i\boldsymbol{q}\cdot\boldsymbol{r}} + c.c. \tag{4.89}$$

Bulk-to-bulk and surface-to-surface transitions contribute to the bulk and surface conductivity tensors, respectively. Surface-to-bulk transitions contribute to the surface conductivity tensor only. They have to be handled with more care, as briefly described below.

Generally, the electron and current densities expressed in terms of the density matrix are given by

$$n(\boldsymbol{r}) = \sum_{\alpha\beta} n_{\beta\alpha}(\boldsymbol{r})\rho_{\alpha\beta},\ \boldsymbol{j}(\boldsymbol{r}) = \sum_{\alpha\beta}\boldsymbol{j}_{\beta\alpha}(\boldsymbol{r})\rho_{\alpha\beta}, \tag{4.90}$$

$$n_{\beta\alpha} = \Psi^*_\beta\Psi_\alpha,\ \boldsymbol{j}_{\beta\alpha} = \frac{1}{2}\left[\Psi^*_\beta\left(\hat{\boldsymbol{j}}\Psi_\alpha\right) + \left(\hat{\boldsymbol{j}}^*\Psi^*_\beta\right)\Psi_\alpha\right], \tag{4.91}$$

where $\hat{\boldsymbol{j}} = e\hat{\boldsymbol{v}}$.

The Fourier harmonics of the the electron and current densities are

$$\boldsymbol{j}(\boldsymbol{r}) = \frac{1}{2}\sum_{\boldsymbol{q}} \boldsymbol{j}^{(\boldsymbol{q})} e^{i\boldsymbol{q}\boldsymbol{r}} + c.c.,\ n(\boldsymbol{r}) = \frac{1}{2}\sum_{\boldsymbol{q}} n^{(\boldsymbol{q})} e^{i\boldsymbol{q}\boldsymbol{r}} + c.c.,$$

where

$$\frac{1}{2}\boldsymbol{j}^{(\boldsymbol{q})} = \frac{1}{V}\int_V \boldsymbol{j}(\boldsymbol{r}) e^{-i\boldsymbol{q}\boldsymbol{r}} d^3r,\ \frac{1}{2}n^{(\boldsymbol{q})} = \frac{1}{V}\int_V n^{(\boldsymbol{q})} e^{-i\boldsymbol{q}\boldsymbol{r}} d^3r.$$

For their matrix elements one has

$$\boldsymbol{j}^{(\boldsymbol{q})} = \sum_{\alpha\beta} \boldsymbol{j}^{(\boldsymbol{q})}_{\beta\alpha}\rho_{\alpha\beta}, \quad n^{(\boldsymbol{q})} = \sum_{\alpha\beta} n^{(\boldsymbol{q})}_{\beta\alpha}\rho_{\alpha\beta}, \tag{4.92}$$

where

$$\boldsymbol{j}^{(\boldsymbol{q})}_{\beta\alpha} = 2\left\langle\beta|e^{-i\boldsymbol{q}\boldsymbol{r}}\hat{\boldsymbol{j}}|\alpha\right\rangle, \quad n^{(\boldsymbol{q})}_{\beta\alpha} = 2\left\langle\beta|e^{-i\boldsymbol{q}\boldsymbol{r}}|\alpha\right\rangle \tag{4.93}$$

To find the current without the effect of a boundary one can use the states given by Eq. (4.78).

Now consider the states near the surface. Let the bulk states be denoted by Latin indices and surface states by Greek ones. For convenience I will rewrite them, having in mind an upper boundary $z = 0$ with the WSM located at $z < 0$:

$$|\Psi_m\rangle = \frac{e^{ik_x x + ik_y y}}{2\sqrt{V}}\left[\begin{pmatrix}\sqrt{1+s\cos\theta_{\boldsymbol{k}_\parallel}}e^{-i\theta_{\boldsymbol{k}_\perp}}\\ s\sqrt{1-s\cos\theta_{\boldsymbol{k}_\parallel}}\end{pmatrix}e^{ik_z z} - \begin{pmatrix}\sqrt{1-s\cos\theta_{\boldsymbol{k}_\parallel}}e^{i\theta_{\boldsymbol{k}_\perp}}\\ s\sqrt{1+s\cos\theta_{\boldsymbol{k}_\parallel}}\end{pmatrix}e^{-ik_z z}\right], \tag{4.94}$$

where $E_m = s\hbar v_F\sqrt{\left(\frac{k_x^2+k_y^2-b^2}{2b}\right)^2 + k_y^2 + k_z^2}$ is the eigenenergy, $s = \pm 1$ is the band index, the values $k_{x,y}$ can be of either sign whereas $k_z > 0$; $\cos\theta_{\boldsymbol{k}_\parallel} = \dfrac{k_z}{|E|/(\hbar v_F)}$.

$$|\Psi_\alpha\rangle = \sqrt{\frac{2\kappa}{S}}\begin{pmatrix}1\\0\end{pmatrix}\Theta(-z)e^{ik_x x + ik_y y + \kappa z}, \tag{4.95}$$

where S is the area; the energy of the state is $E_\alpha = -\hbar v_F k_y$, $\kappa = \dfrac{b^2 - k_x^2 - k_y^2}{2b}$, $\sqrt{k_x^2 + k_y^2} < b$.

Let us limit the surface states by the condition $\kappa > \kappa_{min}$, where the latter could be a typical scattering length $\sim \kappa_{min}^{-1}$. It is assumed that κ_{min}^{-1} is much smaller than L, which enters the quantization volume $V = SL$ in Eq. (4.94). The matrix elements of the interaction Hamiltonian in the von Neumann equation, the matrix elements $V_{mn}^{(int)}$,$V_{\alpha\beta}^{(int)}$ and $V_{m\alpha}^{(int)}$ have no peculiarities: the integration is carried out over the whole volume. However, when calculating the matrix elements of the density and current, and if at least one of the indices belongs to the surface state, one should perform the integration over dz as:

$$n_{\beta\alpha} = \int_{-\infty}^{0} \Psi_\beta^* \Psi_\alpha dz, \quad n_{m\alpha} = \int_{-\infty}^{0} \Psi_m^* \Psi_\alpha dz, \tag{4.96}$$

$$\boldsymbol{j}_{\beta\alpha} = \frac{1}{2}\int_{-\infty}^{0} \left[\Psi_\beta^* \left(\hat{\boldsymbol{j}}\Psi_\alpha\right) + \left(\hat{\boldsymbol{j}}^*\Psi_\beta^*\right)\Psi_\alpha\right] dz, \; \boldsymbol{j}_{m\alpha} = \frac{1}{2}\int_{-\infty}^{0} \left[\Psi_m^* \left(\hat{\boldsymbol{j}}\Psi_\alpha\right) + \left(\hat{\boldsymbol{j}}^*\Psi_m^*\right)\Psi_\alpha\right] dz. \tag{4.97}$$

These quantities will depend only on x and y, and therefore determine the surface current and density.

The following current component is nontrivial: $\sum_{\alpha\beta}(j_z)_{\beta\alpha}\rho_{\alpha\beta} + \sum_{m\alpha}(j_z)_{m\alpha}\rho_{\alpha m}$. It determines the polarization of a thin double layer:

$$\partial_t p_z(x,y) = \sum_{\alpha\beta}(j_z)_{\beta\alpha}\rho_{\alpha\beta} + \sum_{m\alpha}(j_z)_{m\alpha}\rho_{\alpha m}, \tag{4.98}$$

This layer radiates, but not normally to the layer, and it cannot affect the surface density of carriers.

With properly defined matrix elements of the current and density, the continuity equation is satisfied automatically, so one can consider the volume current flowing toward the boundary $\left(\sum_{mn}(j_z)_{nm}\rho_{mn}\right)_{z=0}$ as a source in the surface continuity equation.

4.4.1 Evaluation of Tensors of the Bulk and Surface Conductivity

The matrix elements of the Fourier components of the current density operator are evaluated below. After evaluating them, one uses the Kubo-Greenwood formula to calculate the bulk and

surface conductivity tensors, respectively; e.g.

$$\sigma_{\alpha\beta}(\omega) = g\frac{i\hbar}{V}\sum_{mn}\left(\frac{f_n - f_m}{E_m - E_n}\right)\frac{\langle n|\hat{j}_\alpha|m\rangle\ \langle m|\hat{j}_\beta|n\rangle}{\hbar(\omega + i\gamma) + (E_n - E_m)}, \tag{4.99}$$

for the bulk conductivity, where $g = 2$ is the spin degeneracy factor and α, β denote Cartesian coordinate components. The surface conductivity tensor has a similar structure, but the contribution is summed over surface-to-surface and surface-to-bulk transitions, and the normalization is over the surface area S instead of a volume V. Both interband and intraband transitions are included. Three-dimensional integrals over electron momenta that arise in the Kubo-Greenwood formula cannot be evaluated analytically, except in the limiting cases of small frequencies or small b. As such, integrals were calculated numerically (at zero temperature) for all plots below.

4.4.1.1 The Matrix Elements of the Current Density Operator

Recall that everywhere the bulk states are denoted by Latin letters, and the surface states by Greek letters, i.e. $|n\rangle = |B\rangle$, $|\mu\rangle = |S\rangle$. This section deals with the evaluation of the matrix elements of the current density operator that enter Eq. (4.99) for the components of bulk and surface conductivity tensors. The current density operator is calculated by using

$$\hat{\boldsymbol{j}} = e\hat{\boldsymbol{v}} \tag{4.100}$$

$$\hat{\boldsymbol{v}} = \frac{d\hat{\boldsymbol{r}}}{dt} = -\frac{i}{\hbar}[\hat{\boldsymbol{r}}, \hat{H}] \tag{4.101}$$

$$
\begin{aligned}
(j_x)_{nm} =& \langle n|\hat{j}_x|m\rangle \\
=& \frac{ev_F}{\hbar b}\int d^3r \Psi^{B\dagger}_{\boldsymbol{k}_n,s_n}(\boldsymbol{r})\left(-i\hbar\partial_x\right)\hat{\sigma}_x\Psi^{B}_{\boldsymbol{k}_m,s_m}(\boldsymbol{r}) \\
=& \frac{ev_F}{2b}k_{nx}\delta_{\boldsymbol{k}_n,\boldsymbol{k}_m} \\
\times& \left[s_m\sqrt{\left(1+s_m\cos\theta_{\boldsymbol{k}_n}\right)\left(1-s_n\cos\theta_{\boldsymbol{k}_n}\right)}e^{i\phi_{\boldsymbol{k}_n}} + s_n\sqrt{\left(1+s_n\cos\theta_{\boldsymbol{k}_n}\right)\left(1-s_m\cos\theta_{\boldsymbol{k}_n}\right)}e^{-i\phi_{\boldsymbol{k}_n}}\right]
\end{aligned}
\tag{4.102}
$$

$$
(j_x)_{\mu\nu} = \langle\mu|\hat{j}_x|\nu\rangle = \frac{ev_F}{\hbar b}\int d^3r \Psi^{S\dagger}_{\boldsymbol{k}_\mu}(\boldsymbol{r})\left(-i\hbar\partial_x\right)\hat{\sigma}_x\Psi^{S}_{\boldsymbol{k}_\nu}(\boldsymbol{r}) = 0, \tag{4.103}
$$

$$
\begin{aligned}
(j_x)_{\mu m} =& \langle\mu|\hat{j}_x|m\rangle = \frac{ev_F}{\hbar b}\int d^3r \Psi^{S\dagger}_{\boldsymbol{k}_\mu}(\boldsymbol{r})\left(-i\hbar\partial_x\right)\hat{\sigma}_x\Psi^{B}_{\boldsymbol{k}_m,s_m}(\boldsymbol{r}) \\
=& \frac{2ev_F s_m k_{mx}k_{mz}}{ib(\kappa_m^2+k_{mz}^2)}\sqrt{\frac{\kappa_m\left(1+s_m\cos\theta_{\boldsymbol{k}_m}\right)}{L_z}}\delta_{k_{mx},k_{\mu x}}\delta_{k_{my},k_{\mu y}}
\end{aligned}
\tag{4.104}
$$

$$
\begin{aligned}
(j_y)_{nm} =& \frac{ev_F}{\hbar b}\int d^3r \Psi^{B\dagger}_{\boldsymbol{k}_n,s_n}(\boldsymbol{r})\left[(-i\hbar\partial_y)\hat{\sigma}_x - \hbar b\hat{\sigma}_z\right]\Psi^{B}_{\boldsymbol{k}_m,s_m}(\boldsymbol{r}) \\
=& \frac{ev_F}{2b}k_{ny}\delta_{\boldsymbol{k}_n,\boldsymbol{k}_m} \\
\times& \left[s_m\sqrt{\left(1+s_m\cos\theta_{\boldsymbol{k}_n}\right)\left(1-s_n\cos\theta_{\boldsymbol{k}_n}\right)}e^{i\phi_{\boldsymbol{k}_n}} + s_n\sqrt{\left(1+s_n\cos\theta_{\boldsymbol{k}_n}\right)\left(1-s_m\cos\theta_{\boldsymbol{k}_n}\right)}e^{-i\phi_{\boldsymbol{k}_n}}\right] \\
+& \frac{ev_F}{2}\delta_{\boldsymbol{k}_n,\boldsymbol{k}_m}\left[s_n s_m\sqrt{\left(1+s_n\cos\theta_{\boldsymbol{k}_n}\right)\left(1+s_m\cos\theta_{\boldsymbol{k}_n}\right)} - \sqrt{\left(1-s_n\cos\theta_{\boldsymbol{k}_n}\right)\left(1-s_m\cos\theta_{\boldsymbol{k}_n}\right)}\right]
\end{aligned}
\tag{4.105}
$$

$$
(j_y)_{\mu\nu} = \frac{ev_F}{\hbar b}\int d^3r \Psi^{S\dagger}_{\boldsymbol{k}_\mu}(\boldsymbol{r})\left[(-i\hbar\partial_y)\hat{\sigma}_x - \hbar b\hat{\sigma}_z\right]\Psi^{S}_{\boldsymbol{k}_\nu}(\boldsymbol{r}) = -ev_F\delta_{k_{\mu x},k_{\nu x}}\delta_{k_{\mu y},k_{\nu y}} \tag{4.106}
$$

$$(j_y)_{\mu m} = \frac{ev_F}{\hbar b}\int d^3r \Psi^{S\dagger}_{\boldsymbol{k}_\mu}(\boldsymbol{r})\left[(-i\hbar\partial_y)\hat{\sigma}_x - \hbar b\hat{\sigma}_z\right]\Psi^{B}_{\boldsymbol{k}_m,s_m}(\boldsymbol{r})$$
$$= \frac{2ev_F s_m k_{my}k_{mz}}{ib(\kappa_m^2+k_{mz}^2)}\sqrt{\frac{\kappa_m\left(1+s_m\cos\theta_{\boldsymbol{k}_m}\right)}{L_z}}\delta_{k_{mx},k_{\mu x}}\delta_{k_{my},k_{\mu y}}; \tag{4.107}$$

$$(j_z)_{nm} = ev_F\int d^3r \Psi^{B\dagger}_{\boldsymbol{k}_n,s_n}(\boldsymbol{r})\hat{\sigma}_y\Psi^{B}_{\boldsymbol{k}_m,s_m}(\boldsymbol{r}) = i\frac{ev_F}{2}\delta_{\boldsymbol{k}_n,\boldsymbol{k}_m}$$
$$\times\left[s_n\sqrt{\left(1+s_n\cos\theta_{\boldsymbol{k}_n}\right)\left(1-s_m\cos\theta_{\boldsymbol{k}_n}\right)}e^{-i\phi_{\boldsymbol{k}_n}} - s_m\sqrt{\left(1+s_m\cos\theta_{\boldsymbol{k}_n}\right)\left(1-s_n\cos\theta_{\boldsymbol{k}_n}\right)}e^{i\phi_{\boldsymbol{k}_n}}\right] \tag{4.108}$$

$$(j_z)_{\mu\nu} = ev_F\int d^3r \Psi^{S\dagger}_{\boldsymbol{k}_\mu}(\boldsymbol{r})\hat{\sigma}_y\Psi^{S}_{\boldsymbol{k}_\nu}(\boldsymbol{r}) = 0, \tag{4.109}$$

$$(j_z)_{\mu m} = ev_F\int d^3r \Psi^{S\dagger}_{\boldsymbol{k}_\mu}(\boldsymbol{r})\hat{\sigma}_y\Psi^{B}_{\boldsymbol{k}_m,s_m}(\boldsymbol{r})$$
$$= -\frac{2ev_F s_m k_{mz}}{\kappa_m^2+k_{mz}^2}\sqrt{\frac{\kappa_m\left(1+s_m\cos\theta_{\boldsymbol{k}_m}\right)}{L_z}}\delta_{k_{mx},k_{\mu x}}\delta_{k_{my},k_{\mu y}}, \tag{4.110}$$

where $\kappa = \frac{b^2-\left(k_x^2+k_y^2\right)}{2b}$ was used.

4.4.1.2 The Bulk Optical Conductivity Tensor

The 3D integrals over electron momenta cannot be evaluated analytically in most cases, even in the zero temperature limit. Whenever the integrals remain in the final expression, they were evaluated numerically for the plots.

(i) Contribution of Intraband Transitions ($s=+1 \to s=+1$)

In this case the matrix elements $\boldsymbol{j}_{nm}^{(\boldsymbol{q})}$ of the current density operator reduce to

$$(j_x)_{nn} = ev_F s_n \frac{k_{nx}}{b} \left|\sin\theta_{\boldsymbol{k}_n}\right| \cos\phi_{\boldsymbol{k}_n}, \tag{4.111}$$

$$(j_y)_{nn} = ev_F s_n \left(\frac{k_{ny}}{b} \left|\sin\theta_{\boldsymbol{k}_n}\right| \cos\phi_{\boldsymbol{k}_n} + \cos\theta_{\boldsymbol{k}_n}\right), \tag{4.112}$$

$$(j_z)_{nn} = ev_F s_n \left|\sin\theta_{\boldsymbol{k}_n}\right| \sin\phi_{\boldsymbol{k}_n}. \tag{4.113}$$

Therefore, from the Kubo formula one obtains for the conductivity

$$\begin{aligned}
\sigma_{xx}^{intra}(\omega) &= g\frac{i\hbar}{V}\sum_{mn}\left(\frac{f_n - f_m}{E_m - E_n}\right)\frac{\left|\langle n|\hat{j}_x|m\rangle\right|^2}{\hbar(\omega+i\gamma)+(E_n-E_m)} \\
&= \frac{ige^2v_F^2}{b^2(\omega+i\gamma)}\frac{1}{V}\sum_n\left(-\frac{\partial f_n}{\partial E_n}\right)k_{nx}^2\sin^2\theta_{\boldsymbol{k}_n}\cos^2\phi_{\boldsymbol{k}_n} \\
&= \frac{ige^2v_F^2}{b^2(\omega+i\gamma)}\int_\infty\frac{d^3k}{(2\pi)^3}\delta(E_B-E_F)k_x^2\sin^2\theta_{\boldsymbol{k}}\cos^2\phi_{\boldsymbol{k}} \\
&= \frac{ige^2v_F}{4\pi^3b^2k_F\hbar(\omega+i\gamma)}\int_{-\infty}^{\infty}dk_x\int_{-\infty}^{\infty}dk_y\frac{k_x^2K_x^2\Theta\left(k_F-\sqrt{K_x^2+k_y^2}\right)}{\sqrt{k_F^2-\left(K_x^2+k_y^2\right)}}
\end{aligned} \tag{4.114}$$

Here $\Theta(k)$ is the step function and $\cos\theta_{\boldsymbol{k}} = \dfrac{k_y}{\sqrt{K_x^2+k_y^2+k_z^2}}$, $e^{i\phi_{\boldsymbol{k}}} = \dfrac{K_x+ik_z}{\sqrt{K_x^2+k_z^2}}$, $K_x \equiv \dfrac{\left(k_x^2+k_y^2\right)-b^2}{2b}$, and $k_F \equiv [E_F/(\hbar v_F)]$ were used.

Similarly,

$$\sigma_{yy}^{intra}(\omega) = \frac{ige^2v_F}{4\pi^3b^2k_F\hbar(\omega+i\gamma)}\int_{-\infty}^{\infty}dk_x\int_{-\infty}^{\infty}dk_y\frac{k_y^2\left(K_x+b\right)^2\Theta\left(k_F-\sqrt{K_x^2+k_y^2}\right)}{\sqrt{k_F^2-\left(K_x^2+k_y^2\right)}} \tag{4.115}$$

$$\sigma_{zz}^{intra}(\omega)=\frac{ige^2v_F}{4\pi^3k_F\hbar(\omega+i\gamma)}\int_{-\infty}^{\infty}dk_x\int_{-\infty}^{\infty}dk_y\Theta\left(k_F-\sqrt{K_x^2+k_y^2}\right)\sqrt{k_F^2-\left(K_x^2+k_y^2\right)} \tag{4.116}$$

$$\sigma_{xy}^{intra}(\omega)=\sigma_{xz}^{intra}(\omega)=\sigma_{yz}^{intra}(\omega)=0. \tag{4.117}$$

(ii) Contribution of Interband Transitions ($s\rightarrow -s$)

In this case, i.e. $s_m=-s_n=\pm 1$, $n\neq m$, the matrix elements $\boldsymbol{j}_{nm}^{(q)}$ of the current density operator reduce to

$$(j_x)_{nm}=ev_Fs_n\delta_{\boldsymbol{k}_n,\boldsymbol{k}_m}\frac{k_{nx}}{b}\left(s_n\cos\theta_{\boldsymbol{k}_n}\cos\phi_{\boldsymbol{k}_n}-i\sin\phi_{\boldsymbol{k}_n}\right), \tag{4.118}$$

$$(j_y)_{nm}=ev_Fs_n\delta_{\boldsymbol{k}_n,\boldsymbol{k}_m}\left[\frac{k_{ny}}{b}\left(s_n\cos\theta_{\boldsymbol{k}_n}\cos\phi_{\boldsymbol{k}_n}-i\sin\phi_{\boldsymbol{k}_n}\right)-s_n\left|\sin\theta_{\boldsymbol{k}_n}\right|\right], \tag{4.119}$$

$$(j_z)_{nm}=ev_Fs_n\delta_{\boldsymbol{k}_n,\boldsymbol{k}_m}\left(i\cos\phi_{\boldsymbol{k}_n}+s_n\cos\theta_{\boldsymbol{k}_n}\sin\phi_{\boldsymbol{k}_n}\right), \tag{4.120}$$

where $n\neq m$. Therefore, one obtains

$$
\begin{aligned}
\sigma_{xx}^{inter}(\omega) &= g\frac{i\hbar}{V}\sum_{s=\pm1}\sum_{mn}\left(\frac{f_{n,-s}-f_{m,s}}{E_{m,s}-E_{n,-s}}\right)\frac{\left|\left\langle -s,n|\hat{j}_x|s,m\right\rangle\right|^2}{\hbar(\omega+i\gamma)+(E_{n,-s}-E_{m,s})} \\
&= i\hbar g\sum_{s=\pm1}\int_{\infty}\frac{d^3k}{(2\pi)^3}\left(\frac{f_{\boldsymbol{k},-s}-f_{\boldsymbol{k},s}}{E_{\boldsymbol{k},s}-E_{\boldsymbol{k},-s}}\right)\frac{e^2v_F^2k_x^2\left(\cos^2\theta_{\boldsymbol{k}}\cos^2\phi_{\boldsymbol{k}}+\sin^2\phi_{\boldsymbol{k}}\right)}{b^2\left[\hbar(\omega+i\gamma)+(E_{\boldsymbol{k},-s}-E_{\boldsymbol{k},s})\right]} \\
&= \frac{ige^2\left(\omega+i\gamma\right)}{8\pi^3b^2\hbar v_F}\int_{-\infty}^{\infty}dk_x\int_{-\infty}^{\infty}dk_y\left[\Theta\left(k_F-\sqrt{K_x^2+k_y^2}\right)\right. \\
&\times 2k_x^2\left(\frac{K_x^2\sqrt{k_F^2-K_x^2-k_y^2}}{k_F\left(\frac{\omega+i\gamma}{v_F}\right)^2\left(K_x^2+k_y^2\right)}+\frac{\left[\left(\frac{\omega+i\gamma}{v_F}\right)^2-4K_x^2\right]\arctan\left[\frac{\left(\frac{\omega+i\gamma}{v_F}\right)\sqrt{k_F^2-K_x^2-k_y^2}}{k_F\sqrt{4\left(K_x^2+k_y^2\right)-\left(\frac{\omega+i\gamma}{v_F}\right)^2}}\right]}{\left(\frac{\omega+i\gamma}{v_F}\right)^3\sqrt{4\left(K_x^2+k_y^2\right)-\left(\frac{\omega+i\gamma}{v_F}\right)^2}}\right) \\
&-\Theta\left(K-\sqrt{K_x^2+k_y^2}\right) \\
&\left.\times 2k_x^2\left(\frac{K_x^2\sqrt{K^2-K_x^2-k_y^2}}{K\left(\frac{\omega+i\gamma}{v_F}\right)^2\left(K_x^2+k_y^2\right)}+\frac{\left[\left(\frac{\omega+i\gamma}{v_F}\right)^2-4K_x^2\right]\arctan\left[\frac{\left(\frac{\omega+i\gamma}{v_F}\right)\sqrt{K^2-K_x^2-k_y^2}}{K\sqrt{4\left(K_x^2+k_y^2\right)-\left(\frac{\omega+i\gamma}{v_F}\right)^2}}\right]}{\left(\frac{\omega+i\gamma}{v_F}\right)^3\sqrt{4\left(K_x^2+k_y^2\right)-\left(\frac{\omega+i\gamma}{v_F}\right)^2}}\right)\right]
\end{aligned}
\tag{4.121}
$$

where $K_x \equiv \dfrac{\left(k_x^2+k_y^2\right)-b^2}{2b} = -\kappa$, $\cos\theta_{\boldsymbol{k}}\left(-k_x\right) = \cos\theta_{\boldsymbol{k}}\left(k_x\right)$, $\sin\theta_{\boldsymbol{k}}\left(-k_x\right) = \sin\theta_{\boldsymbol{k}}\left(k_x\right)$, $\cos\phi_{\boldsymbol{k}}\left(-k_x\right) = \cos\phi_{\boldsymbol{k}}\left(k_x\right)$, and $\sin\phi_{\boldsymbol{k}}\left(-k_x\right) = \sin\phi_{\boldsymbol{k}}\left(k_x\right)$ were used.

Similarly,

$$\sigma_{yy}^{inter}(\omega)=\frac{ige^2(\omega+i\gamma)}{4\pi^3b^2\hbar v_F}\int_{-\infty}^{\infty}dk_x\int_{-\infty}^{\infty}dk_y\Bigg[\Theta\big(k_F-\sqrt{K_x^2+k_y^2}\big)\times$$
$$\Bigg(\frac{(b+K_x)^2k_y^2\sqrt{k_F^2-K_x^2-k_y^2}}{k_F\left(\frac{\omega+i\gamma}{v_F}\right)^2\left(K_x^2+k_y^2\right)}$$
$$+\frac{\left[\left(\frac{\omega+i\gamma}{v_F}\right)^2\left(b^2+k_y^2\right)-4\left(b+K_x\right)^2k_y^2\right]\arctan\left[\frac{\left(\frac{\omega+i\gamma}{v_F}\right)\sqrt{k_F^2-K_x^2-k_y^2}}{k_F\sqrt{4\left(K_x^2+k_y^2\right)-\left(\frac{\omega+i\gamma}{v_F}\right)^2}}\right]}{\left(\frac{\omega+i\gamma}{v_F}\right)^3\sqrt{4\left(K_x^2+k_y^2\right)-\left(\frac{\omega+i\gamma}{v_F}\right)^2}}\Bigg)$$
$$-\Theta\left(K-\sqrt{K_x^2+k_y^2}\right)\Bigg(\frac{\left(b+K_x\right)^2k_y^2\sqrt{K^2-K_x^2-k_y^2}}{K\left(\frac{\omega+i\gamma}{v_F}\right)^2\left(K_x^2+k_y^2\right)}$$
$$+\frac{\left[\left(\frac{\omega+i\gamma}{v_F}\right)^2\left(b^2+k_y^2\right)-4\left(b+K_x\right)^2k_y^2\right]\arctan\left[\frac{\left(\frac{\omega+i\gamma}{v_F}\right)\sqrt{K^2-K_x^2-k_y^2}}{K\sqrt{4\left(K_x^2+k_y^2\right)-\left(\frac{\omega+i\gamma}{v_F}\right)^2}}\right]}{\left(\frac{\omega+i\gamma}{v_F}\right)^3\sqrt{4\left(K_x^2+k_y^2\right)-\left(\frac{\omega+i\gamma}{v_F}\right)^2}}\Bigg)\Bigg] \tag{4.122}$$

$$\sigma_{zz}^{inter}(\omega)=\frac{ige^2(\omega+i\gamma)}{8\pi^3\hbar v_F}\int_{-\infty}^{\infty}dk_x\int_{-\infty}^{\infty}dk_y\left(K_x^2+k_y^2\right)\Bigg[\Theta\left(K-\sqrt{K_x^2+k_y^2}\right)$$
$$\times\left(\frac{2\sqrt{K^2-K_x^2-k_y^2}}{K\left(\frac{\omega+i\gamma}{v_F}\right)^2\left(K_x^2+k_y^2\right)}-\frac{8\left[\left(\frac{\omega+i\gamma}{v_F}\right)^2-4K_x^2\right]\arctan\left[\frac{\left(\frac{\omega+i\gamma}{v_F}\right)\sqrt{K^2-K_x^2-k_y^2}}{K\sqrt{4\left(K_x^2+k_y^2\right)-\left(\frac{\omega+i\gamma}{v_F}\right)^2}}\right]}{\left(\frac{\omega+i\gamma}{v_F}\right)^3\sqrt{4\left(K_x^2+k_y^2\right)-\left(\frac{\omega+i\gamma}{v_F}\right)^2}}\right)$$
$$-\Theta\left(k_F-\sqrt{K_x^2+k_y^2}\right)$$
$$\times\left(\frac{2\sqrt{k_F^2-K_x^2-k_y^2}}{k_F\left(\frac{\omega+i\gamma}{v_F}\right)^2\left(K_x^2+k_y^2\right)}-\frac{8\left[\left(\frac{\omega+i\gamma}{v_F}\right)^2-4K_x^2\right]\arctan\left[\frac{\left(\frac{\omega+i\gamma}{v_F}\right)\sqrt{k_F^2-K_x^2-k_y^2}}{k_F\sqrt{4\left(K_x^2+k_y^2\right)-\left(\frac{\omega+i\gamma}{v_F}\right)^2}}\right]}{\left(\frac{\omega+i\gamma}{v_F}\right)^3\sqrt{4\left(K_x^2+k_y^2\right)-\left(\frac{\omega+i\gamma}{v_F}\right)^2}}\right)\Bigg]. \tag{4.123}$$

The only nonzero off-diagonal element is $\sigma_{zy}^{inter}(\omega) = -\sigma_{yz}^{inter}(\omega)$:

$$\sigma_{yz}^{inter}(\omega) = \frac{-ge^2}{4\pi^3 b\hbar}\int_{-\infty}^{\infty} dk_x \int_{-\infty}^{\infty} dk_y \left(k_y^2 - bK_x\right)$$
$$\times \left(\Theta\left(k_F - \sqrt{K_x^2 + k_y^2}\right) \frac{2\arctan\left[\frac{\left(\frac{\omega+i\gamma}{v_F}\right)\sqrt{k_F^2 - K_x^2 - k_y^2}}{k_F\sqrt{4\left(K_x^2+k_y^2\right) - \left(\frac{\omega+i\gamma}{v_F}\right)^2}}\right]}{\left(\frac{\omega+i\gamma}{v_F}\right)\sqrt{4\left(K_x^2+k_y^2\right) - \left(\frac{\omega+i\gamma}{v_F}\right)^2}} \right.$$
$$\left. -\Theta\left(K - \sqrt{K_x^2 + k_y^2}\right) \frac{2\arctan\left[\frac{\left(\frac{\omega+i\gamma}{v_F}\right)\sqrt{K^2 - K_x^2 - k_y^2}}{K\sqrt{4\left(K_x^2+k_y^2\right) - \left(\frac{\omega+i\gamma}{v_F}\right)^2}}\right]}{\left(\frac{\omega+i\gamma}{v_F}\right)\sqrt{4\left(K_x^2+k_y^2\right) - \left(\frac{\omega+i\gamma}{v_F}\right)^2}} \right) \tag{4.124}$$

Here, a cutoff at $k = K$ in the integration over electron momenta was introduced in order to regularize the divergent integral $\int \frac{d^3k}{(2\pi)^3}$ which comes from $\frac{1}{V}\sum_n \to \int \frac{d^3k}{(2\pi)^3}$. The divergence is an artifact of the effective Hamiltonian Eq. (4.72) which has a "bottomless" valence band with electrons occupying all states to $k \to \infty$. The regularization makes the valence band bounded from below. The cutoff is chosen at the momentum corresponding to the energy of 2 eV, i.e. much higher than the range of interest to us near the Weyl nodes. In the numerical examples in the paper the value of half-separation between Weyl nodes $\hbar v_F b$ is chosen to be 100 meV. It was verified that an exact value of the cutoff has a negligible effect on the low-energy optical response below 350 meV, as long as K is large enough.

4.4.1.3 The Surface Conductivity Tensor

(i) Surface-to-Surface States Intraband Transitions

$$\sigma_{yy}^{intra}(\omega) = g\frac{i\hbar}{S}\sum_{\mu\nu}\left(\frac{f_\mu - f_\nu}{E_\nu - E_\mu}\right)\frac{\left|\langle\mu|\hat{j}_y|\nu\rangle\right|^2}{\hbar(\omega+i\gamma)+(E_\mu - E_\nu)}$$
$$= \frac{ig\hbar e^2 v_F^2}{S}\sum_{\mu}\left(-\frac{\partial f_\mu}{\partial E_\mu}\right)\frac{1}{\hbar(\omega+i\gamma)} = \Theta(b-k_F)\frac{ige^2 v_F\sqrt{b^2-k_F^2}}{2\pi^2\hbar(\omega+i\gamma)}. \tag{4.125}$$

All other tensor components are equal to zero.

(ii) Surface-to-Bulk States Transitions

$$\sigma_{xx}^{inter}(\omega) = g\frac{i\hbar}{S}\sum_{s=\pm1}\sum_{m\mu}\left(\frac{f_\mu - f_{m,s}}{E_{m,s}-E_\mu}\right)\frac{\left|\langle\mu|\hat{j}_x|m,s\rangle\right|^2}{\hbar(\omega+i\gamma)+(E_\mu - E_{m,s})}$$
$$= \frac{i4ge^2v_F^2\hbar}{b^2}\sum_{s=\pm1}\int_\infty\frac{d^3k}{(2\pi)^3}\Theta\left[b^2-\left(k_x^2+k_y^2\right)\right]\Theta(k_z)$$
$$\times\left(\frac{f_{\boldsymbol{k}}^S - f_{\boldsymbol{k}(s)}}{E_{\boldsymbol{k}(s)}-E_{\boldsymbol{k}}^S}\right)\frac{k_x^2k_z^2\kappa(1+s\cos\theta_{\boldsymbol{k}})}{(\kappa^2+k_z^2)^2\left[\hbar(\omega+i\gamma)+(E_{\boldsymbol{k}}^S-E_{\boldsymbol{k}(s)})\right]}$$
$$= \frac{ige^2}{h}\int_0^\infty dk_z\int_{-\infty}^\infty dk_x\int_{-\infty}^\infty dk_y\Theta\left[b^2-\left(k_x^2+k_y^2\right)\right]\frac{k_z^2k_x^2K_x}{\pi^2(K_x^2+k_z^2)^2b^2}$$
$$\times\left[\frac{\Theta\left(k_F-\sqrt{K_x^2+k_y^2+k_z^2}\right)-\Theta(k_F+k_y)}{\sqrt{K_x^2+k_y^2+k_z^2}\left[(\frac{\omega+i\gamma}{v_F}-k_y)-\sqrt{K_x^2+k_y^2+k_z^2}\right]}\right.$$
$$\left.-\frac{\Theta(-k_F-k_y)}{\sqrt{K_x^2+k_y^2+k_z^2}\left[(\frac{\omega+i\gamma}{v_F}-k_y)+\sqrt{K_x^2+k_y^2+k_z^2}\right]}\right] \tag{4.126}$$

Similarly,

$$\sigma_{yy}^{inter}(\omega) = \frac{ige^2}{h}\int_0^\infty dk_z\int_{-\infty}^\infty dk_x\int_{-\infty}^\infty dk_y\Theta\left[b^2-\left(k_x^2+k_y^2\right)\right]\frac{k_z^2k_y^2K_x}{\pi^2(K_x^2+k_z^2)^2b^2}$$
$$\times\left[\frac{\Theta\left(k_F-\sqrt{K_x^2+k_y^2+k_z^2}\right)-\Theta(k_F+k_y)}{\sqrt{K_x^2+k_y^2+k_z^2}\left[(\frac{\omega+i\gamma}{v_F}-k_y)-\sqrt{K_x^2+k_y^2+k_z^2}\right]}\right.$$
$$\left.-\frac{\Theta(-k_F-k_y)}{\sqrt{K_x^2+k_y^2+k_z^2}\left[(\frac{\omega+i\gamma}{v_F}-k_y)+\sqrt{K_x^2+k_y^2+k_z^2}\right]}\right] \tag{4.127}$$

$$\sigma_{zz}^{inter}(\omega)=\frac{ige^2}{h}\int_0^\infty dk_z\int_{-\infty}^\infty dk_x\int_{-\infty}^\infty dk_y\Theta\left[b^2-\left(k_x^2+k_y^2\right)\right]\frac{k_z^2K_x}{\pi^2(K_x^2+k_z^2)^2}$$
$$\times\left[\frac{\Theta\left(k_F-\sqrt{K_x^2+k_y^2+k_z^2}\right)-\Theta\left(k_F+k_y\right)}{\sqrt{K_x^2+k_y^2+k_z^2}\left[\left(\frac{\omega+i\gamma}{v_F}-k_y\right)-\sqrt{K_x^2+k_y^2+k_z^2}\right]}\right.$$
$$\left.-\frac{\Theta\left(-k_F-k_y\right)}{\sqrt{K_x^2+k_y^2+k_z^2}\left[\left(\frac{\omega+i\gamma}{v_F}-k_y\right)+\sqrt{K_x^2+k_y^2+k_z^2}\right]}\right]. \tag{4.128}$$

The only nonzero off-diagonal element is

$$\sigma_{yz}^{inter}(\omega)=\frac{-ge^2}{h}\int_0^\infty dk_z\int_{-\infty}^\infty dk_x\int_{-\infty}^\infty dk_y\Theta\left[b^2-\left(k_x^2+k_y^2\right)\right]\frac{k_z^2k_yK_x}{\pi^2(K_x^2+k_z^2)^2b}$$
$$\times\left[\frac{\Theta\left(k_F-\sqrt{K_x^2+k_y^2+k_z^2}\right)-\Theta\left(k_F+k_y\right)}{\sqrt{K_x^2+k_y^2+k_z^2}\left[\left(\frac{\omega+i\gamma}{v_F}-k_y\right)-\sqrt{K_x^2+k_y^2+k_z^2}\right]}\right.$$
$$\left.-\frac{\Theta\left(-k_F-k_y\right)}{\sqrt{K_x^2+k_y^2+k_z^2}\left[\left(\frac{\omega+i\gamma}{v_F}-k_y\right)+\sqrt{K_x^2+k_y^2+k_z^2}\right]}\right]. \tag{4.129}$$

In Eqs. (4.126)-(4.129) the integral over k_z can be carried out analytically in terms of elementary functions. Such expressions are very lengthy and will not be addressed here. The remaining integration was carried out numerically. All integrals are finite, i.e. no cutoff is necessary.

4.4.1.4 Drude-like Low-Frequency Limit

In the limit when the frequency and the Fermi energy are much smaller than $\hbar v_F b$, only the electron momenta close to the corresponding Weyl point $k_x=\pm b$ matter. Therefore, one can introduce $\delta k_x=k_x-b$ for electron states near one Weyl point and replace the degeneracy factor by $2\times g$ to account for the contribution from the second Weyl point. In this case, $K_x\sim\dfrac{(k_x-b)(k_x+b)}{2b}\approx\delta k_x$, $k_x=b+\delta k_x$ and all diagonal intraband components have the same Drude form:

$$\sigma_{xx}^{intra}(\omega)=\sigma_{yy}^{intra}(\omega)=\sigma_{zz}^{intra}(\omega)=\frac{ge^2v_Fk_F^2}{3\pi^2\hbar(-i\omega+\gamma)}. \tag{4.130}$$

All off-diagonal conductivity elements are zero in this limit.

4.4.1.5 Small b Expansion

In the limit $b \ll 1$, one can expand the conductivity in powers of b to the leading order: $b \ll 1$, $\frac{1}{b} \gg 1$, $K_x = \dfrac{\left(k_x^2 + k_y^2\right) - b^2}{2b} \sim \dfrac{\left(k_x^2 + k_y^2\right)}{2b} \sim \dfrac{\left(k_x^2 + k_y^2 + k_z^2\right)}{2b} \gg k_{x,y,z}, \dfrac{\omega}{v_F}$ for $k_{x,y,z} \neq 0$. Then one obtains

$$\sigma_{yz}^{B}(\omega) \approx \frac{-ge^2}{3\sqrt{2}\pi^2\hbar} \frac{b^{3/2}}{k_F^{1/2}} \tag{4.131}$$

$$\sigma_{xx}^{B}(\omega) \approx \frac{ge^2 k_F^2 v_F}{3\pi^2\hbar(-i\omega+\gamma)} + \frac{2\sqrt{2}ge^2(-i\omega+\gamma)}{45\pi^2\hbar v_F} \frac{b^{3/2}}{k_F^{3/2}} \tag{4.132}$$

$$\sigma_{yy}^{B}(\omega) \approx \frac{ge^2 k_F^2 v_F}{3\pi^2\hbar(-i\omega+\gamma)} + \frac{7\sqrt{2}ge^2(-i\omega+\gamma)}{360\pi^2\hbar v_F} \frac{b^{3/2}}{k_F^{3/2}} \tag{4.133}$$

$$\sigma_{zz}^{B}(\omega) \approx \frac{ge^2 k_F^2 v_F}{3\pi^2\hbar(-i\omega+\gamma)} + \frac{ge^2(-i\omega+\gamma)}{6\sqrt{2}\pi^2\hbar v_F} \frac{b^{3/2}}{k_F^{3/2}} \tag{4.134}$$

$$\sigma_{xx}^{S}(\omega) = \sigma_{yy}^{S}(\omega) = \sigma_{zz}^{S}(\omega) \approx \frac{ge^2 v_F}{2\sqrt{2k_F}\pi^3\hbar(-i\omega+\gamma)} b^{\frac{3}{2}}. \tag{4.135}$$

All off-diagonal surface terms are zero.

4.4.2 Discussion of the Conductivities

The bulk (3D) conductivity tensor due to low-energy electrons near Weyl points is

$$\sigma_{ij}^{B}(\omega)=\begin{pmatrix}\sigma_{xx}^{B} & 0 & 0\\ 0 & \sigma_{yy}^{B} & \sigma_{yz}^{B}\\ 0 & \sigma_{zy}^{B} & \sigma_{zz}^{B}\end{pmatrix} \tag{4.136}$$

where $\sigma_{zy}^{B}=-\sigma_{yz}^{B}$. The surface conductivity tensor at $z=0$ has a similar structure, with superscript B replaced by S and $\sigma_{zy}^{S}=-\sigma_{yz}^{S}$.

The background bulk dielectric tensor in the most general form which corresponds to the one for a two-axial nongyrotropic crystal is

$$\varepsilon_{ij}^{(0)}(\omega)=\begin{pmatrix}\varepsilon_{xx}^{(0)} & 0 & 0\\ 0 & \varepsilon_{yy}^{(0)} & 0\\ 0 & 0 & \varepsilon_{zz}^{(0)}\end{pmatrix} \tag{4.137}$$

so that the total dielectric permittivity tensor is

$$\varepsilon_{ij}(\omega)=\varepsilon_{ij}^{(0)}(\omega)+i\frac{4\pi\sigma_{ij}^{B}(\omega)}{\omega}=\begin{pmatrix}\varepsilon_{xx} & 0 & 0\\ 0 & \varepsilon_{yy} & ig\\ 0 & -ig & \varepsilon_{zz}\end{pmatrix} \tag{4.138}$$

where

$$g=\frac{4\pi\sigma_{yz}^{B}}{\omega}. \tag{4.139}$$

Note that for Hamiltonian 3 one would have $\sigma_{yy}^{B}=\sigma_{zz}^{B}$, whereas for Hamiltonian 2 (used in all calculations of the conductivity tensors in this paper) one has $\sigma_{yy}^{B}\neq\sigma_{zz}^{B}$. Therefore, even if the background dielectric tensor is isotropic, the contribution of massless Weyl electrons will create a two-axial anisotropy. In the numerical plots below I will consider an isotropic background dielectric tensor and neglect its frequency dependence at low frequencies, $\varepsilon_{xx}^{(0)}=\varepsilon_{yy}^{(0)}=\varepsilon_{zz}^{(0)}=10$,

so that all nontrivial effects of anisotropy and gyrotropy are due to Weyl fermions.

The salient feature of both bulk and surface conductivity tensor is the presence of nonzero off-diagonal (gyrotropic) components due to time-reversal symmetry breaking in the Hamiltonian. These terms originate from the finite separation of the Weyl nodes in momentum space and the existence of surface states (Fermi arcs). The gyrotropic effects in the propagation, reflection, and transmission of bulk and surface modes can serve as a definitive diagnostic of Weyl nodes, surface states, and Fermi surface. They could also find applications in optoelectronic devices such as Faraday isolators, modulators etc.

Figures 4.3-4.6 show spectra of $\varepsilon_{xx}(\omega)$, $\varepsilon_{yy}(\omega)$, $\varepsilon_{zz}(\omega)$, and $g(\omega)$ for several values of the Fermi momentum k_F (at zero temperature), when the Weyl node separation $2\hbar v_F b = 200$ meV. The characteristic feature in all plots is strong absorption and dispersion at the onset of interband transitions, when $\omega = 2v_F k_F$. Another common feature is a Drude-like increase in the absolute value of all tensor components at low frequencies. Indeed, as shown in Sec. 4.4.1.4, in the limit $\omega \ll v_F k_F \ll v_F b$ when only the intraband transitions in the vicinity of each Weyl point are important, the off-diagonal components are equal to zero and the diagonal conductivity components are reduced to the same Drude form:

$$\sigma_{xx}^{intra}(\omega) = \sigma_{yy}^{intra}(\omega) = \sigma_{zz}^{intra}(\omega) = \frac{ge^2 v_F k_F^2}{3\pi^2\hbar(-i\omega+\gamma)}. \tag{4.140}$$

Note an absorption peak at $\omega = 100$ meV at low Fermi momenta, which corresponds to a Van Hove singularity at the interband transitions between saddle points of conduction and valence bands at $k = 0$, i.e. in the middle between the Weyl points.

Note also that diagonal and off-diagonal parts of the conductivity tensor are of the same order at low frequencies comparable to the Weyl node separation, which indicates that gyrotropic effects should be quite prominent.

All figures in this paper are plotted for a relatively high dephasing rate $\gamma = 10$ meV, which smoothes out all spectral features and introduces strong losses for electromagnetic eigenmodes

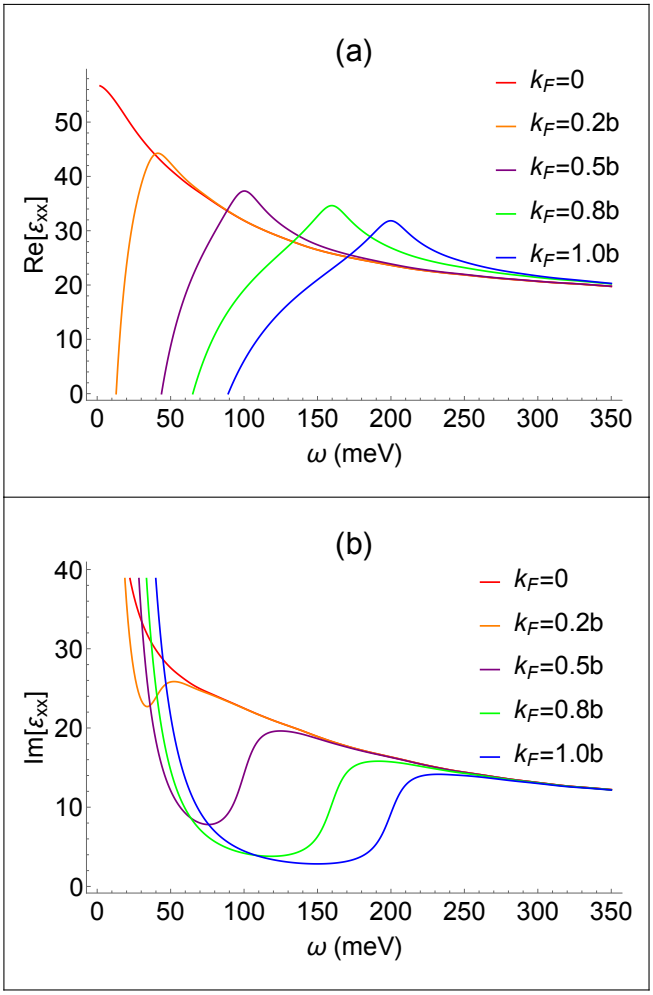

Figure 4.3: Real and imaginary parts of the ε_{xx} component of the dielectric tensor as a function of frequency for $\hbar v_F b = 100$ meV, dephasing rate $\gamma = 10$ meV, and $\varepsilon_{xx}^{(0)} = 10$. Reprinted with permission from [59].

even below the interband transition edge. The dephasing rate originates from electron scattering and obviously depends on the temperature and material quality in realistic materials. Its derivation is beyond the scope of the present paper.

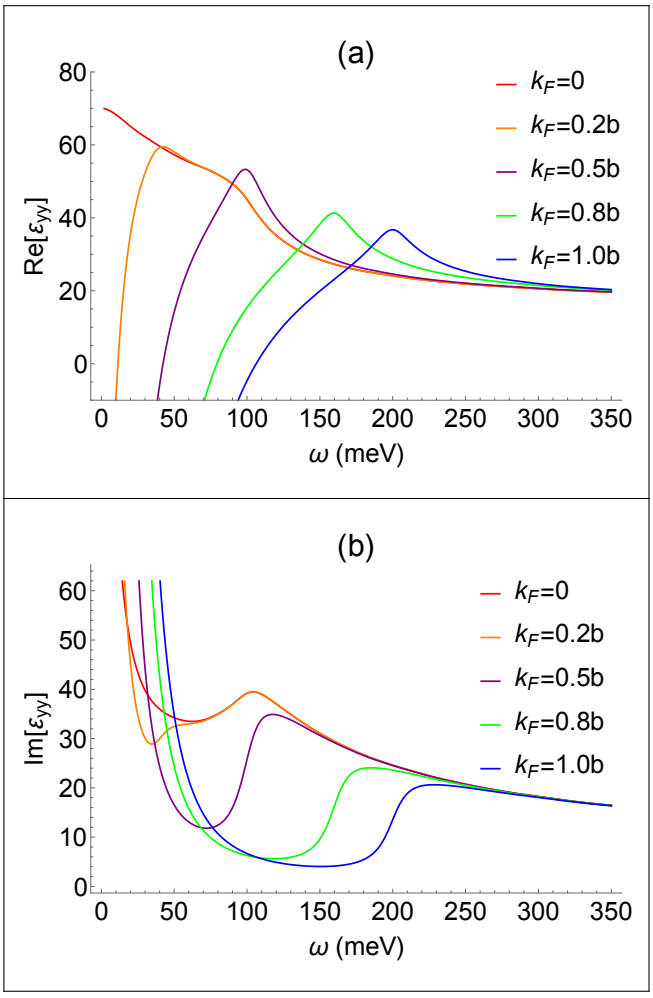

Figure 4.4: Real and imaginary parts of the ε_{yy} component of the dielectric tensor as a function of frequency for $\hbar v_F b = 100$ meV, dephasing rate $\gamma = 10$ meV, and $\varepsilon_{yy}^{(0)} = 10$. Reprinted with permission from [59].

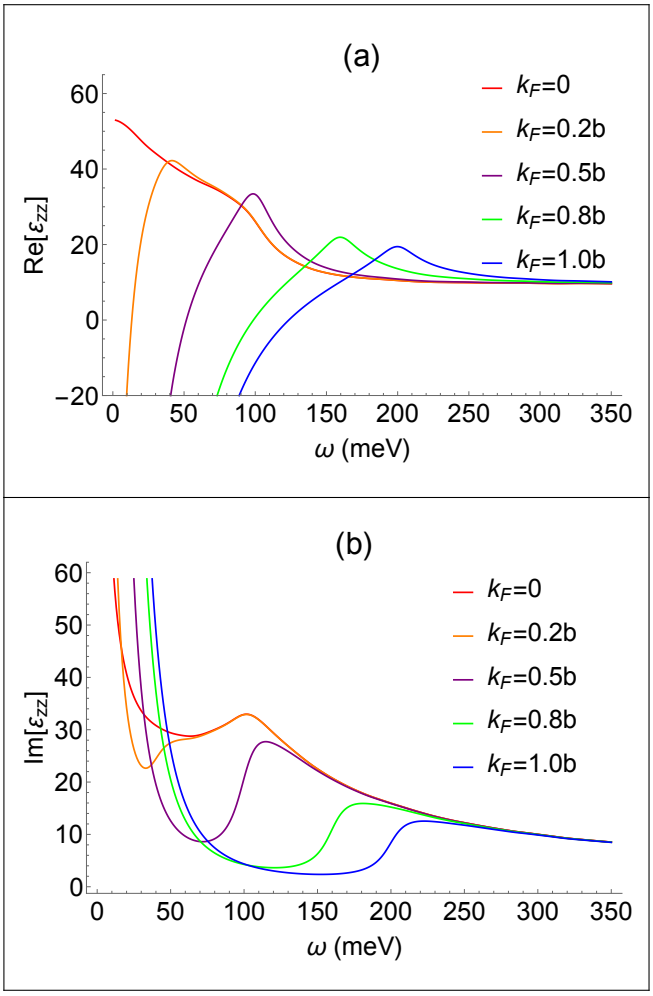

Figure 4.5: Real and imaginary parts of the ε_{zz} component of the dielectric tensor as a function of frequency for $\hbar v_F b = 100$ meV, dephasing rate $\gamma = 10$ meV, and $\varepsilon_{zz}^{(0)} = 10$. Reprinted with permission from [59].

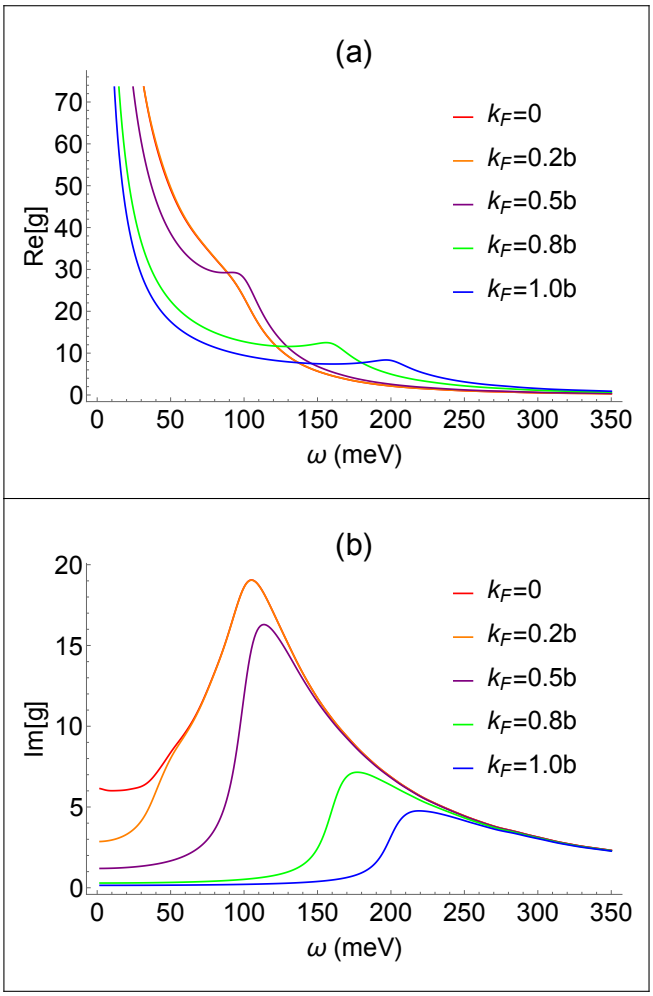

Figure 4.6: Real and imaginary parts of $g = \frac{4\pi\sigma^B_{yz}}{\omega}$ as a function of frequency for $\hbar v_F b = 100$ meV and dephasing rate $\gamma = 10$ meV.

4.5 Bulk Polaritons in Weyl Semimetals

Consider first the propagation of plane monochromatic waves in a bulk Weyl semimetal. For complex amplitudes of the electric and induction fields, $(\boldsymbol{D}, \boldsymbol{E})e^{i\boldsymbol{kr}-i\omega t}$, where $\boldsymbol{D} = \hat{\varepsilon}\boldsymbol{E}$ and $\hat{\varepsilon}$ is a bulk dielectric tensor, Maxwell's equations give $\boldsymbol{n} \cdot \boldsymbol{D} = 0$, where $\boldsymbol{n} = c\boldsymbol{k}/\omega$. The resulting dispersion equations are

$$(n_i n_j - n^2\delta_{ij} + \varepsilon_{ij})E_j = 0, \tag{4.141}$$

or

$$\begin{pmatrix} \varepsilon_{xx} - n^2 + n_x^2 & n_x n_y & n_x n_z \\ n_y n_x & \varepsilon_{yy} - n^2 + n_y^2 & ig + n_y n_z \\ n_z n_x & -ig + n_z n_y & \varepsilon_{zz} - n^2 + n_z^2 \end{pmatrix} \begin{pmatrix} E_x \\ E_y \\ E_z \end{pmatrix} = 0; \tag{4.142}$$

$n^2 = n_x^2 + n_y^2 + n_z^2$. The structure of these equations indicate strongly anisotropic and gyrotropic properties of bulk polaritons. The dispersion is drastically different for normal modes propagating perpendicular to the x-axis and to the y-axis. For each direction, there are furthermore two normal modes with different refractive indices. Each case will be considered separately.

4.5.1 Propagation Perpendicular to the Anisotropy Axis

The anisotropy axis is the x axis. For propagation perpendicular to the x axis one has $n_x = 0$, $n^2 = n_y^2 + n_z^2$, $n_z = n\cos\theta$, $n_y = n\sin\theta$, where θ is the angle between the wave vector and z-axis. From Eqs. (4.142) one obtains two normal modes that can be called an ordinary (O) and extraordinary (X) wave. An O-wave has an electric field along x and the refractive index

$$n_O^2 = \varepsilon_{xx}. \tag{4.143}$$

Therefore, its dispersion and absorption are completely described by the spectrum of $\varepsilon_{xx}(\omega)$. As shown in Fig. 4.7, at low frequencies the O-mode experiences strong metallic absorption and at $\omega = 2E_F = 160$ meV there is an onset of interband transitions.

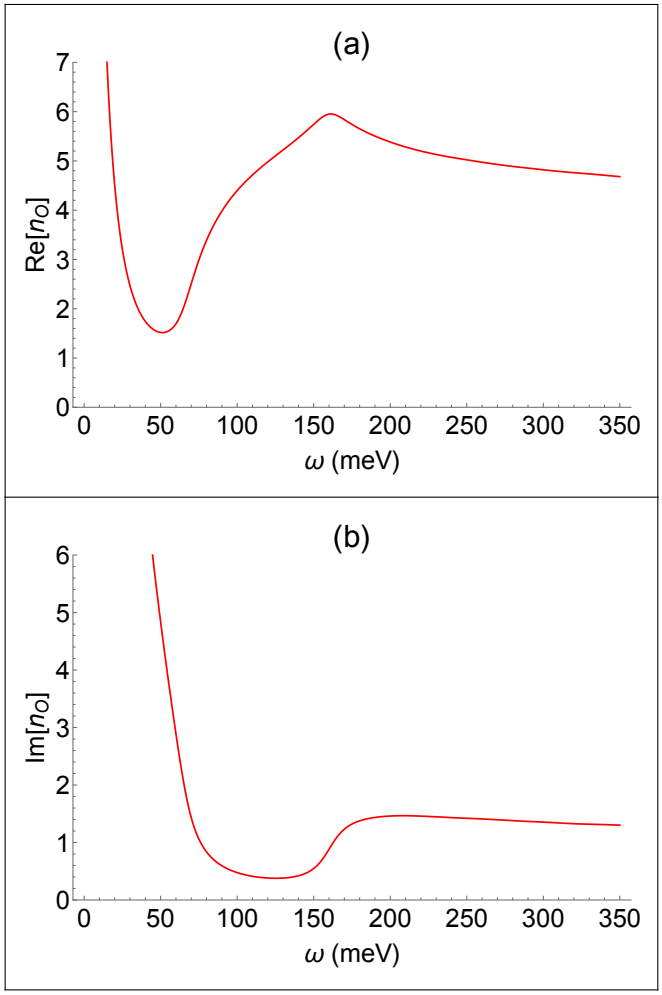

Figure 4.7: Real and imaginary parts of the refractive index n_O of an O-wave as a function of frequency for $E_F = 80$ meV, $\hbar v_F b = 100$ meV, and dephasing rate $\gamma = 10$ meV. Reprinted with permission from [59].

An X-wave have an electric field in the (y, z) plane and the refractive index showing strong θ-dependence and resonances:

$$n_X^2 = \frac{\varepsilon_{yy}\varepsilon_{zz} - g^2}{\cos^2\theta\varepsilon_{zz} + \sin^2\theta\varepsilon_{yy}}. \tag{4.144}$$

For normal incidence $\theta = 0$,

$$n_X^2 = \varepsilon_{yy} - \frac{g^2}{\varepsilon_{zz}}. \tag{4.145}$$

It is obvious from Eq. (4.144) that the refractive index for an X-wave is strongly enhanced (i.e. singular in the absence of losses) when

$$\cos^2\theta\varepsilon_{zz} + \sin^2\theta\varepsilon_{yy} = 0 \tag{4.146}$$

which corresponds to the bulk plasmon excitation. Indeed, from Maxwell's equations in the Coulomb gauge one can show that $|\frac{1}{c}\frac{\partial A}{\partial t}|/|\nabla\varphi| \sim |\frac{\omega^2}{\omega^2 - c^2k^2}||\frac{j_\perp}{j_\parallel}|$, where $\boldsymbol{j} = \boldsymbol{j}_\perp + \boldsymbol{j}_\parallel$, $\nabla \times \boldsymbol{j}_\parallel = 0$, $\nabla \cdot \boldsymbol{j}_\perp = 0$. Therefore, if $|\boldsymbol{j}_\perp| \sim |\boldsymbol{j}_\parallel|$, which corresponds to a general oblique propagation in an anisotropic medium, the wave is quasi-electrostatic at $n^2 \gg 1$. Eq. (4.146) corresponds to the condition $\boldsymbol{n} \cdot \boldsymbol{D} = 0$ for $\boldsymbol{E} = -\nabla\varphi \parallel \boldsymbol{n}$. If $\varepsilon_{yy} = \varepsilon_{zz} = \varepsilon_\perp$ the dispersion equation for a plasmon propagating in the plane orthogonal to the x-axis has a simple form $\varepsilon_\perp = 0$.

Figure 4.8 shows the real and imaginary parts of the refractive index n_X of an X-wave as a function of frequency for different values of the propagation angle θ. Near the bulk plasmon resonance, i.e. around 100 meV for normal incidence, the value of n_X^2 becomes negative in the absence of losses according to Eq. (4.145). This corresponds to a non-propagating photonic gap. Since significant loss rate $\gamma = 10$ meV is included in all simulations, the real part of n_X does not go all the way to zero, but there is a strong absorption peak in the imaginary part of n_X. It will be shown later that this spectral region leads to a telltale change of phase in reflection. The second feature in all plots is an onset of interband transitions at $2E_F = 160$ meV.

The real part of the bulk plasmon resonance frequency at normal incidence as a function of the Fermi energy is shown in Fig. 4.9. Note that according to Eq. (4.145) the magnitude of the refractive index at frequencies around plasmon resonance is determined by the value of the off-diagonal component of the dielectric tensor g. Therefore, measurements of the transmission and reflection provide a sensitive measure of the Weyl node separation.

The same is true about the polarization effects. From the third row of Eqs. (4.142) one can get

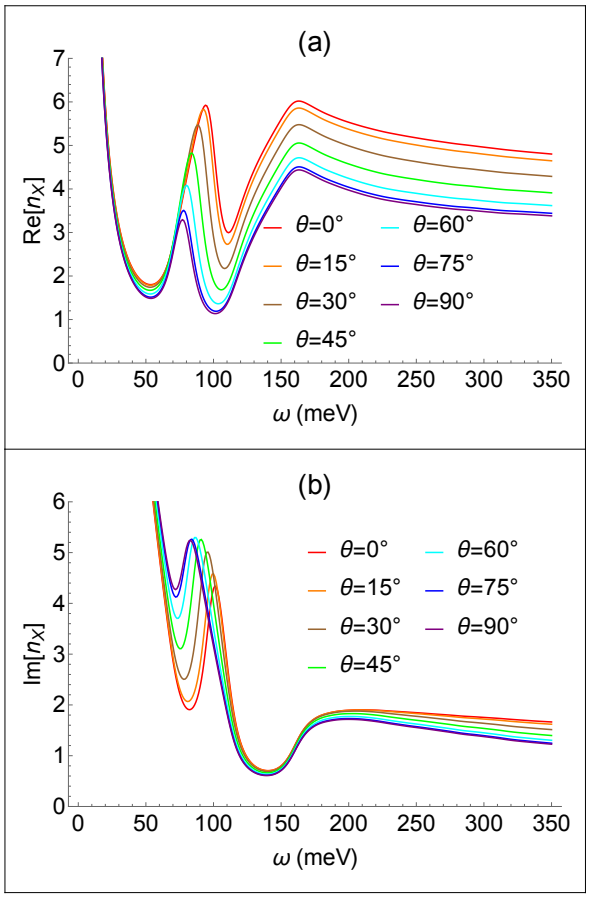

Figure 4.8: Real and imaginary parts of the refractive index n_X of an X-wave as a function of frequency for different values of the propagation angle θ. Other parameters are $E_F = 80$ meV, $\hbar v_F b = 100$ meV, and dephasing rate $\gamma = 10$ meV. Reprinted with permission from [59].

the expression for the polarization coefficient:

$$K_X = \frac{E_z}{E_y} = \frac{ig - n_X^2 \sin\theta\cos\theta}{\varepsilon_{zz} - n_X^2 \sin^2\theta}. \tag{4.147}$$

Substituting Eq. (4.144) into Eq. (4.147) one gets

$$K_X = \frac{ig\left(\cos^2\theta\varepsilon_{zz} + \sin^2\theta\varepsilon_{yy}\right) - \left(\varepsilon_{yy}\varepsilon_{zz} - g^2\right)\sin\theta\cos\theta}{\varepsilon_{zz}\left(\cos^2\theta\varepsilon_{zz} + \sin^2\theta\varepsilon_{yy}\right) - \left(\varepsilon_{yy}\varepsilon_{zz} - g^2\right)\sin^2\theta}. \tag{4.148}$$

At the resonant plasmon frequency defined by $\cos^2\theta\varepsilon_{zz} + \sin^2\theta\varepsilon_{yy} = 0$ one obtains $K_X = \frac{1}{\tan\theta}$,

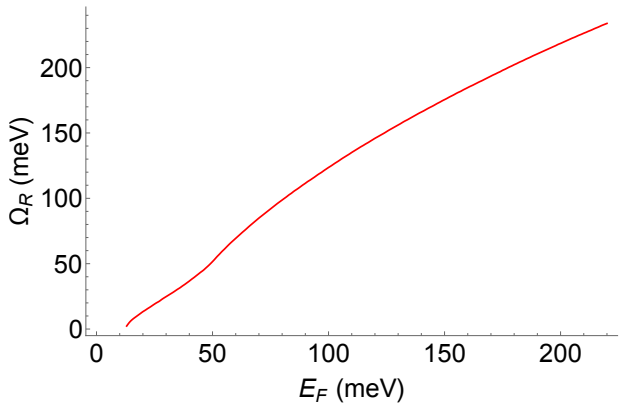

Figure 4.9: Real part of the bulk plasmon resonance frequency at normal incidence $\theta = 0$ as a function of the Fermi energy. Reprinted with permission from [59].

which is expected. If one sets $\theta = 0$, which corresponds to normal incidence, $K_X = \dfrac{ig}{\varepsilon_{zz}}$, i.e. again proportional to g. In this case, the plasmon frequency is given by $\varepsilon_{zz} = 0$, and $K_X \to \infty$ in the absence of losses. If $\varepsilon_{yy} = \varepsilon_{zz} = \varepsilon_\perp$, Eq. (4.148) gives

$$K_X = \frac{ig\varepsilon_\perp - (\varepsilon_\perp^2 - g^2)\sin\theta\cos\theta}{\varepsilon_\perp^2\cos^2\theta + g^2\sin^2\theta}. \tag{4.149}$$

For an isotropic medium, when $g^2 = 0$, the last expression gives $K_X = -\tan\theta$, as it should be for a transverse wave in an isotropic medium.

4.5.2 Propagation Perpendicular to the y Axis

For propagation transverse to the y axis $n_y = 0$, $n^2 = n_x^2 + n_z^2$, $n_x = n\cos\phi$, $n_z = n\sin\phi$;

$$\begin{pmatrix} \varepsilon_{xx} - n_z^2 & 0 & n_x n_z \\ 0 & \varepsilon_{yy} - n^2 & ig \\ n_z n_x & -ig & \varepsilon_{zz} - n_x^2 \end{pmatrix} \begin{pmatrix} E_x \\ E_y \\ E_z \end{pmatrix} = 0 \tag{4.150}$$

$$\left(\sin^2\phi\varepsilon_{zz}+\cos^2\phi\varepsilon_{xx}\right)n^4-n^2\left[\varepsilon_{xx}\varepsilon_{zz}+\varepsilon_{yy}\left(\sin^2\phi\varepsilon_{zz}+\cos^2\phi\varepsilon_{xx}\right)-\sin^2\phi g^2\right]$$
$$+\varepsilon_{xx}\left(\varepsilon_{yy}\varepsilon_{zz}-g^2\right)=0. \qquad (4.151)$$

Note that the solution of Eq. (4.151) at $\phi=\frac{\pi}{2}$ corresponds to the normal incidence propagation along z and therefore should coincide with Eqs. (4.143), (4.144) at $\theta=0$. Indeed, from Eq. (4.151) for $\phi=\frac{\pi}{2}$ one obtains

$$\left(n^2-\varepsilon_{xx}\right)\left[n^2-\left(\varepsilon_{yy}-\frac{g^2}{\varepsilon_{zz}}\right)\right]=0; \qquad (4.152)$$

from which $n_O^2=\varepsilon_{xx}$, $n_X^2=\varepsilon_{yy}-\dfrac{g^2}{\varepsilon_{zz}}$, as expected.

The case $n^2\to\infty$ in the absence of losses, when

$$\sin^2\phi\varepsilon_{zz}+\cos^2\phi\varepsilon_{xx}=0 \qquad (4.153)$$

corresponds to the condition $\boldsymbol{n}\cdot\boldsymbol{D}=0$ where $\boldsymbol{E}=-\nabla\varphi\parallel\boldsymbol{n}$. From Eq. (4.151) one obtains

$$n_{O,X}^2=\frac{\varepsilon_{xx}\varepsilon_{zz}+\varepsilon_{yy}\left(\sin^2\phi\varepsilon_{zz}+\cos^2\phi\varepsilon_{xx}\right)-\sin^2\phi g^2}{2\left(\sin^2\phi\varepsilon_{zz}+\cos^2\phi\varepsilon_{xx}\right)}\pm$$
$$\frac{\sqrt{\left[\varepsilon_{xx}\varepsilon_{zz}+\varepsilon_{yy}\left(\sin^2\phi\varepsilon_{zz}+\cos^2\phi\varepsilon_{xx}\right)-\sin^2\phi g^2\right]^2-4\left(\sin^2\phi\varepsilon_{zz}+\cos^2\phi\varepsilon_{xx}\right)\varepsilon_{xx}\left(\varepsilon_{yy}\varepsilon_{zz}-g^2\right)}}{2\left(\sin^2\phi\varepsilon_{zz}+\cos^2\phi\varepsilon_{xx}\right)} \qquad (4.154)$$

In Eq. (4.154) the signs $\pm$ are chosen for $n_{O,X}^2$ according to the limiting case $\phi=\frac{\pi}{2}$.

For the propagation along the x-axis of anisotropy, when $\phi=0$, Eq. (4.151) gives

$$n_{O,X}^2=\frac{\varepsilon_{zz}+\varepsilon_{yy}}{2}\pm\sqrt{\left(\frac{\varepsilon_{zz}-\varepsilon_{yy}}{2}\right)^2+g^2} \qquad (4.155)$$

Note that the x-axis is also a gyrotropy axis related to the Weyl node separation along x. Therefore, the propagation along x is similar to the Faraday geometry in a magnetic field. In our case the

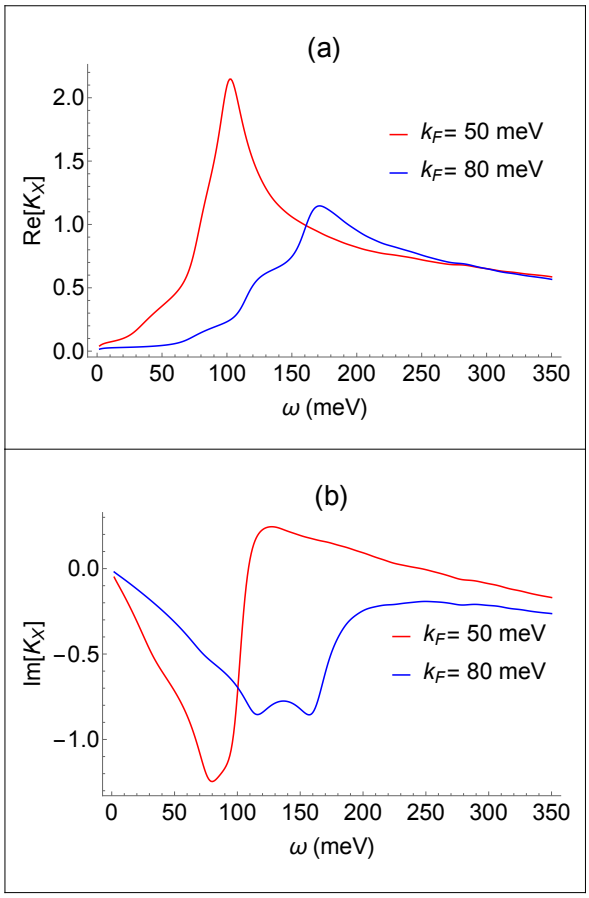

Figure 4.10: Spectra of real and imaginary parts of the polarization coefficient $K_X = E_z/E_y$ for an incident wave linearly polarized in y-direction after traversing a 1-μm film in x-direction. Reprinted with permission from [59].

normal modes are elliptically polarized. So an incident linearly polarized wave experiences Faraday rotation and gains ellipticity after traversing a sample in x-direction. To quantify the effect, Fig. 4.10 shows the polarization coefficient $K_X = E_z/E_y$ after traversing a 1-μm thick film for a wave initially linearly polarized in y-direction. The real part of K_X is a measure of the polarization rotation whereas its imaginary part is a measure of ellipticity. Clearly, a rotation by $\sim \pi/2$ by very thin (0.5-1 μm) Weyl semimetal films is possible at frequencies near the interband absorption edge. This is a giant Faraday rotation, comparable to the one observed at THz frequencies in narrow-gap semiconductors in the vicinity of a cyclotron resonance in Tesla-strength magnetic fields; see e.g. [96] for the review. Note that in our case no magnetic field is needed and the effect is controlled by

the Weyl node separation and by the Fermi level. Previously Faraday rotation and nonreciprocity in light propagation associated with it was studied in [66, 80] using the model with an axion θ-term in the electromagnetic field action.

4.5.3 Oblique Propagation of Bulk Polaritons

In the general case the direction of the wave vector is determined by two angles θ and ϕ:

$$n_x = n\cos\phi\,, n_z = n\sin\phi\cos\theta\,, n_y = n\sin\phi\sin\theta.$$

The general expression for $n^2_{O,X}$ is quite cumbersome. At the same time, in the particular case of $\varepsilon_{yy} = \varepsilon_{zz} = \varepsilon_\perp$, the result should not depend on the angle θ and should coincide with the one for a magnetized plasma:

$$n^2_{O,X} = \frac{\varepsilon_\perp\left[\varepsilon_{xx}\left(1+\cos^2\phi\right)+\sin^2\phi\varepsilon_\perp\right]-\sin^2\phi g^2}{2\left(\sin^2\phi\varepsilon_\perp+\cos^2\phi\varepsilon_{xx}\right)}\pm \\ \frac{\sqrt{\left(\varepsilon_\perp\left[\varepsilon_{xx}\left(1+\cos^2\phi\right)+\sin^2\phi\varepsilon_\perp\right]-\sin^2\phi g^2\right)^2-4\varepsilon_{xx}\left(\sin^2\phi\varepsilon_\perp+\cos^2\phi\varepsilon_{xx}\right)\left(\varepsilon_\perp^2-g^2\right)}}{2\left(\sin^2\phi\varepsilon_\perp+\cos^2\phi\varepsilon_{xx}\right)} \tag{4.156}$$

The condition $\boldsymbol{n}\cdot\boldsymbol{D}=0$ at $\boldsymbol{E}=-\nabla\varphi\parallel\boldsymbol{n}$ in the case of an oblique propagation gives

$$\varepsilon_{xx}\cos^2\phi+\sin^2\phi\left(\sin^2\theta\varepsilon_{yy}+\cos^2\theta\varepsilon_{zz}\right)=0. \tag{4.157}$$

Therefore, Eq. (4.157) determines the frequencies of bulk plasmons in the general case. Under the condition $\varepsilon_{yy} = \varepsilon_{zz} = \varepsilon_\perp$ the plasmon dispersion equation takes a form similar to plasmons in a magnetized plasma:

$$\varepsilon_{xx}\cos^2\phi+\sin^2\phi\varepsilon_\perp=0. \tag{4.158}$$

4.6 Boundary Conditions

So far I considered propagation and transmission of electromagnetic waves in bulk samples. Now I will turn to effects of reflection and surface wave propagation that are equally sensitive to the electronic structure of WSMs. Moreover, in many situations they are easier to observe than bulk propagation effects.

I will start with the derivation of the boundary conditions at $z = 0$ surface. Assume that there is an isotropic dielectric medium with dielectric constant $n_{up}^2 = \varepsilon_{up}$ above a WSM. The boundary conditions include:

(i) Gauss' law for the normal components of the electric induction vector:

$$\varepsilon_{up} E_z\left(z=+0\right) - D_z\left(z=-0\right) = 4\pi\rho^S = -i\frac{4\pi}{\omega}\left(\partial_x j_x^S + \partial_y j_y^S\right) \tag{4.159}$$

where ρ^S, j_x^S and j_y^S are the surface charge and components of the surface current that are connected by the continuity equation. For the wave field one has $\partial_x, \partial_y \to ik_{x,y}$.

(ii) Equations for the magnetic field components:

$$B_z\left(z=-0\right) = B_z\left(z=+0\right), \tag{4.160}$$

$$B_y\left(z=+0\right) - B_y\left(z=-0\right) = -\frac{4\pi}{c} j_x^S, \tag{4.161}$$

$$B_x\left(z=+0\right) - B_x\left(z=-0\right) = \frac{4\pi}{c} j_y^S. \tag{4.162}$$

Due to the presence of the components of the surface conductivity σ_{zz}^S and $\sigma_{zy}^S = -\sigma_{yz}^S$ a surface dipole layer is formed at the boundary between the two media. Its dipole moment is

$$\begin{aligned} \boldsymbol{d} &= \mathrm{Re}\left[\boldsymbol{e}_z d_z e^{-i\omega t + ik_x x + ik_y y}\right], \\ d_z &= \frac{i}{\omega}\left[\sigma_{zy}^S E_y\left(z=-0\right) + \sigma_{zz}^S E_z\left(z=-0\right)\right]. \end{aligned} \tag{4.163}$$

Note that when dealing with a surface response, the fields are always chosen at $z = -0$ in

Eq. (4.163) and similar relationships. The presence of the dipole layer changes the boundary conditions for the tangential field components of $\boldsymbol{E}$. Consider Maxwell's equations

$$\frac{\partial E_z}{\partial y} - \frac{\partial E_y}{\partial z} = i\frac{\omega}{c}B_x,\ \frac{\partial E_x}{\partial z} - \frac{\partial E_z}{\partial x} = i\frac{\omega}{c}B_y.$$

For convenience, assume that the dipole layer has a small but finite thickness L:

$$|k_{x,y}|L \ll 1 \quad \text{and} \quad \frac{\omega}{c}L \ll 1.$$

Using $\partial_x, \partial_y \to ik_{x,y}$ and integrating $\int_{-\frac{L}{2}}^{\frac{L}{2}} \ldots dz$, one obtains

$$ik_{x,y}\int_{-\frac{L}{2}}^{\frac{L}{2}} E_z\, dz = E_{x,y}\left(z = \frac{L}{2}\right) - E_{x,y}\left(z = -\frac{L}{2}\right) \tag{4.164}$$

The integral over the magnetic field components were neglected assuming that $\frac{\omega}{c}L \to 0$. Next if one uses Gauss' law under the condition $|k_{x,y}|L \to 0$, it will yield in the region of the dipole layer:

$$\frac{\partial E_z}{\partial z} = 4\pi\rho\left(z\right), \quad \rho\left(z\right) = -\left(\frac{\partial P_z}{\partial z} + \frac{\partial p_z}{\partial z}\right).$$

Here P_z is a component of the volume polarization whereas p_z describes the distribution of the polarization in the dipole layer, so that

$$\int_{-\frac{L}{2}}^{\frac{L}{2}} \frac{\partial p_z}{\partial z}\, dz = 0 \quad \text{and} \quad \int_{-\frac{L}{2}}^{\frac{L}{2}} p_z\, dz = d_z.$$

Substituting $E_z = -4\pi\left(P_z + p_z\right)$ into Eq. (4.164) and integrating over dz at $|k_{x,y}|L \to 0$ and finite P_z, one obtains

$$E_{x,y}\left(z = \frac{L}{2}\right) - E_{x,y}\left(z = -\frac{L}{2}\right) = -i4\pi k_{x,y}d_z \tag{4.165}$$

The boundary condition Eq. (4.165) looks unusual but it can be easily deduced from the radiation

field of an individual dipole.

Figures 4.11-4.14 show spectra of the surface conductivity components for different values of the Fermi momentum. Note that the surface conductivity in Gaussian units has a dimension of velocity and its value is normalized by $e^2/(2\pi\hbar) \simeq 3.5 \times 10^7$ cm/s in all plots. In contrast with the bulk conductivity, the surface conductivity had a Drude-like behavior at low frequencies only for the yy-component because of the surface state dispersion $E = -\hbar v_F k_y$. The surface optical response decreases with increasing Fermi energy and vanishes when all surface states within $k_x^2 + k_y^2 < b^2$ are occupied.

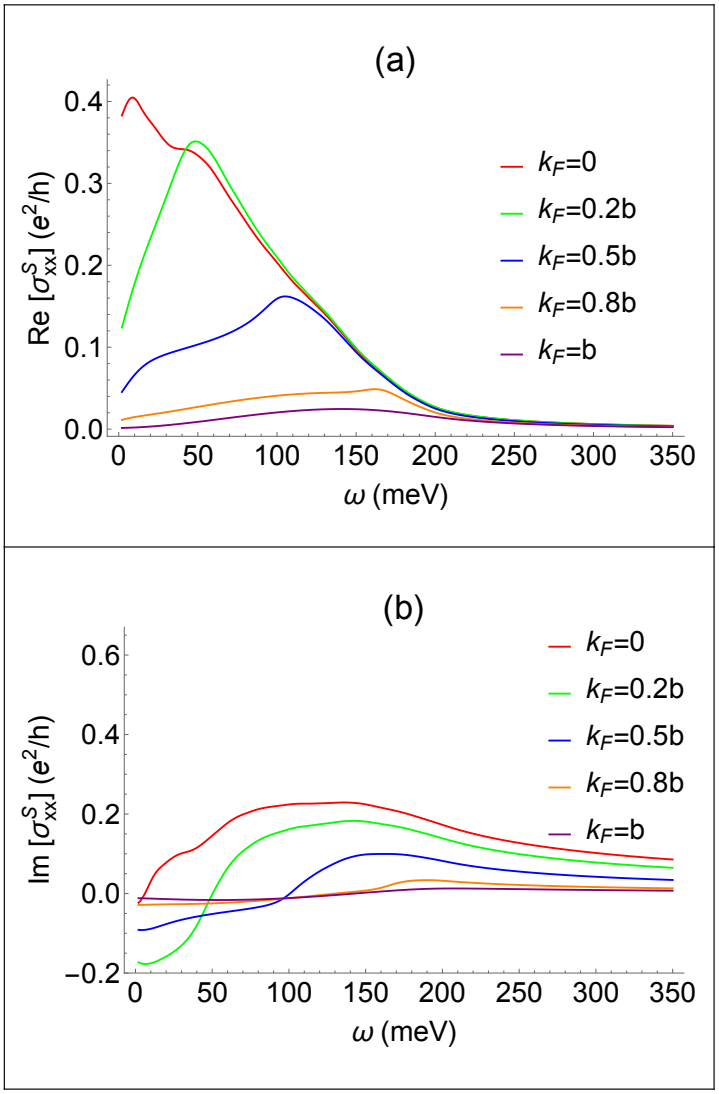

Figure 4.11: Spectra of the real and imaginary parts of the xx component of the surface conductivity at several values of the Fermi momentum for $\hbar v_F b = 100$ meV and dephasing rate $\gamma = 10$ meV. Reprinted with permission from [59].

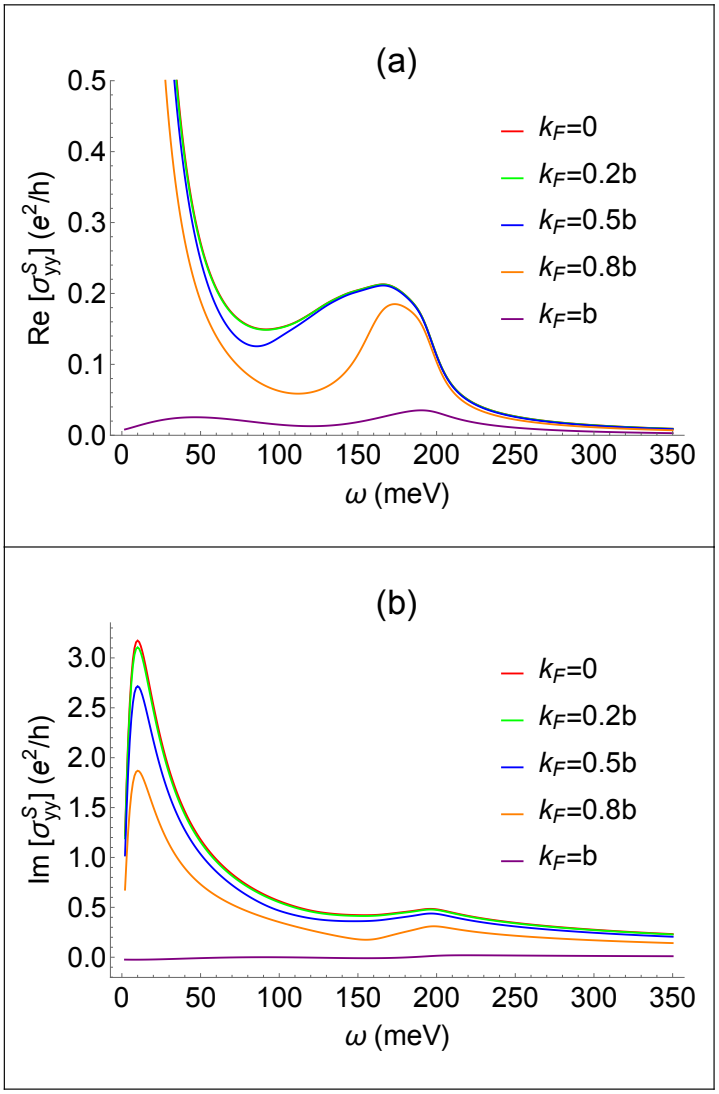

Figure 4.12: Spectra of the real and imaginary parts of the yy component of the surface conductivity at several values of the Fermi momentum for $\hbar v_F b = 100$ meV and dephasing rate $\gamma = 10$ meV. Reprinted with permission from [59].

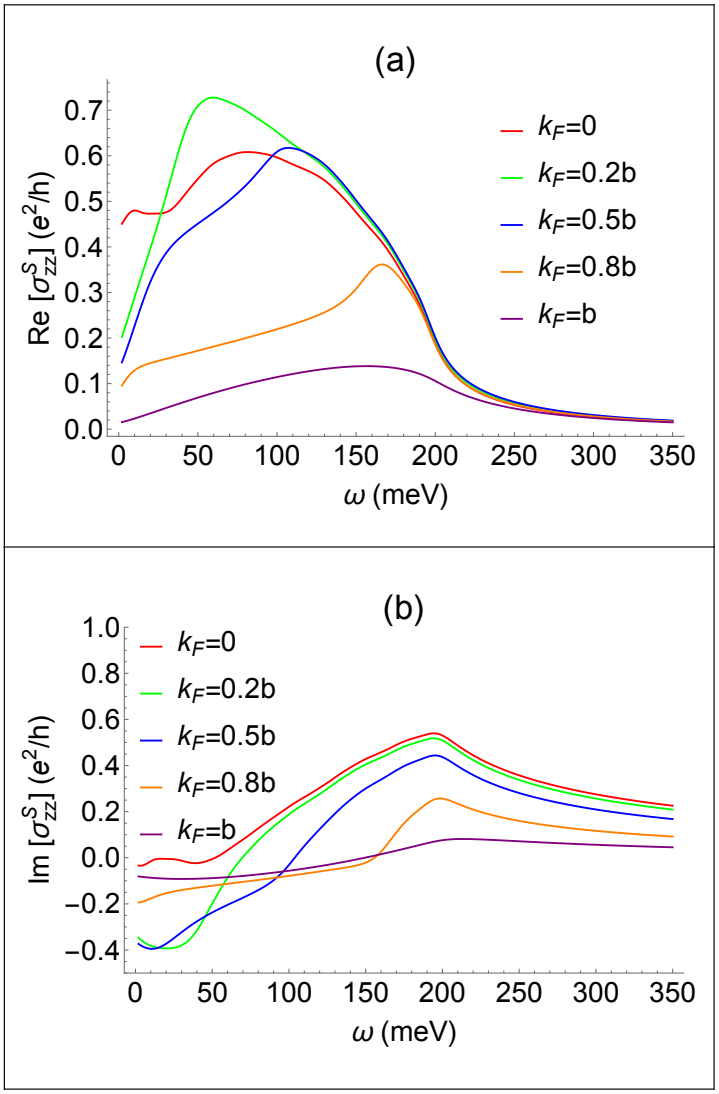

Figure 4.13: Spectra of the real and imaginary parts of the zz component of the surface conductivity at several values of the Fermi momentum for $\hbar v_F b = 100$ meV and dephasing rate $\gamma = 10$ meV. Reprinted with permission from [59].

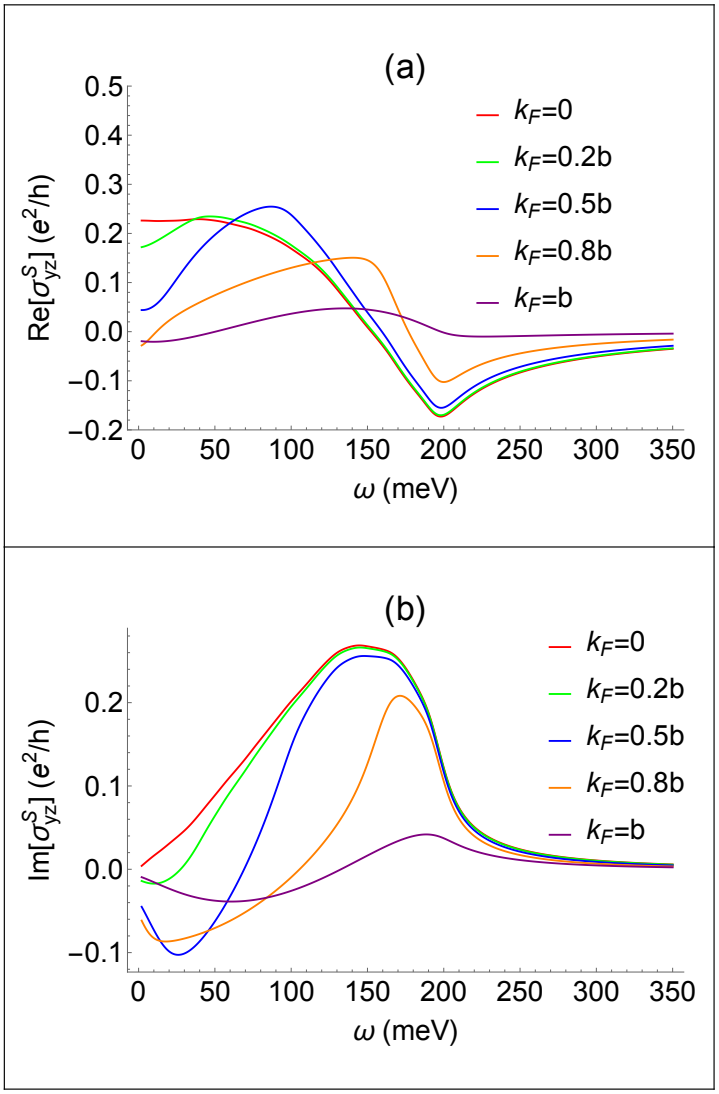

Figure 4.14: Spectra of the real and imaginary parts of the yz component of the surface conductivity at several values of the Fermi momentum for $\hbar v_F b = 100$ meV and dephasing rate $\gamma = 10$ meV. Reprinted with permission from [59].

4.7 Reflection from the Surface of a Weyl Semimetal

Consider radiation incident from a medium with refractive index n_{up} on a WSM at an angle θ between the wavevector of the wave and the normal to a WSM. For simplicity consider the propagation transverse to the x-axis. The reflection spectra provide information about both bulk and surface conductivity components. Here I will pay particular attention to the case when the contribution of the surface states becomes significant or dominant, thus allowing one to probe surface states by optical means.

4.7.1 Reflection with Excitation of an O-mode

In this geometry, the complex amplitudes of the electric field of the incident E_1, reflected E_2, and transmitted E_O wave are parallel to the x-axis. The refractive index of the transmitted wave is $n_O^2 = \varepsilon_{xx} = \varepsilon_{xx}^{(0)} + i\dfrac{4\pi}{\omega}\sigma_{xx}^B$ (see Eq. (4.143)).

Applying Maxwell's equations with standard boundary conditions including the surface current, one arrives at

$$R = \frac{E_2}{E_1} = -\frac{\cos\theta_O\sqrt{\varepsilon_{xx}^{(0)} + i\frac{4\pi}{\omega}\sigma_{xx}^B} + \frac{4\pi}{c}\sigma_{xx}^S - \cos\theta n_{up}}{\cos\theta_O\sqrt{\varepsilon_{xx}^{(0)} + i\frac{4\pi}{\omega}\sigma_{xx}^B} + \frac{4\pi}{c}\sigma_{xx}^S + \cos\theta n_{up}} \tag{4.166}$$

where $n_{up}\sin\theta = n_O\sin\theta_O$. Assuming $\sigma_{xx}^S = 0$ one obtains $R = \dfrac{E_2}{E_1} = \dfrac{\cos\theta n_{up} - \cos\theta_O n_O}{\cos\theta_O n_O + \cos\theta n_{up}}$, which is a standard Fresnel formula.

For the same magnitude of σ_{xx}^S, the relative contribution of surface states to the reflected field depends on the parameter $\dfrac{|\varepsilon_{xx}^{(0)}|}{4\pi|\sigma_{xx}^B|/\omega}$. If $\dfrac{\omega|\varepsilon_{xx}^{(0)}|}{4\pi|\sigma_{xx}^B|} \gg 1$, the relative contribution of surface states is determined by the expression: $\dfrac{2\omega|\sigma_{xx}^S|/c}{|\sigma_{xx}^B|/|\varepsilon_{xx}^{(0)}|}$. If $\dfrac{\omega|\varepsilon_{xx}^{(0)}|}{4\pi|\sigma_{xx}^B|} \ll 1$, one needs to evaluate the ratio $\dfrac{2\sqrt{\pi}\sigma_{xx}^S/c}{\sqrt{\sigma_{xx}^B/\omega}}$.

4.7.2 Reflection with Excitation of an X-mode

In this geometry, the complex Fourier harmonics for the incident and reflected waves are

$$\left(\boldsymbol{e}_y \mp \boldsymbol{e}_z \tan\theta\right) E_{1,2} e^{\mp i\frac{\omega}{c} n_{up}\cos\theta z - i\frac{\omega}{c} n_{up}\sin\theta y - i\omega t}.$$

The transmitted wave is

$$\left(\boldsymbol{e}_y + \boldsymbol{e}_z K_X\right) E_X e^{-i\frac{\omega}{c} n_X \cos\theta_X z - i\frac{\omega}{c} n_X \sin\theta_X y - i\omega t},$$

where n_X^2 and K_X are given by Eqs. (4.144) and (4.147), in which one should substitute $\theta \to \theta_X$. The corresponding complex amplitudes of the magnetic field are $B_{1x} = \dfrac{n_{up}}{\cos\theta} E_1$, $B_{2x} = -\dfrac{n_{up}}{\cos\theta} E_2$, $B_{(X)x} = n_X\left(\cos\theta_X - \sin\theta_X K_X\right) E_X$.

At the plasmon frequency, when $K_X = \dfrac{1}{\tan\theta_X}$, the last equation gives $B_{(X)x} = 0$, as should be expected. For an isotropic medium, when $K_X = -\tan\theta_X$, one obtains $B_{(X)x} = \dfrac{n_X}{\cos\theta_X} E_X$ which is also expected for a transverse wave (note that E_X is an amplitude of the y-component of the extraordinary (X-)mode).

I will use the boundary conditions

$$E_1 + E_2 - E_X = i\omega\frac{4\pi}{c} n_{up}\sin\theta d_z, \quad d_z = \frac{i}{\omega}\left(\sigma_{zy}^S + \sigma_{zz}^S K_X\right) E_X \tag{4.167}$$

$$\frac{n_{up}}{\cos\theta}\left(E_1 - E_2\right) - n_X\left(\cos\theta_X - \sin\theta_X K_X\right) E_X = \frac{4\pi}{c} j_y^S, \quad j_y^S = \left(\sigma_{yy}^S + \sigma_{yz}^S K_X\right) E_X \tag{4.168}$$

to obtain

$$R = \frac{E_2}{E_1} = \frac{n_{up}\left[1 - \frac{4\pi n_{up}\sin\theta}{c}\left(\sigma_{zy}^S + \sigma_{zz}^S K_X\right)\right] - n_X\cos\theta\left(\cos\theta_X - \sin\theta_X K_X\right) + \frac{4\pi\cos^2\theta}{c}\left(\sigma_{yy}^S + \sigma_{yz}^S K_X\right)}{n_X\cos\theta\left(\cos\theta_X - \sin\theta_X K_X\right) + \frac{4\pi\cos^2}{c}\left(\sigma_{yy}^S + \sigma_{yz}^S K_X\right) + n_{up}\left[1 - \frac{4\pi n_{up}\sin\theta}{c}\left(\sigma_{zy}^S + \sigma_{zz}^S K_X\right)\right]} \tag{4.169}$$

where $n_{up}\sin\theta = n_X \sin\theta_X$. In the limit of an isotropic medium, where $K_X = -\tan\theta_X$, $\sigma^S_{ij} = 0$, one obtains $R = \dfrac{E_2}{E_1} = \dfrac{n_{up}\cos\theta_X - n_X\cos\theta}{n_X\cos\theta + n_{up}\cos\theta_X}$ which is a standard Fresnel equation.

For the normal incidence the expressions are simplified:

$$n_X^2 = \varepsilon_{yy} - \frac{g^2}{\varepsilon_{zz}} = \varepsilon^{(0)}_{yy} + i\frac{4\pi}{\omega}\sigma^B_{yy} - \frac{\left(\frac{4\pi\sigma^B_{yz}}{\omega}\right)^2}{\varepsilon^{(0)}_{zz} + i\frac{4\pi}{\omega}\sigma^B_{zz}}, \quad K_X = \frac{ig}{\varepsilon_{zz}} = i\frac{\frac{4\pi\sigma^B_{yz}}{\omega}}{\varepsilon^{(0)}_{zz} + i\frac{4\pi}{\omega}\sigma^B_{zz}},$$

which gives

$$R = \frac{n_{up} - n_X + \frac{4\pi}{c}\left(\sigma^S_{yy} + i\sigma^S_{yz}\frac{g}{\varepsilon_{zz}}\right)}{n_{up} + n_X + \frac{4\pi}{c}\left(\sigma^S_{yy} + i\sigma^S_{yz}\frac{g}{\varepsilon_{zz}}\right)} \tag{4.170}$$

The contribution of surface states is less trivial for X-mode excitation as compared to the excitation of an O-mode. For normal incidence (see Eq. (4.170)) one can see that at the plasmon resonance frequency, when $\varepsilon_{zz} \to 0$ in the absence of losses, the contribution of the surface conductivity can become dominant. Indeed, in Eq. (4.170) the term $\sigma^S_{yz}\dfrac{g}{\varepsilon_{zz}}$ diverges as $\dfrac{1}{\varepsilon_{zz}}$, whereas the refractive index n_X diverges weaker, as $\dfrac{1}{\sqrt{\varepsilon_{zz}}}$. When $\sigma^S_{ij} = 0$ while $n_X \gg n_{up}$ one has $R = -1$ (taking into account that the magnitude of n_X is large at the plasmon frequency). In the opposite case, when the contribution of the surface conductivity dominates, i.e. $\dfrac{4\pi}{c}|\sigma^S_{yz}\dfrac{g}{\varepsilon_{zz}}| \gg |n_X| \approx \dfrac{g}{\sqrt{|\varepsilon_{zz}|}}$, one obtains $R = +1$, i.e. the phase of the reflected field is rotated by 180 degrees.

The enhanced contribution of the surface conductivity at normal incidence in the vicinity of the bulk plasmon resonance is expected. Indeed, at plasmon resonance the z-component E_z of the field in the medium becomes very large, which leads to a dominant contribution of the surface current $j^S_y = \sigma^S_{yz}E_z$.

For oblique incidence $\theta \neq 0$ and small losses the calculations of the reflection in the vicinity of plasmon resonance have a technical subtlety, related to the presence of the term $n_X\cos\theta\left(\cos\theta_X - \sin\theta_X K_X\right)$ in Eq. (4.169). Indeed, at the plasmon frequency $n_X \to \infty$ as losses $\gamma \to 0$; however, for a plasmon one also has $K_X \to \dfrac{1}{\tan\theta_X}$, i.e. $\left(\cos\theta_X - \sin\theta_X K_X\right) \to 0$. One needs to treat the resulting uncertainty of the product with caution. The details are presented below

.

4.7.2.1 Reflection in The Vicinity of Plasmon Resonance

For oblique incidence $\theta \neq 0$ and small losses the calculations of the reflection in the vicinity of plasmon resonance have a technical subtlety, related to the presence of the term $n_X \cos\theta \left(\cos\theta_X - \sin\theta_X K_X\right)$ in Eq. (4.169). Indeed, at the plasmon frequency $n_X \to \infty$ as losses $\gamma \to 0$; however, for a plasmon one also has $K_X \to \dfrac{1}{\tan\theta_X}$, i.e. $\left(\cos\theta_X - \sin\theta_X K_X\right) \to 0$. One needs to treat the resulting uncertainty of the product with caution.

Substituting the relationship $\sin\theta_X = \dfrac{n_{up}\sin\theta}{n_X}$ into the expression for the refractive index of an extraordinary wave gives:

$$n_X^2 = \frac{\varepsilon_{yy}\varepsilon_{zz} - g^2}{\cos^2\theta_X \varepsilon_{zz} + \sin^2\theta_X \varepsilon_{yy}} = \frac{\varepsilon_{yy}\varepsilon_{zz} - g^2}{\varepsilon_{zz} - \sin^2\theta \left(\frac{n_{up}}{n_X}\right)^2 \left(\varepsilon_{zz} - \varepsilon_{yy}\right)},$$

which gives

$$n_X^2 = \varepsilon_{yy} - \frac{g^2}{\varepsilon_{zz}} + \sin^2\theta n_{up}^2 \left(1 - \frac{\varepsilon_{yy}}{\varepsilon_{zz}}\right) \tag{4.171}$$

In the case $\varepsilon_{yy} = \varepsilon_{zz} = \varepsilon_\perp$, Eq. (4.171) for an arbitrary angle θ leads to the familiar expression $n_X^2 = \varepsilon_\perp - \frac{g^2}{\varepsilon_\perp}$. Next I will use Eq. (4.147):

$$K_X = \frac{ig - n_X^2 \sin\theta_X \cos\theta_X}{\varepsilon_{zz} - n_X^2 \sin^2\theta_X} = \frac{ig - n_{up}\sin\theta n_X \sqrt{1 - \left(\frac{\sin\theta n_{up}}{n_X}\right)^2}}{\varepsilon_{zz} - \sin^2\theta n_{up}^2}.$$

Consider the expression $n_X \cos\theta \left(\cos\theta_X - \sin\theta_X K_X\right)$:

$$
\begin{aligned}
& n_X \cos\theta \left(\cos\theta_X - \sin\theta_X K_X\right) \\
& \quad = n_X \cos\theta \left(\cos\theta_X - \frac{ig \sin\theta_X - \sin\theta_X n_{up} \sin\theta n_X \sqrt{1 - \left(\frac{\sin\theta n_{up}}{n_X}\right)^2}}{\varepsilon_{zz} - \sin^2\theta n_{up}^2} \right) \\
& \quad = n_X \cos\theta \left(\sqrt{1 - \left(\frac{\sin\theta n_{up}}{n_X}\right)^2} - \frac{ig\frac{\sin\theta n_{up}}{n_X} - \sin^2\theta n_{up}^2 \sqrt{1 - \left(\frac{\sin\theta n_{up}}{n_X}\right)^2}}{\varepsilon_{zz} - \sin^2\theta n_{up}^2} \right).
\end{aligned}
$$

The condition $\frac{n_X}{n_{up}} \gg 1$, which is satisfied at the plasmon frequency, allows one to simplify the above expressions for any angle of incidence θ

$$
K_X = \frac{ig - n_X^2 \sin\theta_X \cos\theta_X}{\varepsilon_{zz} - n_X^2 \sin^2\theta_X} \approx \frac{ig - n_X n_{up} \sin\theta}{\varepsilon_{zz} - \sin^2\theta n_{up}^2} \tag{4.172}
$$

$$
n_X cos\theta \left(\cos\theta_X - \sin\theta_X K_X\right) \approx n_X \cos\theta \left(1 - \frac{ig\frac{\sin\theta n_{up}}{n_X} - \sin^2\theta n_{up}^2}{\varepsilon_{zz} - \sin^2\theta n_{up}^2}\right) \tag{4.173}
$$

Since for $\frac{n_X}{n_{up}} \gg 1$ one always has $\sin\theta_X \ll 1$, the plasmon frequency always corresponds to $|\varepsilon_{zz}| \ll 1$ (at normal incidence, $\varepsilon_{zz} = 0$ exactly). Taking into account Eq. (4.171), one obtains $1 \gg |\varepsilon_{zz}| \sim n_X^{-2}$.

Now consider the range of incidence angles close to normal incidence, when $\sin^2\theta \ll 1$. Two cases need to be treated separately: $|\varepsilon_{zz}| \ll \sin^2\theta n_{up}^2 \ll 1$ and $\sin^2\theta n_{up}^2 \ll |\varepsilon_{zz}| \ll 1$.

(i) $|\varepsilon_{zz}| \ll sin^2\theta n_{up}^2 \ll 1$

In this case

$$
n_X^2 \approx \varepsilon_{yy} - \frac{g^2}{\varepsilon_{zz}}, \quad K_X \approx \frac{n_X}{n_{up} sin\theta} \tag{4.174}
$$

$$
n_X \cos\theta \left(1 - \frac{ig\frac{\sin\theta n_{up}}{n_X} - \sin^2\theta n_{up}^2}{\varepsilon_{zz} - \sin^2\theta n_{up}^2}\right) \approx \frac{ig}{sin\theta n_{up}} \tag{4.175}
$$

where $g = \frac{4\pi\sigma^B_{yz}}{\omega}$,

$$R \approx \frac{n_{up}^2 \sin\theta - i\frac{4\pi\sigma^B_{yz}}{\omega} + \frac{4\pi}{c}\sigma^S_{yz} n_X}{n_{up}^2 \sin\theta + i\frac{4\pi\sigma^B_{yz}}{\omega} + \frac{4\pi}{c}\sigma^S_{yz} n_X}. \tag{4.176}$$

For real $\sigma^{(B,S)}_{yz}$ one has $|R| = 1$; however, the phase of the reflected field depends on the contribution of surface states. Since in the vicinity of plasmon resonance $n_X \sim \frac{1}{\sqrt{|\varepsilon_{zz}|}} \gg 1$, at these frequencies the contribution of surface states may become important. This is especially clear in the limit of small enough angles, when $n_{up}^2 sin\theta \ll |\frac{4\pi\sigma^B_{yz}}{\omega}|$. In this case

$$R \approx \frac{-i\frac{4\pi\sigma^B_{yz}}{\omega} + \frac{4\pi}{c}\sigma^S_{yz} n_X}{+i\frac{4\pi\sigma^B_{yz}}{\omega} + \frac{4\pi}{c}\sigma^S_{yz} n_X}. \tag{4.177}$$

When the bulk contribution dominates one has $R = -1$, whereas if the surface contribution dominates one obtains $R = +1$, i.e. the phase of the reflected field flips.

The relative contribution of surface states is determined by the ratio $\frac{|\sigma^S_{yz} n_X|}{\frac{c}{\omega}|\sigma^B_{yz}|}$. Taking into account that $|n_X| \approx \frac{|g|}{\sqrt{|\varepsilon_{zz}|}}$ and $|g| = \frac{4\pi|\sigma^B_{yz}|}{\omega}$, the above ratio can be reduced to $\frac{\frac{4\pi|\sigma^S_{yz}|}{c}}{\sqrt{|\varepsilon_{zz}|}}$.

(ii) $\sin^2\theta n_{up}^2 \ll |\varepsilon_{zz}| \ll 1$

This case is similar to the one at $\theta = 0$. Indeed, for this range of parameters one obtains

$$n_X^2 \approx \varepsilon_{yy} - \frac{g^2}{\varepsilon_{zz}}, \quad K_X \approx \frac{ig}{\varepsilon_{zz}} \tag{4.178}$$

$$n_X cos\theta \left(1 - \frac{ig\frac{sin\theta n_{up}}{n_X} - sin^2\theta n_{up}^2}{\varepsilon_{zz}}\right) \approx n_X. \tag{4.179}$$

$$R \approx \frac{-n_X + \frac{4\pi}{c}\sigma^S_{yz}\frac{ig}{\varepsilon_{zz}}}{n_X + \frac{4\pi}{c}\sigma^S_{yz}\frac{ig}{\varepsilon_{zz}}} \tag{4.180}$$

Eqs. (4.178), (4.179) are the same as for the normal incidence. Eq. (4.180) can be obtained from the normal incidence formula Eq. (4.170) if $|\sigma^S_{yy}| \ll |\sigma^S_{yz}\frac{g}{\varepsilon_{zz}}|$ and $n_X \gg n_{up}$; the latter inequalities

are valid near the plasmon resonance, where $n_X \sim \dfrac{1}{\sqrt{|\varepsilon_{zz}|}} \to \infty$.

For real values of $\sigma_{yz}^{(S)}$ one has $|R| = 1$, but the phase of the reflected field depends on the contribution of surface states. Again, when the bulk contribution dominates one has $R = -1$, whereas if the surface contribution dominates one obtains $R = +1$; see Figs. 4.15 and 4.16.

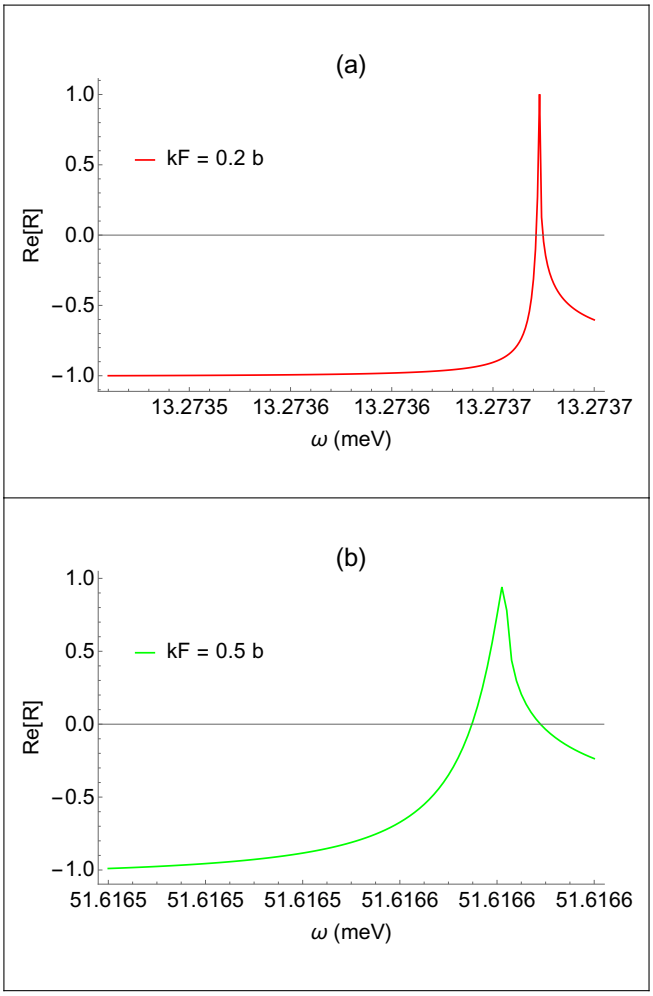

Figure 4.15: Real part reflection obtained from equation Eq. (4.180) for $n_{up} = 1$, $\hbar v_F b = 100$ meV and two values of the electron Fermi momentum $k_F = 0.2b$ and $0.5b$.

The relative contribution of surface states is determined by the ratio $\dfrac{\frac{4\pi}{c}|\sigma_{yz}^{S}\frac{g}{\varepsilon_{zz}}|}{|n_X|}$. Again taking

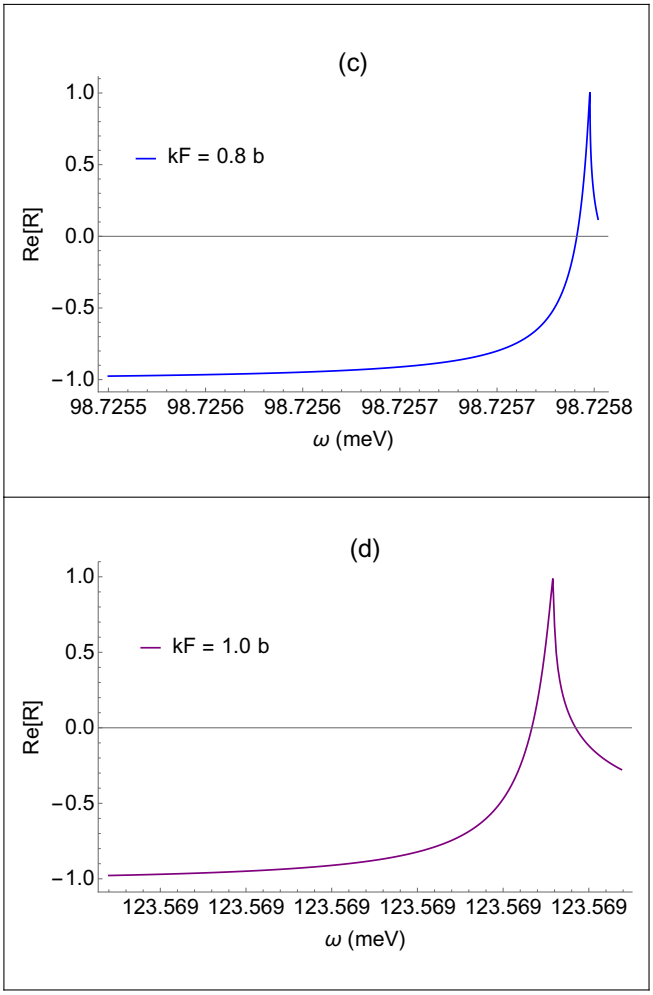

Figure 4.16: Real part reflection obtained from equation Eq. (4.180) for $n_{up} = 1$, $\hbar v_F b = 100$ meV and two values of the electron Fermi momentum $k_F = 0.8b$ and $1.0b$.

into account $|n_X| \approx \dfrac{|g|}{\sqrt{|\varepsilon_{zz}|}}$ and $|g| = \dfrac{4\pi|\sigma^B_{yz}|}{\omega}$ one obtains that the above ratio is reduced to exactly the same expression as before: $\dfrac{4\pi|\sigma^S_{yz}|/c}{\sqrt{|\varepsilon_{zz}|}}$.

To summarize, the effect of surface states on the reflected wave is determined by the ratio

$$\frac{|\sigma^S_{yz}|}{c\sqrt{|\varepsilon_{zz}|}/4\pi}$$

and therefore becomes significant or dominant at the plasmon resonance frequency, when $\varepsilon_{zz} =$

$\varepsilon_{zz}^{(0)} + i\frac{4\pi}{\omega}\sigma_{zz}^{B} \to 0$.

The main result is that the contribution of surface states to the reflected wave is determined by the ratio

$$\frac{|\sigma_{yz}^{S}|}{c\sqrt{|\varepsilon_{zz}|}/4\pi}$$

and therefore becomes significant or dominant at the plasmon resonance frequency, when $\varepsilon_{zz} = \varepsilon_{zz}^{(0)} + i\frac{4\pi}{\omega}\sigma_{zz}^{B} \to 0$. When the bulk contribution dominates the reflection coefficient R is close to -1. When the surface contribution dominates, R is close to $+1$ i.e. the phase of the reflected field flips.

4.8 Surface Plasmon-Polaritons

Surface plasmon-polaritons can be supported by both bulk and surface electron states. Here I will derive dispersion relations for surface waves including both bulk and surface conductivity for several specific cases. Emphasis is placed on the situations where the dispersion is significantly affected or dominated by surface states and can therefore be used for diagnostics of surface states and Fermi arcs. Previously, surface plasmons in WSMs have been considered in the low-frequency limit within a semiclassical description of particle motion with added ad hoc anomalous Hall term [97] and with a quantum-mechanical description [84] based on the Hamiltonian in [83]. Both studies indicated strong anisotropy and dispersion of surface plasmons.

4.8.1 Quasielectrostatic Approximation

Within the quasielectrostatic approximation the electric field can be defined through the scalar potential:

$$\mathcal{E} = \mathrm{Re}\left[\boldsymbol{E}\left(z\right)e^{ik_x x + ik_y y - i\omega t}\right] = -\nabla\mathcal{F}, \quad \mathcal{F} = \mathrm{Re}\left[\Phi\left(z\right)e^{ik_x x + ik_y y - i\omega t}\right].$$

Using the electric induction vector$\boldsymbol{\mathcal{D}} = \mathrm{Re}\left[\boldsymbol{D}\left(z\right)e^{ik_x x + ik_y y - i\omega t}\right] = \hat{\varepsilon}\mathcal{E}$ and Gauss' law for each halfspace gives :

$$\nabla \cdot \boldsymbol{\mathcal{D}} = 0. \tag{4.181}$$

In general, there can be an electric dipole layer at the boundary between the two media. The dipole layer has a jump in the scalar potential $\Phi(z)$,

$$\Phi(z=+0)-\Phi(z=-0)=4\pi d_z, \tag{4.182}$$

where d_z is determined by Eqs. (4.163).

Next, I define the scalar potential $\Phi(z)$ for the surface mode as

$$\Phi(z>0)=\Phi_{up}e^{-\kappa_{up}z}, \quad \Phi(z<0)=\Phi_W e^{+\kappa_W z}.$$

Using Eq. (4.181) in each halfspace, one obtains

$$k_x^2+k_y^2-\kappa_{up}^2=0, \tag{4.183}$$

$$k_x^2\varepsilon_{xx}+k_y^2\varepsilon_{yy}-\kappa_W^2\varepsilon_{zz}=0. \tag{4.184}$$

Using the boundary condition Eq. (4.159) one gets

$$n_{up}^2\kappa_{up}\Phi_{up}-\left[\varepsilon_{zz}\left(-\kappa_W\Phi_W\right)+\varepsilon_{zy}\left(-ik_y\Phi_W\right)\right]=-i\frac{4\pi}{\omega}\left(\frac{\partial}{\partial x}j_x^S+\frac{\partial}{\partial y}j_y^S\right)$$

which gives

$$n_{up}^2\kappa_{up}\Phi_{up}+\left[\kappa_W\left(\varepsilon_{zz}+\frac{4\pi}{\omega}k_y\sigma_{yz}^S\right)+gk_y+i\frac{4\pi}{\omega}\left(k_x^2\sigma_{xx}^S+k_y^2\sigma_{yy}^S\right)\right]\Phi_W=0 \tag{4.185}$$

where $\varepsilon_{yz}=-\varepsilon_{zy}=ig=i\frac{4\pi\sigma_{yz}^B}{\omega}$. Using also the boundary condition Eq. (4.182) together with Eqs. (4.163), one obtains

$$\Phi_{up}+\left(i\frac{4\pi}{\omega}\kappa_W\sigma_{zz}^S-\frac{4\pi}{\omega}k_y\sigma_{zy}^S-1\right)\Phi_W=0 \tag{4.186}$$

From these relationships one can get the dispersion equation for surface waves. Note that the

confinement constants κ_W and κ_{up} are generally complex-valued. Their imaginary parts give rise to a Poynting flux away from the surface which contributes to surface wave attenuation.

4.8.1.1 Neglecting Surface States

First, I neglect the surface conductivity to consider surface plasmons supported by bulk carriers only. In this case from Eqs. (4.183), (4.186) one gets $\kappa_{up} = \sqrt{k_x^2 + k_y^2}$, $\Phi_{up} = \Phi_W$. Denoting $k_x^2 + k_y^2 = k^2$, $k_x = k\cos\phi$, $k_y = k\sin\phi$, one obtains from Eq. (4.184)

$$\kappa_W = k\sqrt{\frac{\cos^2\phi\varepsilon_{xx} + \sin^2\phi\varepsilon_{yy}}{\varepsilon_{zz}}}. \tag{4.187}$$

Furthermore, from Eq. (4.185) for $\kappa_{up} = k$ and $\Phi_{up} = \Phi_W$ one has

$$n_{up}^2 k + \kappa_W \varepsilon_{zz} + gk\sin\phi = 0, \tag{4.188}$$

where $\varepsilon_{yz} = ig = i\frac{4\pi\sigma_{yz}^B}{\omega}$. Substituting Eq. (4.187) into Eq. (4.188), one obtains the dispersion relation

$$D(\omega,\phi) = n_{up}^2 + \varepsilon_{zz}\sqrt{\frac{\cos^2\phi\varepsilon_{xx} + \sin^2\phi\varepsilon_{yy}}{\varepsilon_{zz}}} + g\sin\phi = 0. \tag{4.189}$$

The dispersion equation Eq. (4.189) gives the dependence $\omega(\phi)$, but does not have any dependence on the magnitude of k. This situation is similar to the dispersion relation for bulk plasmons in the quasielectrostatic approximation, Eq. (4.157). It is also similar to waves in classical magnetized plasmas. Of course the range of values of k is constrained by the validity of the quasielectrostatic approximation.

4.8.1.2 Including Surface States

If one now include the surface conductivity, Eqs. (4.183)-(4.186) give

$$D(\omega,\phi)-\frac{4\pi}{\omega}k\left[\sqrt{\frac{\cos^2\phi\varepsilon_{xx}+\sin^2\phi\varepsilon_{yy}}{\varepsilon_{zz}}}\left(in_{up}^2\sigma_{zz}^S-\sin\phi\sigma_{yz}^S\right)\right.$$
$$\left.-n_{up}^2\sin\phi\sigma_{yz}^S-i\left(\cos^2\phi\sigma_{xx}^S+\sin^2\phi\sigma_{yy}^S\right)\right]=0 \quad (4.190)$$

where the function $D(\omega,\phi)$ is determined by Eq. (4.189). Taking the surface conductivity into account brings the dependence on the magnitude of the wave vector k into the dispersion relation. Therefore, measuring the frequency dispersion of the surface plasmon resonance provides a direct characterization of surface states.

Figure 4.17 shows the surface plasmon dispersion for propagation along y, i.e. transverse to the gyrotropy x-axis, for two values of the Fermi momentum. The real part of the surface plasmon frequency ignoring the contribution of the surface conductivity is shown as a dashed horizontal line for each value of k_F. Clearly, the contribution of surface electron states is important everywhere, except maybe in a narrow region of small wavenumbers k where the quasistatic approximation breaks down. The plot has a horizontal axis ck in units of meV in order to directly compare with frequencies. The inequality $ck \gg \omega$ is satisfied almost everywhere.

The fact that the contribution of the surface current is so important, can be understood from the structure of Eq. (4.190). Clearly, the relative contribution of the bulk and surface terms can be estimated by comparing the magnitudes of $|\sigma^B|$ and $|k\sigma^S|$ where σ^B and σ^S are appropriate components of bulk and surface conductivity tensors and k is a wavenumber of a given electromagnetic mode. This is true not only for surface modes but also for other electromagnetic wave processes at the boundary such as reflection. In the mid/far-infrared spectral region of interest to us, $|k\sigma^S| \ll |\sigma^B|$ for vacuum wavelengths $ck \sim \omega$. However, for large surface plasmon wavenumbers shown in Fig. 4.17 the opposite condition $|k\sigma^S| \geq |\sigma^B|$ is satisfied.

Note the dispersion in Fig. 4.17 is stronger (the slope is steeper) at frequencies corresponding

to $\mathrm{Re}[\epsilon_{zz}] \approx 0$, i.e. near the resonance for bulk plasmons propagating along z. This follows from Eq. (4.190) where the surface terms contain a factor $1/\sqrt{\epsilon_{zz}}$. Physically, this is expected: as already mentioned, at the plasmon resonance the z-component E_z of the field in the medium becomes very large, which leads to an enhanced contribution of the surface current $j_y^S = \sigma_{yz}^S E_z$.

4.8.2 Surface Waves Beyond the Quasielectrostatic Approximation

For small wavenumbers the quasielectrostatic approximation is no longer valid. On the other hand, in this case one can neglect the surface conductivity as pointed out in the previous paragraph. This is not an interesting limit as far as the spectroscopy of surface states is concerned, but resulting dispersion relation will still be derived for completeness. For the electric field of a surface mode in the upper halfspace with the refractive index n_{up},

$$\boldsymbol{\mathcal{E}}_{up} = \mathrm{Re}\left[\boldsymbol{E}_{up} e^{ik_x x + ik_y y - \kappa_{up} z - i\omega t}\right],$$

the Maxwell's equation for $\nabla \times \boldsymbol{\mathcal{E}}$ gives

$$k_y E_z - i\kappa_{up} E_y = \frac{\omega}{c} B_x, \quad k_x E_z - i\kappa_{up} E_x = -\frac{\omega}{c} B_y, \quad k_x E_y - k_y E_x = \frac{\omega}{c} B_z. \tag{4.191}$$

For the field in the Weyl semimetal,

$$\boldsymbol{\mathcal{E}}_{W} = \mathrm{Re}\left[\boldsymbol{E}_{W} e^{ik_x x + ik_y y + \kappa_W z - i\omega t}\right]$$

the same equation gives, after replacing $\kappa_{up} \to -\kappa_W$ in Eq. (4.191),

$$k_y E_z + i\kappa_W E_y = \frac{\omega}{c} B_x, \quad k_x E_z + i\kappa_W E_x = -\frac{\omega}{c} B_y, \quad k_x E_y - k_y E_x = \frac{\omega}{c} B_z. \tag{4.192}$$

The inverse decay length for the field in the upper halfspace is given by $\kappa_{up}^2 = k^2 - n_{up}^2 \dfrac{\omega^2}{c^2}$.

In a WSM one can use a version of Eq. (4.142) after replacing $k_z \to -i\kappa_W$:

$$\begin{pmatrix} \frac{\omega^2}{c^2}\varepsilon_{xx} - k_y^2 + \kappa_W^2 & k_x k_y & -ik_x\kappa_W \\ k_y k_x & \frac{\omega^2}{c^2}\varepsilon_{yy} - k_x^2 + \kappa_W^2 & i\frac{\omega^2}{c^2}g - ik_y\kappa_W \\ -ik_x\kappa_W & -i\frac{\omega^2}{c^2}g - ik_y\kappa_W & \frac{\omega^2}{c^2}\varepsilon_{zz} - k^2 \end{pmatrix} \begin{pmatrix} E_x \\ E_y \\ E_z \end{pmatrix} = 0, \tag{4.193}$$

where $k^2 = k_x^2 + k_y^2$.

Consider again a surface wave propagating transverse to the anisotropy axis ($k_x = 0$). In this case, there are two solutions to the dispersion equation Eq. (4.193), an O-wave and an X-wave. However, one can show that an O-wave with $E_x \neq 0$ does not exist as a surface wave. Moreover, this statement remains true even with the surface current taken into account. Only the X-wave with $E_{y,z} \neq 0$ can exist as a surface wave. Its inverse confinement length in the Weyl semimetal is given by

$$\kappa_W^2 = \frac{\varepsilon_{yy}}{\varepsilon_{zz}}\left(k^2 - n_X^2\frac{\omega^2}{c^2}\right) \tag{4.194}$$

where

$$n_X^2 = \varepsilon_{zz} - \frac{g^2}{\varepsilon_{yy}}$$

is the refractive index of an extraordinary wave propagating in the volume in the y-direction (see Eq. (4.144) for $\theta = \frac{\pi}{2}$). The polarization of an extraordinary wave is determined by

$$i\left(\frac{\omega^2}{c^2}g + k\kappa_W\right)E_y = \left(\frac{\omega^2}{c^2}\varepsilon_{zz} - k^2\right)E_{zW} \tag{4.195}$$

which follows from Eq. (4.193). After some straightforward algebra, one obtains the dispersion relation for a surface wave:

$$\left(k^2 - \frac{\omega^2}{c^2}n_{up}^2\right)\left(gk + \varepsilon_{zz}\sqrt{\frac{\varepsilon_{yy}}{\varepsilon_{zz}}}\sqrt{k^2 - \frac{\omega^2}{c^2}n_X^2}\right) + \sqrt{k^2 - \frac{\omega^2}{c^2}n_{up}^2}\left(k^2 - \frac{\omega^2}{c^2}\varepsilon_{zz}\right)n_{up}^2 = 0. \tag{4.196}$$

In the limit of large wavenumbers k this equation becomes the quasielectrostatic dispersion relation

Eq. (4.189) at $\phi = \frac{\pi}{2}$.

For the propagation in x-direction, one can repeat the above analysis for the case $k_y = 0$ and obtain that there are no surface wave solutions when the surface conductivity is neglected.

One interesting solution of the dispersion equation Eq. (4.196) is a strongly nonelectrostatic case when the surface mode is weakly localized in a medium above the WSM surface, e.g. in the air. The energy of this wave is mostly contained in an ambient medium above the WSM surface where there is no absorption. Therefore, such surface waves can have a long propagation length; see e.g. [98, 99, 100].

To find this solution I assume $n_{up}^2 = 1$ and introduce the notation $\frac{\omega}{c} = k_0$. A weak localization outside a WSM means that $|\kappa_{up}| \ll k_0$. Then, assuming $k \simeq k_0 + \delta k$, where $k_0 \gg |\delta k|$, one obtains $\kappa_{up} \simeq \sqrt{2k_0\delta k}$. From Eqs. (4.196) and (4.194) in the first order with respect to $\sqrt{\frac{\delta k}{k_0}}$ one gets

$$\delta k \simeq \frac{k_0}{2} \frac{\left(\varepsilon_{zz} - 1\right)^2}{\left[g + \sqrt{\varepsilon_{zz}\varepsilon_{yy}\left(1 - \varepsilon_{zz} + \frac{g^2}{\varepsilon_{yy}}\right)}\right]^2}, \tag{4.197}$$

$$\mathrm{Re}\kappa_W^2 \simeq \mathrm{Re}\left[k_0^2 \frac{\varepsilon_{yy}}{\varepsilon_{zz}}\left(1 - \varepsilon_{zz} + \frac{g^2}{\varepsilon_{yy}}\right)\right]. \tag{4.198}$$

This solution describes surface waves if $\mathrm{Re}[\kappa_W] > 0$ and $\mathrm{Re}[\kappa_{up}] > 0$. In addition, $|\delta k| \ll k_0$ has to be satisfied. It was checked that all three inequalities are satisfied for the numerical parameters chosen to calculate the conductivity tensor. As an example, Fig. 4.18 shows normalized confinement constants $\mathrm{Re}[\kappa_W]/k_0$ and $\mathrm{Re}[\kappa_{up}]/k_0 \simeq \mathrm{Re}[\sqrt{2\delta k/k_0}]$ as functions of frequency, for the Fermi momentum $k_F = 0.5b$. Clearly, the solution describes a surface wave which is weakly confined in the air and strongly confined in the WSM. The spectra remain qualitatively the same with increasing Fermi momentum, but the oscillating feature moves to higher energies, roughly following the spectral region where the real parts of ε_{zz} and ε_{yy} cross zero. Note again that the confinement constants κ_W and κ_{up} are complex-valued. Their imaginary parts give rise to a Poynting flux away from the surface which contributes to surface wave attenuation.

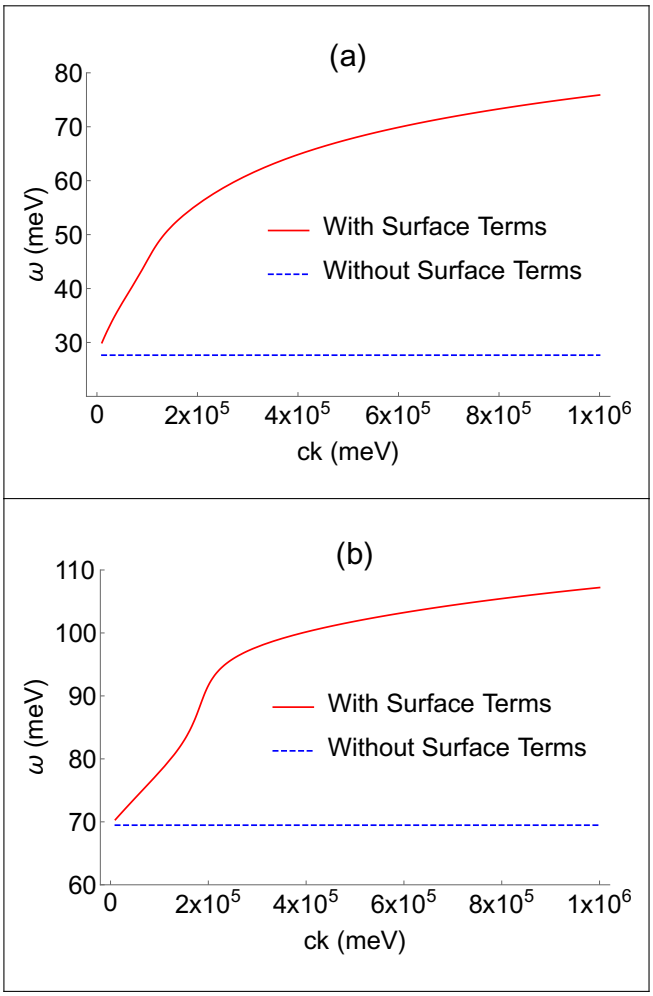

Figure 4.17: Real part of the surface plasmon frequency as a function of real plasmon wavenumber obtained as a solution to the dispersion equation Eq. (4.190) for $\phi = \pi/2$, $\hbar v_F b = 100$ meV and two values of the electron Fermi momentum $k_F = 0.5b$ and $0.8b$. The surface plasmon frequency neglecting surface conductivity contribution is shown as a dashed line. Reprinted with permission from [59].

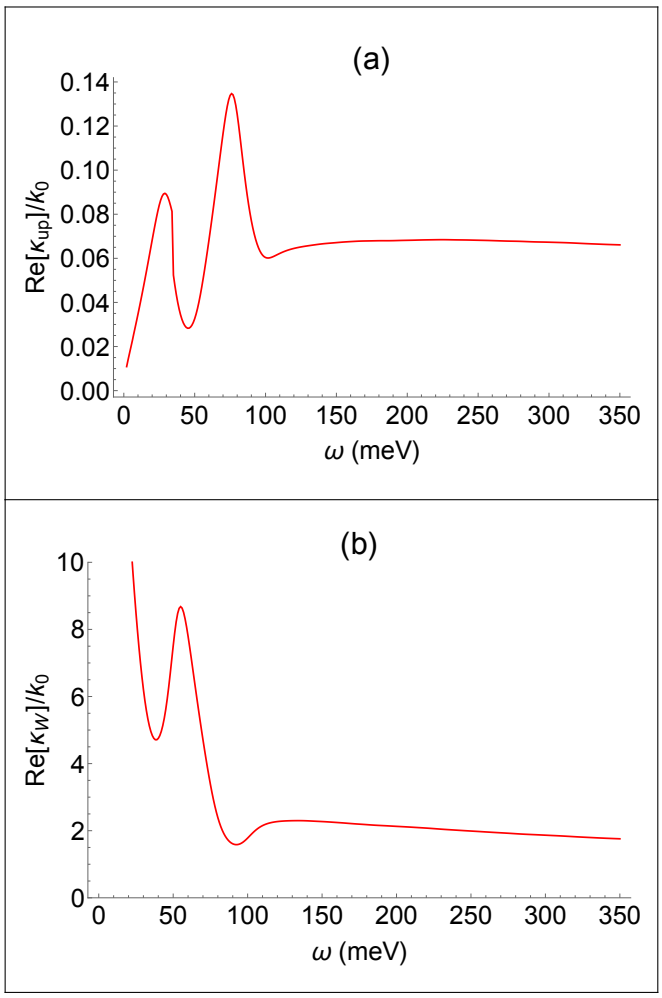

Figure 4.18: Normalized confinement constants (a) $\mathrm{Re}[\kappa_{up}]/k_0 \simeq \mathrm{Re}[\sqrt{2\delta k/k_0}]$ and (b) $\mathrm{Re}[\kappa_W]/k_0$ as functions of frequency, for the Fermi momentum $k_F = 0.5b$. Other parameters are $\hbar v_F b = 100$ meV and $\gamma = 10$ meV. Reprinted with permission from [59].

4.9 Summary

Starting with a microscopic Hamiltonian for a time-reversal breaking Weyl semimetal the tensors of the bulk and surface conductivities were derived. The properties of the conductivities are determined, in part, by the Weyl nodes and the surface states of the WSM. Since there is an interplay between an optical field and the conductivities of the WSM one may use reflection, transmission and polarization of an EM mode as a probe of the WSMs electronic properties. Moreover, the frequency dispersion of surface plasmon-polariton modes, and strong anisotropy of surface plasmon-polaritons with respect to their propagation direction and polarization serves as a sensitive diagnostic tool for the WSMs surface states. WSMs may find potential optoelectronic applications such as a Faraday rotator or even in the field of plasmonics since it demonstrated tight confinement of SPPs.

5. CONCLUSION

In conclusion, I investigated an electric-dipole-forbidden process of THz difference frequency generation in Landau-quantized graphene. The second-order susceptibility turned out to be surprisingly high, equivalent to the bulk magnitude of about 3×10^{-3} m/V. I applied the formalism to the DFG of THz surface plasmon-polaritons in graphene integrated into a dielectric waveguide or cavity with strong vertical confinement of the optical pump modes. The DFG power conversion efficiency of the order of tens μW/W^2 is predicted for structures of size around 100 μm. Analytic expressions for the DFG power were obtained and the results were presented for different structure geometries, composition, and magnetic field strengths.

The feasibility of observing both spontaneous and stimulated parametric decay of photons of a strong laser pump obliquely incident on graphene was demonstrated. The flux of surface plasmons and idler photons generated by parametric decay of the pump was calculated and it was shown that these modes are entangled.

Systematic studies of the optical properties and electromagnetic modes of Weyl semimetals were presented. Both bulk and surface conductivity tensors were derived from a single microscopic Hamiltonian. The presence of separated Weyl nodes and associated surface states give rise to distinct signatures in the transmission, reflection, and polarization of bulk and surface electromagnetic waves. These signatures can be used for quantitative characterization of electronic structure of Weyl semimetals. Particularly sensitive spectroscopic probes of bulk electronic properties include strong anisotropy in propagation of both bulk and surface modes, birefringent dispersion and absorption spectra of ordinary and extraordinary normal modes, the frequency of bulk plasmon resonance as a function of incidence angle and doping level, and the polarization rotation and ellipticity for incident linearly polarized light. The sensitive characterization of surface electronic states can be achieved by measuring the phase change of the reflection coefficient of incident plane waves, the frequency dispersion of surface plasmon-polariton modes, and strong anisotropy of surface plasmon-polaritons with respect to their propagation direction and polarization. In the mid-

infrared and THz spectral regions WSMs (studied here) displayed strong anisotropy, gyrotropy, birefringence, giant polarization rotation (for propagation along axis of gyrotropy), and strong localization of surface plasmon-polariton modes. These effects are tunable by doping. The field of optoelectronics could find applications of WSMs as Faraday isolators, rotators, etc.

REFERENCES

[1] Boyd, R. W. *Nonlinear Optics* (Academic, New York, 2008), 3 rd. edn.

[2] Marder, M. P. *Condensed Matter Physics* (Wiley, New York, 2000).

[3] Kubo, R. *J. Phys. Soc. Jpn.* **12**, 570 (1957).

[4] Katnelson, M. *Graphene Carbon in Two Dimensions* (Cambridge, New York, 2012).

[5] Neto, A. H. C., Guinea, F., Peres, N. M. R., Novoselov, K. S. & Geim, A. K. *Rev. Mod. Phys.* **81**, 109 (2009).

[6] Wallace, P. R. *Phys. Rev.* **71**, 622 (1947).

[7] Novoselov, K. S. *et al. Science* **306**, 666 (2004).

[8] Goerbig, M. O. *Rev. Mod. Phys.* **83**, 1193 (2011).

[9] Fusch, J.-N. & Goerbig, M. O. Introduction to the physical properties of graphene (2008). [Online] http://web.physics.ucsb.edu/~phys123B/w2015/pdf_CoursGraphene2008.pdf.

[10] Ando, T. *J. Phys. Soc. Jpn.* **74**, 777 (2005).

[11] Zheng, Y. & Ando, T. *Phys. Rev. B* **65**, 245420 (2002).

[12] Booshehri, L. G. *et al. Phys. Rev. B* **85**, 205407 (2012).

[13] Kutayiah, A. R., Tokman, M. D., Wang, Y. & Belyanin, A. *Phys. Rev. B* **98**, 115410 (2018).

[14] Grigorenko, A. N., Polini, M. & Novoselov, K. S. *Nat. Photonics* **6**, 749 (2012).

[15] Bludov, Y. V., Ferreira, A., Peres, N. M. R. & Vasilevskiy, M. I. *International Journal of Modern Physics B* **27**, 1341001 (2013).

[16] Rana, F. *IEEE Transactions on Nanotechnology* **7**, 91 (2008).

[17] Jablan, M., Buljan, H. & Soljacic, M. *Phys. Rev. B* **80**, 245435 (2009).

[18] Koppens, F. H. L., Chang, D. E. & de Abajo, F. J. G. *Nano Lett.* **11**, 3370 (2011).

[19] Craciun, M. F., Russo, S., Yamamoto, M. & Tarucha, S. *Nano Today* **6**, 42 (2011).

[20] Mikhailov, S. A. *Phys. Rev. B* **79**, 241309(R) (2009).

[21] Hendry, E., Hale, P. J., Moger, J., Savchenko, A. K. & Mikhailov, S. A. *Phys. Rev. Lett.* **105**, 097401 (2010).

[22] Yao, X. & Belyanin, A. *Phys. Rev. Lett.* **108**, 255503 (2012).

[23] Yao, X., Tokman, M. D. & Belyanin, A. *Phys. Rev. Lett.* **112**, 055501 (2014).

[24] Wang, Y., Tokman, M. & Belyanin, A. *Phys. Rev. B* **94**, 195442 (2016).

[25] Mikhailov, S. A. *Phys. Rev. B* **84**, 045432 (2011).

[26] Dean, J. J. & van Driel, H. M. *Phys. Rev. B* **82**, 125411 (2010).

[27] Tokman, M., Wang, Y., Oladyshkin, I., Kutayiah, A. R. & Belyanin, A. *Phys. Rev. B* **93**, 235422 (2016).

[28] Cheng, J. L., Vermeulen, N. & Sipe, J. E. *Sci. Rep.* **7**, 43843 (2017).

[29] Jamalpoor, K., Zarifkar, A. & Miri, M. *Photonics and Nanostructures - Fundamentals and Applications* **26**, 80 (2017).

[30] Yao, B. *et al. Nature Photonics* **12**, 22 (2017).

[31] Cao, J., Kong, Y., Gao, S. & Liu, C. *Opt. Commun.* **406**, 183 (2018).

[32] Giovannetti, G., Khomyakov, P. A., Brocks, G., Kelly, P. J. & van den Brink, J. *Phys. Rev. B* **76**, 073103 (2007).

[33] Decker, R. *et al. Nano Lett.* **11**, 2291 (2011).

[34] Yang, W. *et al. Nat. Mater.* **12**, 792 (2013).

[35] Rosencher, E. & Vinter, B. *Optoelectronics* (Cambridge, New York, 2002). (P. Piva, Trans.).

[36] Yang, C. H., Peeters, F. M. & Xu, W. *Phys. Rev. B* **82**, 205428 (2010).

[37] Funk, H., Knorr, A., Wendler, F. & Malic, E. *Phys. Rev. B* **92**, 205428 (2015).

[38] Wang, Y., Tokman, M. & Belyanin, A. *Phys. Rev. A* **91**, 033821 (2015).

[39] Tokman, M., Yao, X. & Belyanin, A. *Phys. Rev. Lett.* **110**, 077404 (2013).

[40] Shearer, C. J., Slattery, A. D., Stapleton, A. J., Shapter, J. G. & Gibson, C. T. *Nanotechnology* **27**, 125704 (2016).

[41] Yao, X. & Belyanin, A. *J. Phys.: Condens. Matter* **25**, 054203 (2013).

[42] Smirnova, D., Shadrivov, I. V., Miroshnichenko, A. E., Smirnov, A. & Kivshar, Y. S. *Phys. Rev. B* **90**, 035412 (2014).

[43] Kwiat, P. G. *et al. Phys. Rev. Lett.* **75**, 4337 (1995).

[44] Shen, Y. R. *The Principles of Nonlinear Optics* (Wiley, New Jersey, 2003).

[45] Scully, M. & Zubairy, M. *Quantum Optics* (Cambridge, New York, 1997).

[46] Garrison, J. C. & Chiao, R. Y. *Quantum Optics* (Oxford, New York, 2008).

[47] Lukin, M. D. *Rev. Mod. Phys.* **75**, 457 (2003).

[48] Vdovin, V. & Tokman, M. *Phys. Rev. A* **87**, 012323 (2013).

[49] Fain, V. M. & Khanin, Y. I. *Quantum Electronics*, vol. 1 (MIT, Massachusetts, 1969).

[50] Tokman, M., Wang, Y. & Belyanin, A. *Phys. Rev. B* **92**, 075409 (2015).

[51] Tokman, M. D., Erukhimova, M. A. & Vdovin, V. V. *Annals of Physics* **360**, 571 (2015).

[52] Bekefi, G. *Radiation Processes in Plasmas* (Wiley, New Jersey, 1966).

[53] Constant, T. J., Hornett, S. M., Chang, D. E. & Hendry, E. *Nature Phys.* **12**, 124 (2016).

[54] Belkin, M. *et al. Nat. Photonics* **1**, 288 (2007).

[55] Mikhailov, S. A. *Phys. Rev. B* **90**, 241301(R) (2014).

[56] Il'inskii, Y. A. & Keldysh, L. V. *Electromagnetic Response of Material Media* (Springer, New York, 1994).

[57] Tokman, M. D. & Erukhimova, M. A. *Phys. Rev. E* **84**, 056610 (2011).

[58] Zhang, H. J. *et al. Nat. Phys.* **5**, 438 (2009).

[59] Chen, Q., Kutayiah, A. R., Oladyshkin, I., Tokman, M. & Belyanin, A. *Phys. Rev. B* **99**, 075137 (2019).

[60] Volovik, G. E. Quantum phase transitions from topology in momentum space. In Unruh, W. & Schutzhold, R. (eds.) *Quantum Analogues: From Phase Transitions to Black Holes and Cosmology*, Lecture Notes in Physics, 31 (Springer-Verlag Berlin Heidelberg, New York, 2007).

[61] Hosur, P. & Qi, X. *Compt. Rend. Phys.* **14**, 857 (2013).

[62] Yan, B. & Felser, C. *Annu. Rev. Condens. Matter Phys.* **8**, 337 (2017).

[63] Hasan, M. Z., Xu, S.-Y., Belopolski, I. & Huang, S.-M. *Annu. Rev. Condens. Matter Phys.* **8**, 289 (2017).

[64] Armitage, N. P., Mele, E. J. & Vishwanath, A. *Rev. Mod. Phys.* **90**, 015001 (2018).

[65] Burkov, A. A. *Annu. Rev. Condens. Matter Phys.* **9**, 359 (2018).

[66] Kotov, O. V. & Lozovik, Y. E. *Phys. Rev. B* **98**, 195446 (2018).

[67] Sushkov, A. B. *et al. Phys. Rev. B* **92**, 241108(R) (2015).

[68] Spivak, B. Z. & Andreev, A. V. *Phys. Rev. B* **93**, 085107 (2016).

[69] Zhou, J., Chang, H. & Xiao, D. *Phys. Rev. B* **91**, 035114 (2015).

[70] Pellegrino, F. M. D., Katsnelson, M. I. & Polini, M. *Phys. Rev. B* **92**, 201407(R) (2015).

[71] Tabert, C. J., Carbotte, J. P. & Nicol, E. J. *Phys. Rev. B* **93**, 085426 (2016).

[72] Ashby, P. E. C. & Carbotte, J. P. *Phys. Rev. B* **89**, 245121 (2014).

[73] Ma, J. & Pesin, D. A. *Phys. Rev. B* **92**, 235205 (2015).

[74] Gorbar, E. V., Miransky, V. A., Shovkovy, I. A. & Sukachov, P. O. *Phys. Rev. B* **95**, 115202 (2017).

[75] Ashby, P. E. C. & Carbotte, J. P. *Phys. Rev. B* **87**, 245131 (2013).

[76] Long, Z., Wang, Y., Erukhimova, M., Tokman, M. & Belyanin, A. *Phys. Rev. Lett.* **120**, 037403 (2018).

[77] Chen, R. Y. *et al. Phys. Rev. Lett.* **115**, 176404 (2015).

[78] Tabert, C. J. & Carbotte, J. P. *Phys. Rev. B* **93**, 085442 (2016).

[79] Zyuzin, A. A. & Burkov, A. A. *Phys. Rev. B* **86**, 115133 (2012).

[80] Kargarian, M., Randeria, M. & Trivedi, N. *Sci. Rep.* **5**, 12683 (2015).

[81] Hofmann, J. & Sarma, S. D. *Phys. Rev. B* **91**, 241108 (2016).

[82] Ukhtary, J. M. S., Nugraha, A. R. T. & Saito, R. *J. Phys. Soc. Jpn.* **86**, 104703 (2017).

[83] Okugawa, R. & Murakami, S. *Phys. Rev. B* **89**, 235315 (2014).

[84] Andolina, G. M., Pellegrino, F. M. D., Koppens, F. H. L. & Polini, M. *Phys. Rev. B* **97**, 125431 (2018).

[85] Asbóth, J. K., Oroszlány, L. & Pályi, A. A short course on topological insulators: Band-structure topology and edge states in one and two dimensions (2015). arXiv:1509.02295.

[86] Pal, P. B. *Am. J. Phys.* **79**, 485 (2011).

[87] Lancaster, T. & Blundell, S. J. *Quantum Field Theory for the Gifted Amateur* (Oxford, New York, 2014).

[88] Zee, A. *Quantum Field Theory in a Nutshell* (Princeton, New Jersey, 2003).

[89] Pal, P. B. Representation-independent manipulations with dirac matrices and spinors (2007). arXiv:physics/0703214.

[90] Turner, A. M. & Vishwanath, A. Beyond band insulators: Topology of semi-metals and interacting phases (2013). arXiv:1301.0330.

[91] Griffiths, D. J. *Introduction to Quantum Mechanics* (Pearson Prentice Hall, New Jersey, 2005), 2 nd. edn.

[92] Xiao, D., Chang, M.-C. & Niu, Q. *Rev. Mod. Phys.* **82**, 1959 (2010).

[93] Pinto, A. C. A., Nemes, M. C., de Faria, J. G. P. & Thomaz, M. T. *Am. J. Phys.* **68**, 955 (2000).

[94] Berry, M. V. *Proc. R. Soc. Lond.* **A 394**, 45 (1984).

[95] Lu, H.-Z. & Shen, S.-Q. *Frontiers of Physics* **12**, 127201 (2017).

[96] Arikawa, T., Zhang, Q., Ren, L., Belyanin, A. A. & Kono, J. *J. Infrared Millim. Terahertz Waves* **34**, 724 (2013).

[97] Song, J. C. W. & Rudner, M. S. *Phys. Rev. B* **96**, 205443 (2017).

[98] Barnes, W. L., Dereux, A. & Ebbesen, T. W. *Nature* **424**, 824 (2003).

[99] Homola, J., Yee, S. S. & Gauglitz, G. *Sensors and Actuators B: Chemical* **54**, 3 (1999).

[100] Agranovich, M. & Mills, D. L. (eds.) *Surface Polaritons - Electromagnetic Waves at Surfaces and Interfaces*, vol. 1 of *Modern Problems in Condensed Matter Sciences* (Elsevier, New York, 1982).